



DISLOCATION ARRANGEMENTS IN
DEFORMED ALPHA-ZIRCONIUM

A.J. BEDFORD
(B.App.Sc., Hons)

DEPARTMENT OF
CHEMICAL ENGINEERING
(MATERIALS SCIENCE)

Ph.D THESIS
DECEMBER 1970

TABLE OF CONTENTS

	SUMMARY.....	1
	DECLARATION	4
	ACKNOWLEDGEMENTS	5
	PREFACE	7
1.	INTRODUCTION	10
1.1	Slip in H.C.P. Metals	12
1.2	Deformation Modes in Zirconium	17
1.3	Electron Microscope Studies	22
2.	EXPERIMENTAL	26
2.1	Materials and Specimen Preparation	26
2.2	Preparation of Specimens for Electron Microscopy	30
2.3	Electron Microscope Calibration and Stereomicroscopy	49
2.4	Deformation Apparatus	52
3.	CRYSTALLOGRAPHY	61
3.1	Lattice Notation and the Reciprocal Lattice	62
3.2	Kikuchi Maps	66
3.3	Burgers Vector Determination	72
3.4	Discussion of Crystallography	75

4.	ELECTRON MICROSCOPE STUDY OF DEFORMED ZIRCONIUM	95
4.1	Introduction	95
4.2	Slow Strain Rate Experiments	96
4.3	Higher Strain Rate Experiments	99
4.4	Discussion of Dislocation Behaviour in Deformed Zirconium	120
4.5	Recovery of Deformed Zirconium	135
4.6	Hexagonal Networks of Dislocations	145
4.7	Mechanisms of Dislocation Network Formation	153
5.	STRAIN-AGEING BEHAVIOUR	176
5.1	Introduction	176
5.2	Internal Friction Results	190
5.3	Electron Microscopy	192
5.4	Discussion of Strain-Ageing in Zirconium.	211
6.	SUMMARY, CONCLUSIONS AND SUGGESTIONS FOR FUTURE WORK	229
APPENDIX 1.	HYDRIDES AND ZIRCONIUM THIN FOILS ..	239
A.	Hydride Precipitate Shape	240
B.	Nucleation Sites for Precipitates ..	241
C.	Habit Planes of Hydrides	244

APPENDIX 2.	CRYSTALLOGRAPHIC DATA	253
APPENDIX 3.	PUBLISHED PAPERS	259
A.	Crystallographic Procedures for the Electron Microscopy of Hexagonal Metals	
	A.J. Bedford and D.R. Miller	259
B.	On Indexing Electron Diffraction Patterns for Hexagonal Zirconium Alloys.	
	A.J. Bedford	275
BIBLIOGRAPHY		286



SUMMARY

A study of the dislocation structures which result from the deformation of relatively pure polycrystalline alpha-zirconium has been made in an attempt to explain some of the yielding phenomena in zirconium. Specimens were strained in tension at one of two strain rates (10^{-4} sec^{-1} and 10^{-5} sec^{-1}) and all experiments were carried out in a vacuum of the order of 10^{-5} torr at temperatures between 0 and 600°C .

The production of thin zirconium foils suitable for study by transmission electron microscopy was examined in some detail, and particular reference was made to hydride precipitation during foil preparation.

The crystallography of hexagonal lattices was examined and simplified procedures for carrying out tilting experiments in the electron microscope were developed. The complexity of the analysis of electron diffraction results from hexagonal lattices has been considerably reduced by following simple, but important, rules regarding the interrelations between electron images (real space) and their diffraction patterns (reciprocal space). A Kikuchi map covering a large range of orientations was produced to aid in the above procedures and analyses. Throughout the thesis, emphasis has been placed on the use of three-axis, three-index,

"Miller" notation for planes and directions in the hexagonal lattices and several advantages over the "Miller-Bravais" notation, for the kind of problem encountered in the present work, are discussed.

The behaviour of dislocations during slow strain rate deformation of α -zirconium at various temperatures in the range 0 - 600°C was examined. The dislocation arrangements produced by deformation varied in a quite complex manner with temperature and could be roughly classified into four groups. Between 0 and 200°C, strains up to about 4% produced a relatively random dislocation array. In the range 200-350°C a dislocation cell structure was produced but at temperatures between 350 and 450°C a relatively uniform dislocation array was again observed. Finally, above 500°C a cellular subgrain type structure, which contained hexagonal dislocation networks, was developed.

Hexagonal dislocation networks could be produced either by straining above 500°C or by straining at room temperature followed by recovery between 400° and 600°C and these networks were shown to be non-coplanar. Such networks were analysed and mechanisms to explain their formation have been put forward. The mechanisms are based on the fact that the Burgers vectors of all dislocations in deformed zirconium were of the type $\langle 100 \rangle$, (i.e. $1/3 \langle 11\bar{2}0 \rangle$), and the dislocations

could almost always be shown to have slipped on the prism planes $\{100\}$, (i.e. $\{10\bar{1}0\}$).

Correlations between surface slip lines and dislocation structures were made for specimens deformed in each of the temperature ranges.

The creep rate of zirconium alloys in the range 200 - 500°C has been previously found to be anomalously low and this has been associated with strain-ageing behaviour. Results from the Australian Atomic Energy Commission's program on Zircaloy-2 and zirconium oxygen alloys were examined in the light of electron microscope results obtained in the present work. An explanation of the strain-ageing phenomenon has been proposed and is supported to some extent by internal friction results obtained by a colleague in this laboratory. In short, the explanation is based on a dislocation locking effect due to both dislocation-dislocation interactions and pinning due to interstitial oxygen atoms.

DECLARATION.

To the best of the author's knowledge and belief, the material in this thesis, except where due reference is made or where common knowledge is assumed, is original. No part of this work has been submitted for any other degree or award in any university.

A.J. BEDFORD.

ACKNOWLEDGEMENTS.

The author is deeply indebted to Professor D.R. Miller, not only for his guidance and interest throughout the work, but for the way in which he allowed a great deal of freedom during the investigation while simultaneously making the author the beneficiary of his intellect and experience.

Mr. P.G. Fuller gave the author permission to use unpublished work and also lent assistance in the understanding of internal friction phenomena for which the author is particularly grateful.

The Australian Atomic Energy Commission partly financed the research (contract 69/C/13) and also contributed significantly to the experimental results on strain-ageing behaviour. In particular, thanks are due to Dr. W.B. Rotsey for his collaboration and helpful discussions.

Financial assistance was given by the Australian Research Grants Committee to Professor Miller for this research and this is gratefully acknowledged. The author is indebted to the Commonwealth of Australia, Department of Supply, for a Post-Graduate studentship. The continued support of Dr. L.E. Samuels of the Defence Standards

Laboratories was appreciated.

The author would also like to register his appreciation to his colleagues in the Materials Science Group of the Chemical Engineering Department of the University of Adelaide and also to the workshop staff for the assistance given. Particular thanks are due to Mr. B.H.Ide who significantly contributed to the design, construction and maintenance of the apparatus associated with this project. The help of Dr. J.R. Baxter at the Weapons Research Establishment, Salisbury, in the selection and construction of the specimen heating facilities was appreciated.

PREFACE

The work reported in this thesis constitutes an attempt to interpret and explain several mechanical properties of zirconium in terms of the dislocation substructures produced during deformation and heat treatment. This has formed part of a more general research program in the Materials Science Group, which is aimed at investigating the behaviour of dislocations during deformation, and the effects of interstitial atoms, on the mechanical properties of zirconium and its alloys. The research has been carried out in close collaboration with the Materials Division of the Australian Atomic Energy Commission Research Establishment, from whom many of the high temperature yielding results were obtained.

Emphasis has been placed on the transmission electron microscopy of zirconium thin foils and the nature of the topics covered in this project has meant that, for clarity, a number of different sections have been treated as separate subjects, and a discussion has been included at the end of each of these sections.

The introduction gives an outline of the relevance of the research and it contains a brief review of the published literature on deformation mechanisms in pure

zirconium.

Chapter 2 is concerned with apparatus and experimental techniques and in particular includes a section on the electropolishing procedures for producing thin foils for the electron microscope.

During a preliminary study on the electron microscopy of zirconium, it was found that many of the previously published papers contained errors which arose because of the lack of understanding of the more complex crystallographic procedures for hexagonal metals. To overcome these problems some simplified procedures have been adopted and these are discussed in Chapter 5 of the thesis.

The deformation of zirconium at elevated temperatures is outlined in Chapter 4 and the discussions primarily concern the interpretation of electron microscope results obtained from foils prepared from the deformed specimens. Dislocation reactions which occur during high temperature deformation and recovery are discussed in detail.

In chapter 5, observations of dislocation structures in deformed zirconium are used to explain the strain-ageing behaviour which occurs in zirconium at high temperatures. These observations, together with the internal friction results obtained by Fuller of this laboratory, enable an explanation of the dynamic strain-ageing to be put forward,

which in turn is related to the anomalies in the creep of zirconium in this same temperature range.

CHAPTER 1.

INTRODUCTION

Zirconium alloys are used in nuclear applications because of their low neutron absorption cross section, their high resistance to corrosion and the relative ease with which they may be formed. Since Australia's first nuclear reactor may use natural uranium fuel, the importance of zirconium alloys has been highlighted in this country. A commonly used zirconium alloy is Zircaloy-2 ($Zr+1.5Sn+0.15Fe+0.10Cr+0.10Ni$) and although this alloy has been used in nuclear reactors, its mechanical properties are not yet fully understood. In particular the creep rate appears to be anomalously low near $300^{\circ}C$ and since this lies within the temperature range ($200-500^{\circ}C$) to which pressure tubes and casing tubes are subjected, the behaviour has important consequences. Although quite a large amount of work has been done on Zircaloy-2 and zirconium-niobium alloys, the really fundamental studies, to provide information on the basic deformation mechanisms, are best carried out on pure zirconium. In the present investigation use was made of zirconium of the highest purity available.

In the studies of the mechanical properties of zirconium which have been made (Tresco (1953), Manjoine and Mudge (1954), Keeler (1955), Guard and Keeler (1957),

Coleman and Hardie (1966), Edmonds and Beevers (1968), Baldwin and Reed-Hill (1968), Weinstein (1969)), the materials used contained differing and sometimes uncertain levels of impurities. The mechanical tests were often carried out over small temperature ranges and these were not necessarily the ones of interest for the nuclear applications. In addition the above authors have not really interpreted their observations in terms of the changes in dislocation structure which occur and it is this aspect of the work which is, in part, covered in this thesis.

Due to the difficulty in carrying out true creep tests over very long time intervals, the procedure adopted was to deform specimens by low strain rate tensile testing on the assumption that, as with other metals (e.g. Al, Cu, etc.) the dislocation reactions occurring could be related to the structural changes which occur in genuine creep conditions. The strain rates used fell between the very low creep strain rate regime and the fast strain rate tensile test regime.

Previously reported work on the deformation mechanisms in zirconium have relied mainly on mechanical test results and optical microscope examinations. Only a limited amount has been reported on electron microscopy of thin zirconium foils. Since zirconium has a close packed hexagonal

structure (below 860°C) the interpretation of electron micrographs is complex but in Chapter 3 procedures which were derived to simplify specimen manipulations in the microscope and the interpretation of the electron micrographs and diffraction patterns are discussed.

The following sections of the introduction give a general outline of the reported deformation mechanisms in zirconium. Results which are particularly related to high temperature deformation and strain-ageing behaviour are surveyed and discussed in chapters 4 and 5.

1.1 SLIP IN H.C.P. METALS

Pure zirconium has an axial ratio of 1.593 and the basic slip systems known to occur in zirconium fit a general behaviour pattern which occurs in many hcp metals. Table I shows the relative packing densities of the first order prism and pyramidal planes, based on a packing density of unity for the basal planes, and both Tables I and II indicate the slip systems observed in the hcp metals. From the simple isotropic elasticity theory it can be concluded that the initiation of slip in a metal crystal should be easiest in the most closely packed plane and in the direction of closest packing within this plane. Therefore, in zirconium, the prism planes,

$\{10\bar{1}0\}$ (i.e. $\{100\}$), would be expected to be the primary slip planes with a slip direction $\langle 11\bar{2}0 \rangle$ (i.e. $\langle 100 \rangle$). However, it would also be anticipated that for zirconium and titanium, the basal plane would offer an almost equal chance of slip. The anomaly to this rule is beryllium for which the predominant slip plane is the basal plane.

A more advanced theoretical approach has been made by taking into account the axial ratios, stacking fault energies and anisotropy of elastic constants (Roy (1967), Tyson (1967), Yoo and Wei (1967), Fisher and Alfred (1968), Tyson (1969)). This somewhat modified the order of the likely slip planes and was able to account for the apparent anomaly in the behaviour of beryllium. Therefore, to some extent, the validity of the anisotropic elasticity approach was established.

TABLE I RELATIVE PACKING DENSITIES OF BASAL, PRISM AND PYRAMIDAL PLANES IN H.C.P. METALS ^{1,2}

METAL	c/a	PACKING DENSITIES			OBSERVED SLIP PLANES IN ORDER OF EASE OF OPERATION.			
		(0001)	(10 $\bar{1}$ 0)	(10 $\bar{1}$ 1)				
CADMIUM	1.886	1.000	0.918	0.816	(0001)	(10 $\bar{1}$ 0)	(10 $\bar{1}$ 1)	(11 $\bar{2}$ 2)
ZINC	1.856	1.000	0.933	0.846	(0001)	(10 $\bar{1}$ 0)	(11 $\bar{2}$ 2)	(10 $\bar{1}$ 1)
MAGNESIUM	1.624	1.000	1.066	0.940	(0001)	(10 $\bar{1}$ 1)	(10 $\bar{1}$ 0)	
TITANIUM	1.587	1.000	1.092	0.959	(10 $\bar{1}$ 0)	(0001)	(10 $\bar{1}$ 1)	
ZIRCONIUM	1.593	1.000	>1.0	<1.0	(10 $\bar{1}$ 0)	(0001)	(10 $\bar{1}$ 1)	(11 $\bar{2}$ 2)
BERYLLIUM	1.568	1.000	>1.0	-	(0001)	(10 $\bar{1}$ 0)	(10 $\bar{1}$ 1)	
COBALT	1.623	1.000	≈1.06	≈0.94	(0001)			
THALLIUM	1.598	1.000	-	-	(10 $\bar{1}$ 0)			(0001)

The order of ease of operation varies slightly in some reports.

1. HONEYCOMBE, R.W., - Deformation of Metal Crystals. p.111
2. YOO, M.H., and WEI, G.T. (1967) J. App. Phys. 38, 4317

TABLE II SLIP SYSTEMS IN HEXAGONAL CRYSTALS ^{1,2}.

METAL OR ALLOY	AXIAL RATIO	SLIP SYSTEMS	REMARKS
CADMIUM	1.886	(0001) [11 $\bar{2}$ 0]	Principal Slip system.
		(1 $\bar{1}$ 00) [11 $\bar{2}$ 0]	High temperature ^{1,2}
		(1 $\bar{1}$ 01) [11 $\bar{2}$ 0]	Room temperature ²
		(11 $\bar{2}$ 2) [11 $\bar{2}$ 0]	Room, high or low temperature ²
ZINC	1.856	(0001) [11 $\bar{2}$ 0]	Principal Slip System
		(1 $\bar{1}$ 00) [11 $\bar{2}$ 0]	High temperature ¹
		(1 $\bar{1}$ 01) [11 $\bar{2}$ 0]	Room temperature ²
		(11 $\bar{2}$ 2) [11 $\bar{2}$ 3]	Room temperature ²
MAGNESIUM	1.624	(0001) [11 $\bar{2}$ 0]	Principal Slip System
		(1 $\bar{1}$ 00) [11 $\bar{2}$ 0]	All temperatures
		(1 $\bar{1}$ 01) [11 $\bar{2}$ 0]	All temperatures - mainly high temp.
COBALT	1.621	(0001) [11 $\bar{2}$ 0]	Only slip system (Ref 2)
		(11 $\bar{2}$ 2) [11 $\bar{2}$ 3]	Secondary Slip system (Ref.1)
ZIRCONIUM	1.593	(0001) [11 $\bar{2}$ 0]	Room temperature ²
		(1 $\bar{1}$ 00) [11 $\bar{2}$ 0]	Principal Slip System
		(1 $\bar{1}$ 01) [11 $\bar{2}$ 0]	low or high temp ²
		(11 $\bar{2}$ 2) [11 $\bar{2}$ 3]	low or high temp ²

TABLE II (CONTINUED)

METAL OR ALLOY	AXIAL RATIO	SLIP SYSTEMS	REMARKS
TITANIUM	1.587	(0001) [11 $\bar{2}$ 0]	More common in impure metal ²
		(1 $\bar{1}$ 00) [11 $\bar{2}$ 0]	Principal Slip System
		(1 $\bar{1}$ 01) [11 $\bar{2}$ 0]	All temps ² . In impure metal ¹
BERYLLIUM	1.567	(0001) [11 $\bar{2}$ 0]	Principal Slip System
		(1 $\bar{1}$ 00) [11 $\bar{2}$ 0]	All temperatures ²
		(1 $\bar{1}$ 01) [11 $\bar{2}$ 0]	All temperatures ²
ϵ -Ag-Zn ¹	1.557	(0001) [11 $\bar{2}$ 0]	Non-basal slip
		(1 $\bar{1}$ 00) [11 $\bar{2}$ 0]	increases with
Solid to Solution	1.571	(1 $\bar{1}$ 01) [11 $\bar{2}$ 0]	decreasing c/a ratio
γ -Ag ₂ Al ¹	1.588	(0001) [11 $\bar{2}$ 0]	
		(1 $\bar{1}$ 00) [11 $\bar{2}$ 0]	

1. HONEYCOMBE, R.W., Deformation of Metal Crystals .
2. YOO, M.H., and WEI, C.T., (1967) J. App. Phys., 38,4317.

The above approach is based on elasticity theories and therefore has some limitations when applied to plastic behaviour. A more rigorous approach to plastic behaviour has recently been made by Regnier and Dupouy (1970) who considered the relative ease of dislocation dissociations in basal and prismatic planes. By analysing the dislocations and the energies involved they were able to propose an explanation of the slip systems likely to operate. This too, has been shown to favour the apparent abnormal basal slip in beryllium..

The above theories predict that the primary slip system for zirconium and titanium is $\{10\bar{1}0\} \llbracket 11\bar{2}0 \rrbracket$, (or $\{100\} \llbracket 100 \rrbracket$). The stacking fault energy is generally believed to be high and extended dislocations would not be expected.

1.2 DEFORMATION MODES IN ZIRCONIUM

As a general rule, the approaches made to the determination of deformation modes in zirconium have been based on slip trace analyses on specimens deformed in tension or compression. Almost invariably the test temperature chosen was near -196° , 25° or 300°C or within the range $500 - 800^{\circ}\text{C}$. It is perhaps unfortunate that the detailed mechanical properties in the range $200-500^{\circ}\text{C}$ have not been adequately studied. This is the important operating range of

nuclear reactors and the mechanical property data in this range are discussed in Chapters 4 and 5. The following sections give a summary of the deformation modes reported in pure zirconium or zirconium containing relatively small amounts of impurity.

1.2.1 Prismatic Slip

At -196°C , Rapperport and Hartley (1960) observed only the $\{10\bar{1}0\} \langle 11\bar{2}0 \rangle$ slip system in specimens loaded in tension. The same slip system was observed by Baldwin and Reed-Hill (1965) at -196°C but they also noted slip traces parallel to $\{10\bar{1}1\}$ and $\{11\bar{2}2\}$ planes.

In specimens tested at room temperature, the primary slip system observed was $\{10\bar{1}0\} \langle 11\bar{2}0 \rangle$ (Rapperport (1959), Baldwin and Reed-Hill (1965), Martin and Reed-Hill (1964), Westlake (1965)), and the active slip system at 300°C was also found to be $\{10\bar{1}0\} \langle 11\bar{2}0 \rangle$.

Rapperport and Hartley (1960) have reported investigations at 800°C and they observed only the $\{10\bar{1}0\} \langle 11\bar{2}0 \rangle$ slip system.

1.2.2 Basal Slip

There has been some contention over the occurrence

of basal slip in zirconium. Rapperport and Hartley (1960) reported that basal slip was not observed on deforming large grained pure zirconium (200 ppm O_2 impurity) at -196° , 300° and $800^\circ C$. Very severe tests in which the resolved shear stress on the basal plane was nine to twenty five times that on the $\{10\bar{1}0\}$ prism planes still failed to induce basal slip. They therefore concluded that the critical resolved shear stress for slip on the basal plane was very much higher than that on the prism planes $\{10\bar{1}0\}$. Rapperport and Hartley further concluded that basal slip became more difficult in both zirconium and titanium as the purity was increased.

Baldwin and Reed-Hill (1965) have, however, observed the presence of basal slip as well as prism slip at test temperatures of -196° , 25° and $350^\circ C$ in torsional straining tests. Their method of applying the stress could have resulted in very high resolved shear stresses on the basal planes.

Martin and Reed-Hill (1964) found that the only slip system which could explain their observations of kink bands was the $\{0002\} \langle 11\bar{2}0 \rangle$ system. They implied that basal slip was a secondary slip system in zirconium and that the likelihood of basal slip became greater as the temperature increased from -196° to $540^\circ C$.

Bailey (1962) also reported that basal slip could

occur, under the influence of suitable stress fields, in thin zirconium foils.

1.2.3 Other Slip Systems

Dislocation motion was induced in thin zirconium foils in an electron microscope by beam heating techniques (Howe et al. (1962)). The major slip system observed was $\{10\bar{1}0\}\langle 11\bar{2}0\rangle$ but slip on $\{10\bar{1}3\}$ and $\{11\bar{2}1\}$ planes in the $\langle 11\bar{2}0\rangle$ directions was also observed. It was noticed that dislocation motion was made easier in the presence of surface contamination (oxide). The zone axes of the foils in which the observations were made were near $[1\bar{1}00]$ and $[11\bar{2}0]$. These zone axes would not be expected to occur in textured polycrystalline zirconium produced by normal cold rolling and annealing procedures. No selected area diffraction patterns were published and no estimate of the temperatures attained in the foils was given and therefore the results must be viewed with caution.

In summarizing their recent work on polycrystalline zirconium, Reed-Hill et al. (1969) concluded that zirconium was able to deform by slip on all the planes previously identified as major slip planes in other hexagonal metals. They also noted that the greater ductility shown by zirconium at sub-ambient temperatures was related to the large

number of active slip planes it possesses and that the high temperature ductility was due to the ability of zirconium to slip on the basal plane.

1.2.4 Twinning.

In contrast to many metals, both the strength and ductility of zirconium increase with decreasing temperature and this has been related to the fact that twinning becomes profuse and complex at lower temperatures (Douglass (1963), Reed-Hill et al. (1965)).

It has been generally agreed that there are four main twinning planes in zirconium; $\{10\bar{1}2\}$, $\{11\bar{2}1\}$, $\{11\bar{2}2\}$ and $\{11\bar{2}3\}$. Rapperport and Hartley (1960) studied the effect of temperature on twinning and found that the above twin planes were operative at all temperatures from 77° to 1075°K . The $\{11\bar{2}1\}$ and $\{10\bar{1}2\}$ planes were the primary twinning planes. The difference between a $\{10\bar{1}2\}$ and a $\{11\bar{2}1\}$ twin can be easily seen under the optical microscope. $\{10\bar{1}2\}$ twins have a lenticular shape whereas $\{11\bar{2}1\}$ twins have straight parallel boundaries. The contribution of each of the two main twinning modes varies with temperature and type of deformation, and depends also on the twinning shear which takes place. The latter parameter is much larger for $\{11\bar{2}1\}$ twins than for $\{10\bar{1}2\}$ twins.

The role of twinning can be quite large at 77°K (Reed-Hill et al. (1965)) especially at small strains, but at larger strains or at higher temperatures, the contribution to the plastic strain by twinning is diminished. The role of twinning has also been associated with re-orientation of the lattice so that the new orientations may favour slip. In addition to this, twinning has been shown to nucleate slip in some regions.

1.3 ELECTRON MICROSCOPE STUDIES

A limited amount of work has been published on the electron microscopy of zirconium. Howe et al. (1962) studied the effects of dislocation movements in thin zirconium foils. Their annealed zirconium contained a relatively high density of dislocations which may have been due to damage of the thin foils or it may indicate that the zirconium used contained large amounts of impurities. Annealed zirconium generally contains a low dislocation density (Douglass, 1963) and small hydrides, usually precipitated during electropolishing, can sometimes make resolution of the dislocations difficult. Moreover, some dislocations may run out of the foil during thinning since there are fewer obstacles to their motion as the specimen thickness is reduced.

Howe et al. (1962) heated foils in the electron microscope and studied the behaviour of dislocation traces.

Since their observations were due to interactions between moving dislocations and an oxide layer, their results would appear to be of little consequence to the deformation of bulk material. Bailey (1962) also studied the effect of heating thin foils and suggested that dislocation climb at temperatures between 400° and 600°C could be an important mechanism of deformation or recovery. In each of the heating experiments, the predominant slip system was found to be $\{10\bar{1}0\}\langle 11\bar{2}0\rangle$ but Howe and his colleagues claimed to have observed slip on the $\{1\bar{1}03\}$ planes.

The effect of purity of zirconium on the dislocation structures, observed after room temperature deformation, was examined by Bailey (1962). In commercial purity zirconium (0.1 wt % (O+N); 185 ± 5 HV; 20μ grain size) the predominant slip system was $\{10\bar{1}0\}\langle 11\bar{2}0\rangle$. Long screw dislocations with Burgers vectors $1/3 \langle 11\bar{2}0\rangle$ were observed in large numbers. These dislocations appeared to be heavily jogged, the extent of which increased with increasing deformation.

Some evidence for basal slip was obtained when dislocations were punched out by hydride precipitates (Bailey, 1962). Furthermore, in well annealed commercial zirconium, hexagonal dislocation networks which appeared to lie on the basal planes were observed. The formation of such networks was assumed to involve glide on the basal planes and

so this also provided evidence for basal slip.

Bailey deformed crystal bar zirconium of higher purity (0.03% wt (O+N); 100 ± 3 HV; grain size 10μ) at room temperature and the resulting dislocation structure consisted of a complex tangled array. Dislocation loops were observed but the contrast conditions were not specified and the presence of small hydrides may have led to similar contrast effects. Since heavy tangling occurred, it was assumed that the dislocations no longer lay predominantly in the prism planes but that extensive joggling, cross slip and perhaps climb had occurred. Dislocation dipoles were observed and these were associated with the motion of jogged screw dislocations. Threefold nodes sometimes resulted from the interactions between dislocations.

Comparison of the two grades of zirconium used by Bailey showed that dislocation movement was less restricted in crystal bar zirconium and it was suggested that this was due to a relative increase in the mobility of glide dislocations in the basal plane with increasing purity. There is, therefore, some conflict between these results and the observations of Rapperport and Hartley (1960) who claimed that, in titanium and zirconium, basal slip became more difficult as the purity of the material increased.

From the foregoing, it can be concluded that the principal slip system in α -zirconium is $\{100\} \langle 100 \rangle$, (i.e. $\{10\bar{1}0\} \langle 11\bar{2}0 \rangle$), but that there is some doubt as to the likelihood of slip on other planes. However, it would appear that slip on the (001) and $\{101\}$, (i.e. (0001) and $\{10\bar{1}1\}$) planes can occur in a secondary role. In the present tests, which used a slow strain rate in the temperature range 0-600°C, twinning would not be expected unless the texture was such that the formation of twins was particularly favoured.

Finally, it is evident that the direction required for work on zirconium and its alloys is toward a much more detailed appraisal of the deformation properties and dislocation behaviour in the temperature range 200-500°C.

CHAPTER 2

EXPERIMENTAL

2.1 MATERIALS AND SPECIMEN PREPARATION.

High purity zirconium used in the majority of this work was supplied to the Australian Atomic Energy Commission by the Wah Chang Corporation. The analysis supplied by the manufacturer for the iodide crystal bar zirconium is given in table III. The specified hardness of the supplied crystal bar was 77-91 HB50 but full annealing after arc melting resulted in an average hardness of 65HV10.

Strip material required for specimen preparation was produced from the crystal bar by melting, rolling and annealing. The argon arc furnace used for melting consisted of a water cooled copper hearth at the bottom of a stainless steel vacuum vessel. A tungsten electrode was used to strike the arc and easy movement was achieved via a flexible bellows arrangement.

A strict melting procedure was observed. Firstly, after placement of the zirconium on the hearth, the furnace was evacuated to a pressure of 10^{-3} torr. Several flushes with argon gas were then made. Water vapour was removed by P_2O_5 . Finally argon was bled into the furnace to a pressure of 8 mm Hg. A zirconium getter was melted for a period of thirty minutes before the crystal bar material was exposed to the arc.

A cigar shaped ingot was produced in the argon arc

TABLE III ANALYSIS OF IODIDE CRYSTAL BAR ZIRCONIUM
(WAH CHANG CORPORATION - SUPPLIED TO AAEC
OCTOBER 1968)

Zr 99.95%.

ELEMENT	AVERAGE IMPURITY LEVEL (ppm by weight)	ELEMENT	AVERAGE IMPURITY LEVEL (ppm by weight)
Al	< 42	Mn	< 10
B	< 0.8	Mo	< 20
C	< 10	N	< 12
Ca	< 15	Na	< 20
Cd	< 0.5	Ni	< 15
Co	< 5	O	< 30
Cr	< 18	Pb	< 10
Cu	< 10	Si	< 25
Fe	< 75	Sn	< 10
H	< 6	Ti	< 10
Hf	80	W	< 25
Mg	< 10		

furnace and this was subsequently forged to give two parallel sides. The specimen was then cold rolled in several passes to approximately 50-80% reduction in thickness. (Percent reduction in thickness = $\frac{\text{reduction in thickness}}{\text{original thickness}} \times 100$).

Hardness after rolling was usually in the range 150-190HV10.

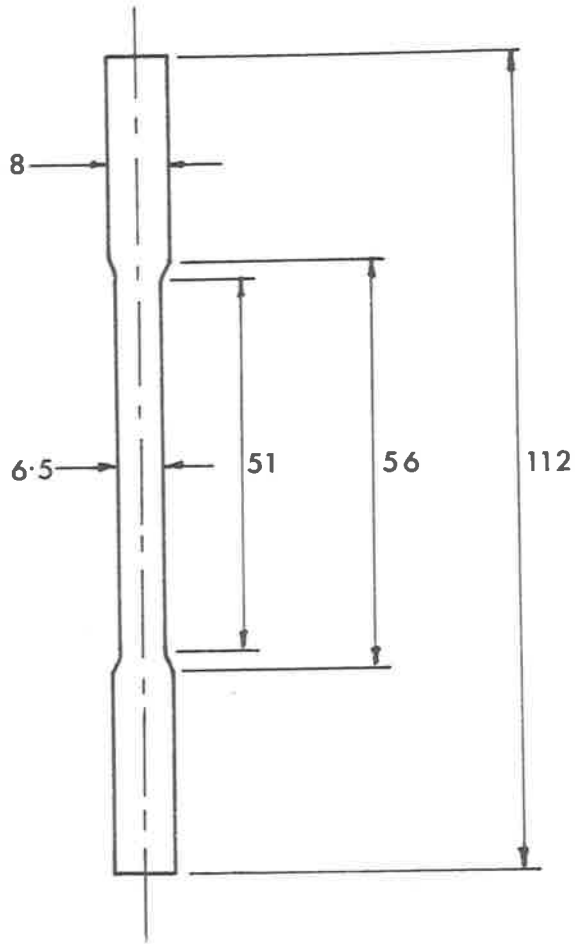
During production of material of thickness 0.25 - 0.50 mm intermediate anneals were used. Prior to each annealing step, the zirconium was thoroughly cleaned and then chemically polished in a solution of 46% Nitric acid, 46% water and 8% Hydrofluoric acid. Annealing was carried out at 760 - 800°C in a vacuum of better than 10^{-5} torr, in a furnace used only for zirconium. The final hardness of the annealed material was 65-68 HV10 which showed that contamination was minimal.

The grain size of the sheet material could be controlled by varying the final rolling procedure, the annealing temperature and the annealing time. Large grain sizes, of the order of 0.3 - 0.5 mm grain diameter, were used for most of the experiments.

Specimens for the constant strain rate tests were machined to the dimensions shown in fig 2.1.

Production of sheet material by cold rolling and annealing techniques produced a preferred orientation. This was expected to be similar to that reported by McGeary

FIG. 2.1 SPECIMEN DIMENSIONS.



DIMENSIONS IN MM.

and Lustman (1953), Keeler et al. (1953) and Picklesimer (1966). Basal planes would be oriented about $30-40^\circ$ around the rolling direction with the $\langle 11\bar{2}0 \rangle$ directions tending to orient parallel to the rolling direction during recrystallization. No texture determinations were carried out on the zirconium used in the present study but the electron microscopy results tend to confirm the suspected texture (Chapter 3). All specimens were prepared with the tensile axis approximately parallel to the rolling direction.

The specimens were either chemically or electro-chemically polished prior to the deformation experiments. This ensured that a relatively scratch free surface was obtained and it also allowed surface examinations to be successfully made before and after the deformation experiments.

2.2 PREPARATION OF SPECIMENS FOR ELECTRON MICROSCOPY.

There is an ever increasing number of techniques becoming available for the preparation of thin foils for transmission electron microscopy. Most of the newer ones are modifications of the basic methods reviewed by Hirsch et al. (1965) and Brammer (1965). There are two main avenues of approach. The first involves the preparation of a thin foil from a flat sheet of material, usually about 5 - 10 mm square and 0.25 - 0.50 mm thick, the final foil being cut with a razor blade or scalpel. The second method has, as the

starting material, a disc with a diameter which is sufficiently small to fit into the electron microscope specimen stage. (2.3 or 3 mm diameter).

The use of 3 mm discs was briefly investigated. A teflon*holder was used in an attempt to thin 3 mm discs, of original thickness 0.25 mm, but the major problem was that oxygen bubbles adhered very strongly to the specimen and the edges of the teflon holder, and this caused preferential perforations near the edge of the disc. Without extensive modifications to stirring and addition of optical assistance for examining the specimens during polishing, this technique held little promise for zirconium. Indeed, only recently, complicated modifications to allow the use of teflon holders to prepare thin foils of difficult materials have been described (Caplan (1967), Wahi et al. (1968)).

A simple method for preparing thin foils of several metals, including zirconium, has been developed by Gidley and Davies (1967). Their method also used a 3 mm disc but the specimen was held by fine pointed, coated tweezers. The recent use of this technique resulted in reasonable thin foils of zirconium.

* Supplied by AEON Ltd London.

The method used to prepare almost all of the thin foils for the present work was a modified window technique. The window technique is attractive because of its simplicity. No special apparatus is required, the basic equipment comprising a power supply, beaker, stirrer, cathode and some cooling medium. However, as is usually the case, the optimum choice of the conditions under which the best thin foils are produced depends largely on the experience of the operator. In an attempt to establish these optimum conditions, several qualitative tests were carried out with particular reference to electrolytes, polishing cell and polishing temperature.

The choice of electrolyte was based on available published data on the electropolishing of zirconium and titanium, (Jaquet (1950), Tegart (1959), Hirsch et al. (1965), Bailey (1962), Howe et al. (1962), Gidley and Davies (1967), Caplan (1967), Blackburn and Williams (1967)). The basic solutions recommended by the above authors are very similar to the ones given in the following as (1) - (4). The others quoted, (5) - (8), are other solutions which were examined in the present work.

To establish the best polishing conditions it is necessary to obtain a plateau on a current density-voltage curve (Tegart (1959), Lorking (1959)). The best method to plot these curves is by the use of a potentiostat, and the

experimental arrangement used was very similar to the one published by Raty et al. (1966). The following solutions were tested at various temperatures.

- (1) 10% Perchloric acid (72%), in acetic acid.
- (2) 6% Perchloric acid, 36% n-Butanol, 58% Methanol
- (3) 6% Perchloric acid in Methanol
- (4) 20% Perchloric acid in Ethanol
- (5) 6% Perchloric acid, 20% n-Butanol, 74% Methanol
- (6) 16% Perchloric acid in Methanol
- (7) 9% Perchloric acid in n-Butanol
- (8) 8% Perchloric acid, 18% Methanol, 74% n-Butanol •

Perchloric acid - acetic anhydride mixtures were not investigated. Solution (1) which was used by Jaquet (1950) and Bailey (1962) could not be used at very low temperatures since acetic acid precipitates out of solution easily. A plateau can be obtained in the current-voltage curve and reasonable polishing is obtained at about 15-20 volts (anode - cathode) at a temperature of 0°C. However, the foils prepared using this solution had a marked surface texture due to an oxide layer. Hydride pick-up was also very marked when this electropolishing solution was used; (More detail is given on the problem of hydride pickup later in this section). Therefore perchloric acid-acetic acid solutions were considered unsatisfactory for preparation of zirconium thin

foils.

Solution (2) is now commonly used for zirconium and titanium, mainly because a well delineated plateau forms at many polishing temperatures. Methanol-based solutions are attractive because a relatively high current density is obtainable (Raty et al. (1966)). Raty et al. also observed the drop in the height of the plateau (which represents a region of constant current density) as the temperature was decreased and this has been attributed to a decrease in the conductivity of the electrolyte (Hirsch et al. (1965)), and to changes in the viscous layer. Current-voltage curves obtained from the present tests for this solution are shown in fig 2.2 * and the conditions referred to by Raty et al. can be seen. The plateau becomes markedly wider as the temperature is decreased. A lower temperature gives slower polishing but much better control of the process can be maintained.

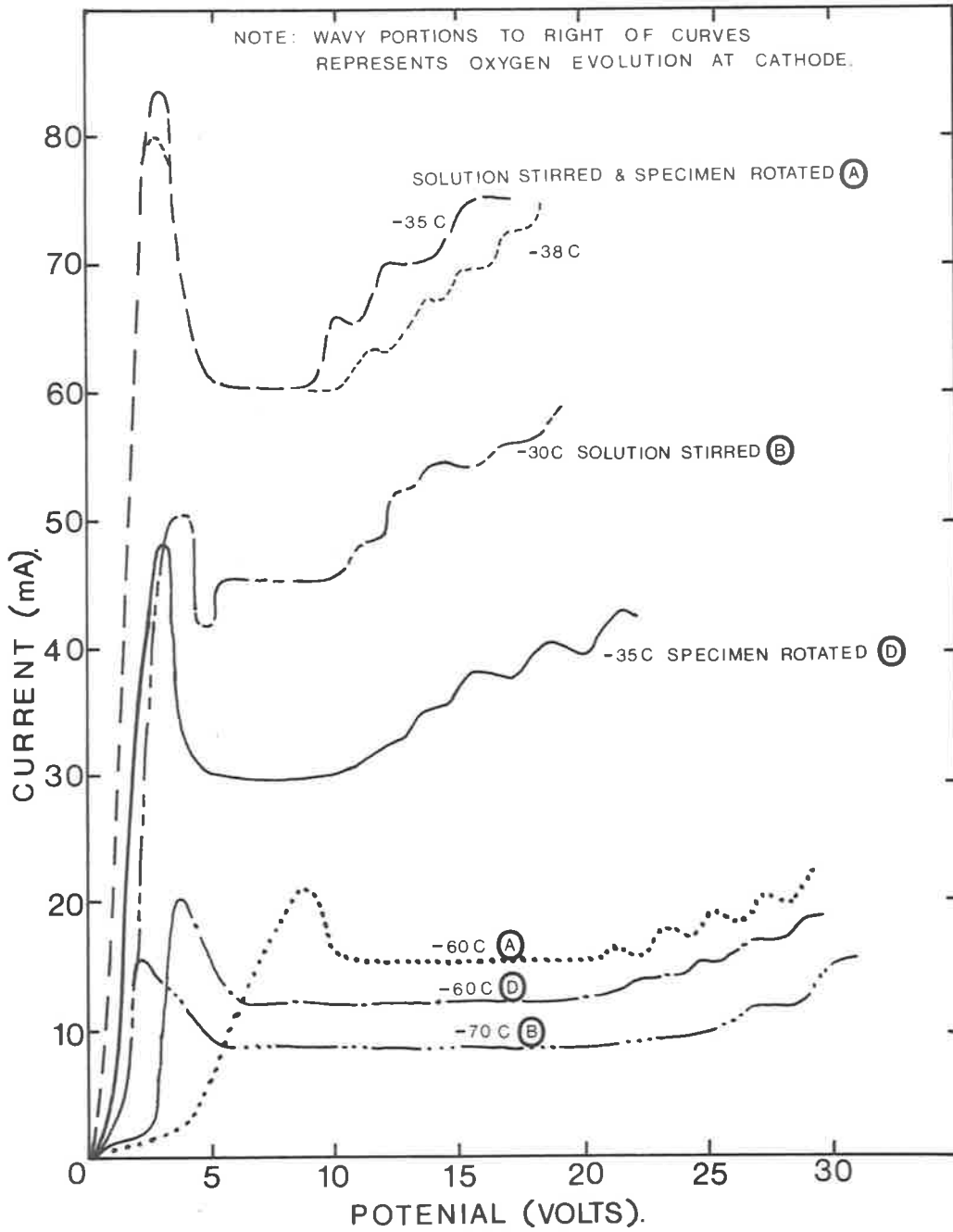
Solutions (3) - (5) also give reasonable plateaux but the polish obtained is not as good as that for solution (2). This is probably due to the type of viscous layer which forms.

Since n-Butanol is usually added to obtain a suitable

* The ordinate represents the current in mA on an area of 3 mm^2 in figs 2.2 and 2.3

FIG.2.2 POTENTIOSTAT CURVES FOR ELECTROLYTE 2

6 HClO₄ ; 36 n-BUTANOL ; 58 METHANOL.



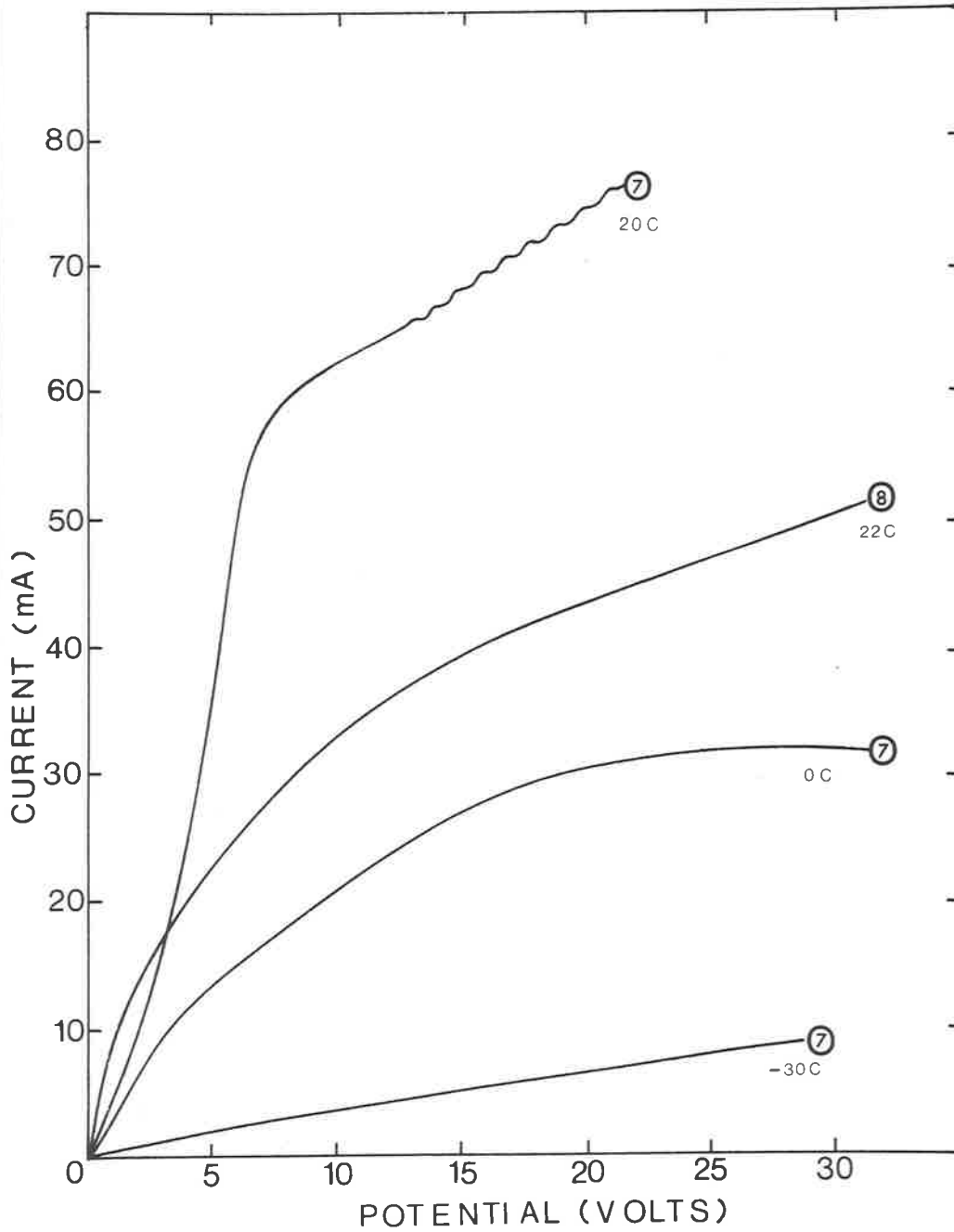
electrolyte viscosity, it was considered useful to test the effect of using butanol alone (or with a small amount of methanol) with perchloric acid. Because of the high viscosity of solutions (7) and (8) it was hoped that these solutions would be suitable for use at room temperature. However, the potentiostat curves showed no plateaux (fig 2.3) and suitable polishing conditions could not be obtained.

Some of the advantages of using low temperatures have been referred to above and one other advantage is that attack on the lacquer (Lacomit) used to blank off edges is reduced at lower temperatures, (Gidley and Davies (1967)).

Stirring of the electrolyte also has an important effect on the electropolishing obtained. Fast stirring causes a breakdown of the viscous layer which results in uneven polishing of the surface. Stirring at very slow rates allows the current density to drop to a very low value and production of a thin foil requires an excessive time. The most important function of stirring was found to be the maintenance of constant temperature in the bath, and this was always sufficiently slow to prevent the formation of a vortex at the surface of the electrolyte. In some tests the effect of mechanically rotating the anode (specimen) was examined and it was found that this caused very slow polishing and was thus unsatisfactory.

FIG.2.3 POTENTIOSTAT CURVES FOR ELECTROLYTES 7,8

⑦ : 9 HClO₄ 91 n-BUTANOL
⑧ : 8 HClO₄ 18 METHANOL 74 n-BUTANOL

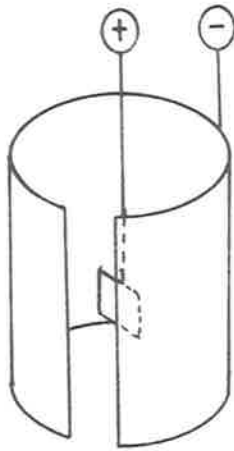


An important variable is the shape of the cathode which determines, to some extent, the current distribution across the surface of the specimen. Therefore if a small specimen is polished from within a deep cylindrical cathode (fig. 2.4 (a)), the specimen would be expected to perforate near its bottom or its top edge, depending on the relative height of the cathode below and above the specimen. Indeed, this is the case and when using this type of cathode it is necessary to turn the specimen end-for-end several times to obtain suitable perforations and thinning, (Hirsch et al. (1965)).

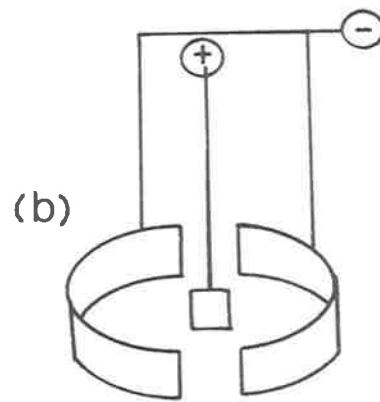
Tests were carried out on various shapes and sizes of cathodes (each being made of stainless steel) and it has been found that a cathode with a depth slightly greater than the specimen will give excellent results (fig. 2.4. (b)). The shape of this cathode makes it possible to position the specimen so its faces are normal to the line which joins the gaps in the cathode. Thus the surfaces can easily be seen and polishing is easily controlled. The back surface of the cathodes can be lacquered and this results in slightly better polishing behaviour.

A further modification to the above is the use of a cylindrical rod cathode, the diameter of the rod being smaller than the width of the specimen (fig. 2.4. (c)).

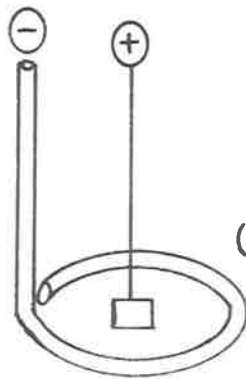
FIG.2.4 ELECTROPOLISHING CATHODES



(a)



(b)



(c)

Both the cathodes shown in figs. 2.4. (b) and (c) allow the production of perforations near the sides of the specimen. The specimen need not be turned during polishing and so the whole process is quite rapid and the final thinning behaviour is such that good thin foils can be obtained by using only one razor cut.

One of the most important stages in thin foil preparation is the washing and drying procedure. Any extraneous impurities in the final washing solution usually causes surface contamination of the foil. In the present work, the specimen, after removal from the polishing bath with the potential still applied, was quickly washed in cool high purity methanol. The specimen was then carefully sprayed with pure ethanol and dried in the warm air blast of a hair dryer. The cooling effect of ethanol is not sufficient to cause precipitation of water from the atmosphere and for this reason it is eminently suitable for the final washing step. If a thin foil appears brilliant under the optical microscope, it is usually very satisfactory in the electron microscope.

Ultrasonic cleaning is unsatisfactory because it is so violent that the thin foils are heavily deformed and are sometimes even torn apart.

It has been noted that hydride contamination can occur during both chemical polishing and electropolishing of

titanium (Blackburn and Williams (1967)) and the same is true of zirconium (Bailey (1963)). Indeed, it appears that hydride can form after the electropolishing has been completed, perhaps during washing, storage, or upon introduction to the electron microscope. The small precipitates in zirconium, which are called hydrides, cannot readily be identified by electron diffraction, but heating experiments in the electron microscope showed that the hydrides diminished and grew along directions and at temperatures which were consistent with the identifiable bulk hydrides (Bailey (1962)).

There are many variables which may have an effect on the amount of hydride produced on the thin foil during electropolishing, but because of the limited number of tests carried out in the present investigation, the results can only be summarized qualitatively.

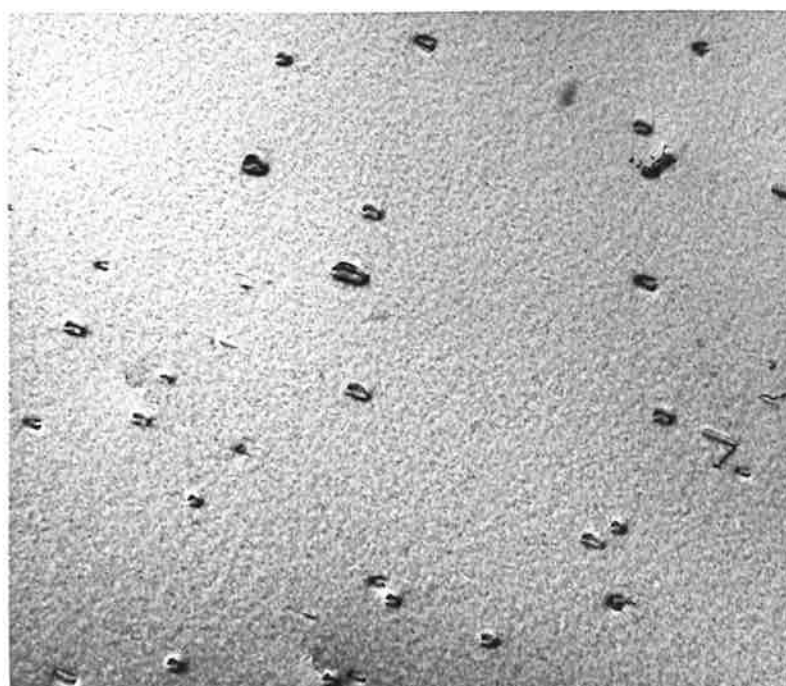
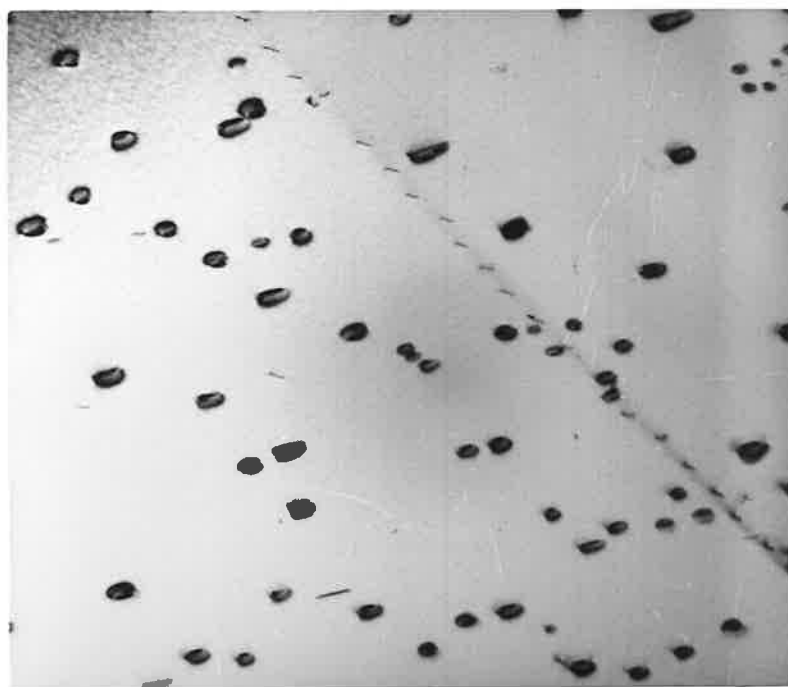
For hydride to be produced, either in the zirconium specimen or on its surface, hydrogen must be present. In all solutions used there would be ample H^+ ions or complex ions present from which hydrogen could be derived. It has been found that an older solution (one that had been used several times previously) will give greater hydride contamination during electropolishing than will a new solution (fig. 2.5.). It is suggested that this occurs because water condenses on the cold apparatus and falls into the solution thus giving

FIG. 2.5(a) Hydride Pickup from fresh
electropolishing solution

0.5μ


FIG. 2.5(b) Hydride pickup from older
electropolishing solution

0.5μ

rise to a higher concentration of hydrogen ions.

Since free hydrogen is produced at the cathode, it can be considered that this is a possible source of hydride contamination. However, tests were carried out in which the cathode and specimen (anode) were separated by sintered glass plugs and this had no advantageous effect on the reduction of hydride contamination.

Ideally, a non-protonic solution should give no hydride contamination but it is difficult to produce such a solution. Magnesium perchlorate was tried in place of perchloric acid but this did not reduce the hydride contamination. The effect of adding extra hydrogen ions to solution (few cc's of HCl added) also did not markedly affect the hydride pickup. It would therefore appear that there is a minimum concentration of hydrogen necessary to cause hydride contamination and that solutions have not yet been produced which contain less than the minimum.

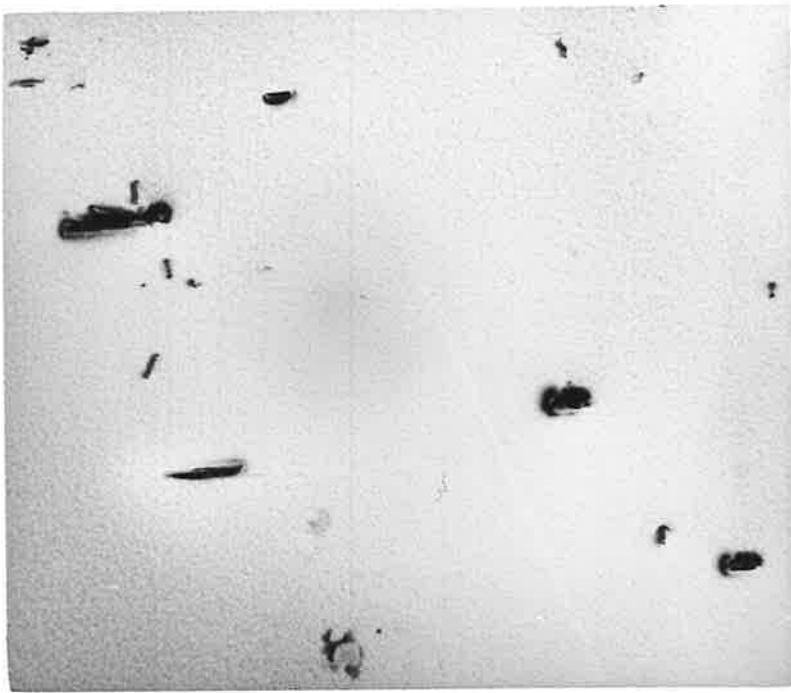
Blackburn and Williams (1967) noted that hydride contamination was usually confined to the thin edges of thin foils of titanium. In zirconium the same effect is observed in that the concentration of hydride precipitated at the thin edges is far higher than in the thicker parts of the foil. An example of this behaviour is shown in fig. 2.6 which was one of the worst cases encountered.

FIG. 2.6(a) Hydride on thin edge of foil

0.5 μ
└───┘

FIG. 2.6(b) Hydride in same specimen as
fig. 2.6(a) but in thicker part
of foil.

0.5 μ
└───┘



Another interesting observation can be made when a specimen has been cleaned and washed but then requires a little more polishing to produce a thin foil. If this specimen is re-inserted into the polishing bath for only a very short time then it is often found that hydride pickup is excessive. The background surface texture is also usually more marked in such cases. However, if a longer time (>2 min) is used for the final polishing step the hydride pickup is much lower. This time effect along with a temperature effect may be one of the factors which governs the hydride pickup in relation to the overall time used for polishing. If a specimen is polished exclusively at -60°C or less (about 4 hours required for a specimen 0.25 mm thick) then hydride contamination is high. On the other hand good results are obtained if the specimen is first polished at about -30°C until a few perforations have been obtained and then finally polished at about -60°C . However, if the specimen is polished entirely at -30°C hydride contamination again becomes excessive. Fig. 2.7 gives examples of the hydride pickup resulting from the use of the latter two procedures.

The final problem regarding hydrogen contamination of zirconium thin foils occurs after the foils have been prepared. Fig. 2.8 shows small hydride precipitates on a slip trace. The slip trace was probably produced either

FIG. 2.7(a) Hydride pickup when final polish
carried out at -60°C

0.5 μ


FIG. 2.7(b) Hydride pickup when final polish
carried out at -30°C

0.5 μ

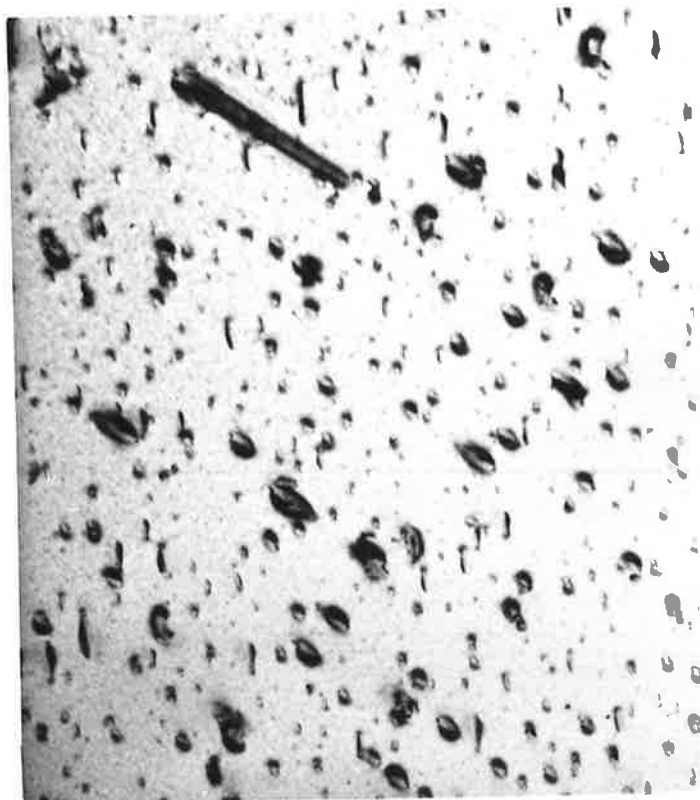
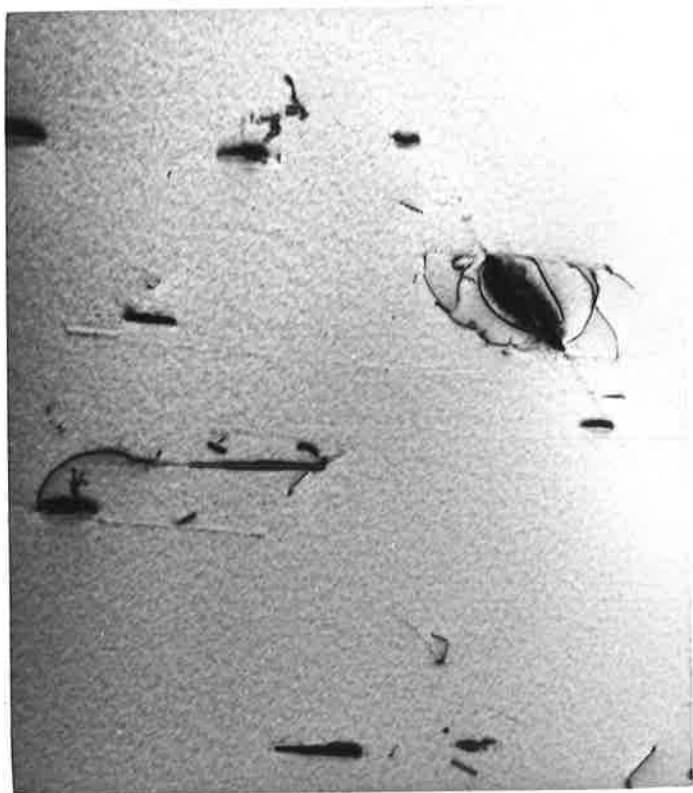
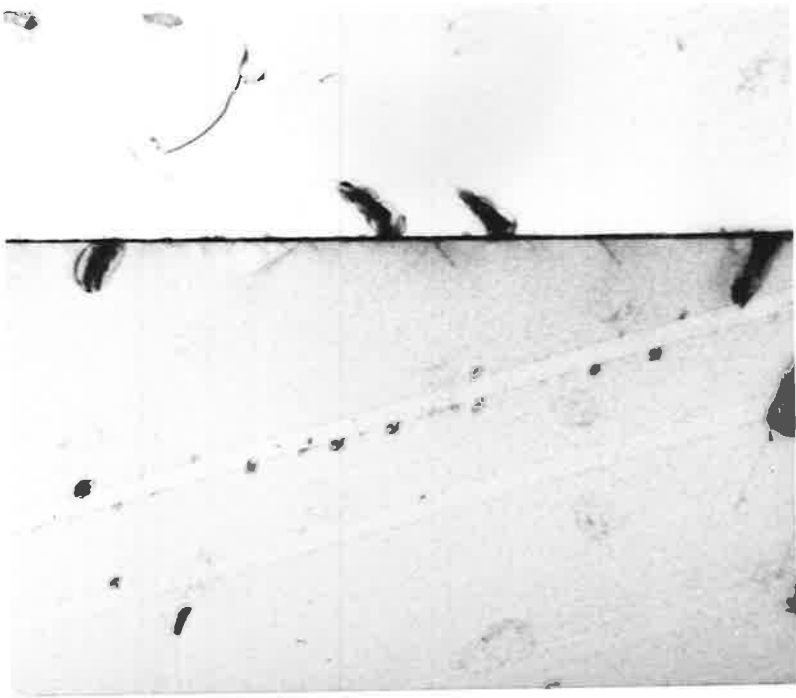



FIG. 2.8 Hydride precipitate on slip trace

0.5 μ

during washing, cutting, or subsequent handling of the foil. Therefore, thin zirconium foils can be contaminated after the final polishing step and up until the foil is viewed in the electron microscope. The above phenomenon has only been observed at the very thin edges of the foils. Hydride pickup can even occur after the electron beam impinges on the specimen. This was especially noticeable in the present work after another user had studied ammonium iodide in the electron microscope. It was concluded that the iodide was decomposed and gave an increased hydrogen concentration in the microscope atmosphere and that this was sufficient to cause hydride to precipitate on the thin foil of zirconium.

Since hydrogen pickup and the presence of hydrides in zirconium is important, some effort was devoted to analyses of hydrides in or on the thin foils by crystallographic techniques. This does not, however, fall into the general sphere of this project, but since it is nevertheless of interest regarding the subject of hydrides in zirconium the results and a discussion are presented in Appendix 1.

In summary, the polishing technique found qualitatively to give the best results was one which involved the use of a solution of 6% perchloric acid, 36% n-butanol and 58% methanol. A slow stirring rate was used and the cathode was a ring of stainless steel rod, the rod diameter being

slightly smaller than the specimen width. The specimens were first polished at -30°C until several perforations occurred and the final polishing was carried out at about -60°C . The specimens were always removed with the potential between the anode and cathode still applied and were then washed in pure methanol, then ethanol, and were finally dried by a warm air blast. The thin foils were cut from the specimen with a clean, sharp razor blade and care was taken to keep the specimen desiccated before being introduced into the electron microscope.

Hydride contamination of the surface of thin foils always occurs but since it is mainly surface hydride (Appendix 1) it can reasonably be assumed that this hydride will have little or no effect on the dislocation structures within the specimens. In fact, the surface hydride may be advantageous in that it will have a locking effect on the dislocation structure and prevent loss from the foil during thinning and thus allow a better representation of the bulk material.

2.3 ELECTRON MICROSCOPE CALIBRATION AND STEREOMICROSCOPY.

To ensure that accurate measurements could be obtained from electron micrographs, the camera constant, magnifications, and the relative rotation between diffraction

pattern and image had to be accurately known. The microscope used in the present study was a Philips model EM 200.

Wherever possible, all micrographs were taken on one of a limited number of magnification settings and the diffraction patterns were almost always recorded at one of two settings. This meant that a minimum number of very accurate calibration constants were required.

The camera constant (or diffraction constant), was determined at regular intervals by using a thin polycrystalline gold foil.

Standard magnifications were calculated from plates and films of cross grating replicas. An optical microscope, which was itself calibrated with inscribed graticules, was used to check the spacing of the lines on the cross grating replicas.

Rotation calibrations were calculated from superimposed exposures of a molybdenum trioxide crystal and its diffraction pattern. Table IV gives the calibration values used in the analysis of the results of the present work.

The technique of stereo-electron-microscopy was used extensively to allow the three dimensional arrangements of dislocations to be studied. To obtain useful stereo-electron-micrographs not only must the tilt axis and angle of tilt be accurately known but the contrast of the image on each

TABLE IV

CALIBRATION OF EM200 ELECTRON MICROSCOPE

OBJECT IMAGE			DIFFRACTION PATTERN			CLOCKWISE ROTATION THROUGH WHICH IMAGE MUST BE ROTATED TO MAKE IT COINCIDENT WITH DIFFRACTION PATTERN (Degrees \pm 1)
MAG. CONTROL.	PROJECTOR CONTROL	MAGNIFICATION 35mm film plates	MAG. CONTROL	PROJ. CONTROL	CAMERA CONSTANT ON 35mm film - (A mm)	
1	M	7000 : 13400	4	M	21 \pm 1	155
1	6	4750 . 9100	4	6	14 \pm 1	155
1	M	7000 : 13400	4	6	14 \pm 1	
6	M	1920				
8	M	1620				
9	M	: 2100				
11	M	: 3300				
12	M	4200				
16	M	12000				

micrograph should be similar (Nankivell, 1963). Thus the same or similar diffracting conditions are necessary and this has been obtained by tilting along a particular Kikuchi line (Basinski, 1962). A goniometer or a double-tilt stage is a significant advantage when this technique is used.

The procedure adopted in the present work was as follows. Each stereo-pair was produced using the same two-beam diffracting conditions. The tilt axis was therefore parallel to the reciprocal lattice vector represented by the two-beam conditions and by recording the position of each of the orientations used in relation to a Kikuchi map the angle of tilt was easily established. (See Chapter 3).

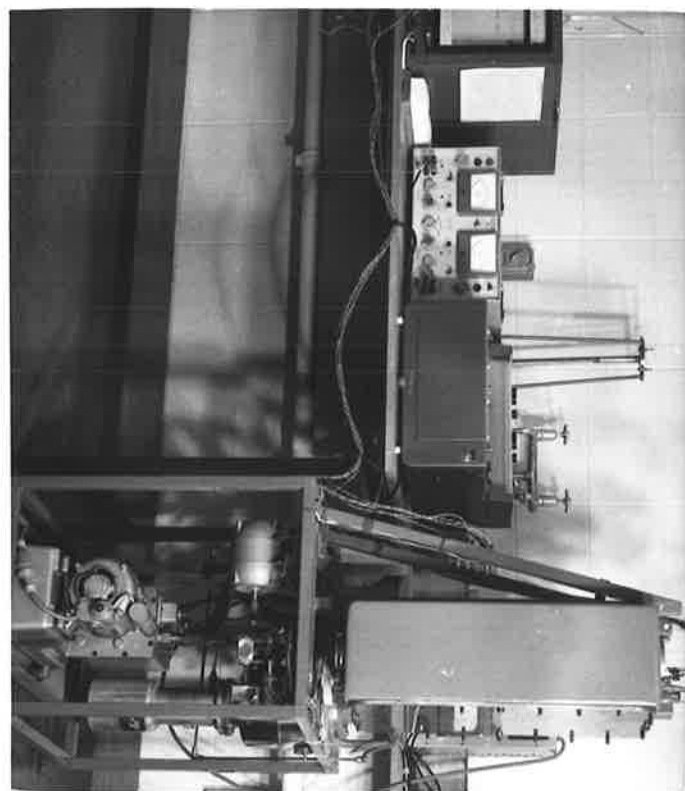
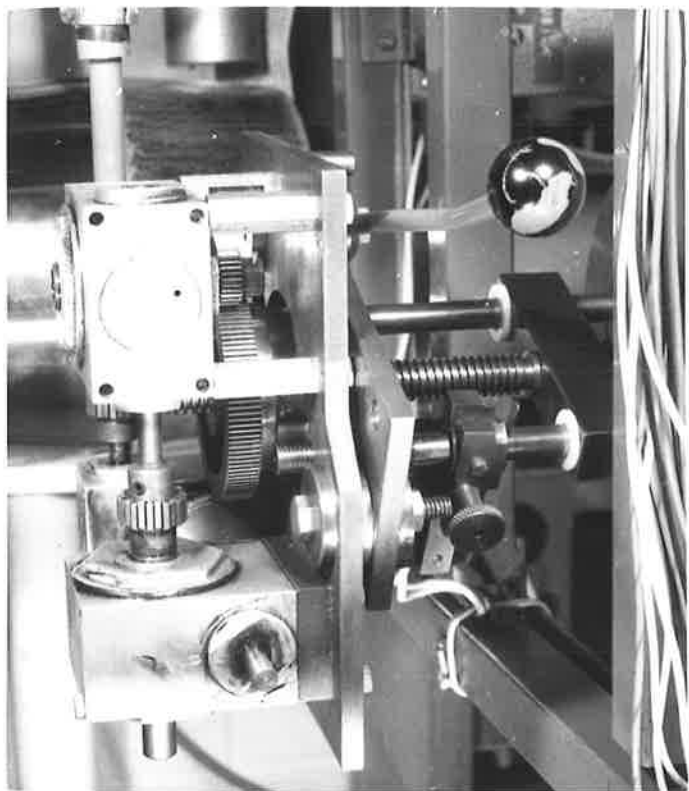
2.4 DEFORMATION APPARATUS.

2.4.1 Vacuum System.

A conventional backing pump - oil diffusion pump vacuum system which incorporated fail-safe valves was connected via copper tube and bellows to a large vacuum vessel. The vessel, of overall dimensions 24" x 12" x 8" was constructed of 1/4" mild steel plate. An overall view of the apparatus is shown in fig 2.9. The front of the vacuum vessel was surface ground and with the door securely bolted down, maintained a pressure better than 10^{-5} torr. Access holes were machined in the top and bottom of the vessel. Two of

FIG. 2.9 Overall view of deformation apparatus.

FIG. 2.10 Geared motor drive.

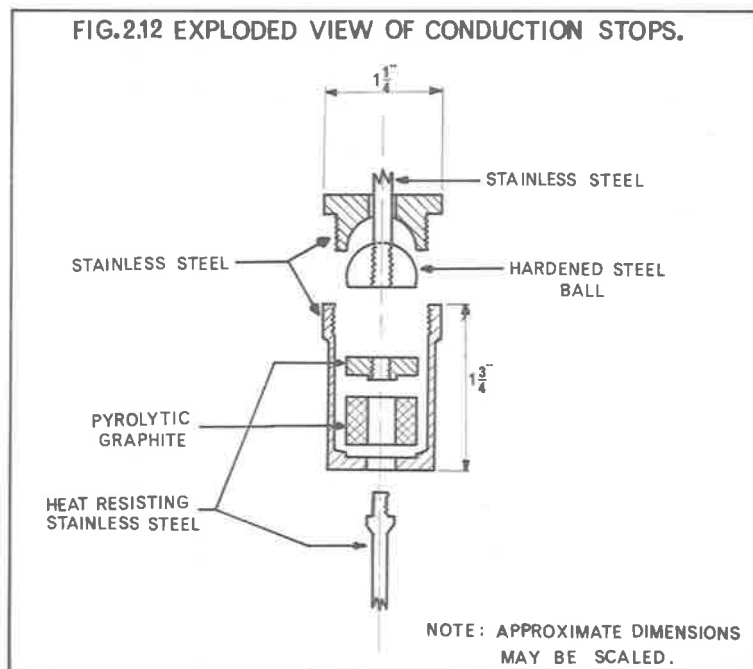
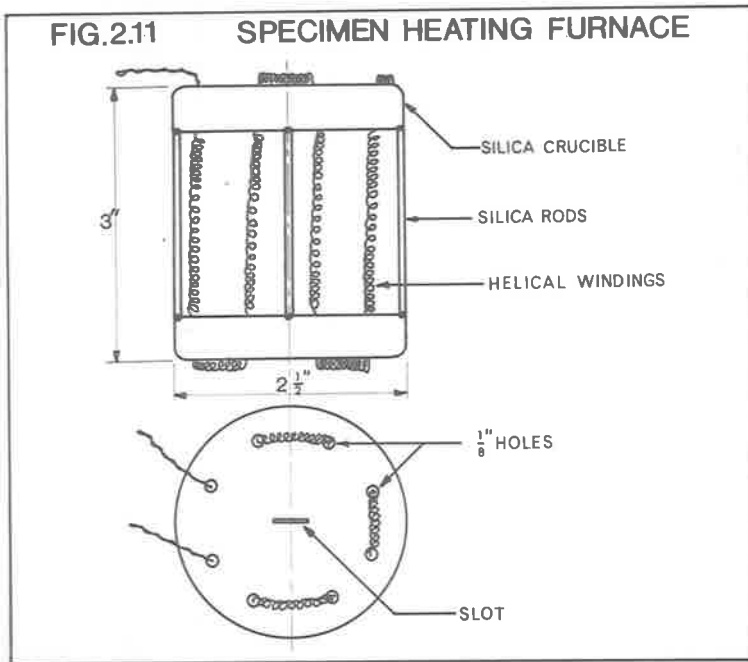


these holes were covered with brass flanges in which glass metal or polymer metal seals were used to provide the electrical connections.

2.4.2 Connections and Heating Furnace for Specimen

Simple split clamps with milled inner faces were used to fix the specimen in position. Incorporated on the clamps were V-blocks in which silica rods could be clamped, these rods being required for mounting the transducer used for elongation measurements, (section 2.4.6.) Heat resisting stainless steel was used for the clamps and the rods connecting them to the rest of the apparatus.

A small furnace, which covered the zirconium specimen only, was used and was found to give a satisfactory temperature distribution in the specimen (see section 2.4.4). A diagram of the furnace is shown in fig. 2.11. Two flat bottomed silica crucibles were separated by silica rods so that the furnace length was about 3". Nichrome wire (28SWG) was used for the furnace winding, the top and bottom ends of the helices being of slightly smaller spacing than the centre windings to compensate for end heat losses. The effectiveness of this construction is noted in section 2.4.4. on calibration. Thin zirconium sheet was used as a radiation shield on the outside circumference of the cylindrical furnace.



To reduce conduction of heat away from the specimen an insulating barrier was included. An exploded view of the section is shown in fig 2.12. A small annular cylinder of pyrolytic graphite, which was machined so that the direction of minimum conductivity was along the length of the annulus, reduced heat conduction from the specimen. The pyrolytic graphite had a high compressive strength in the direction parallel to the length of the annulus which was the direction of load application and hence was highly suited to the above design.

The other end of the support contained a hemispherical bearing so that slight misalignment of the specimen could be tolerated.

2.4.3 Load and Elongation Measurement.

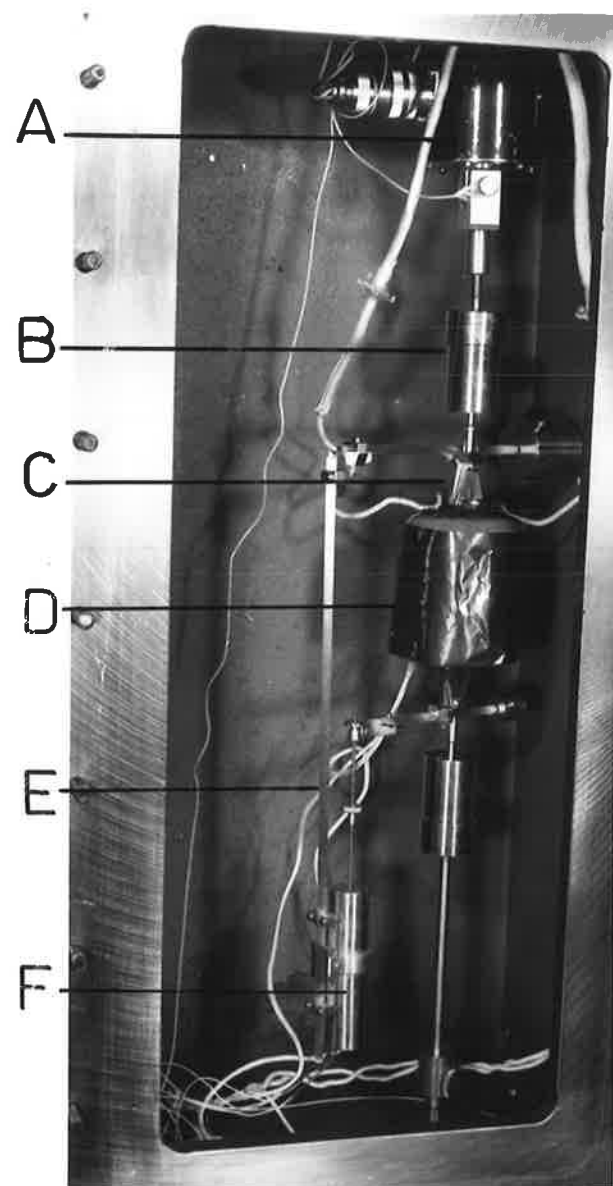
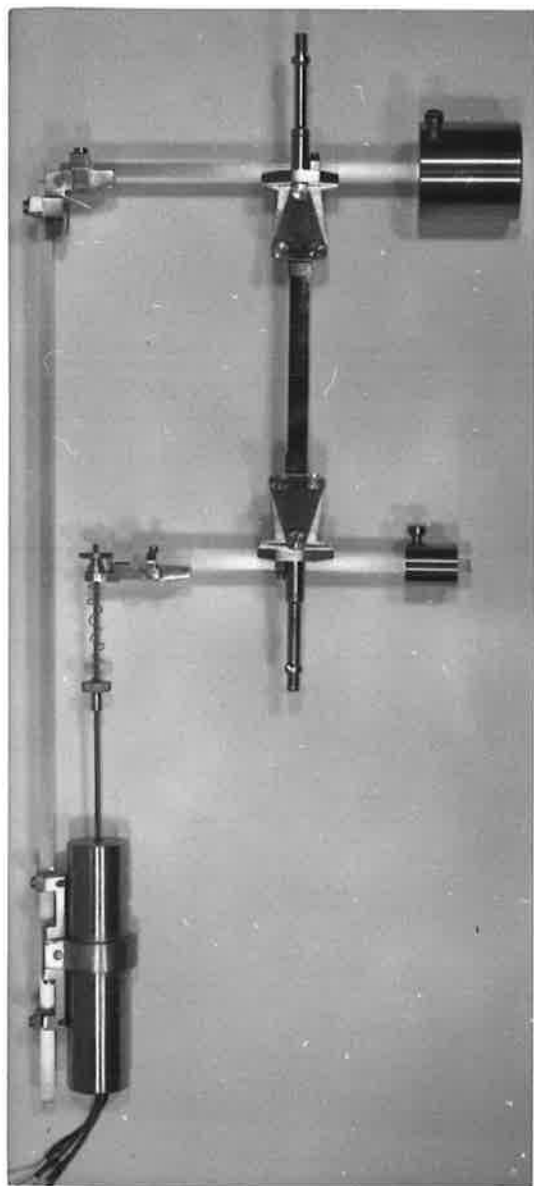
A small strain gauge load cell * was incorporated in the upper section of the apparatus, fig. 2.13, so that readings from the load cell corresponded to the load on the specimen. Only a very small proportion of the load measured was due to the weight of ancilliary parts because of the position of the load cell. The relatively large distance between the load cell and the furnace ensured that the

* Shinkoh LT/50K strain gauge load cell

FIG. 2.13 Assembled straining apparatus

- A. Load Cell
- B. Heat conduction stop
- C. Clamp
- D. Furnace
- E. Silica rods
- F. Elongation transducer.

FIG. 2.14 Elongation measuring arrangement;
Specimen and Clamps.



temperature variation at the load cell was small.

A Linear Voltage Differential Transformer (LVDT)* was used to measure the relative movement which occurred between the clamps. The LVDT was mounted on silica rods so that it was remote from the heated area of the apparatus (figs. 2.13 and 2.14). The silica rods ensured minimal heat conduction and as well, remained dimensionally stable at the temperatures used.

The load cell required a 6 volt D.C. input and the LVDT a 24 Volt D.C. input. A dual stabilized power supply was used and the voltages were set with an accurate voltmeter. The output from the load cell was a d.c. signal up to a maximum of 6mV and the d.c. output of the LVDT varied from 0 to 10 volts.

A dual channel potentiometric recorder was used to simultaneously plot the output signals on a time base.

A six point temperature recorder was used to measure the temperature of the specimen and to monitor the temperatures of the LVDT and the load cell.

2.4.4 Calibration of Measuring Equipment.

The load cell was connected to the power supply and recorder and was tested in a Hounsfield Tensometer so that

* SHAEVITZ MODEL 500-DC

a calibration curve was obtained. Calibration tests were repeated periodically. The effect of a small temperature increase was found to be negligible. A linear calibration graph which varied within very small limits was obtained in all tests.

To check the calibration of the LVDT a micrometer screw was mounted on a rod with the LVDT and the calibration curve was plotted on the recorder.

Temperature variation along the gauge length of the zirconium specimen was checked for the range of temperatures used in the deformation experiments. Three test series were carried out. Firstly, three Chromel-Alumel thermocouples were spot welded (one at each end and one at the centre) to a zirconium specimen and temperature calibration tests performed. Secondly, three thermocouples which just touched the specimen were tested and thirdly three holes into which the thermocouples fitted were drilled in the specimen and a temperature calibration test carried out. All three series of tests gave similar results. The temperature variation from centre to ends of the zirconium specimen was $\pm 2^{\circ}\text{C}$ up to 300°C and rose to $\pm 5^{\circ}\text{C}$ at 600°C .

2.4.5. Straining Mechanism

A geared motor assembly which drove a power screw was

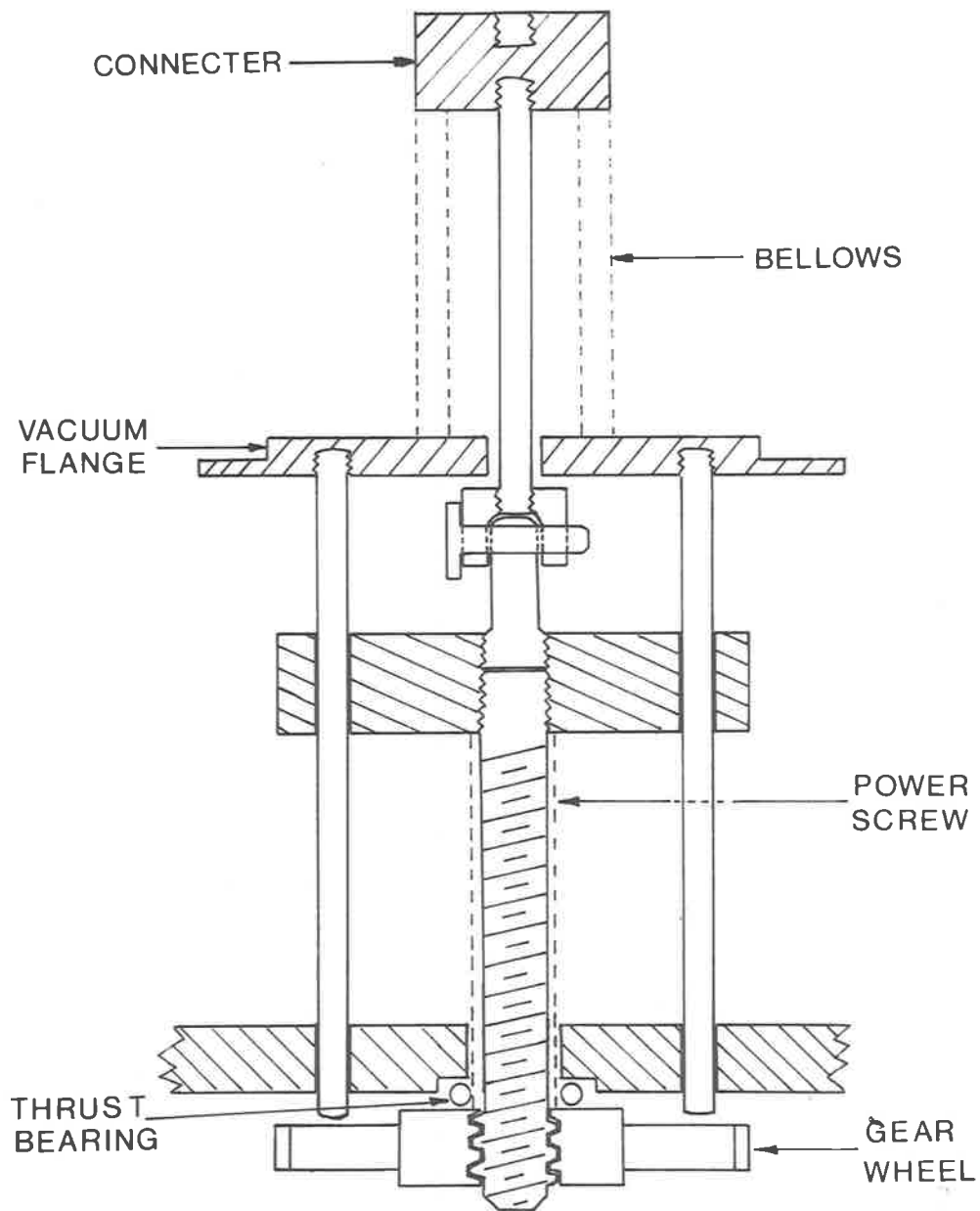
mounted on the bottom of the apparatus (figs. 2.10, 2.9). The linear motion was transferred to the specimen via a double walled gilding-metal bellows (fig 2.15). The drive gears could be changed to accommodate different strain rates. Overload of the load cell was guarded against by a shear pin in the main drive gear and a microswitch prevented the motor from driving the screw to the end of its travel. For quick release of the load the drive gears could be disengaged and the load released manually.

The main purpose of the apparatus was to provide a method of slowly straining thin zirconium specimens. Although load and elongation measurements were made, it was realized that because the specimens were small and were of a large grain size, the stress-strain measurements could only be used to give very approximate correlations with other work.

The vacuum attainable (10^{-5} torr at 400°C rising to 4×10^{-5} torr at 600°C) was adequate to keep contamination to a level which did not affect the optical examinations of the surface of the specimens.

Periodic calibrations of the temperature recording apparatus were made with an accurate potentiometer to ensure that specimens were strained within specified temperature limits.

FIG.2.15 STRAINING MECHANISM



CHAPTER 3. CRYSTALLOGRAPHY.

The crystallography of hexagonal lattices has been studied in detail over the past few years. However, the crystallographic techniques are generally more complex than those for the cubic lattices and this may account in part for the apparent reluctance of metallurgists to study crystallographic problems related to the hexagonal metals. The other important consequence of the complexity of the crystallography is the profusion of errors which appear in papers dealing with hexagonal metals, and although some authors (Partridge (1967), Nicholas (1970)), have drawn attention to the difficulties which can arise, even in very recent literature (Chaturvedi and Singh (1969) and Vahldiek (1969) *) confusing mistakes have been made.

It was necessary, in working on zirconium, to closely examine the literature and to develop techniques to be used to solve the particular kinds of crystallographic problems which arise in the electron microscopy of zirconium. (eg. slip trace analysis, Burgers vector determinations, rapid orientation determinations in the electron microscope as an

* Chaturvedi and Singh inconsistently indexed diffraction patterns and these have been corrected by Bedford (1970) Appendix 3 ... Vahldiek has indexed a diffraction pattern with an [001] zone axis which, on calculation from the published diagram appears to be an [011] zone axis which is 34° from [001] .

aid to specimen manipulation etc.). In this chapter the methods of defining planes and directions in an hexagonal close packed lattice are briefly reviewed, along with the reciprocal lattice which is generated to solve electron diffraction problems. The use of Kikuchi maps, and the production of a Kikuchi map for this study are discussed. Finally, techniques which have been developed to determine the Burgers vectors of dislocations in zirconium are described.

3.1 LATTICE NOTATION AND THE RECIPROCAL LATTICE

The original "Miller-Index" notation was developed for the cubic lattices for which three orthogonal axes could be chosen, these axes being parallel to the unit cube edges. The method of assigning indices to planes is well documented in most metallurgical text books. Directions are also assigned indices based on unit vectors along each of the axes, and it is a consequence of the system of axes used that a direction with indices $[hkl]$ is normal to a plane with indices (hkl) . In the hexagonal system, the axes used by the two common methods of notation are not orthogonal and in general this relationship between the indices of planes and directions normal to them is not observed. The possible methods which may be used to describe directions and planes in an hexagonal lattice have been reviewed and discussed numerous times (Frank (1965), Otte and

Crocker (1965), Nicholas (1966), Partridge (1967), Okamoto and Thomas (1967), Partridge and Gardiner (1967), Levine (1968), Nicholas (1970)).

Orthohexagonal and Rhombohedral indexing (Otte and Crocker (1965), Nicholas (1966)) were examined during preliminary research but the disadvantages were such that these systems of indexing were unsuited to the kinds of problems encountered in this study. The two most common methods of indexing planes and directions in the h.c.p. lattice are the "Miller" (three-axis, three-index) system and the "Miller-Bravais" (four axis, four-index) system.

The principal axes in the Miller system are two basal axes at 120° to each other with a third at 90° to these two. The Miller indices for planes and directions are calculated in the normal manner (Appendix 2).

Miller-Bravais indexing is based on four axes, three of which lie in the basal plane at 120° to each other and a fourth axis which is normal to them. The indices are again calculated in the same way as Miller indices with one index being redundant, but nevertheless retained for reasons of clarity and consistency with the hexagonal unit cell.

The c-axis, at right angles to the basal axes, in the hexagonal lattice has a different unit length to the three basal axes. The unit of length of each of the basal axes is

usually assigned the letter "a" and length of the c-axis assigned the letter "c". Some confusion has arisen in giving Burgers vectors in the hexagonal lattice and Partridge (1967) points out that such confusion may be avoided by referring vectors to unit distances along the respective axes, $\langle aaac \rangle$. For example $1/3 \langle 11\bar{2}0 \rangle$ and $a/3 \langle 11\bar{2}0 \rangle$ are both nominally correct since the c multiplier is zero. However, $a/3 \langle 11\bar{2}3 \rangle$ is incorrect and should be written $a/3 \langle 11\bar{2} (\frac{c}{a}) 3 \rangle$ or more simply $1/3 \langle 11\bar{2}3 \rangle$.

A reciprocal lattice may be generated from the real lattice by using the conventional definition of the reciprocal lattice (Barrett and Massalski (1966)). To do this the three-axis, three-index Miller system is most convenient but the reciprocal lattice axes bear a more complex relation to the real axes than is the case for cubic lattices, (Partridge (1967), Nicholas (1970)). Indices are assigned to the points of the reciprocal lattice, and because of the way in which the reciprocal lattice is defined the indices of these points correspond to the indices of a plane which is normal to the line from the origin of the reciprocal lattice to that point. The distance between the origin and a point of the reciprocal lattice is equal to the reciprocal of the interplanar spacing of the planes represented by that point.

The relation between a direction in reciprocal

space and one in real space is often complex and the methods used in this investigation to overcome this complexity, while still maintaining the conventional definition of reciprocal space are discussed in section 3.4.2.

An alternative approach is that of Okamoto and Thomas (1968) who used a different definition of the reciprocal lattice based on the Miller-Bravais system of notation. This also eliminates some of the problems of relating directions in real and reciprocal space but at the same time it introduces added complications which will be discussed in section 3.4.2.

One of the great aids in interpreting crystallographic problems is the stereographic projection. The fact that indices of directions are not necessarily the same as those of the planes to which they are normal complicates the stereographic projection for hexagonal crystals. In this study the system of two stereographic projections developed by Packer and Miller (1967) was extensively used. One projection was plotted for plane normal indices and the other for directions. Both projections utilized the three-axis, three-index notation and were prepared as transparencies so that they could be superimposed on a Wulff net.

The indices of a direction which is parallel to a certain plane normal (or vice versa) could then be easily determined by superimposing the two projections.

3.2 KIKUCHI MAPS

The familiar spot electron diffraction pattern arises because of coherent or elastic scattering of electrons by the lattice planes of the crystal. Incoherent or inelastic scattering of electrons also occurs giving rise to the background on electron diffraction patterns. Some of the inelastically scattered electrons, which have lost only a small amount of energy, can be subsequently elastically scattered by the lattice planes and a further modification to the background occurs. The result is the presence of a complex array of lines producing what is known as a Kikuchi pattern. This pattern is very sensitive to orientation changes of the crystal whereas no such sensitivity is evident in spot patterns in which the distribution and intensity of the spots alter only slightly. Kikuchi patterns can be used to establish the direction and magnitude of orientation changes in the electron microscope with high accuracy. The detailed aspects of electron diffraction in the electron microscope are given by Hirsch et al. (1965).

Advantages of using Kikuchi patterns to exactly fix the orientation of a foil have been discussed by von Heimendahl et al. (1964), and Thomas (1965). Kikuchi maps, which represent a fairly large variation in orientation of the thin foil were produced when high angle tilting stages were

developed for electron microscopes (Levine et al. (1966), Okamoto et al. (1967), Okamoto and Thomas (1967b)).

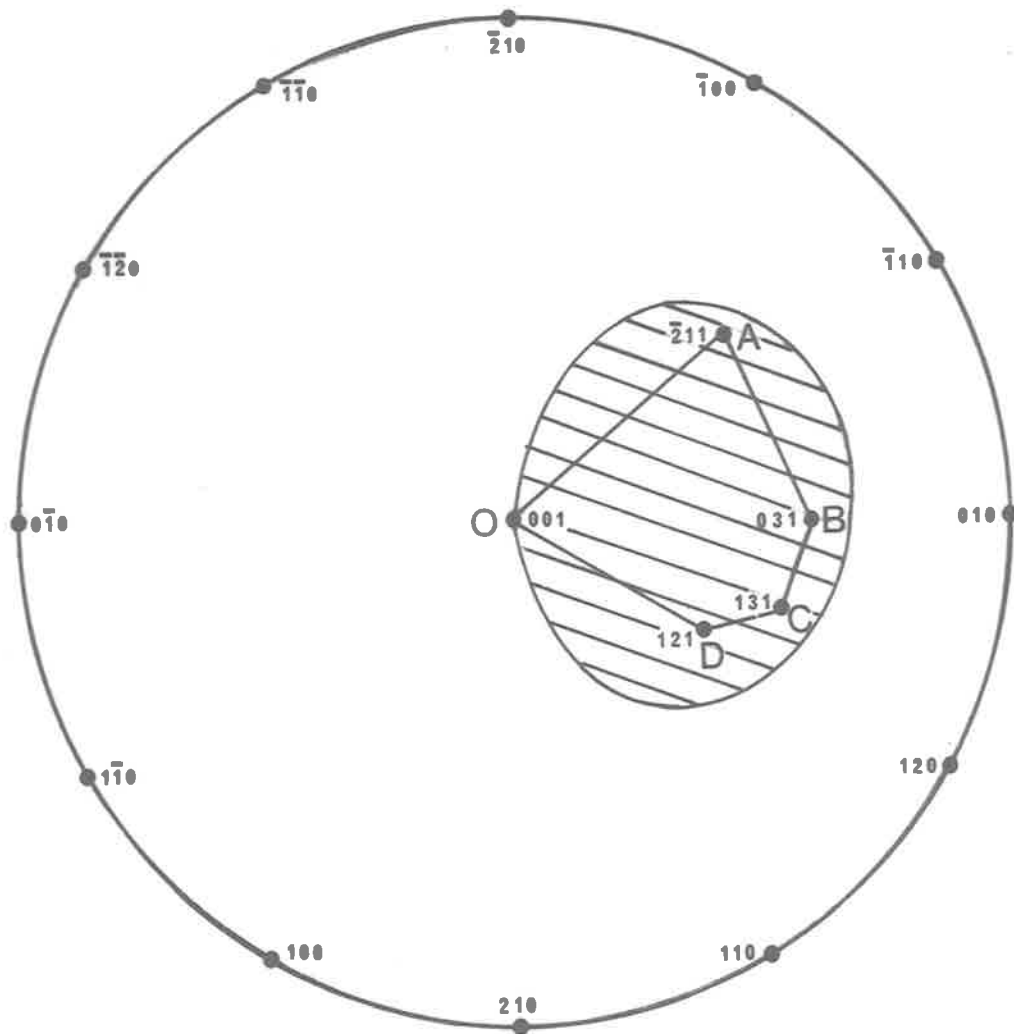
Composite maps were constructed from electron diffraction photographs and indexed diagrams of these maps were produced. The specimen preparation procedure used in this work resulted in a preferred orientation such that the indices of the normals to the grains, present in the thin foils prepared from the specimens, usually lay within the shaded area on the (001) stereographic projection (fig 3.1.). This relatively large range of orientations meant that Kikuchi maps previously published by Levine et al. (1966) and Okamoto and Thomas (1967b), for hexagonal Ag-Al alloys ($c/a = 1.588$) were inadequate, and it was therefore necessary to construct a map covering a very much larger area of the stereographic projection, the area being delineated by OABCD in fig 3.1.

The large Kikuchi map produced is shown in fig 3.2. and because it represents a large range of orientations, this map would be severely distorted if straight Kikuchi lines were used as had been done previously (Levine et al. (1966), Okamoto and Thomas (1967b)). To overcome this distortion the map was produced, following Hirsch et al. (1965) and Ashbee and Heavens (1967), as a stereographic projection thereby allowing continuity of the Kikuchi lines.

To construct the map, shown in fig. 3.2, a large

FIG.3.1 [001] PROJECTION FOR DIRECTIONS
HEXAGONAL $c/a = 1.59$

GENERAL AREA OF ZONE AXES OF GRAINS
LOOKING AT SURFACE OF COLD ROLLED AND
ANNEALED ZIRCONIUM SHEET.
CONFINES OF KIKUCHI MAP MARKED AND INDEXED.



Wulff net was used to outline a stereographic projection of the centre lines of the Kikuchi bands. The spacing of the Kikuchi lines was calculated from reciprocal lattice dimensions and the Kikuchi line pairs were laid on the map. Minor adjustments could easily be made because of the particular method used to construct the lines.

In fig. 3.2 the poles of the Kikuchi map have been indexed in the three-axis, three-index notation. This means that a pole has the indices of a direction which corresponds to the zone axis of the planes which give rise to the Kikuchi lines which converge to that pole. It can be seen that most of the indices are relatively simple.

For cross reference purposes, the poles of the same map were indexed using the four-axis, four-index notation and in fig. 3.3 the complexity of some of the indices can be seen (e.g. the $[\bar{1}52]$ becomes the $[\bar{7}11\bar{4}6]$).

On both maps the Kikuchi lines have been indexed using the Miller notation and the indices refer to the planes from which the diffraction of electrons occurs giving rise to the Kikuchi lines. The indices of the Kikuchi lines in fig. 3.3. have been left in the three-index notation for reasons of clarity and because the interconversion of three to four index notation for plane normal indices is trivial (Appendix 2).

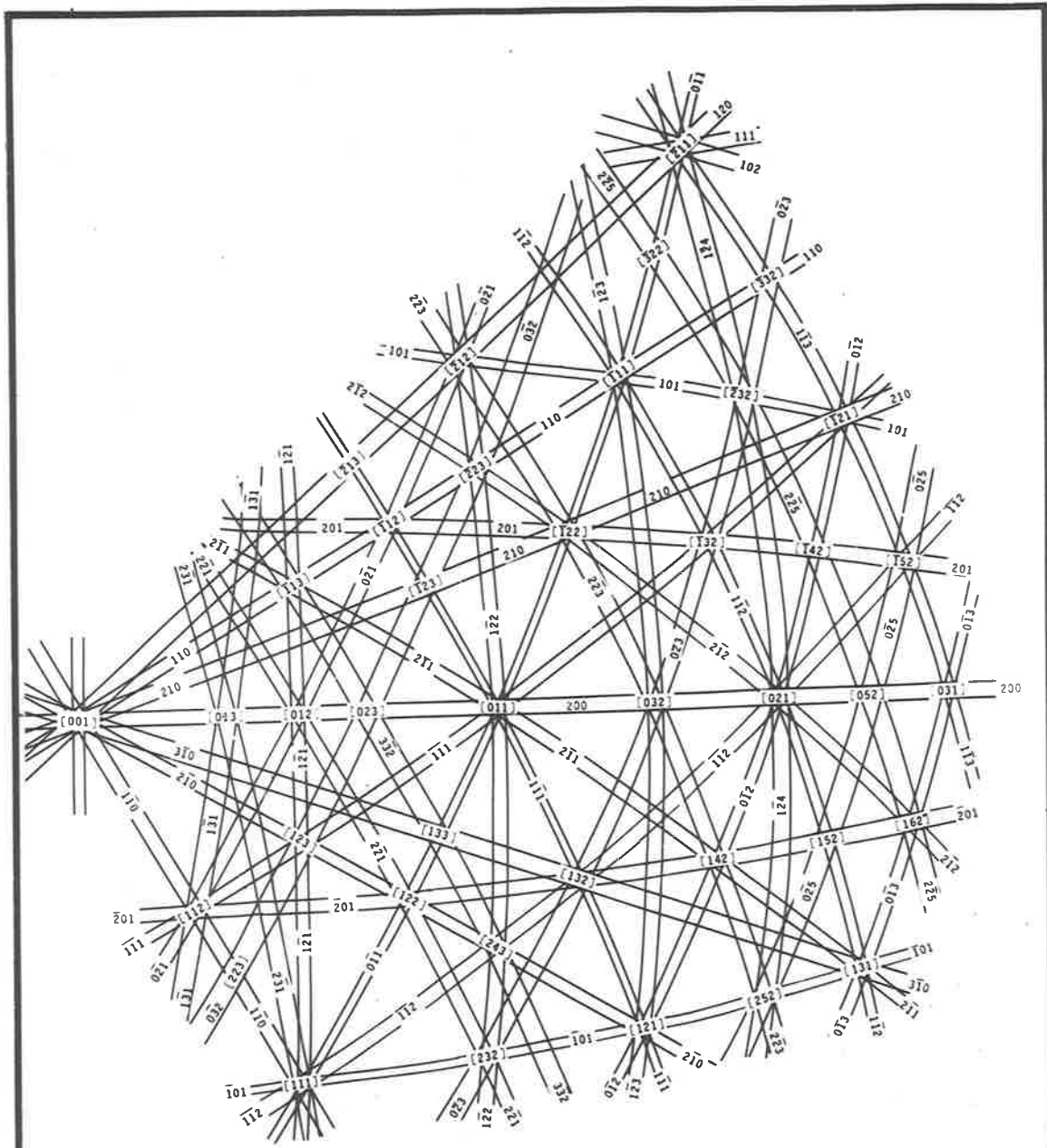


FIG.32 INDEXED KIKUCHI MAP FOR
H.C.P. LATTICE $c/a = 1.59$
Poles in Miller-Bravais directional indices,
Kikuchi lines in Miller plane normal indices.

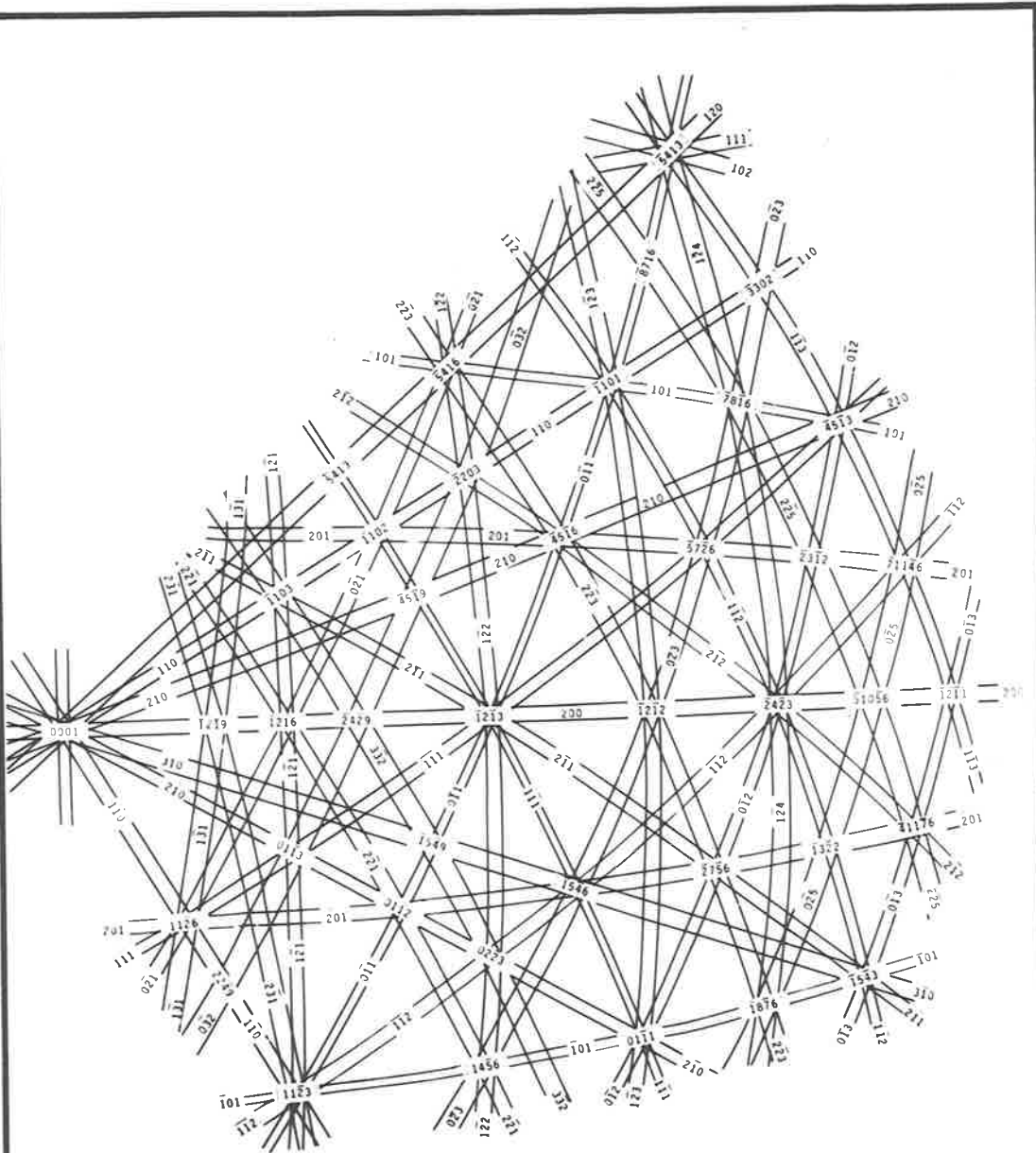


FIG.3.3 INDEXED KIKUCHI MAP FOR
H.C.P. LATTICE $c/a = 1.59$
Poles in Miller-Bravais directional indices;
Kikuchi lines in Miller plane normal indices.

The poles of the map represent "exact orientations" (Thomas, 1965) where the diffraction patterns are symmetrical and distortion is a minimum. It then becomes possible to construct the diffraction pattern from a crystal in each exact orientation and standard diffraction patterns so prepared increase the usefulness of a Kikuchi map by enabling immediate indexing of individual lines and poles to be obtained. Diffraction patterns representing all the important poles on the Kikuchi map were drawn to a scale based on reciprocal lattice dimensions by Bedford and Miller (1970) (Appendix 3).

3.3 BURGERS VECTOR DETERMINATION

The contrast obtained around dislocations during electron microscope observation has been extensively investigated in the last decade, starting with the classical papers of Whelan (1958-9) and Hirsch, Howie and Whelan (1960), and many developments have been well documented in the treatise of Hirsch et al. (1965). Recent refinements based on the Dynamical theory of electron diffraction, which include computer simulations of dislocation images, are aimed at obtaining precise and detailed information on the nature of dislocations. In general for most of the results obtained in the present work, the Kinematical theory provided an adequate explanation of the observations, although occasionally it was apparent that dynamical effects were present.

The unique determination of Burgers vectors by using tilting experiments in the electron microscope requires careful and planned manipulations and it is in this context that the Kikuchi maps, stereographic projections and diffraction patterns referred to previously are invaluable. The first step is to recognize, or have some easy method of analysing and indexing, the diffraction pattern from the specimen while it is being viewed in the electron microscope. The indexed scale drawings of the diffraction patterns are very useful for this step (fig. 4, Bedford and Miller, Appendix 3). Then, by referring to the Kikuchi map, the specimen can be tilted so that a pair of Kikuchi lines radiating from the known pole, can be followed to obtain any required two beam condition, (provided it lies within the tilting range of the stage). The path followed during the tilting experiment can be conveniently plotted on the Kikuchi map so that duplication of results is avoided, a precaution worth taking if the material being examined deteriorates during exposure to the electron beam.

When studying hexagonal metals it is quite often very difficult to recognise a diffraction pattern or Kikuchi pole while the specimen is being examined in the electron microscope because many are very similar. In such cases the following technique for Burgers vector determination can be recommended.

Two beam diffracting conditions which result in the dislocation or set of dislocations giving zero or very weak contrast are established. The nearest pole is photographed along with the image and the original two beam condition. A sketch is made of the Kikuchi pattern observed and this sketch is extended during subsequent tilting experiments. Once the first extinction condition is found it is usually fairly simple to find another two beam condition for which the same dislocations are again out of contrast. This is usually done by moving along a Kikuchi band, often one which makes a high angle with the one corresponding to the first two beam condition, until another set of two beam conditions giving the required extinction is found. This procedure makes use of the fact that the dislocations go out of contrast for the two beam conditions established by any Kikuchi band which converges to the pole which represents the Burgers vector (Okamoto et al. (1967)). Since it is possible that the Burgers vector of the dislocations being examined may have the indices of the first established pole, it is always necessary to commence the tilting experiment by checking the contrast of the dislocations for each of the two beam conditions determined by the Kikuchi bands converging to that pole.

Unambiguous analysis of Burgers vectors requires, in addition to the above procedures, careful indexing of the

orientations used and this is discussed in section 3.4.4.

3.4 DISCUSSION OF CRYSTALLOGRAPHY

3.4.1 The "Miller" and "Miller-Bravais" Indexing Systems.

The main difference between the three-axis, three-index system and the four-axis, four-index system appears at the unit cell definition. In the former case, the unit cell is defined by a parallelepiped (dark outline fig. 3.4.) and only when several of these are stacked together is the symmetry of the hexagonal lattice recognised. The Miller-Bravais notation does not suffer from this short-coming since the unit cell is the smallest hexagonal unit of the lattice. Two of the most commonly quoted advantages of the Miller-Bravais system are

- (1) Symmetrical planes have similar indices
(e.g. Prism planes $\{10\bar{1}0\}$ are $(10\bar{1}0)$, $(1\bar{1}00)$, $(01\bar{1}0)$ etc.).
- (2) directions of a family have indices of the same kind.

A good example of the latter is shown by the indices of the close packed directions in the basal plane (fig. 3.5.). Miller-Bravais indices of the type $\langle 11\bar{2}0 \rangle$ are all easily visualized but Miller indices of the type $\langle 100 \rangle$ do not suggest the inclusion of $[\bar{1}\bar{1}0]$.

FIG.3.4 UNIT CELLS OF H.C.P. LATTICE

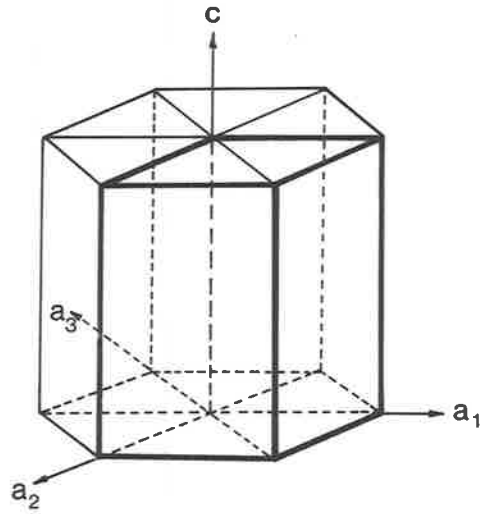
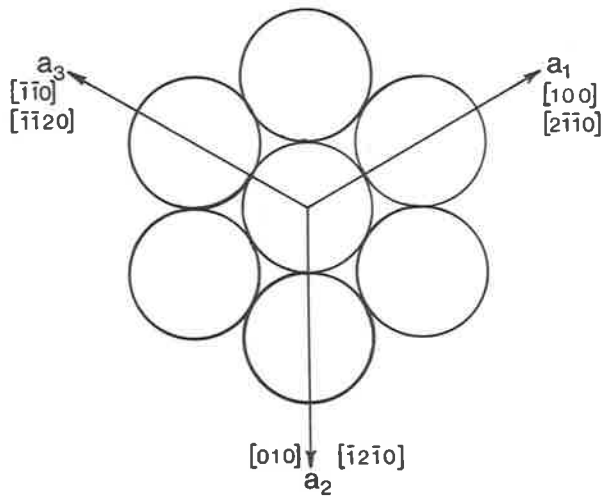


FIG.3.5 CLOSE PACKED DIRECTIONS IN BASAL PLANE



The fact that such symmetry is apparent when use is made of the Miller-Bravais system for indexing planes and directions in h.c.p. lattices is often the main reason for it being preferred. However, there are advantages to be gained by using the Miller system. One advantage is that a direction is often easier to visualize on the three-axis, three-index basis than on the four-axis, four-index basis. This is shown conveniently in the case of the $[111]$ direction (Bedford and Miller (1970); Appendix 3). Other significant advantages are apparent when the three-axis, three-index system is used in conjunction with the reciprocal lattice, section 3.4.2.

An incidental advantage of the use of the Miller system of indexing planes and directions is that it becomes possible to include more points on a stereographic projection. This can be illustrated by comparing the double-stereogram of Rarey et al. (1966) with the stereographic projections of Packer and Miller (1966). In the former case the stereogram includes both plane normal and directional indices which means that a distinction between them must be made (by either marking with different spots or by including brackets), and the fact that the four-index notation is used, means that only low index plane normals and directions can be included because of space limitations. The projections of Packer and Miller do not suffer from these shortcomings since plane normals and

directions are plotted on separate projections and the fact that the three-index notation is employed means that many more points can be included while still retaining clarity and accuracy.

3.4.2 Reciprocal Lattice.

There has been wide ranging discussion on the reciprocal lattice which is generated from an hexagonal lattice in real space. As Nicholas (1970) has recently pointed out there is in fact only one reciprocal lattice for an hexagonal lattice but controversy surrounds the way in which that lattice is best defined and indexed.

There are two main methods used to index the reciprocal lattice; the first is based on the three-axis, three-index system and the second on the four-axis, four-index system. The conventional definition of the reciprocal lattice (Barrett and Massalski, 1966) is based on the three-axis, three-index system and the indexing of points in reciprocal space follows simply from this definition (Otte and Crocker, 1965). On the other hand, Okamoto and Thomas (1967 a and 1968) referred to a concept based on the four-axis system which really amounted to the definition of a new reciprocal lattice containing many more points than the true reciprocal lattice. This difficulty could, however, be overcome by recognising that the points which

correspond to those of the true reciprocal lattice have integral indices.

As Nicholas has pointed out, for crystallographic problems requiring the easy recognition of symmetry, the four-axis, four-index notation for real and reciprocal space has some merit but in the present investigation, the simplest and most convenient means of solving the kinds of crystallographic problem which arise in practical electron microscopy has been found to involve the three-axis, three-index notation for both real and reciprocal space.

One of the major problems which arises concerns the definition of a direction in reciprocal space and the relation between this direction and directions in real space. If a vector in the reciprocal lattice is given directional indices then the relation between these indices and the indices of a conjugate direction in real space is complex because of the relative rotations between the crystallographic axes of the real and reciprocal lattices. For the kind of crystallographic problem encountered in the present work it was found that the difficulty could be overcome very simply by describing directions in reciprocal space only in terms of the reciprocal lattice vector. These reciprocal lattice vectors, g , which are the vectors from the origin to the reciprocal lattice points, represent directions which are normal to the particular sets of planes and so are given plane normal indices. The

length of this vector is equal to the reciprocal of the particular interplanar spacing. That is, in fig. 3.6, the vector $g(101)$ represents a direction parallel to the normal to the (101) planes and its length is the reciprocal of the distance between the (101) planes. Therefore, if all manipulations which require directions are carried out using these reciprocal lattice vectors, the stereographic projection for plane normals can be used. Then, if the final analysis requires that a direction in real space be given, the stereo-graphic projection for directions is superimposed on the plane normal projection and the corresponding directional indices obtained.

3.4.3 Kikuchi Maps

The use of Kikuchi patterns to calculate exact orientations into which thin foils had been tilted was discussed by von Heimendahl et al. (1964), Thomas (1965) and Levine et al. (1966). Subsequently the techniques were extended to include larger ranges of orientations by plotting Kikuchi maps and these were constructed for a number of f.c.c., b.c.c., and h.c.p., structures (Okamoto et al. (1967), Okamoto and Thomas (1967b)).

Thomas (1965) pointed out that spot diffraction patterns are symmetrical and contain least distortion when the

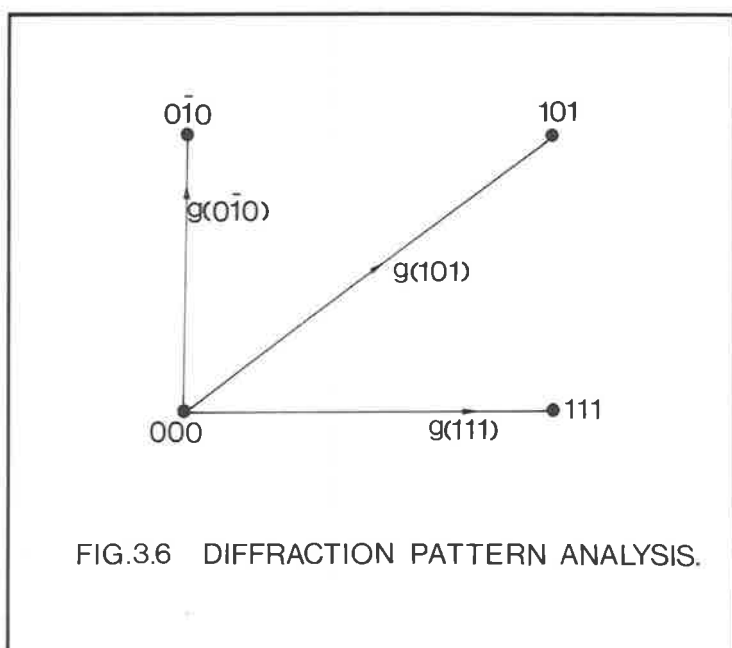


FIG.3.6 DIFFRACTION PATTERN ANALYSIS.

specimen is in an "exact-orientation" (the term "exact-orientation", which Thomas defined as meaning that a plane of the reciprocal lattice lies exactly normal to the incident beam, is somewhat misleading since any orientation is an exact orientation in its own right). In essence, Thomas was referring to the fact that it is only when the diffraction pattern is symmetrical that it can be conveniently used to accurately determine the orientation of the foil, and so he recommended that the more accurate Kikuchi line analysis be used where precise orientation determinations were required. In the present work it was found that analysis of spot diffraction patterns was relatively simple if they were taken at or near poles of the Kikuchi map. One of the most significant advantages of the Kikuchi pattern is, therefore, the fact that it enables the specimen to be tilted to a Kikuchi pole, where a symmetrical spot pattern is produced; the subsequent orientation changes during tilting experiments can be easily referred to these precisely determined orientations. Another advantage of the Kikuchi map is that it facilitates the consistent indexing of several diffraction patterns relative to each other and this important consideration is discussed in section 3.4.4.

The Kikuchi maps shown in figs.3.2 and 3.3 are applicable to hexagonal metals and alloys with axial ratios in

the range 1.58 - 1.60. When used in conjunction with the stereographic projections they provide a most useful aid to the solution of crystallographic problems, and, in spite of Levine's (1968) contrary opinion, are easily constructed and their use quickly compensates for the time and effort used in their production.

3.4.4. Burgers Vector Determination

When the Burgers vector of a dislocation is to be established, using the electron microscope, one of the best methods is to obtain two different two-beam conditions for which the dislocation is out of contrast. Some planning of the tilting experiments can be made on the basis of the likely Burgers vectors of dislocations in hexagonal close packed metals (Damiano (1963), Partridge (1967)). If the dislocations are perfect the $g \cdot b = 0$ criterion can be used and the Burgers vector calculated. This is often done geometrically on a stereographic projection and this method was adopted in the present work. When use is to be made of the above extinction condition, realizing of course its deficiencies for dislocations other than perfect screws (Hirsch et al. 1965), it is essential that internally consistent values of g be used. To do this the diffraction patterns (and thus the orientations of the foil), which are obtained during the tilting experiments, must

be consistently indexed. The following explanation shows the importance of this and a distinction is made between correct and consistent indexing of diffraction patterns.

The spots of a correctly indexed diffraction pattern are assigned indices based on the distance of each spot from the origin (or (000) spot); the reciprocal of this distance corresponds to the interplanar spacing of planes with the same indices in the real lattice. An integral arithmetic relation exists between each spot and its neighbours and when indexed using these principals it is found that the diffraction pattern is given a zone axis which is a member of a family of zone axes. (i.e. the diffraction pattern belongs to a family of orientations, the only difference between each member of the family being the angular rotation between them).

When a number of diffraction patterns are used they must be indexed in a consistent manner because there are, in the hexagonal lattice, many orientations of the same kind fairly close to one another. These, however, must be recognized as different orientations and once a set of indices has been ascribed to one of the diffraction patterns it is essential that the others should be indexed to conform to that system. When the indexing is consistent there are no discontinuities in the Kikuchi lines of the Kikuchi map constructed using the indexed group of diffraction patterns.

An example of consistent and inconsistent indexing is shown in fig. 3.7. In fig. 3.7(a) the diffraction patterns have been indexed such that the Kikuchi lines common to each pair of patterns are continuous. However, in fig. 3.7(b) the same diffraction patterns have been analysed without reference to the Kikuchi map and although the diffraction spots all have indices of the right type (correctly indexed) it can be seen that discontinuities occur in the Kikuchi lines. The Kikuchi band containing A can be indexed from the $[011]$ pattern as an $(0\bar{1}1)$ and from the $[121]$ pattern as a $(1\bar{1}1)$. The error in the Kikuchi band containing B is not as important, but it can be significant.

To illustrate the type of error which can then occur, the $g.b. = 0$ construction is made on a stereographic projection. Firstly, suppose that a dislocation gives little or no contrast for both the two beam conditions A and B. If fig. 3.7(b) is used to index the diffraction vector, the solution to the $g.b. = 0$ criterion will be that shown on the stereographic projection of fig. 3.8(b). The Burgers vector is given as $[100]$. If now, the correctly indexed diagram (fig. 3.7(a)) is used to fix g , then the $g.b. = 0$ construction on the stereographic projection is as shown in fig. 3.8(a) and the Burgers vector is found to be $[121]$. It can be seen that this is the correct solution as the Kikuchi lines converge to

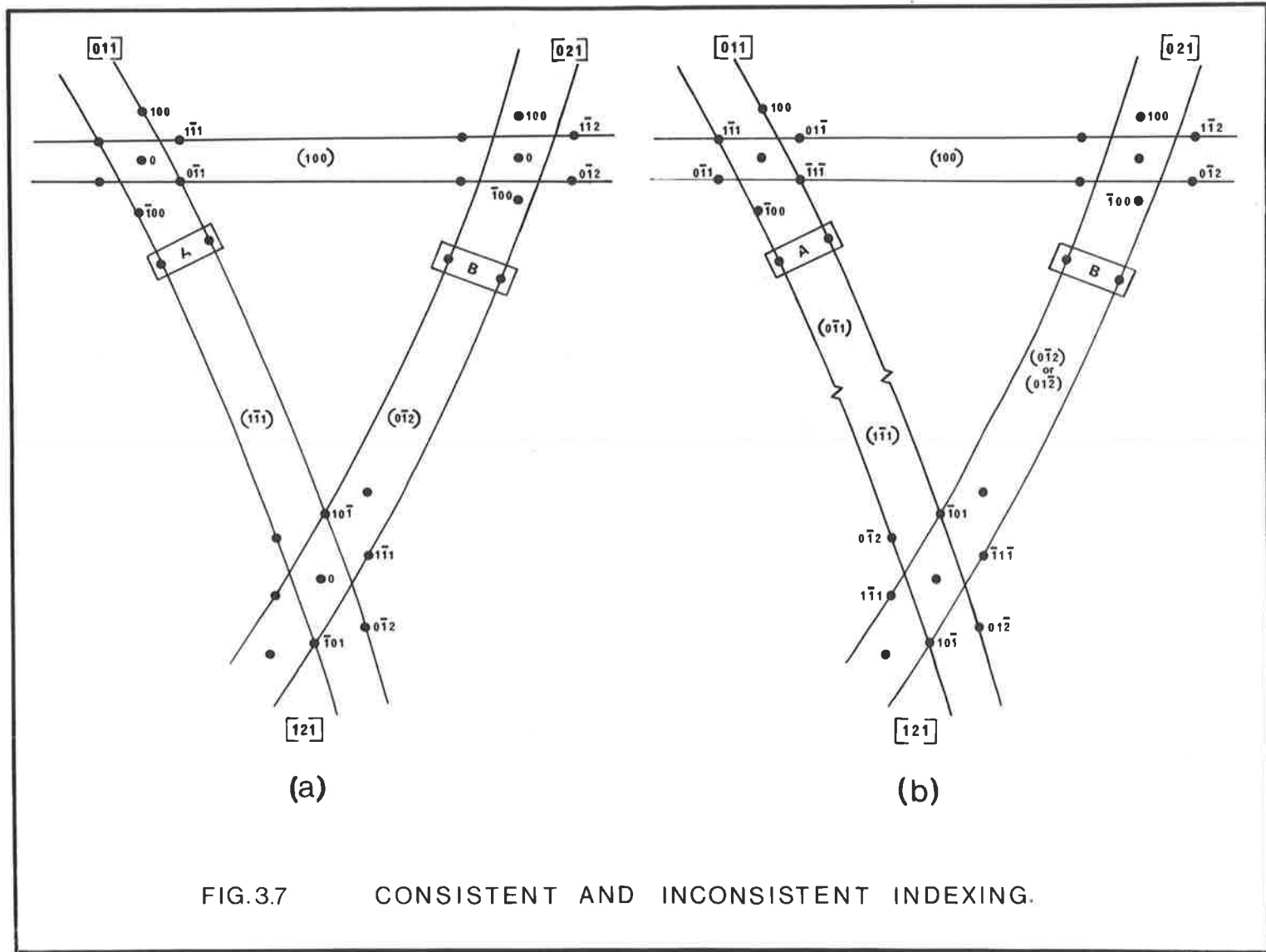


FIG.3.7 CONSISTENT AND INCONSISTENT INDEXING.

the pole of the Burgers vector (Okamoto, Levine and Thomas (1967)).

The above has been illustrated with a rather extreme case but errors of this kind could easily be made if, for example, the diagrams of diffraction patterns published by Chaturvedi and Singh (1969) were used for Burgers vector determinations.

There have been no complete analyses, in the literature, of Burgers vectors in zirconium using an electron microscope. Bailey (1962) studied dislocation arrangements in deformed zirconium and concluded that the Burgers vectors were probably of the type $1/3 \langle 11\bar{2}0 \rangle$. Observations of dislocation movements in thin foils of zirconium (Howe et al. 1962) did not result in any analyses of the Burgers vectors. In neither of the above papers was any complete characterization of the diffracting conditions reported.

Some recent results from electron microscopy of titanium (Williams and Blackburn, 1968) have suggested that dislocations with Burgers vector $1/3 \langle 11\bar{2}3 \rangle$ occur. (Note that the notation given was $\frac{\bar{c}}{3} + \bar{a} \langle 11\bar{2}3 \rangle$ which is incorrect, and, also that $\langle 11\bar{2} \rangle$ instead of $\langle 11\bar{2}3 \rangle$ was included in the manuscript). Again, completely unambiguous results cannot be obtained from the limited diffraction experiments reported in that paper. Williams and Blackburn suggested that the fact that their dislocations were in contrast for $g(0002)$ and out of

contrast for $g(10\bar{1}0)$ established the Burgers vector as $\langle 11\bar{2}3 \rangle$ or $[0001]$. However, there are many other possible Burgers vectors which could satisfy their diffracting conditions (e.g. $\langle 11\bar{2}6 \rangle$ and $\langle 22\bar{4}3 \rangle$). Presumably $\langle 11\bar{2}3 \rangle$ was chosen on the basis of predicted Burgers vectors for hexagonal lattices. Even with quite extensive tilting results, an error of the kind referred to earlier could be made, and the following example shows how important it is to precisely index several diffraction patterns and relate them to the Kikuchi map. This example shows that a Burgers vector $[010]$ could be mistaken for an $[012]$ if a slight error was made in indexing the diffraction patterns and since $[012]$ is of the family $\langle 11\bar{2}6 \rangle$, the following could be compared to the results of Williams and Blackburn.

The dislocations in fig. 3.9 are in strong contrast for the diffracting conditions shown. In fig. 3.10 some of the dislocations are out of contrast for the two beam diffracting conditions shown in the inset, which is indexed with reference to a nearby pole, fig. 3.11, whose zone axis is $[011]$. Therefore the diffracting vector representing the two beam conditions of fig. 3.10 is $g(\bar{1}00)$. The same dislocations are again out of contrast in fig. 3.12. The nearby pole is fig. 3.13 and this may be indexed with a $[\bar{2}12]$ zone axis fig. 3.14 (a) which seems reasonable because of its proximity to the $[011]$ zone

FIG. 3.9 Electron micrograph of dislocations
in a deformed zirconium specimen.
Diffracting conditions are shown
in the inset.

0.5 μ

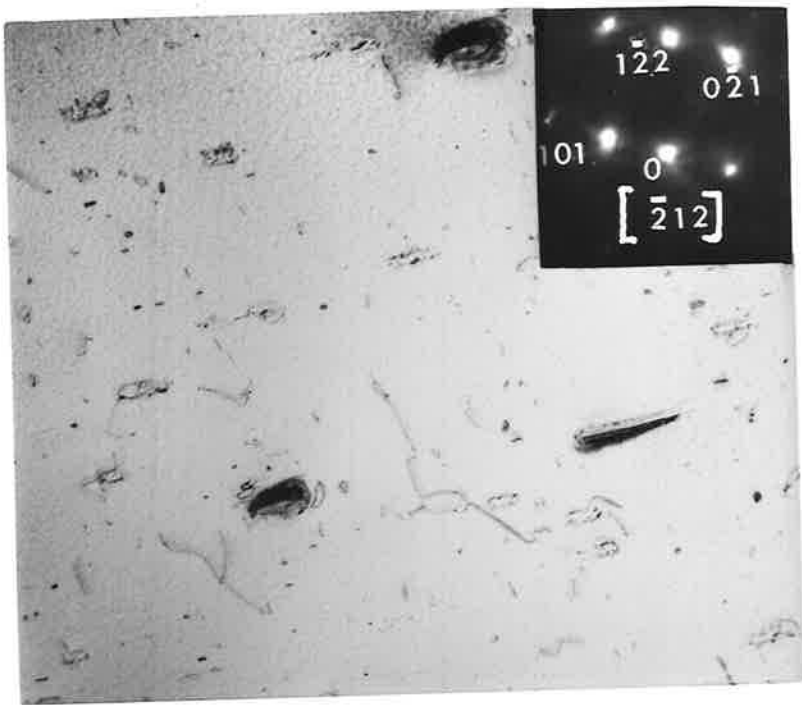


FIG. 3.10 Some of the dislocations (c.f. Fig. 3.9) are out of contrast for the two-beam conditions shown in the inset.

0.5 μ



FIG. 3.11 The spot diffraction pattern from a nearby pole. This is used to index the two-beam conditions of fig. 3.10.

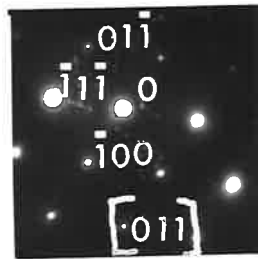
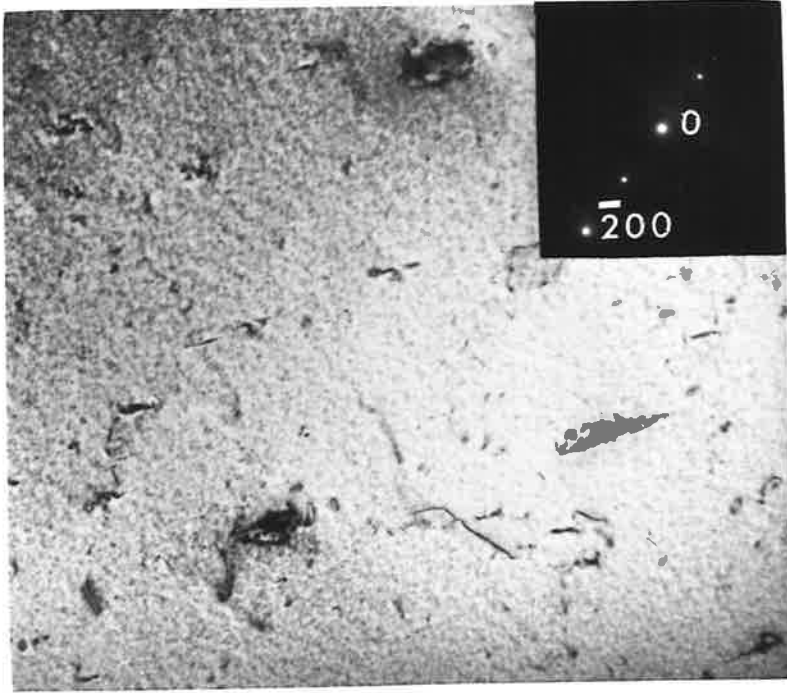
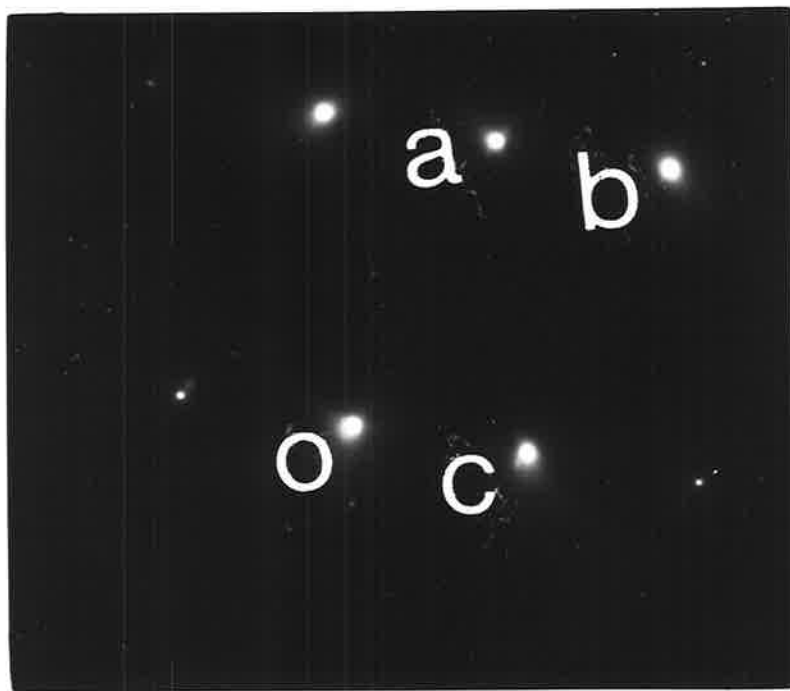
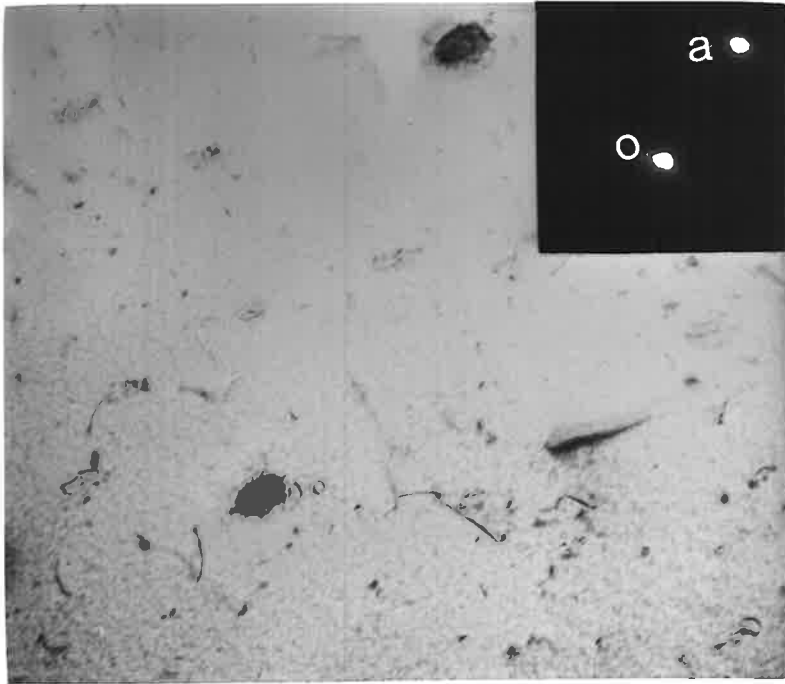
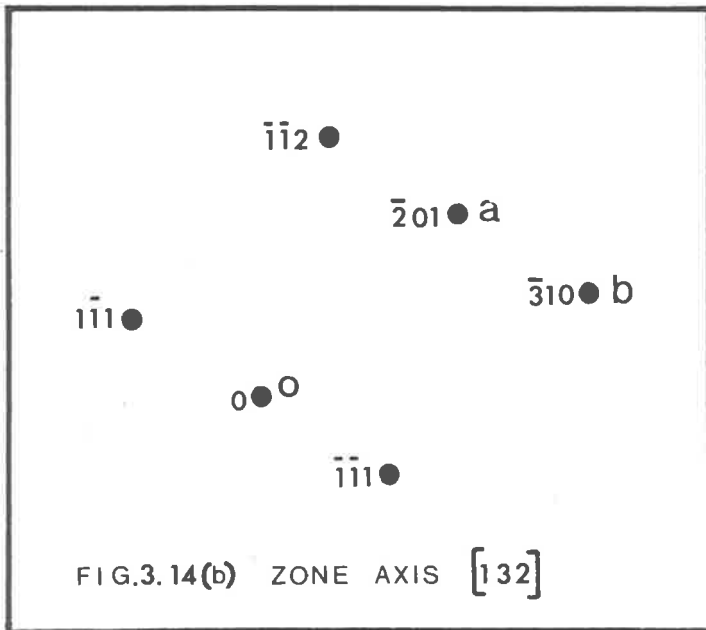
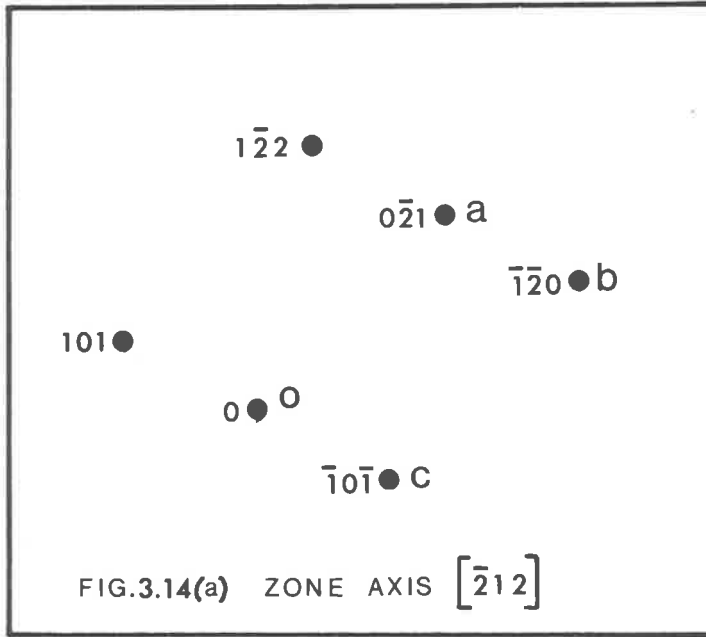


FIG. 3.12 The same dislocations (c.f. fig. 3.10) are out of contrast. The two-beam conditions are shown in the inset.

0.5 μ
└───┘

FIG. 3.13 The spot diffraction pattern at a Kikuchi pole near the conditions of fig. 3.12. This may be indexed as shown in figs. 3.14(a) and (b).





axis fig. 3.15. Thus the diffraction vector representing the two beam conditions of fig. 3.12 is $g(0\bar{2}1)$. By using the $g.b. = 0$ criterion for $g(\bar{1}00)$ and $g(0\bar{2}1)$ the Burgers vector is found to be $[012]$ or $1/3[\bar{1}2\bar{1}6]$. However, fig. 3.13 can also be indexed with a $[132]$ zone axis, which is of the same type as $[\bar{2}12]$ and its position is shown on the Kikuchi map, fig. 3.15. The indexing is then given by fig. 3.14(b) and the diffraction vector for fig. 3.12 is then $g(\bar{2}01)$. Using the $g.b. = 0$ criterion the Burgers vector is now $[010]$, or $1/3[\bar{1}2\bar{1}0]$. This is the expected form of the Burgers vector and the correct nature of this result is also indicated by careful comparison of the diffraction pattern orientations (figs. 3.9 and 3.13.). For analysis purposes the negatives, or asymmetrical prints, were used so that critical alignment procedures could be used.

These examples underline the fact that in order to unambiguously determine the Burgers vectors of dislocations in hexagonal metals it is absolutely essential to consistently index the diffraction patterns. This is particularly important when dislocations with Burgers vectors of the same kind are present in the same specimen: such a situation exists for hexagonal dislocation networks in zirconium which are discussed in Chapter 4.

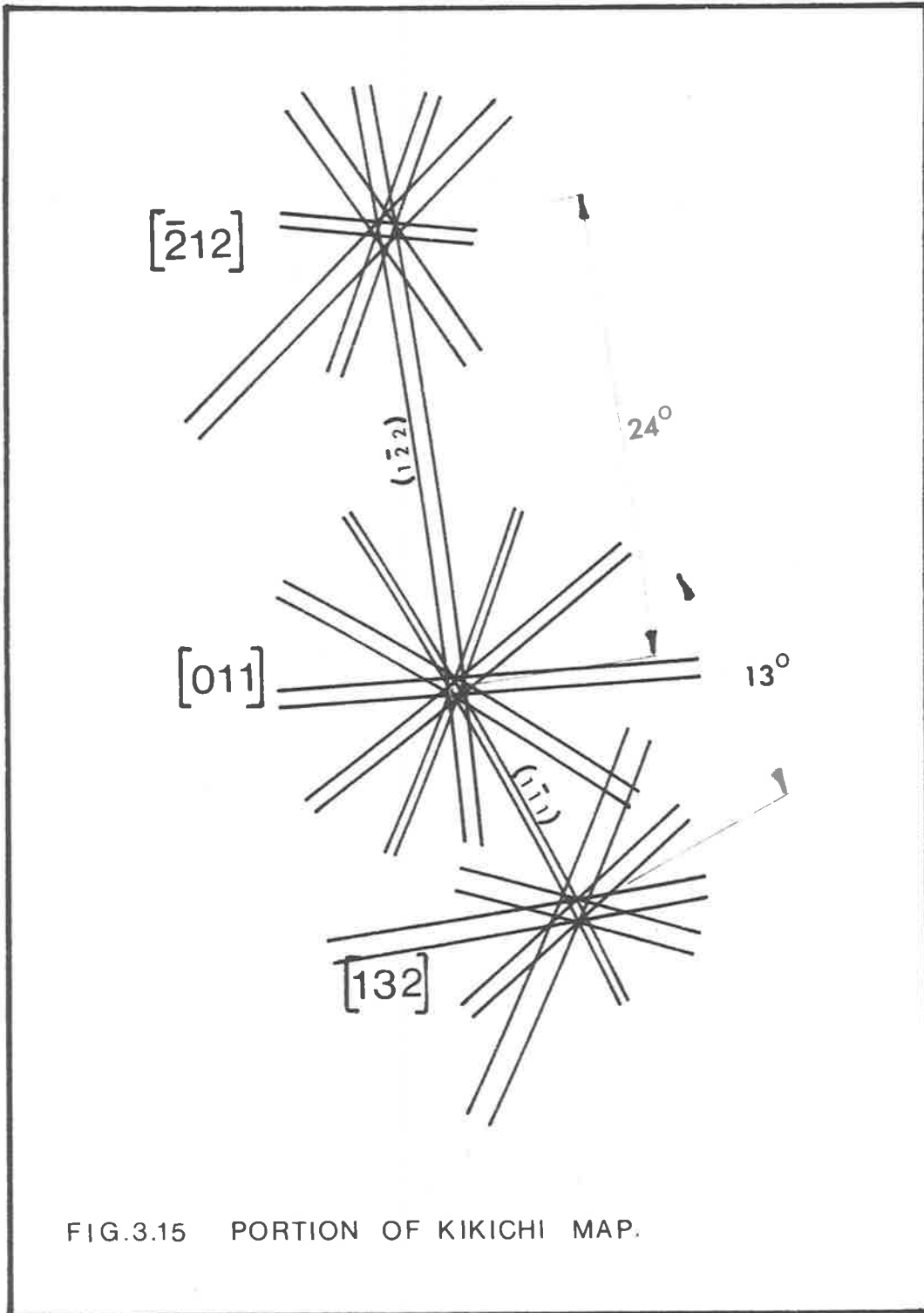


FIG.3.15 PORTION OF KIKICHI MAP.

CHAPTER 4. ELECTRON MICROSCOPE STUDY OF DEFORMED
ZIRCONIUM

4.1 INTRODUCTION.

The previous chapters have shown that there is a need to examine, in detail, the types of dislocation arrangements and the dislocation reactions which take place when zirconium is strained in the temperature range 0 - 600°C. Electron microscopy has been used in the present work to show the dislocation arrangements and, with the crystallographic procedures developed in Chapter 3, a thorough analysis of Burgers vectors of dislocations and the slip systems which operate has been carried out.

It will be shown that the arrangements of dislocations which result when a specimen is strained in the temperature range 200 - 500°C have a strong bearing on the yielding behaviour in this temperature range. High temperature deformation results in the occurrence of dislocation reactions and hexagonal networks of dislocations can be produced as these reactions proceed. Networks which are indistinguishable from these are produced when deformed zirconium specimens are recovered and the mechanisms which can produce these networks have been extensively studied.

4.2 SLOW STRAIN RATE EXPERIMENTS

Specimens strained at room temperature showed a fairly random array of dislocations after small amounts of strain (up to $\approx 5\%$). With increasing strains the dislocations started to form tangles and eventually a cell structure developed. There was always a large number of free* dislocations, within the cells.

Similar behaviour was evident in tests carried out at 100°C and after a strain of 0.015 a random, low dislocation density, array resulted. An increase in the longitudinal strain to 0.04 produced dislocation tangles, and vague cell formation occurred nearer the grain boundaries, fig. 4.1. A large number of free dislocations were present in the cells after a strain of approximately 0.07, and an increase in strain to 0.09 resulted in a similar dislocation substructure, fig. 4.2.

Straining at 200°C produced dislocation cells which were more prevalent, and well formed near high angle grain boundaries, but the cell interiors still contained a significant number of free dislocations fig. 4.3. The cells tended to form at lower strains than those at which they formed at 100°C .

After a strain of 0.05 at 280°C the dislocation cells were bounded by tangled walls which were more ordered than

* Dislocations not associated with tangles or ordered arrays.

FIG. 4.1 Dislocation tangles and vague cell formation. Strain 0.04 Temp. 100°C.
0.5 μ

FIG. 4.2 Dislocation cells containing many free dislocations. Strain 0.09 Temp. 100°C.
0.5 μ

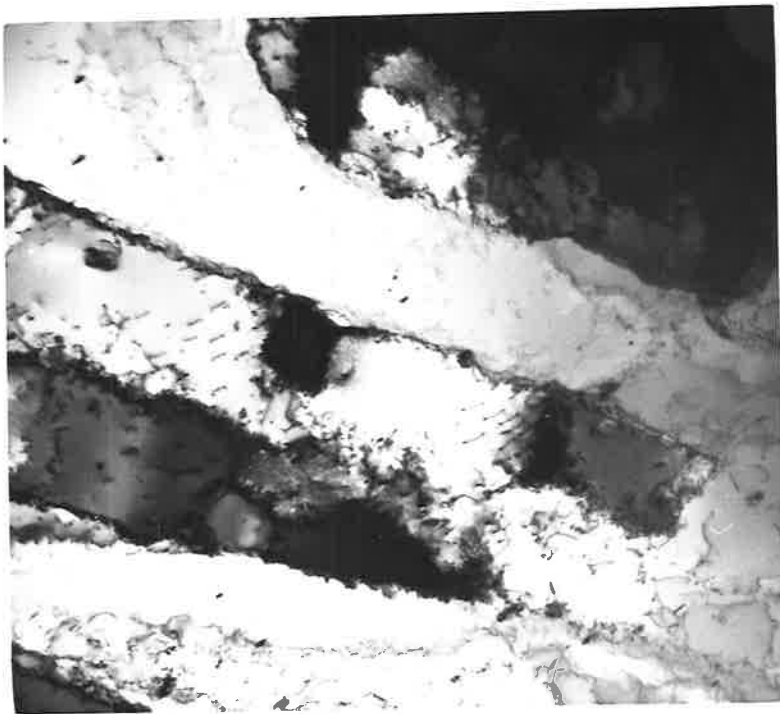
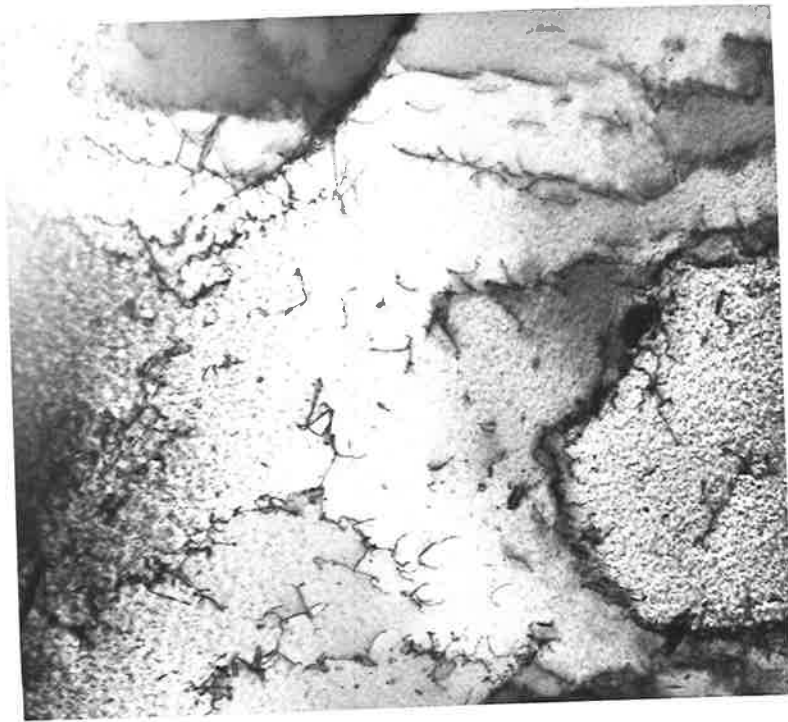
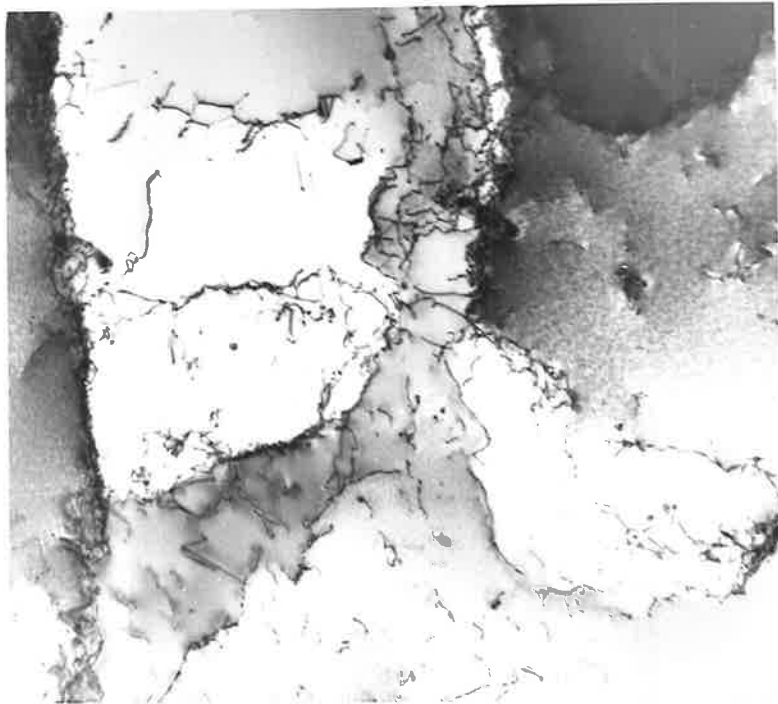
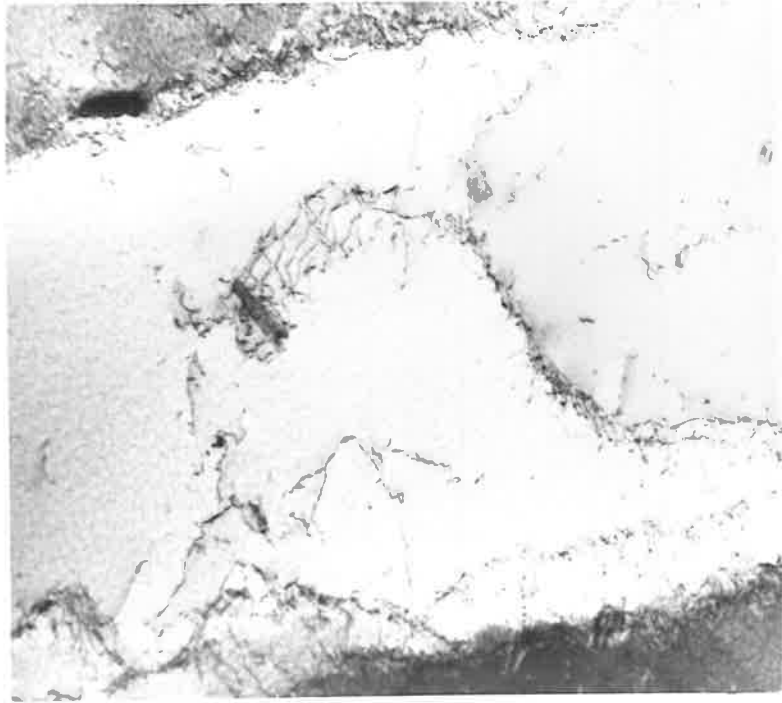


FIG. 4.3 Dislocation cell structure
Strain 0.05 Temp. 200°C.
0.5μ
└───┘

FIG. 4.4 Well formed dislocation cells
Strain 0.05 Temp. 280°C.
0.5μ
└───┘



those formed at lower temperatures and there were also fewer dislocations within the cells, fig. 4.4. The cell structure was similar at strains near 0.07. In both of the above specimens a number of grains contained only a vague cell structure, the interiors of which contained a large number of free dislocations, fig. 4.5.

Straining at 400°C produced a much more open dislocation structure containing longer dislocation segments which often interacted to form three-fold-nodes and these specimens also contained a number of small dislocation loops, (fig. 4.6).

Dislocation networks appeared more frequently after straining at 500°C, fig. 4.7, more loops were present, fig. 4.8 and low angle grain boundaries formed in some instances.

4.3 HIGHER STRAIN RATE EXPERIMENTS.

As well as electron microscopy, optical surface studies were carried out on most of the specimens tested in these experiments. Stress-strain curves were plotted for each of the tests and these are presented in fig. 4.9.

Most grains contained straight slip lines, resulting from slip on one or two slip planes, after a strain of about 0.01 at room temperature, fig. 4.10. The density and width of straight slip lines was greater after a strain of 0.015, and

FIG. 4.5 Free dislocations and vague
cell structure in some grains
Strain 0.07 Temp. 280°C.

0.5 μ
└───┘

FIG. 4.6 Dislocation structure relatively
uniform and contains 3-fold nodes
and small loops. Strain 0.02 Temp.
400°C.

0.5 μ
└───┘

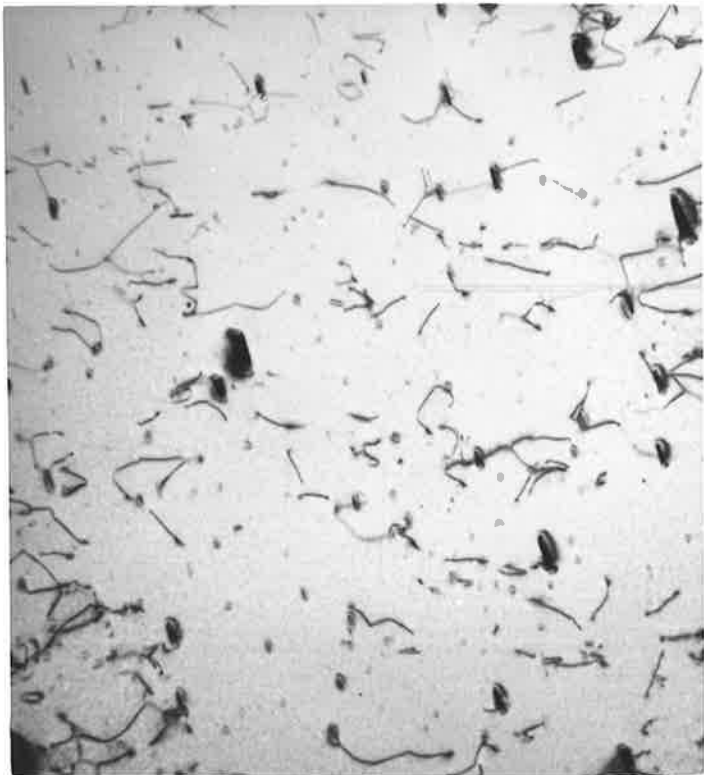
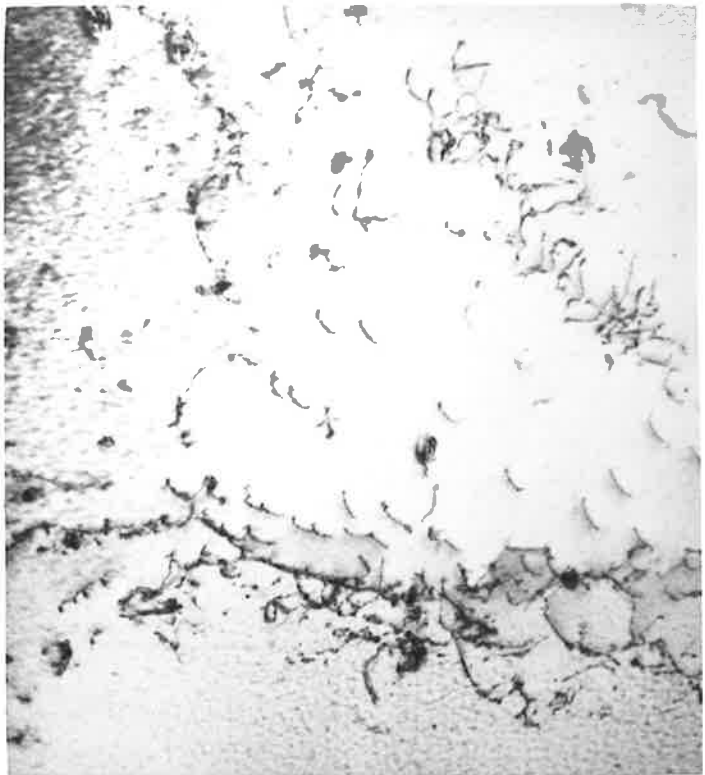




FIG. 4.7 Dislocation network formed during straining at 500°C.

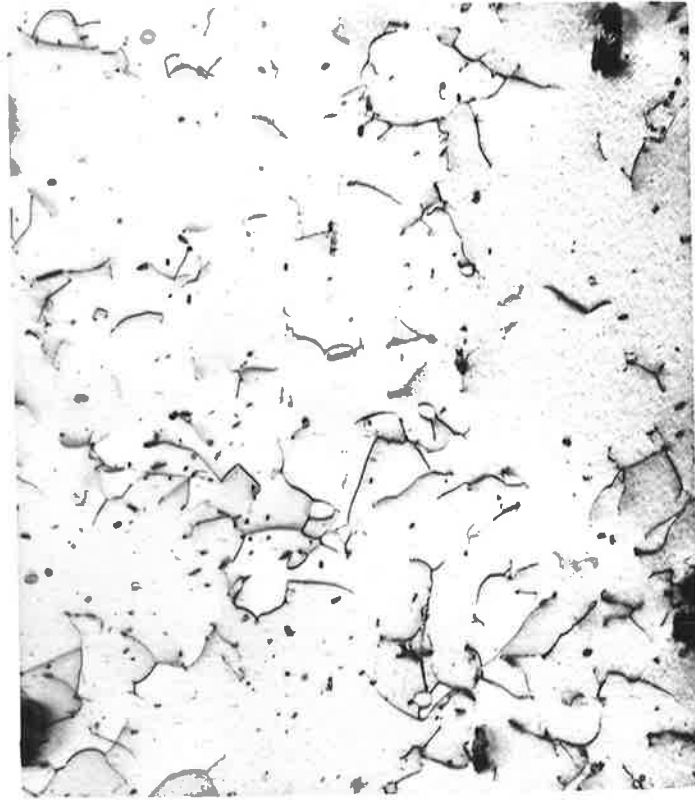
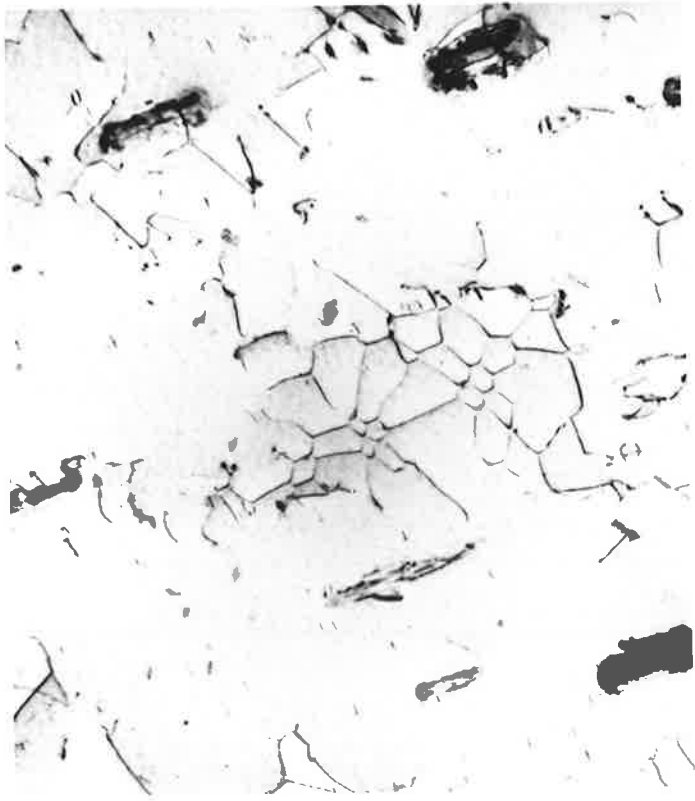
0.5 μ



FIG. 4.8 Dislocation loops present after strain of 0.03 at 500°C. Note pinching off of dislocation dipoles.

0.5 μ





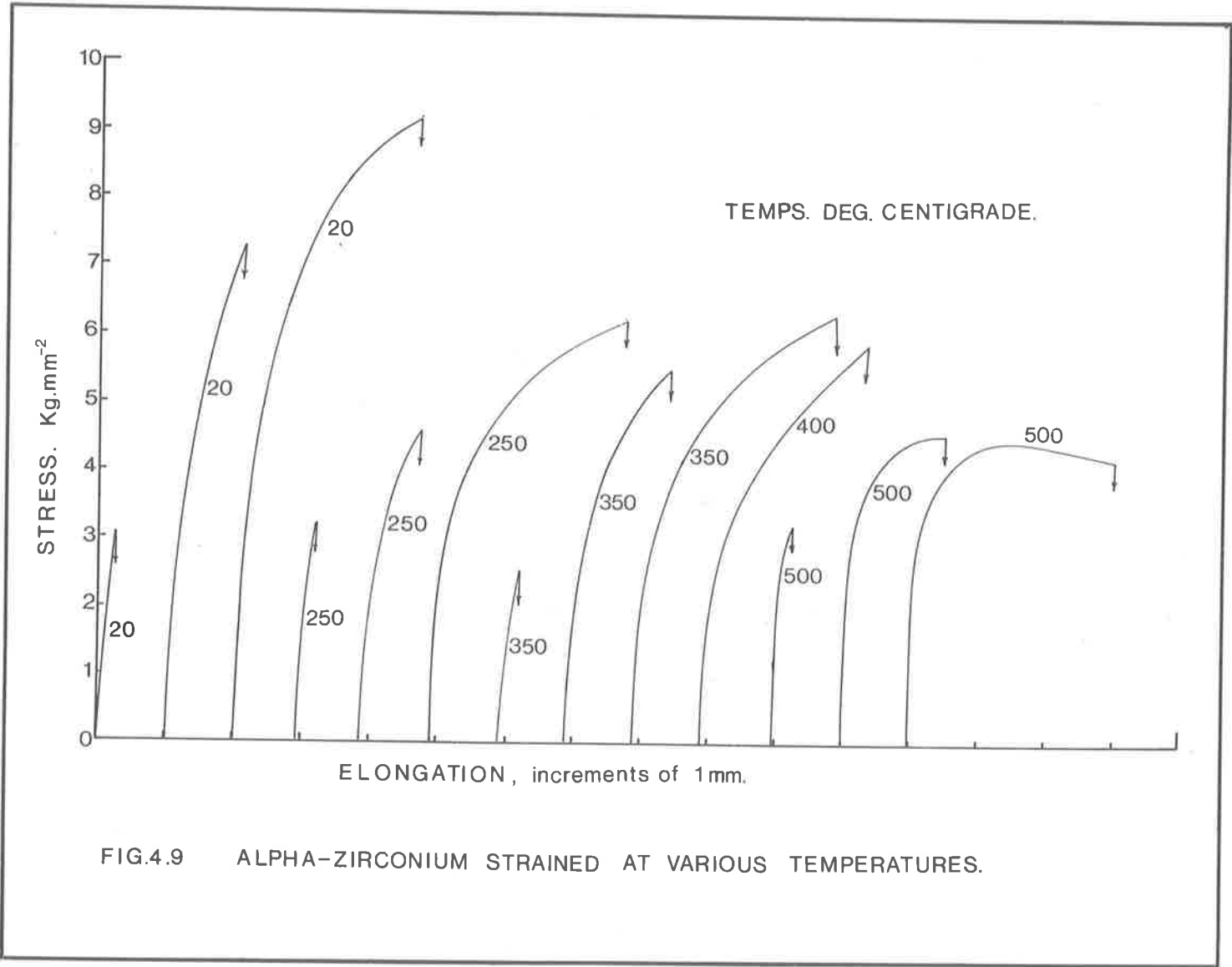
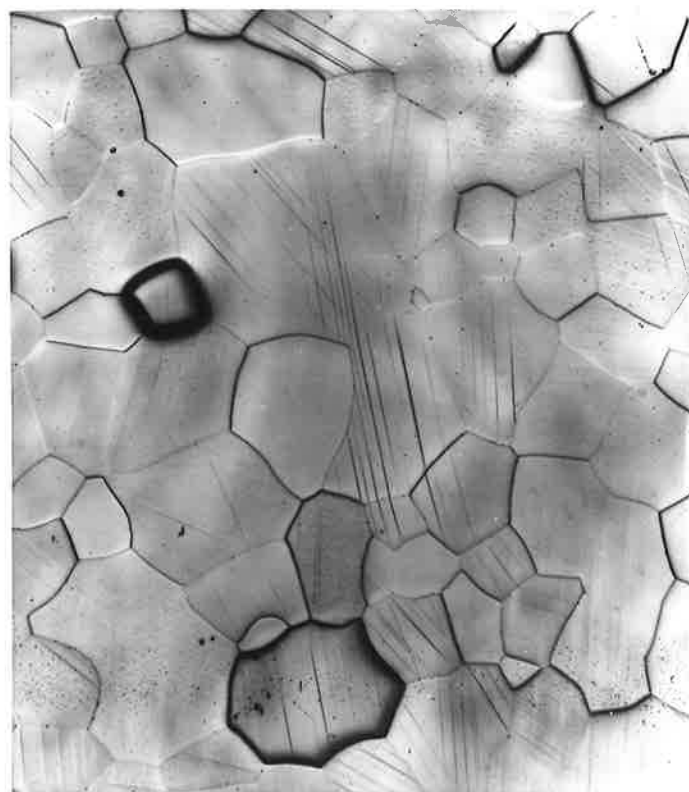


FIG. 4.10 Straight slip lines on specimen
surface. Strain 0.01 Room temp.
Mag.80X

FIG. 4.11 Dense slip lines strain 0.04 Room
Temp.
Mag.80X



at a strain of 0.04 most grains contained at least two groups of intersecting slip lines. Many of the slip lines were bent, probably due to the effects of slip on intersecting slip planes, fig. 4.11. Twins were observed only very occasionally and wavy slip lines were present in isolated cases which indicated that cross slip or cell migration* had occurred

Fig. 4.12 is an electron micrograph of a specimen strained approximately 0.001 at room temperature. There were very few dislocations present but a high density of surface hydride could be seen. This was often the case with thin foils prepared from annealed zirconium (section 2.2. and Appendix 2). The dislocation density was greater after straining to 0.015 and further increased after a strain of 0.04, fig. 4.13 at which strain, a few fairly open dislocation tangles sometimes formed.

As the strain was increased from 0.003 to 0.02 at 250°C the density of straight surface slip lines increased with a corresponding increase in the number of grains which contained slip traces in two directions, fig. 4.14. Wavy slip lines became prominent at a strain of 0.04 along with a much higher slip line density, fig. 4.15.

For low strains (up to 0.01) at 250°C the dislocation density was low, and dislocations were arranged in a

* see section 4.3.

FIG. 4.12 Very few dislocations present after
a strain of 0.001 at room temperature.

0.5 μ


FIG. 4.13 Uniform dislocation array after a
strain of 0.04 at room temperature.

0.5 μ

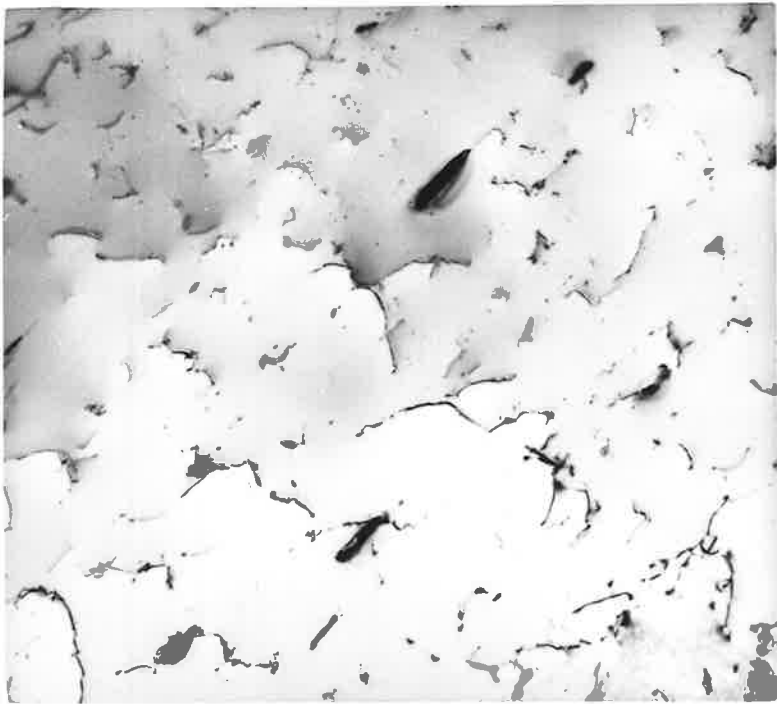
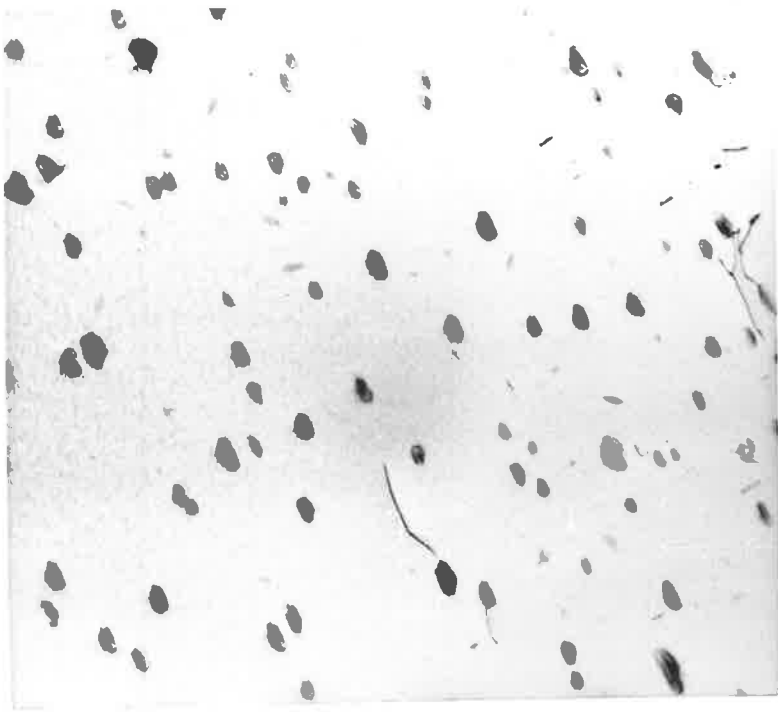
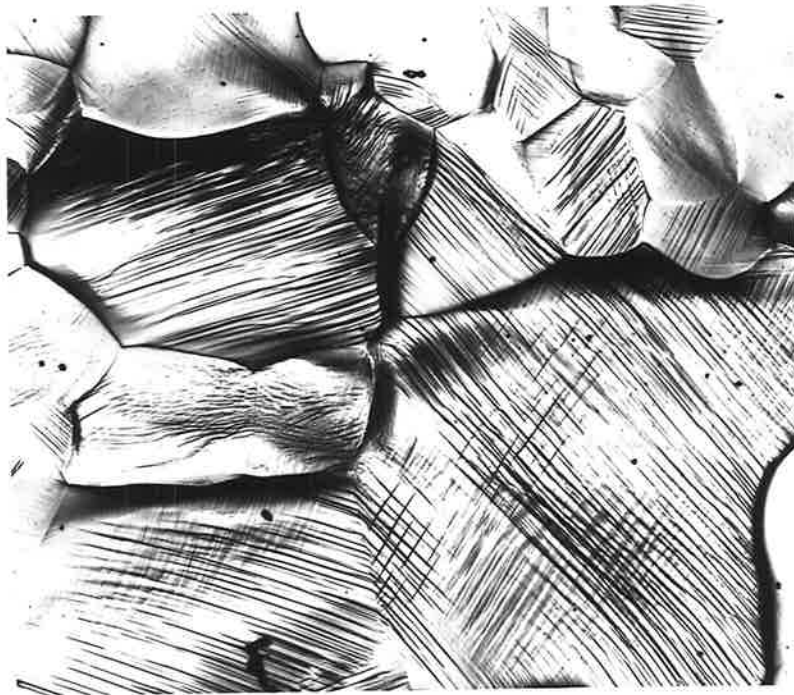
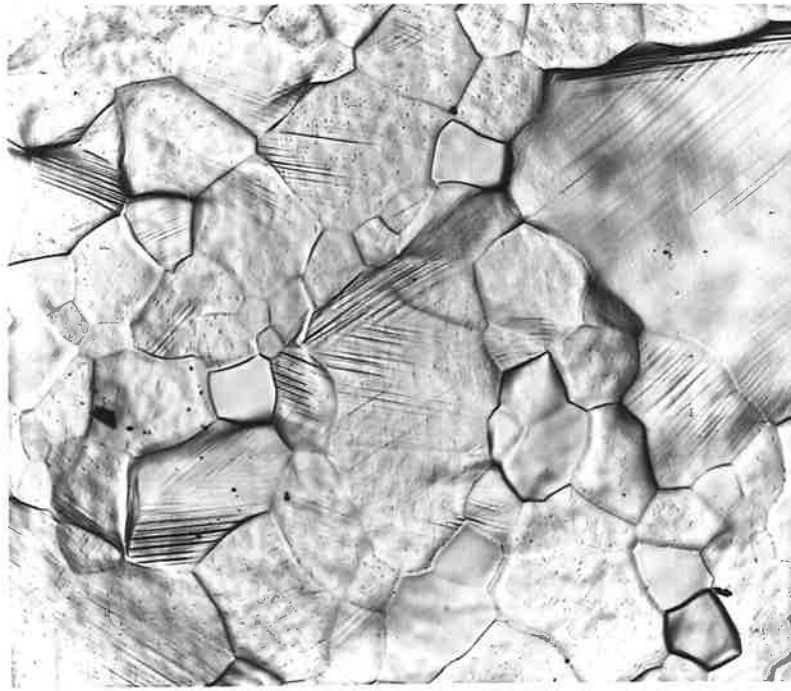



FIG. 4.14 Surface slip line structure after a
strain of 0.02 at 250°C.
Mag. 80X

Fig. 4.15 Wavy slip lines produced by strain-
ing at 250°C to a strain of 0.04
Mag. 80X



fairly random manner. At strains near 0.04 tangles containing loops and dipoles were formed, fig. 4.16, and near the grain boundaries, dislocation cells were usually apparent, fig. 4.17.

For specimens deformed at 350°C the surface structure showed much more prominent wavy slip lines which occurred at lower strains than in the previous specimens, fig. 4.18.

Electron microscopy revealed a similar trend to that which resulted from lower temperature tests. Dense tangles were formed after straining to approximately 0.02, fig. 4.19, and dislocation cells were present. Some of the tangled cell walls consisted mainly of edge dislocations (Burgers vector $[100]^*$) and an example is shown in fig. 4.20 which is a stereo-pair produced by tilting the foil across the 001 pole. The complexity of tangling which occurs in the cell walls can also be seen.

A surface examination of specimens strained at 500°C showed that most grains contained straight slip lines up to strains of about 0.03. Only a few wavy slip lines were observed at higher strains, and in most grains the slip lines appeared narrower than those in specimens given the same strains at lower temperatures. Kink bands were observed in some grains.

Electron microscopy revealed long dislocations with many associated dipoles and loops for strains up to 0.02,

* see end of section 4.3.

FIG. 4.16 Dislocation tangles containing loops
and dipoles. Strain 0.04 Temp 250°C.

0.5μ


FIG. 4.17 Dislocation cell structure best
formed nearer grain boundaries
strain 0.05 Temp. 250°C.

0.5μ

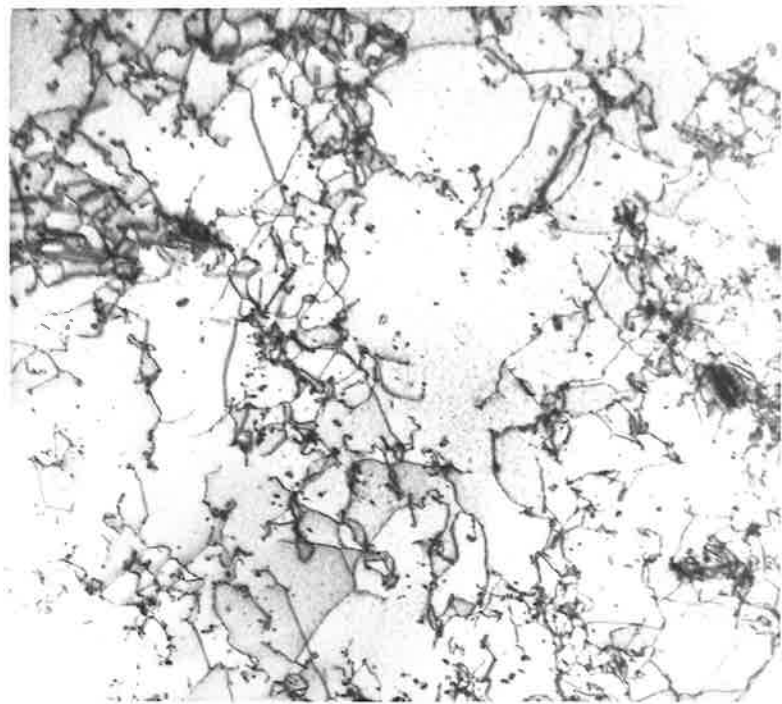
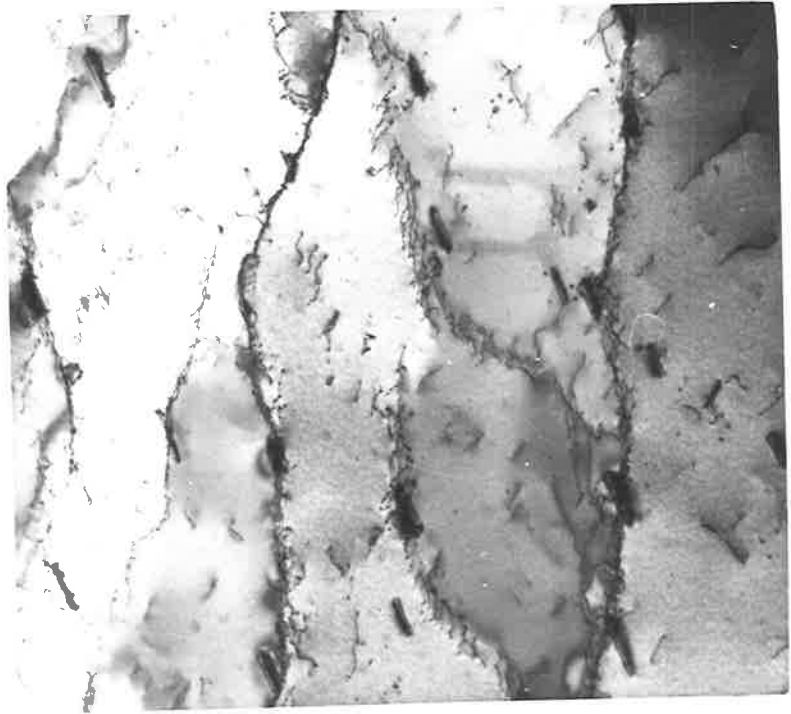



FIG. 4.18 Many wavy slip lines on specimen
strained at 350°C to 0.04 strain.
Mag. 80X

FIG. 4.19 Dislocation tangles formed at strain
of 0.02 at 350°C
0.5μ
└───┘

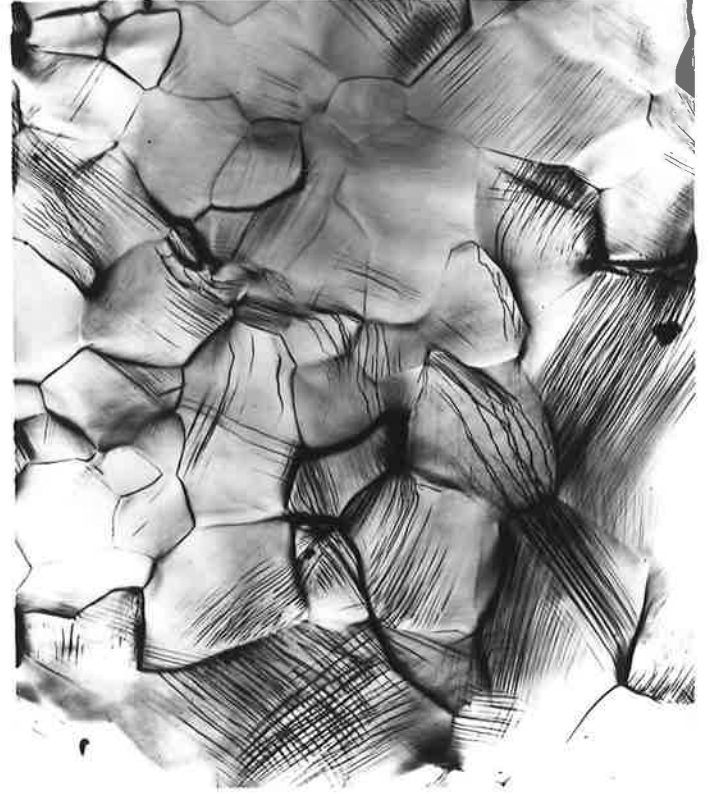
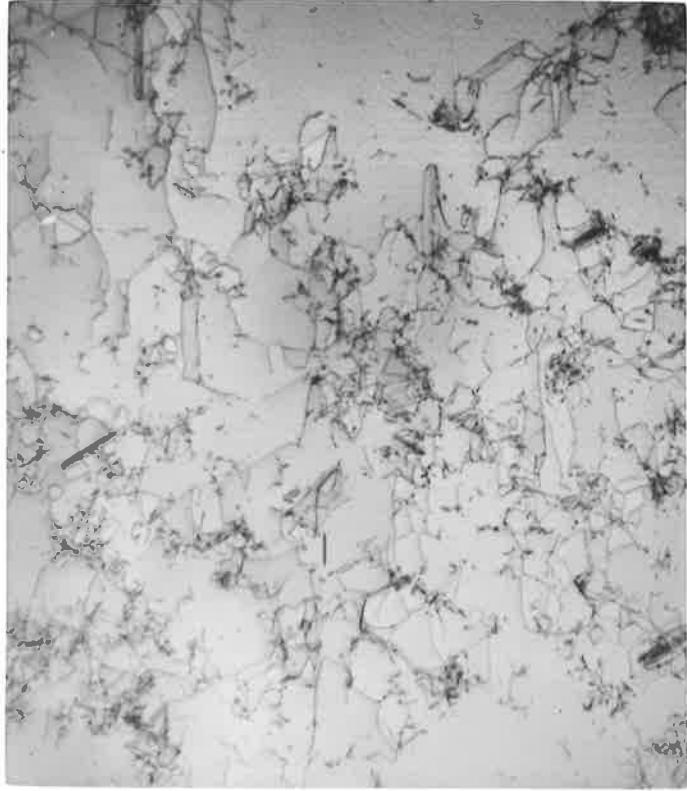
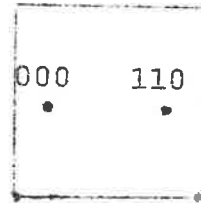


FIG. 4.20
(a) and (b)

Stereo-pair showing tangled nature
of dislocation cell walls. Tilt
axis parallel to $g(110)$, tilted
across $[001]$ pole.

0.5 μ



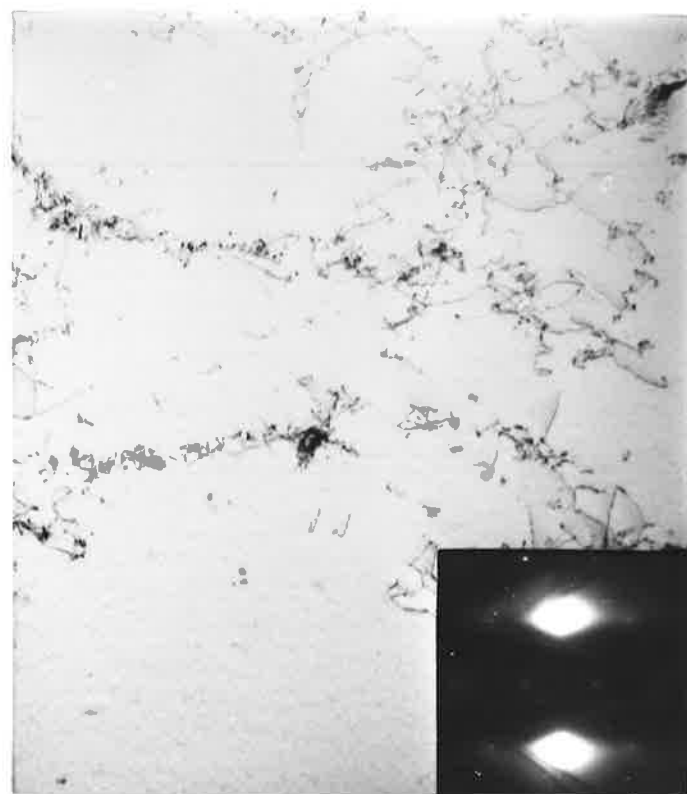
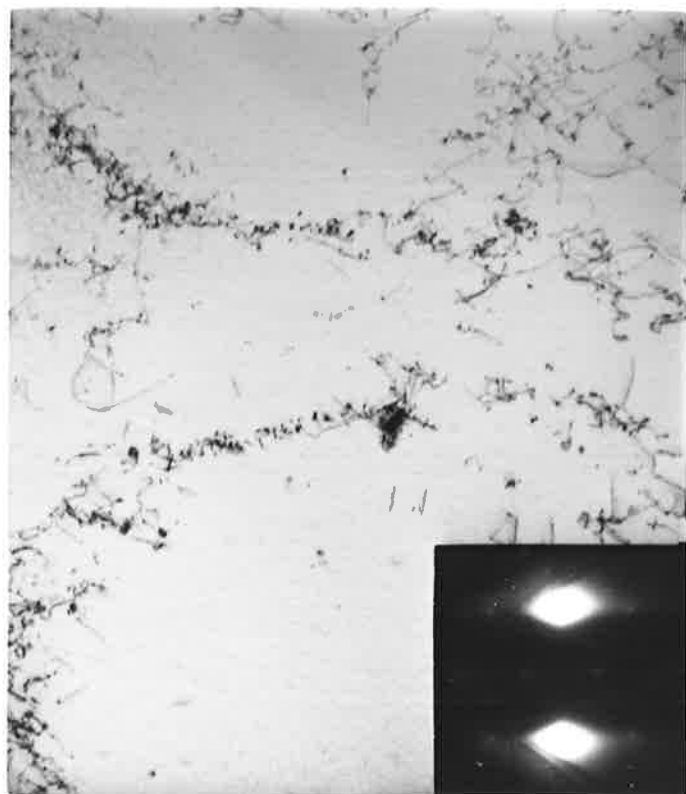


fig. 4.21. Higher strains (0.05) resulted in tangles which were often fairly open and uniform in nature, fig. 4.22, and which also contained many dislocation loops. In some areas a recovered subgrain structure was evident, and a few hexagonal dislocation networks were present.

A specimen strained at 600°C contained a dislocation structure indicative of the higher dynamic recovery rate at this temperature, fig. 4.23.

Analyses of Burgers vectors of dislocations were carried out in many of the specimens following the procedures outlined in Chapter 3. As an example, the analysis of some of the Burgers vectors of dislocations shown in fig. 4.24 has been included. Figs. 4.25 - 4.28 show the details obtained from the tilting experiment which is detailed in fig. 4.29 (a) and (b). In addition to this fig. 4.30 is a stereo-pair of the same area and from this an estimate of the elevation of the dislocation lines in the foil can be made. This information combined with extensive use of the stereographic projections (Chapter 3) leads to the following conclusions;

- (1) The long dislocations A and B (see fig. 4.24b) have the Burgers vector $[010]$ (or $[0\bar{1}0]$). These dislocations appear to lie on a $(\bar{1}00)$ plane and are either edge dislocations or mixed dislocations with a major edge component.

FIG. 4.21 Long dislocations with many associated dipoles and loops after a strain of 0.02 at 500°C.

0.5 μ
└───┘

FIG. 4.22 Open dislocation tangles containing many dislocation loops. Strain 0.05 Temperature 500°C.

0.5 μ
└───┘

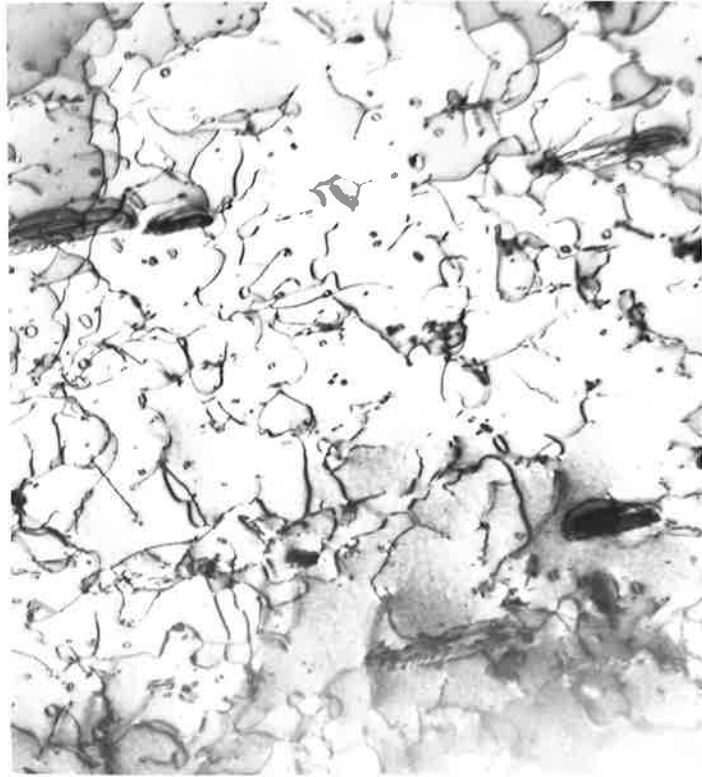
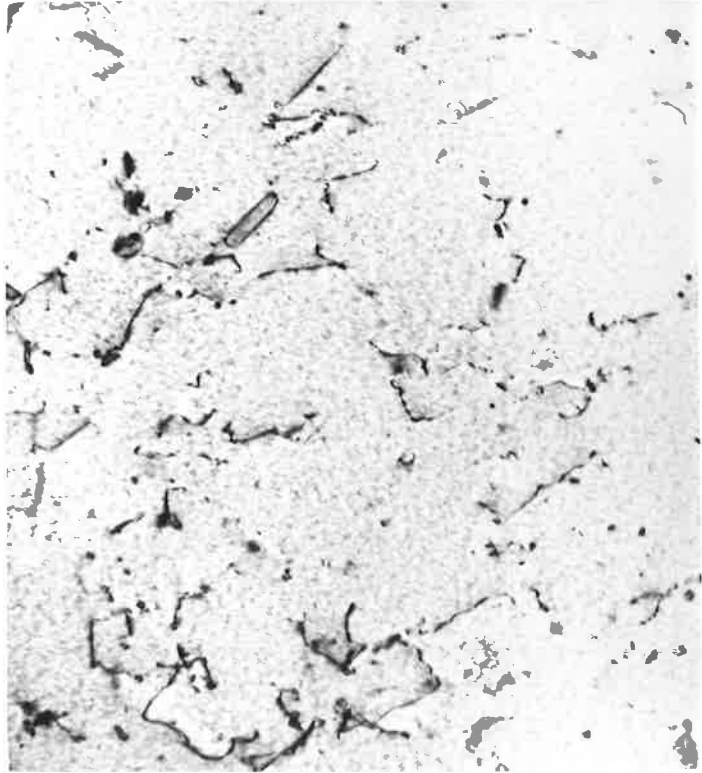


FIG. 4.23 Low angle grain boundaries formed on straining at 600°C. (strained ≈8% at 600°C).

0.5 μ





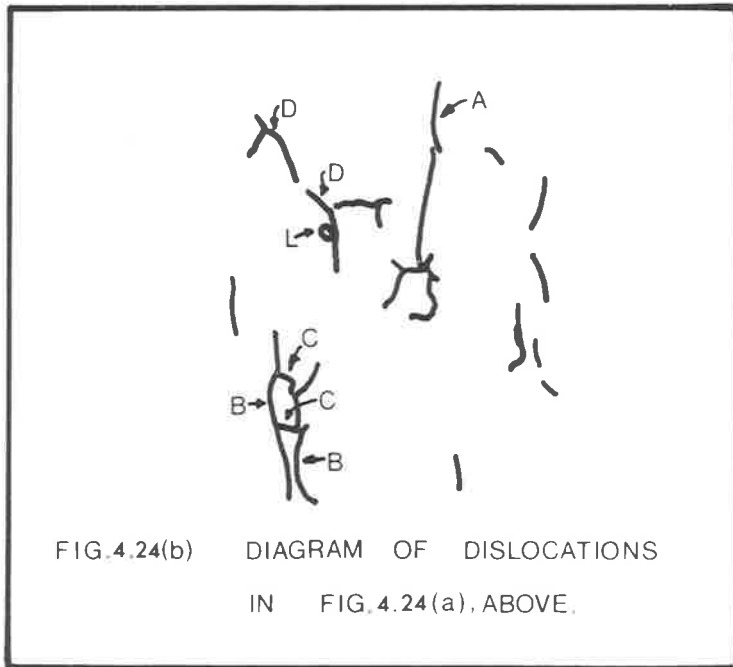
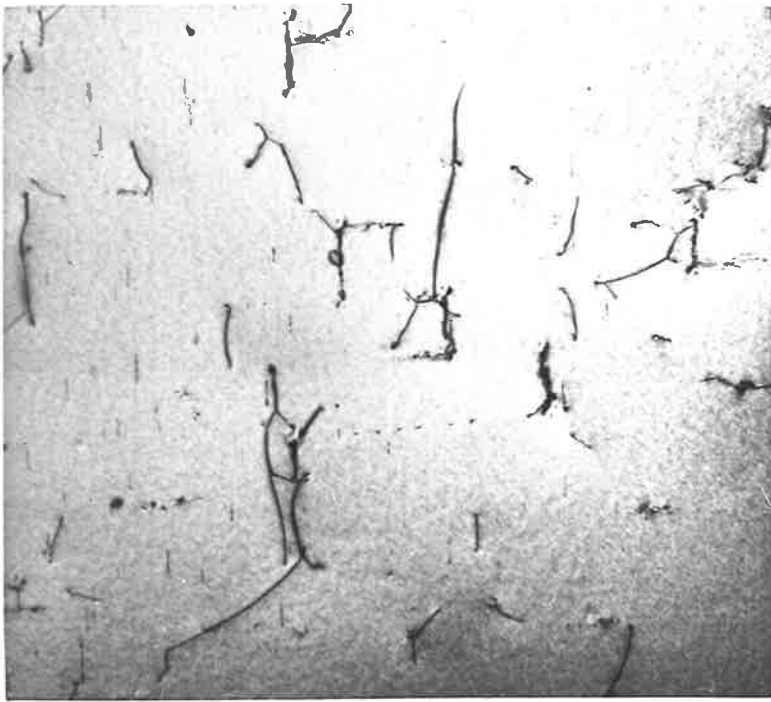


FIG. 4.24(b) DIAGRAM OF DISLOCATIONS
IN FIG. 4.24(a), ABOVE.

FIG. 4.25 Dislocations A, B and L are out of contrast for the two-beam conditions represented by $g(101)$.

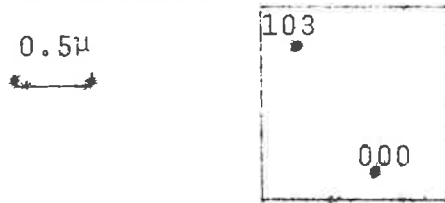
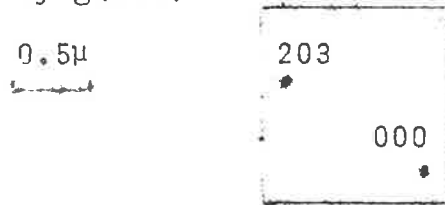


FIG. 4.26 Dislocations A, B, and L are out of contrast for the two-beam conditions represented by $g(103)$.



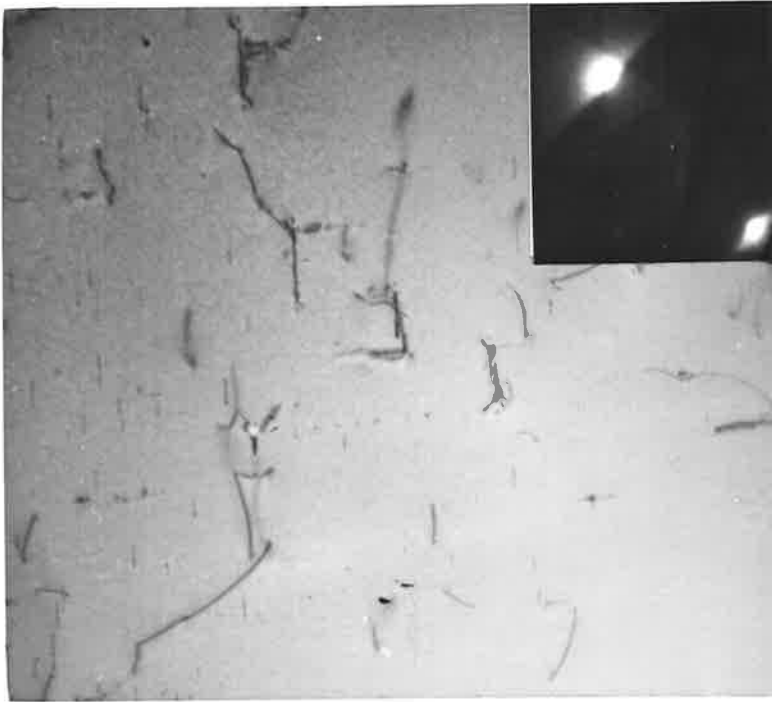
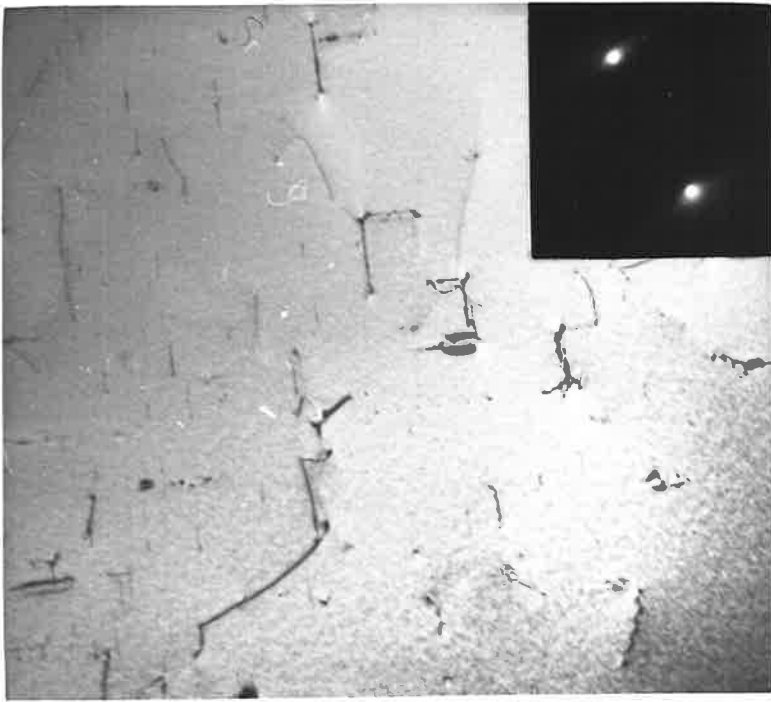


FIG. 4.27 Dislocations C and D out of contrast.

Two-beam conditions $g(0\bar{1}3)$

0.5 μ
←-----→

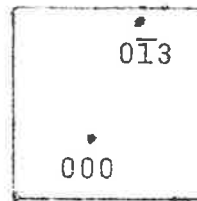
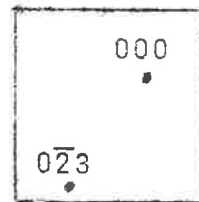


FIG. 4.28 Dislocations C and D out of contrast.

Two-beam conditions $g(0\bar{2}3)$

0.5 μ



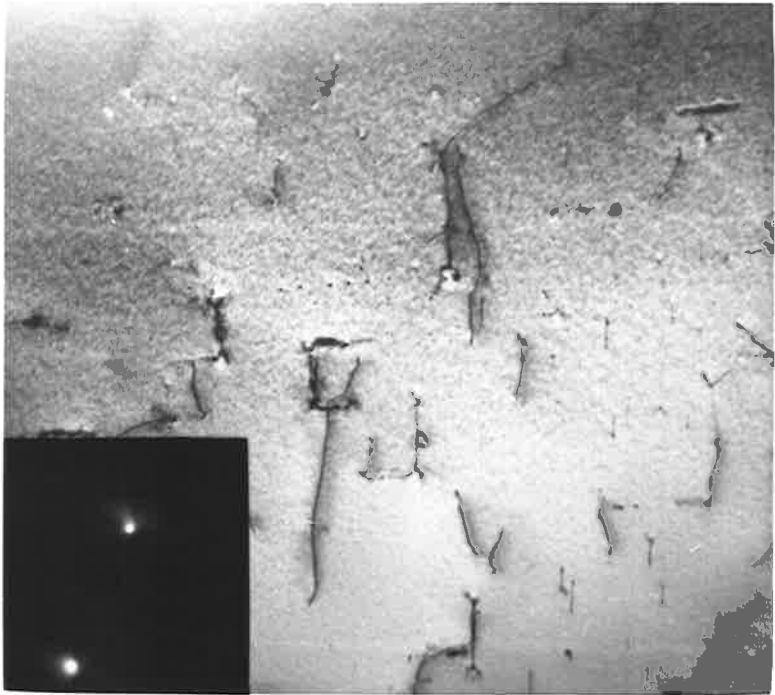
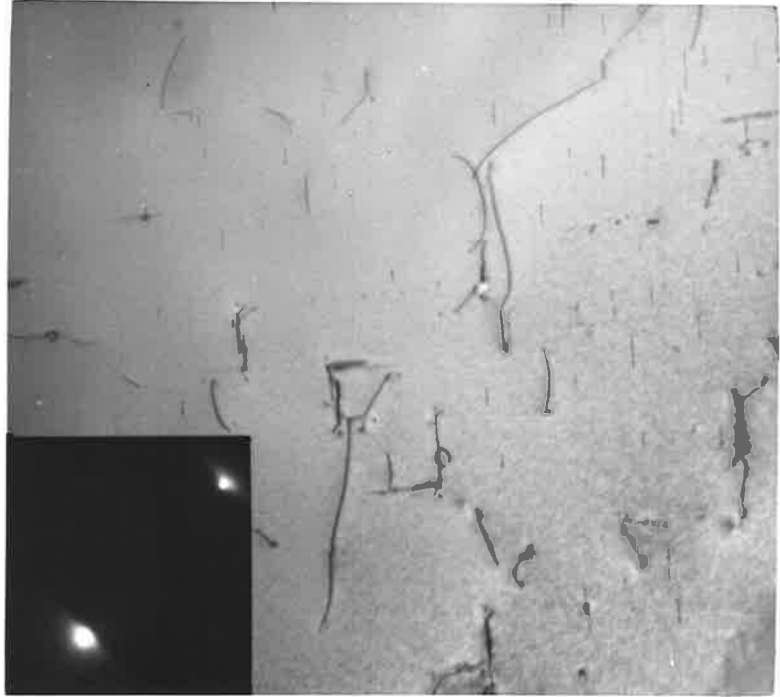


FIG.4.29(a) ANALYSED DIFFRACTION PATTERNS PLACED ON KIKUCHI MAP.

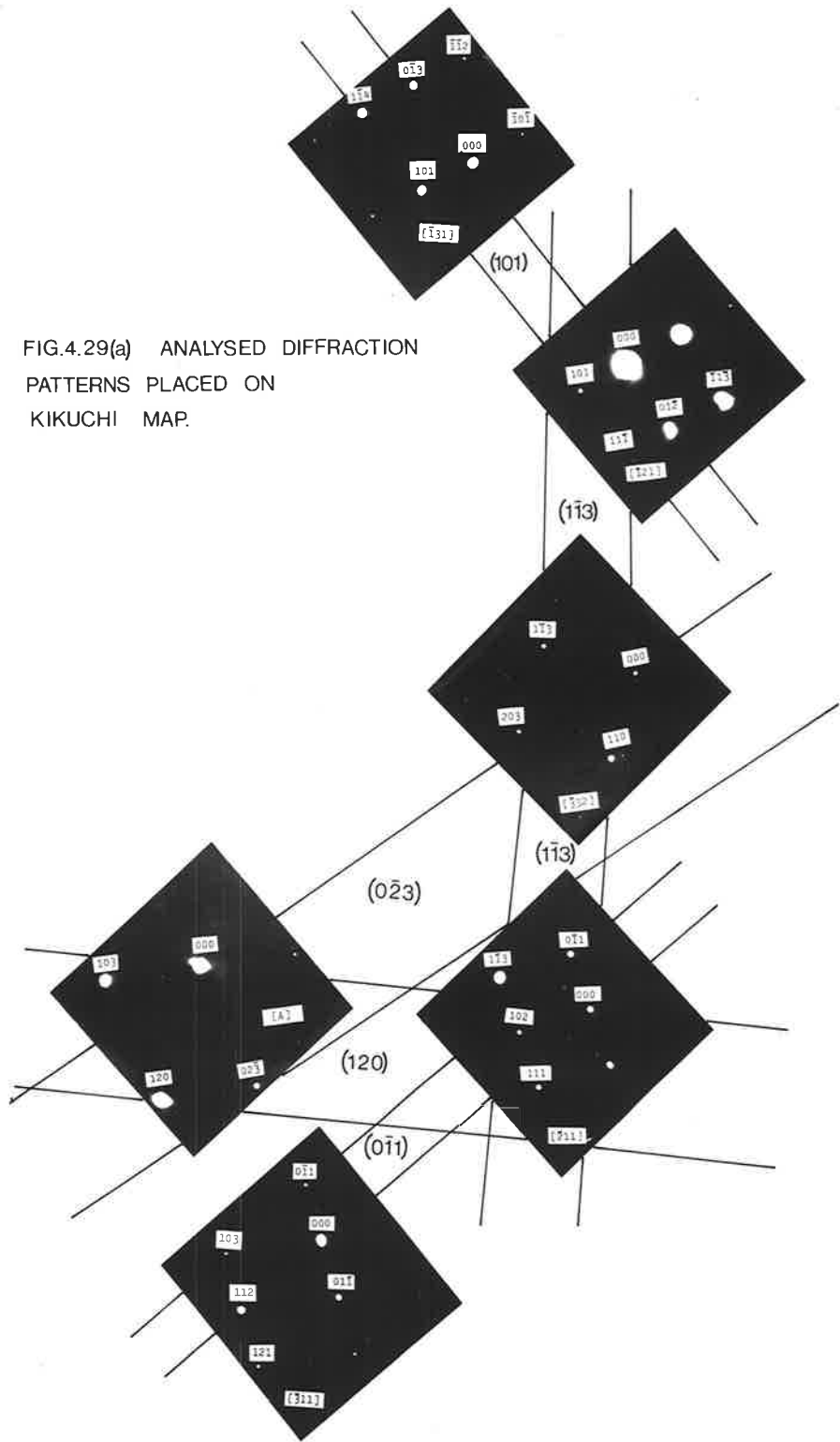
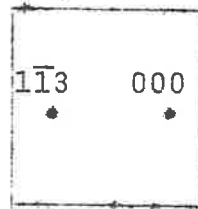
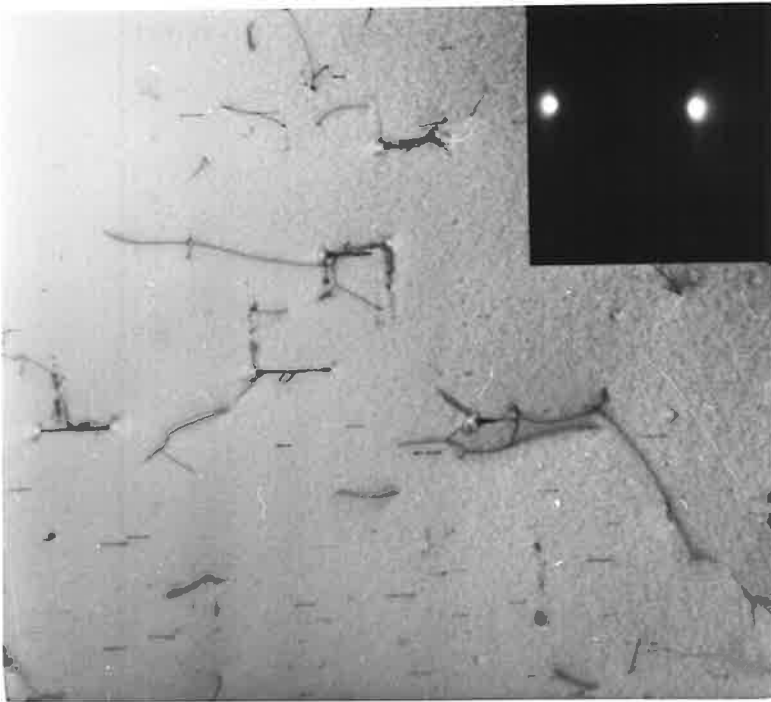


FIG. 4.30
(a) and (b)

Stereo-pair of the same area as
figs. 4.24 - 4.28. Tilt axis
parallel to $g(1\bar{1}3)$

0.5 μ
└───┘





- (2) Dislocations C and D have the Burgers vector $[\bar{1}00]$ (or $[100]$). They are probably screw dislocations lying on a (010) plane.
- (3) The dislocation loop, L, has the Burgers vector $[010]$ and is probably a prismatic loop; (edge dislocation loop).

From analyses of dislocations in many of the above mentioned specimens it was always found that Burgers vectors were of the type $[100]$, (i.e. $1/3[2\bar{1}\bar{1}0]$ or $1/3[11\bar{2}0]$).

In a very few extreme cases dislocations which had the same Burgers vector could be shown to have slipped on (001) planes. This, however, only occurred when the dislocations had been punched out by a hydride precipitate, (see fig. A5, Appendix 1), which suggested that a very high stress was necessary for this process (Bailey (1962)).

An isolated observation was made which indicated that slip had occurred on (110) planes (i.e. $(11\bar{2}0)$) but this was seen in a thin foil which had been very heavily deformed and was not typical of the normally observed behaviour.

In summary, the observations indicated that the majority of slip had occurred on $\{100\}$ planes and that only under extreme conditions was slip on other planes possible. The Burgers vector was always found to be of the type $\langle 100 \rangle$ (i.e. $1/3 \langle 11\bar{2}0 \rangle$).

4.4 DISCUSSION OF DISLOCATION BEHAVIOUR IN DEFORMED ZIRCONIUM

A general summary of the electron microscope results, given in sections 4.2 and 4.3, for thin foils prepared from zirconium specimens deformed in tension can be made. The grain size of the specimens was of the order of the specimen thickness and so the stress-strain curves can only be used to make relative comparisons between the present results.

The most notable features of the dislocation substructure were ;

(1) The qualitative increase in dislocation density with increasing strain at a constant temperature.

(2) The formation of dislocation tangles as the strain was increased; a decrease in temperature caused an increase in the amount of strain necessary to cause tangle formation.

(3) The formation of a dislocation cell structure. The cell walls were made up of a very tangled array of dislocations and the interiors of these cells contained different densities of free dislocations depending on the temperature at which the specimen was deformed.

(4) At temperatures greater than 400°C the dislocation array became more uniform. These specimens contained longer lengths of jog-free dislocations than did the specimens in which dense tangles were formed, and in addition to this,

many more dislocation loops were present in the specimens deformed above 400°C.

(5) Dislocation reactions occurred at temperatures above 400°C with well formed hexagonal dislocation networks appearing in specimens deformed at temperatures greater than 500°C.

(6) The optical surface studies revealed the behaviour of slip lines (or bands) under the particular test conditions. At low strains, less than 0.02, at all temperatures only straight slip lines were present. Duplex slip occurred in many of the grains as the strain approached 0.02. Above this strain, at temperatures between 200 and 350°C, wavy slip lines were formed. At temperatures near 400-500°C wavy slip lines were only occasionally observed and instead straight, densely packed fine slip lines were present (fig. 4.31). Above 500°C wavy slip lines were again formed, (fig. 4.32).

4.4.1 Dislocation Tangles and Cells.

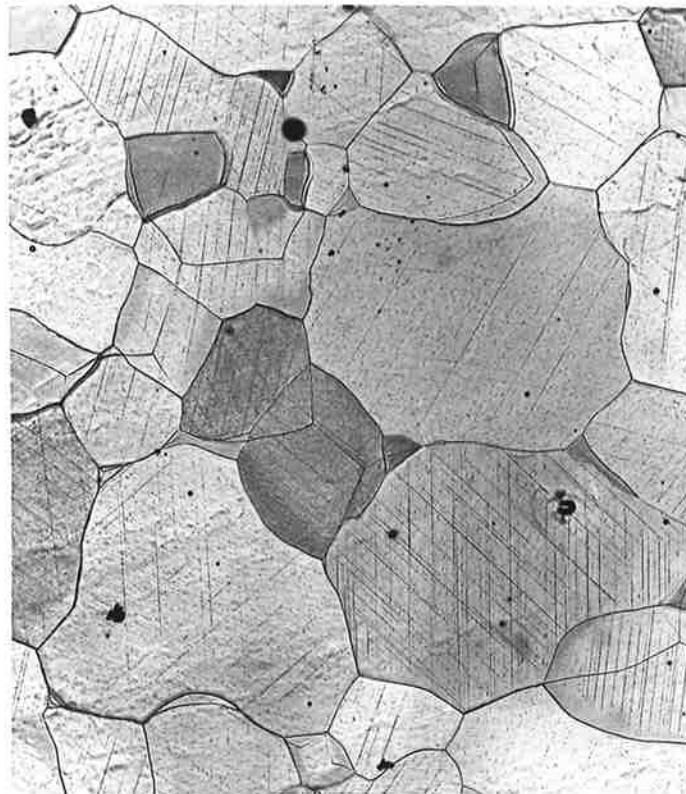
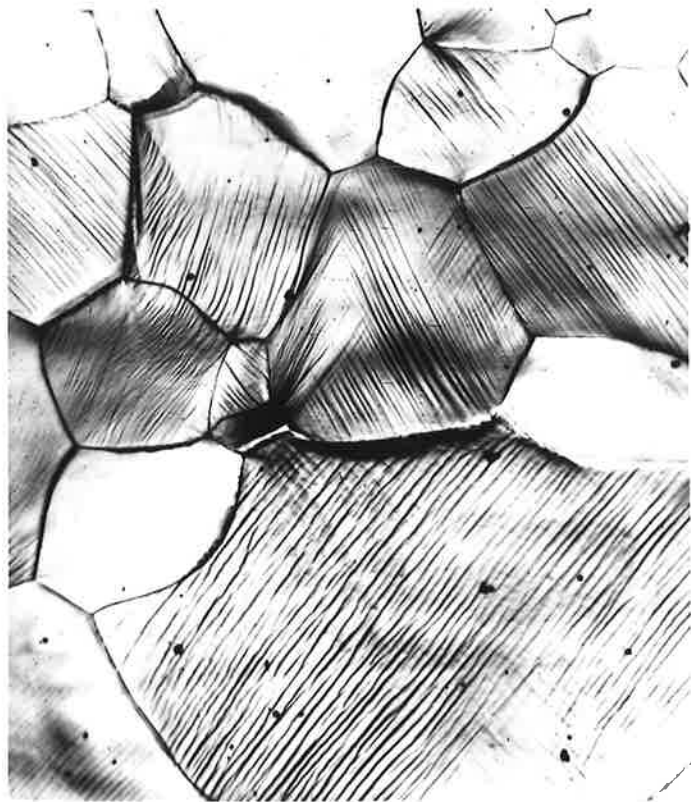
The formation of dislocation tangles, which can lead to the production of a dislocation cell structure, is an important aspect of the deformation of zirconium in the range 0 - 600°C. The above results indicate that dislocation cells may form at all temperatures in the range 0 - 350°C but that

FIG. 4.31 An example of the straight slip lines present after deforming at 400°C. Strain 0.02. High strains increase the density of the slip lines but do not cause wavy slip lines.

mag. 80X

FIG. 4.32 Wavy slip lines present after straining at 600°C Strain 0.05.

mag. 80X



the degree of perfection depends on the amount of strain and on the temperature of deformation. A brief summary of the theories of dislocation tangle and cell formation follows to allow an adequate discussion of the probable processes which occur in zirconium.

The early intuitive theory (McLean, 1962; Swann, 1963) proposed that random distributions of dislocations allowed small clusters of dislocations to collect. Since these clusters were difficult to penetrate they trapped other dislocations and extended forming tangles and eventually cells. This theory gave no indication of the mechanisms involved in the tangle formation but a second theory (McLean, 1962) considered that cross slip was essential to the formation of a cell structure. This, however, also had shortcomings as it required dislocations to cross slip and to move on planes in which there was a high dislocation density, (Bailey and Hirsch, 1960).

Seeger (1956) identified cell walls with tilt boundaries formed by a process involving pile-ups of screw dislocations against a barrier. This theory could not account for all the experimental observations, in particular the large twist component of cell boundaries. However, by allowing that screw dislocations could later add onto tilt boundaries to give the twist component, this problem was to some extent overcome,

(Keh and Weismann, 1963).

A theory proposed by Kuhlman-Wilsdorf et al. (1962) emphasized the interaction between point defect concentrations and dislocations. Screw dislocations in the primary slip plane interacted with voids, vacancies and vacancy aggregates to form superjogs or prismatic loops. These heavily jogged dislocations would be difficult to move, but they could act as dislocation sources on the primary and other slip planes. The process could thus "mushroom" and cause tangle formation which would eventually lead to cell formation.

Kuhlman-Wilsdorf and Wilsdorf (1963) subsequently proposed a modified theory based on the following experimental observations;

(1) Dislocation tangles consisted of irregularly curved lengths of dislocation lines building up in three dimensions.

(2) It appeared that the majority of dislocation kinks in each tangle belonged to the operating primary slip systems and there was always prismatic dislocation loops associated with the tangles.

The basic properties of tangles which had to be explained by the mechanism also included ;

(1) Although dislocations in the tangles were pinned at certain points and were subjected to complicated

stresses by the tangle itself, they were also subject to a considerable frictional force. This meant that the tangles must be caused by an effect which made dislocations move out of their slip planes and at the same time provided a resistance against further glide.

(2) The cause of dislocation tangling had to account for the fact that tangles were not observed in deformed thin foils and so free surfaces reduced the likelihood of tangling.

(3) Obstacles such as precipitates and grain boundaries which were present before deformation did not appear to cause the tangles. Thus some other obstacle on a fine scale must have been present.

(4) Tangling took place during single slip as well as during multiple slip.

The mechanisms which were thought to be able to cause tangling were ;

(1) The formation of jogs and superjogs by processes involving dislocation interactions.

(2) Cross slip.

(3) Interactions between point defects and dislocations.

It was assumed that only one mechanism would account for tangling and neither cross slip nor intersection jogs operating

alone could be the cause. This left the interaction between point defects and dislocations as the cause of tangling. Since point defects were generated during slip, and vacancies and interstitials were always considered to be present in pure metals, the mechanism appeared to be possible. By considering the diffusion of point defects to dislocation cores, which had in themselves an uncertainty associated with atom vibration, and by visualizing dislocation climb in the most general sense, it was postulated that a dislocation tangling process could easily occur.

Kuhlman-Wilsdorf and Wilsdorf summarized their theory by saying that dislocation tangles were due to the co-operative motion of many processes, previously called mushrooming, which were primarily due to slip induced point defect precipitation.

From the above theories it would appear that the process of tangle formation is an extremely complicated one. The theories usually postulate that one mechanism would be responsible for the formation of dislocation tangles. However, it appears much more attractive to assume that more than one process operates. It could, in fact, involve dislocation interactions with point defects, cross slip and intersection of dislocations with kinks. Dislocation loops and dipoles are observed in the tangles and cross slip and jog formation almost

certainly occur to form these. However, dipoles and loops may either be a prerequisite to tangle formation or they may form as a consequence of tangle formation.

There has been some disagreement on the relation between dislocation cells and surface slip bands. Kuhlman-Wilsdorf and Wilsdorf (1963) concluded that the movement of cell walls was responsible for the appearance of slip bands but it was difficult to decide whether cell walls moved as a unit or whether a redistribution of cell walls occurred. Keh and Weissmann (1963) also pointed out that dislocation cell walls could move co-operatively and that although there was no direct evidence for this, there was considerable indirect evidence. It was concluded that cell walls migrated to the surface to form the wavy slip bands.

All this assumes that subgrain boundaries or cell walls can easily migrate under the influence of stress and temperature. In a discussion of sub-boundary migration, Warrington (1970) showed that a large proportion of the strain during creep experiments could be accounted for by sub-boundary migration. This then supports the theories that cell wall migration could be the cause of wavy slip bands.

There does not appear to be any conclusive experimental evidence to show that wavy slip bands are produced by cross slip mechanisms or whether, on the other hand, that

they are formed as a consequence of sub-grain boundary migration. However, recently wavy slip lines have been associated with the dislocation cell structure in deformed iron and steel (Boyd et al., 1969) and it was shown that slip band spacing behaviour corresponded closely with the behaviour of the cell structure at varying strains and temperatures. This therefore also adds support to the cell wall migration mechanism as the cause of wavy slip lines.

The present results at room temperature showed that no dislocation cell structure formed until strains of greater than 4% were imposed. The dislocation structure consisted mainly of a fairly uniform array and even when cells were formed there were plenty of free dislocations randomly dispersed in the cell interiors. Work-hardening occurred at a greater rate at room temperature than at higher temperatures (fig. 4.9) and, in general, the yield stress decreased as the temperature increased. The stress field of a random dislocation array and a higher lattice friction stress at room temperature would account for the above observations. At higher temperatures, 250-350°C, a dislocation cell structure formed and the long range stress field associated with these dislocations would contribute to the work hardening at these temperatures, (Li, 1963). The work hardening rate is, however, lower at these temperatures than at room temperature and this could be

accounted for by the greater relative thermal activation at the higher temperatures.

The dislocation cell structure which occurs in deformed zirconium has a variable nature as indicated by the results in sections 4.2 and 4.3. A random dislocation array is present after strains of up to 0.05 at room temperature and even when a cell structure forms there remains a relatively high density of dislocations within the cells. At 200°C to 350°C relatively well formed dislocation cells occur at strains as low as 0.02 and lower strain rates favour cell formation at lower temperatures. The cell walls consist of heavily tangled dislocation arrays. There is no direct evidence obtainable as to the mechanism of the tangle formation but in the light of the observed occurrence of numerous jogs, dipoles and dislocations which are pinned by invisible defects, it must be assumed that a combination of the processes which have been predicted takes place.

In the present work it was found that the dislocation cell structure formed first near a grain boundary. Grain boundaries are often thought to act as dislocation sources, dislocation sinks or barriers to dislocation motion. It would appear from the present results that dislocations, which are generated either from opposite grain boundaries, point defects or precipitates, or by a multiplication process as

they glide across the grain, begin to pile up at the grain boundary. As more and more tangles are formed the dislocation cell structure would build away from the grain boundary and into the grain itself. Conversely, dislocation tangles may form at many sites in the grain and these tangles may then migrate under the influence of stress and temperature. Such tangles would be more readily held up at grain boundaries than would single dislocations and thus a cell structure could form.

The fact that dipoles and dislocation loops are present in the cell walls suggests that they may be either a cause of dislocation tangling or a consequence of the tangling (Swann 1963). Fig. 4.33 shows tangles containing dipoles which were formed in a specimen strained at 280°C. At higher temperatures, e.g. 400°C, dislocation tangling and cell formation is not prevalent. However, there is a much higher density of dislocation loops present. One method of forming dislocation loops is the pinching off of dipoles by either a cross slip process or a climb process (Price, 1963) and this type of behaviour is suggested in fig. 4.8. This process is expected to occur more readily at higher temperatures and indeed climb is a suggested process for high temperature creep.

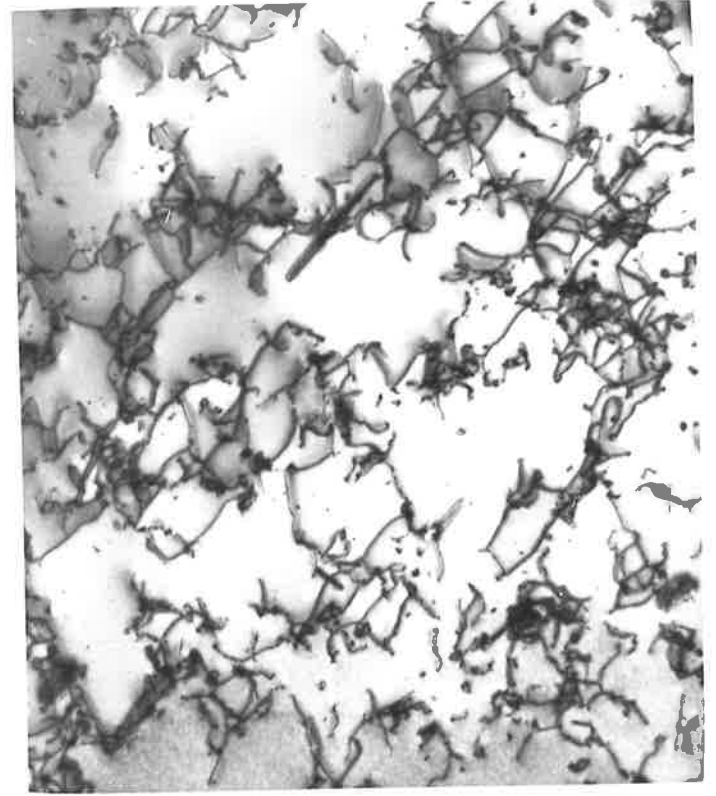
A dislocation cell structure is produced during

FIG. 4.33 Dislocation tangles containing
dipoles. Strain 0.07 Temperature
280°C.

0.5 μ

FIG. 4.34 Dislocation cell structure formed
on straining at 280°C.

0.5 μ



straining at 280°C (fig. 4.34) where few loops are formed whereas at 400°C, where many loops are formed (fig. 4.6) the cell structure is seldom observed. It can therefore be suggested that dislocation dipoles are one of the prerequisites of cell formation, since, when they are easily removed (pinched off) to produce loops, no cells are formed. Some of the theories outlined previously suggested that dislocation dipoles hindered glide and could result in tangling of the dislocations.

4.4.2. Relation between slip lines and Dislocation Structure.

As discussed in section 4.4.1., wavy slip lines have either been attributed to the occurrence of cross slip or to the migration of cell walls. Migration of cell walls could, however, be assumed to indirectly include cross slip since, because of the tangled nature of dislocations in these walls, migration would undoubtedly include slip on planes other than the primary slip planes.

In the present results a relation between a cell structure and slip lines can be seen. For room temperature tests, up to a strain of 0.05, only straight slip lines were observed. The dislocation structure was random. Surface examinations after straining at 250 and 350°C showed many wavy slip lines and a cell structure was apparent at these temperatures. Thus it could be concluded that a relationship between

wavy slip lines and dislocation cells existed. On the other hand it could also be conceded that cross slip had occurred to produce the wavy slip lines and also the cell structure. However, straining at a temperature of 400°C , where there would appear to be no reason for the inhibition of cross slip, wavy slip lines were, on the whole, not observed, (fig. 4.32), (c.f. figs. 4.15, 4.18, at 250 and 350°C). Now the dislocation structure after straining at 400°C is found to consist of a relatively uniform array of dislocations with no apparent cell structure (see fig. 4.6). This, therefore, points to the fact that wavy slip lines do, in fact, result from the co-operative motion of dislocation cell walls to the surface. Furthermore, at 500°C and 600°C , where the substructure is again cell like, (i.e. it consists of low angle grain boundaries forming a sub-grain structure, fig. 4.23) wavy slip lines are again observed after straining (fig. 4.32).

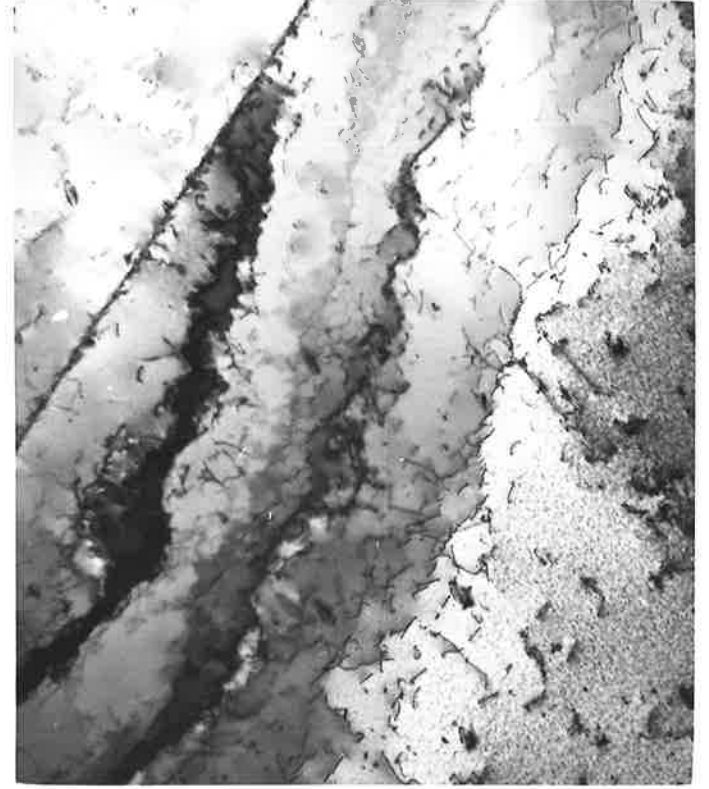
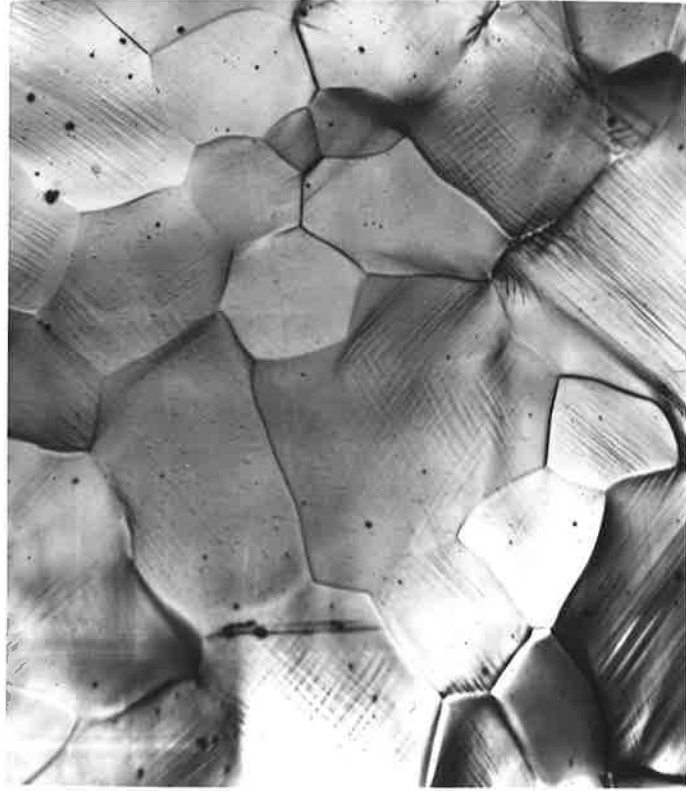
The above is also augmented by the fact that in a few areas of a specimen deformed at 400°C , dislocation cells were observed near grain boundaries (fig. 4.35). A surface examination also revealed that for the few times that wavy slip was observed on these specimens, it always occurred near the grain boundaries (fig. 4.36). Indeed, wavy slip was also most prevalent near the grain boundaries for specimens deformed at 250° and 350°C . (figs. 4.15, 4.18).

FIG. 4.35 Dislocation cell structure formed near grain boundaries in specimens deformed at 400°C.

0.5μ
└───┘

FIG. 4.36 Wavy slip lines formed only near the grain boundaries in specimens deformed at 400°C.

mag. 80X



4.5 RECOVERY OF DEFORMED ZIRCONIUM

As indicated in sections 4.2 and 4.3, deformation of pure zirconium in the range 500-600°C resulted in the formation of hexagonal dislocation networks. Similar networks were observed by Bailey (1963) and he assumed that they lay on the basal planes. To produce these networks, cross slip from prism planes onto basal planes was assumed to be the operative mechanism. In addition to networks, the general recovered structure of zirconium consisted of well formed low angle grain boundaries and these boundaries were either of pure tilt character or consisted of a network formation.

The kinetics of the recovery processes which occur in zirconium have been briefly studied, (Douglass (1963), Desalvo and Zignani (1966)). Recovery at low temperatures, 100 - 400°C, was attributed to migration of point defects and small dislocation rearrangements. The hardness decreased appreciably in the range 400 - 500°C and the controlling processes were said to be the formation of subgrains and annihilation of dislocations by climb. Recrystallization began at temperatures near 550°C and the rate of recrystallization increased as the temperature was increased up to 860°C (α - β transformation temperature), (Bokros, 1960). Grain growth also becomes important at temperatures above 550°C (Tresco, 1956).

Experiments were carried out so that the dislocation structure after recovery of cold worked zirconium could be observed. All specimens were strained at room temperature at a strain rate of about 10^{-5} sec^{-1} . The trend in the dislocation structures which were produced in specimens elongated 3.5, 5, 7.5, 8 and 13% was from a relatively random array of free dislocations for the low strains (fig. 4.37) to a relatively well formed dislocation cell structure for the higher strains (fig. 4.38). However, in some instances in the specimens deformed 8 and 13% there was a large number of free dislocations within the cells or towards the centres of large grains, fig. 4.39.

Parts of these specimens were recovered for $3\frac{1}{2}$ hours at 400°C . Only slight rearrangement occurred after this recovery treatment in a specimen originally strained 3.5% at room temperature but for the specimens originally deformed 5%, a recovered structure of the type shown by fig. 4.40 was produced. It can be seen that low angle grain boundaries and dislocation networks have started to form. Recovery of specimens deformed by greater amounts resulted in an increasing tendency to form low angle grain boundaries and dislocation networks.

Higher temperature recovery was carried out at 600°C for 2 hours on both the specimens which had been

FIG. 4.37 Random dislocation array for a strain of approximately 0.035 at room temperature.

0.5 μ


FIG. 4.38 Dislocation cell structure formed after a strain of 0.08 at room temperature.

0.5 μ

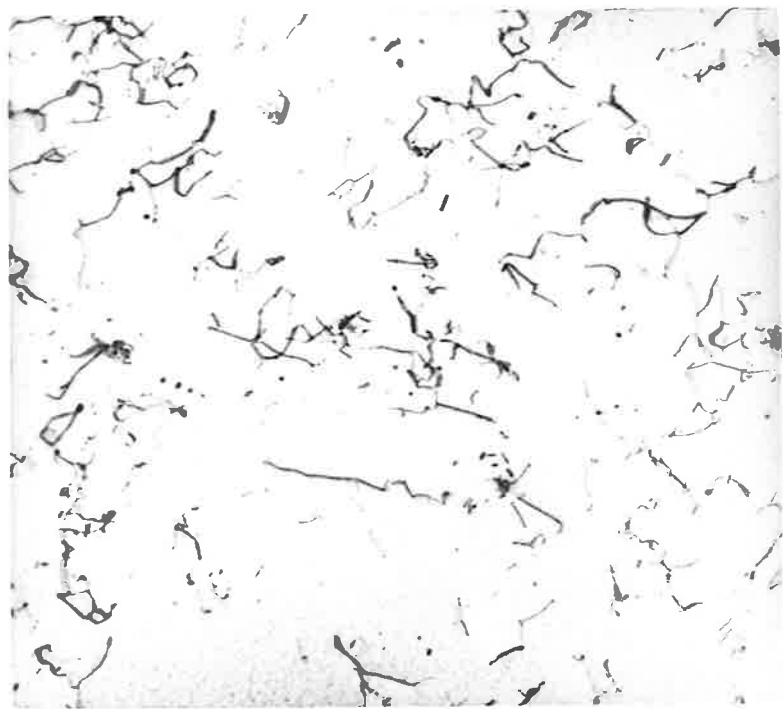
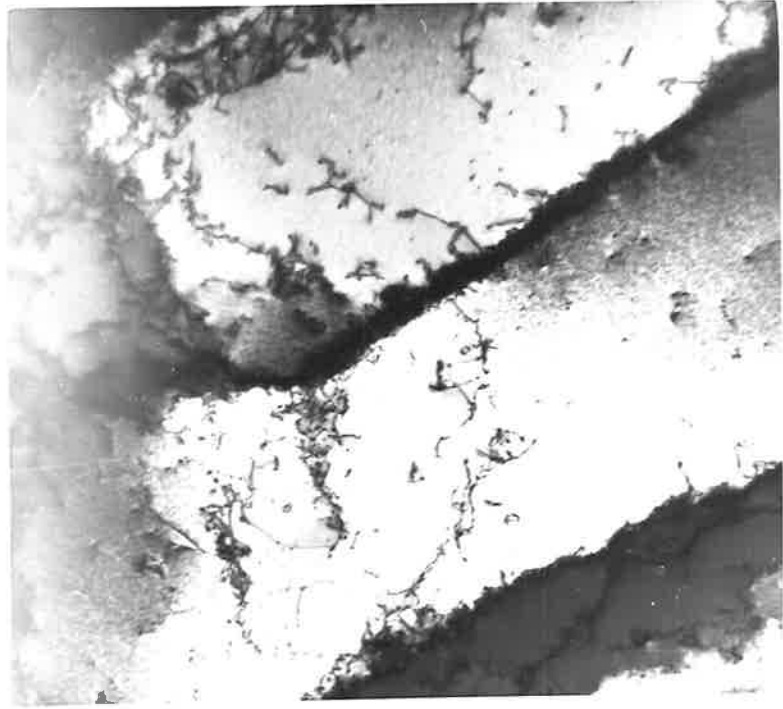
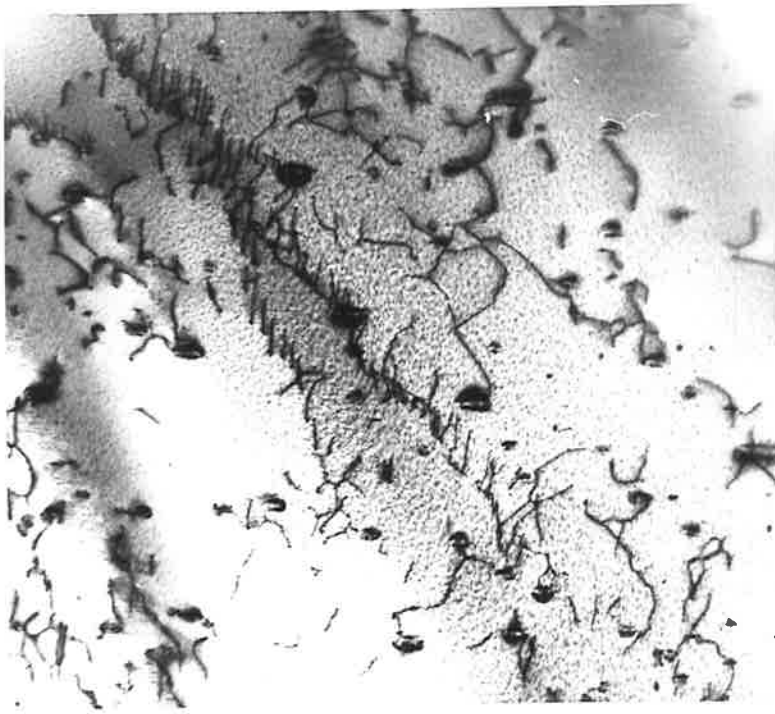
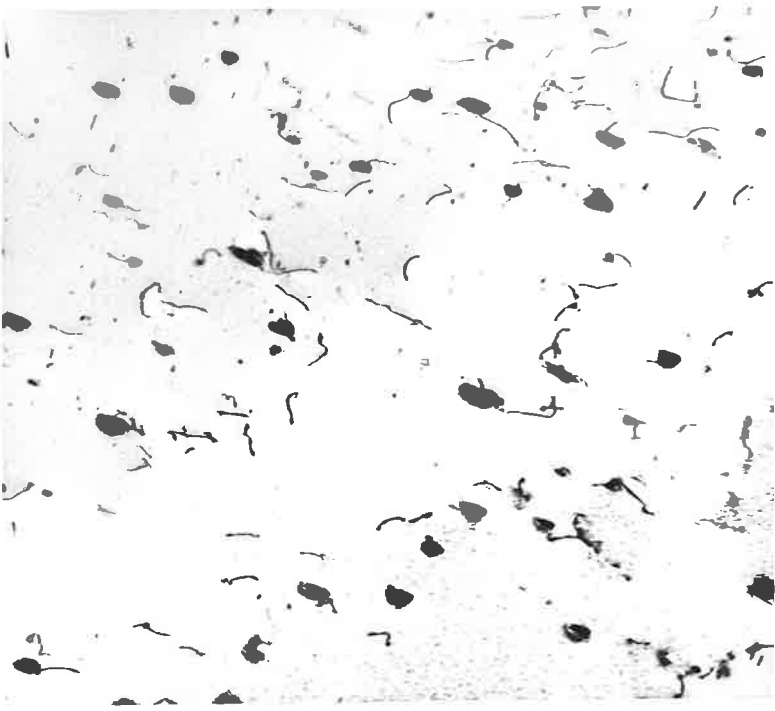



FIG. 4.39 An example of the free dislocations within the cells or towards the centres of large grains. Strain 0.08 at room temperature.

0.5 μ


FIG. 4.40 Recovered substructure from heat treatment at 400°C for 3½ hours of a specimen originally deformed 5% at room temperature.

0.5 μ

deformed at room temperature and those which had already been recovered at 400°C . The structure was then indicative of completely recovered material, figs. 4.41, 4.42. This recovered structure consisted mainly of low angle tilt boundaries which are polygonized arrays of edge dislocations as shown in figs. 4.43 and 4.44, and of twist boundaries which contain predominantly hexagonal networks of dislocations. Fig. 4.43 shows slip traces which suggest that the dislocations line up in the walls in the manner suggested by the polygonized tilt boundary model (e.g. see Dieter, 1961). Figs. 4.45 and 4.46 show that the dislocations in the centre of fig. 4.44 have a Burgers vector $[110]$ and the dislocations are of the edge type. Based on the possible slip planes and on a foil thickness of 3000\AA the plane on which these dislocations would have moved is $(1\bar{1}0)$. Thus this type of boundary forms by the normal glide polygonization reaction.

The other type of boundary which consists of hexagonal dislocation networks is far more complicated. It can be seen in the stereo electron micrographs, figs. 4.47 and 4.48 that the networks are shown quite conclusively not to lie on a single plane, which contrasts with the previous assertions for such networks in the h.c.p. metals zirconium and titanium (Bailey, 1963).

FIG. 4.41 Well formed polygonized tilt boundary. Specimen strained 3.5% at room temperature then recovered for 2 hours at 600°C.

0.5μ


FIG. 4.42 Well formed subgrain structure in specimen recovered at 600°C. Original deformation 3.4% strain at 380°C. This same sort of structure results after recovery of specimens between 5 and 15% at room temperature.

0.5μ

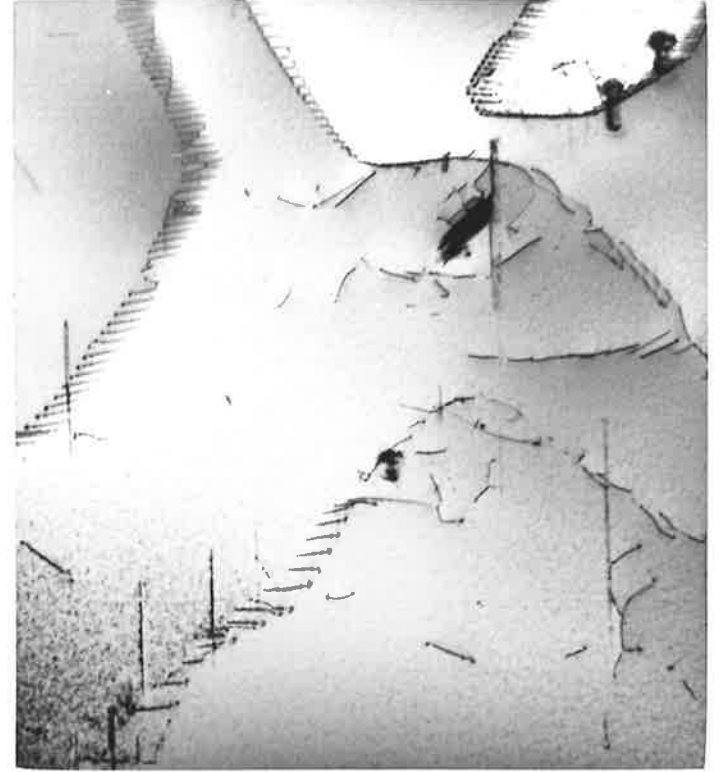
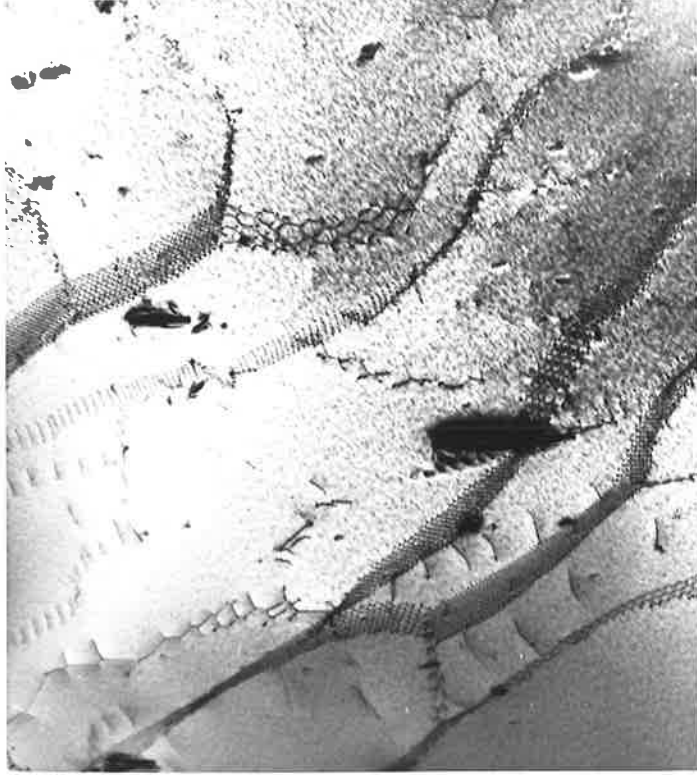



FIG. 4.43 Low angle tilt boundary in specimen recovered at 600°C. Slip traces due to slip on prism planes {100} show that boundary dislocations may have polygonized by glide on these planes.

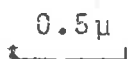
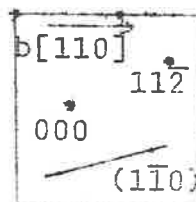


FIG. 4.44 Low angle tilt boundary formed by glide polygonization of [110] dislocations on (110) planes. (See figs. 4.45, 4.46).



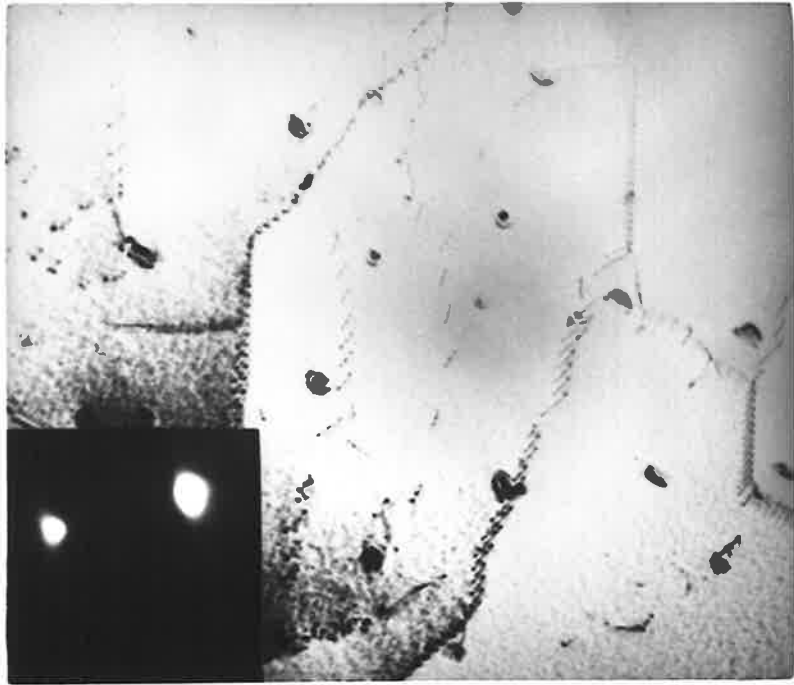


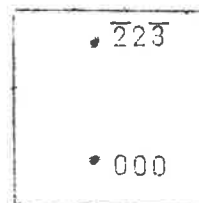
FIG. 4.45 Dislocations are out of contrast for two-beam conditions represented by $g(1\bar{1}1)$.

0.5 μ




FIG. 4.46 Dislocations are again out of contrast for two-beam conditions represented by $g(2\bar{2}3)$

0.5 μ

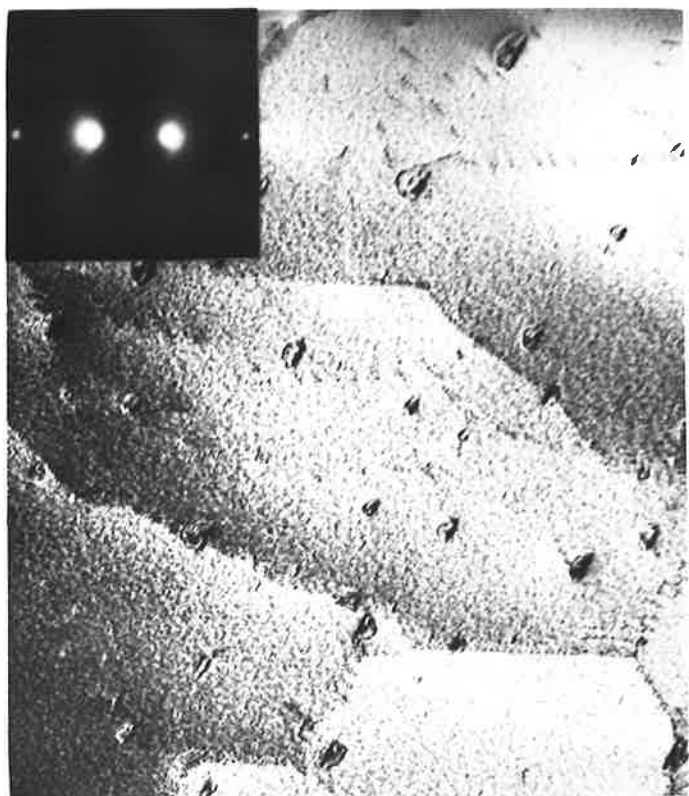


FIG. 4.47 Stereo-pair of dislocation network
(a) and (b). formed in a specimen strained at
room temperature (7.4%) and
recovered at 600°C. Tilt axis \longrightarrow
0.5 μ

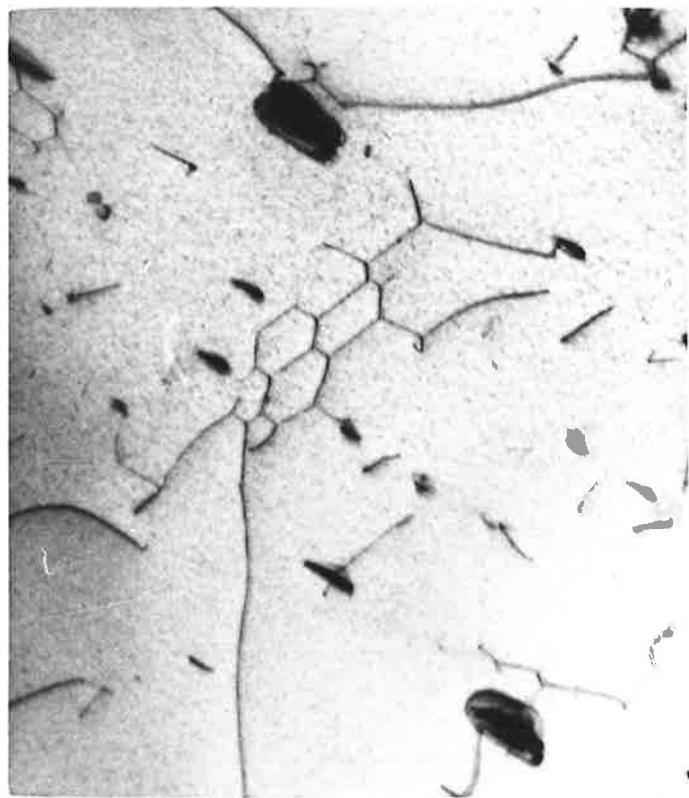
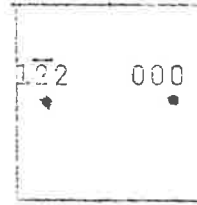
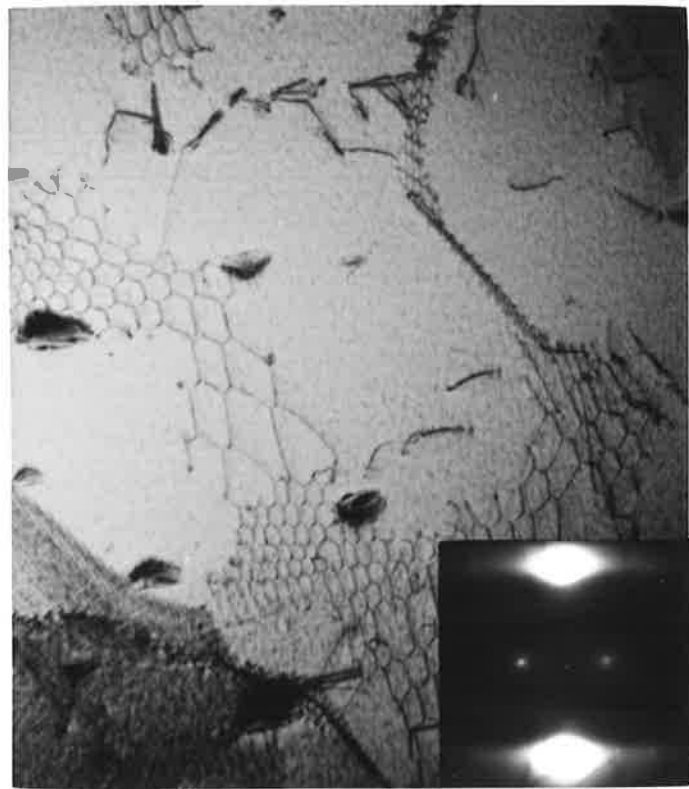
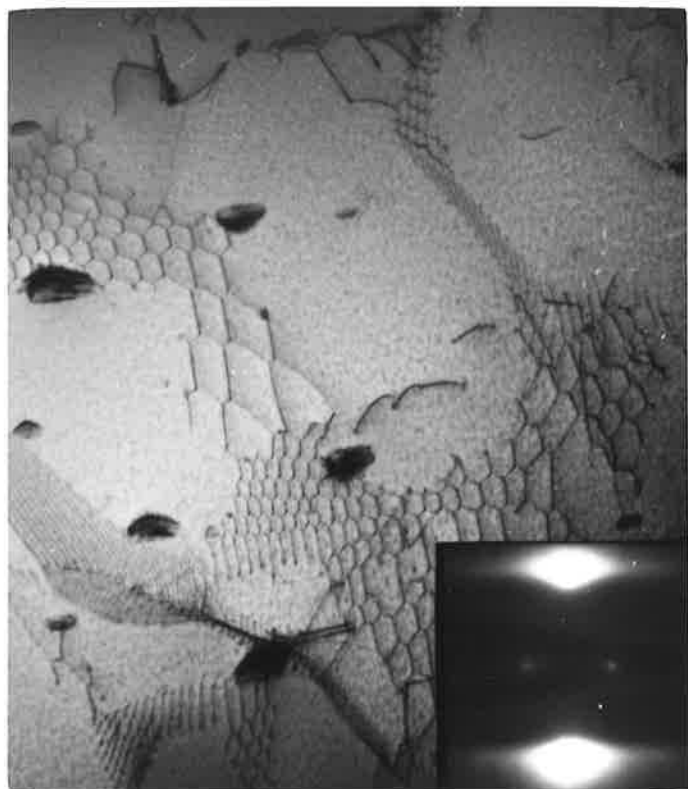


FIG. 4.48 Stereo-pair of a network of dislocations in a specimen recovered at 400 and 600°C after deformation at room temperature. Tilt axis parallel to $g(1\bar{2}2)$

0.5μ
└───┘



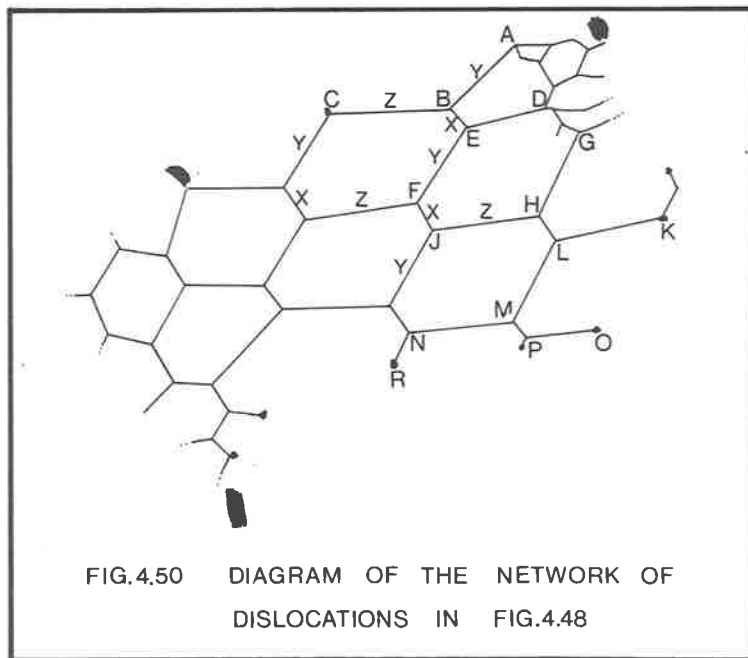
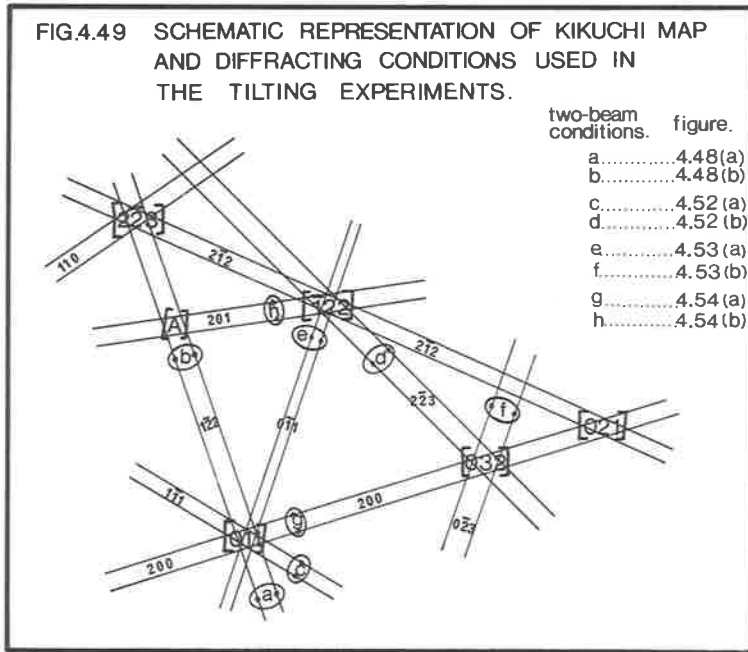


4.6 HEXAGONAL NETWORKS OF DISLOCATIONS.

Complete analyses of well formed dislocation networks were carried out. The networks were produced either as a result of cold deformation followed by high temperature recovery or as a result of high temperature deformation. There was no apparent difference in the structure of the networks formed by these two different methods.

Fig. 4.48 is a stereo pair showing a well formed hexagonal dislocation network in a thin foil which had been prepared from a specimen elongated 13% at room temperature and recovered at 400 and 600°C. The tilting experiment which was used to establish the stereomicrographs is conveniently represented on fig. 4.49, and fig. 4.50 is a diagram of the network in question with different dislocations marked X, Y, Z. Complete tilting experiments were performed to establish the Burgers vectors of the dislocations. Fig. 4.51 shows the actual diffraction patterns at the poles of the Kikuchi map which is represented by fig. 4.49, which also shows the approximate orientations at which the two beam conditions were obtained to allow the calculation of the Burgers vectors.

Each of the dislocations X, Y and Z were obtained in the no-contrast condition for two different two-beam conditions as shown in figs. 4.52 - 4.54. A further stereo-pair was produced, using a different tilt axis to that used



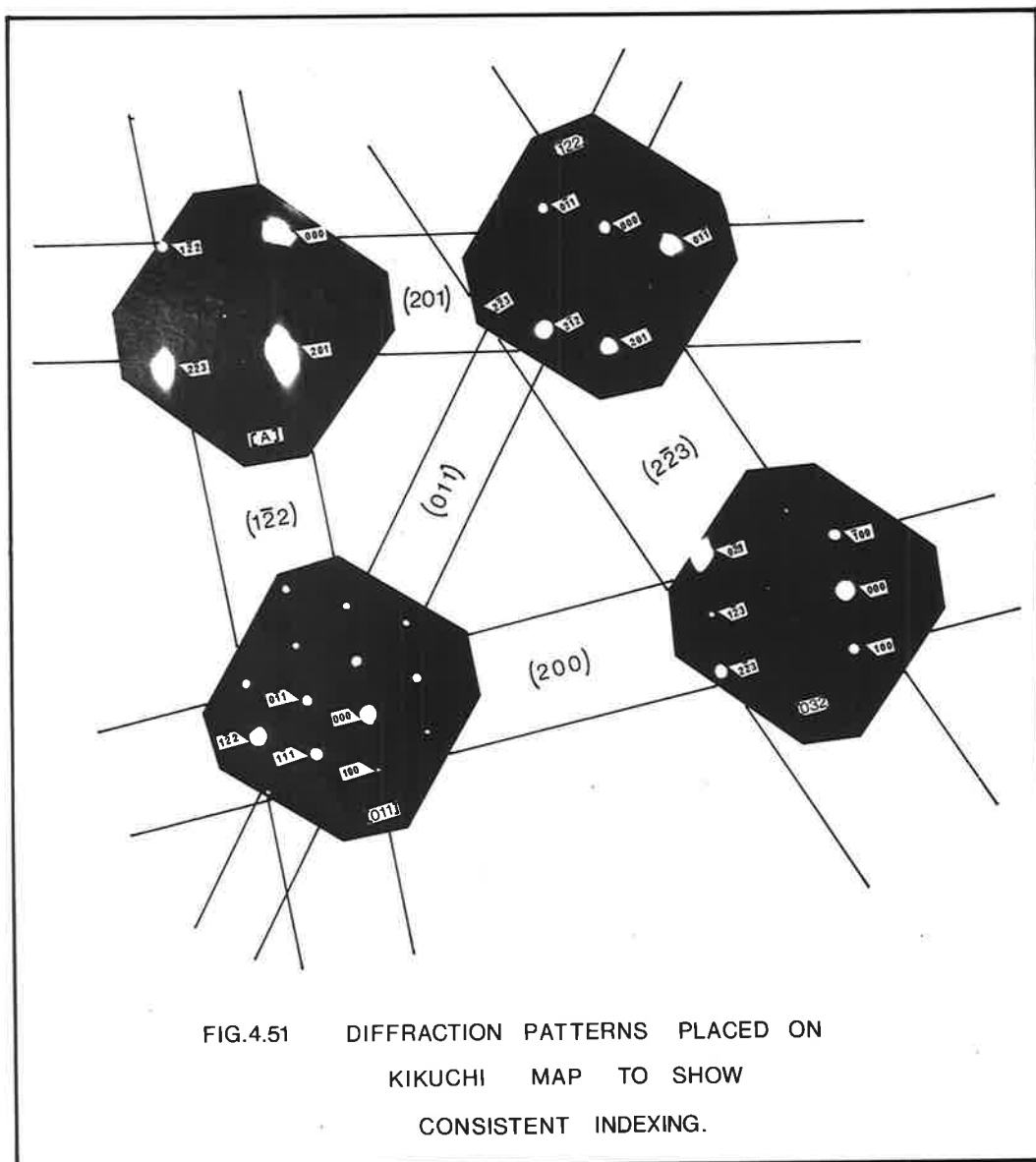
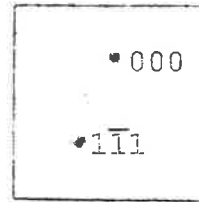


FIG.4.51 DIFFRACTION PATTERNS PLACED ON KIKUCHI MAP TO SHOW CONSISTENT INDEXING.

FIG. 4.52 (a) Dislocations X are out of contrast.

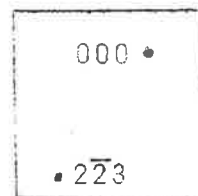
Diffacted beam ($1\bar{1}1$)

0.5 μ
└───┘



(b) Dislocations X are again out of contrast. Diffacted beam ($2\bar{2}3$)

0.5 μ
└───┘



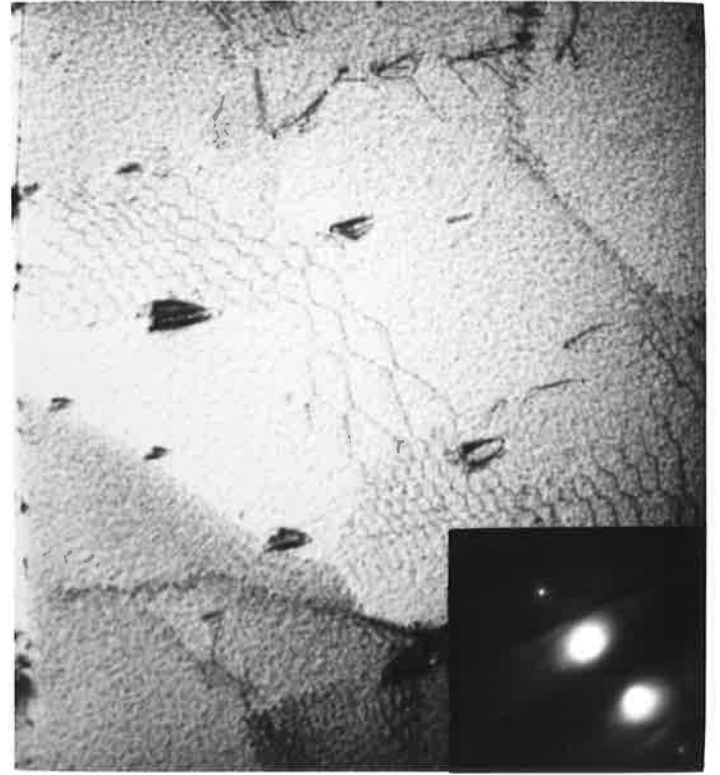
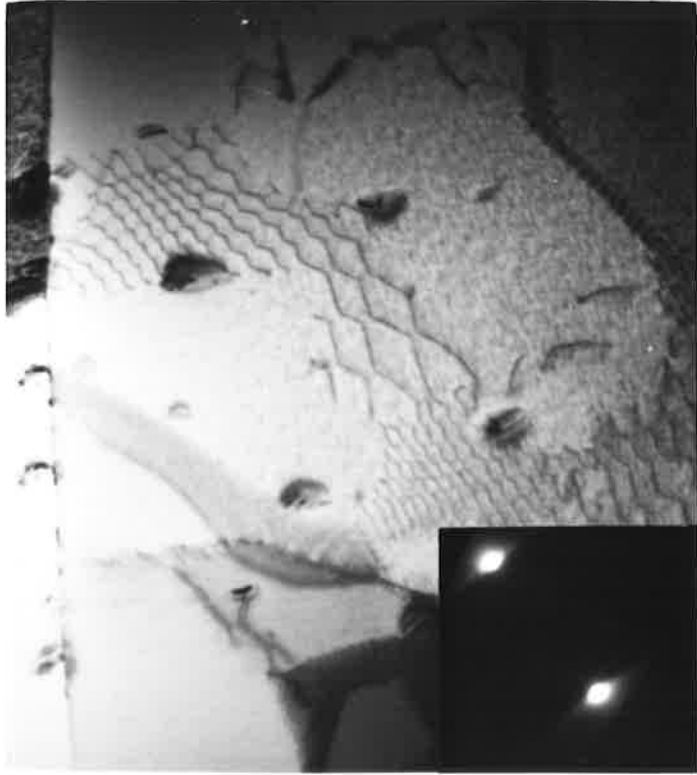
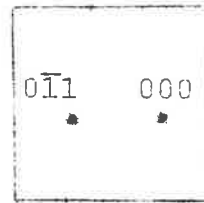


FIG. 4.53(a) Dislocations Y are out of contrast.

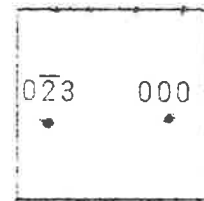
Diffracted beam $(0\bar{1}1)$

0.5 μ
└───┘



(b) Dislocations Y are again out of contrast.
Diffracted beam $(0\bar{2}3)$

0.5 μ
└───┘



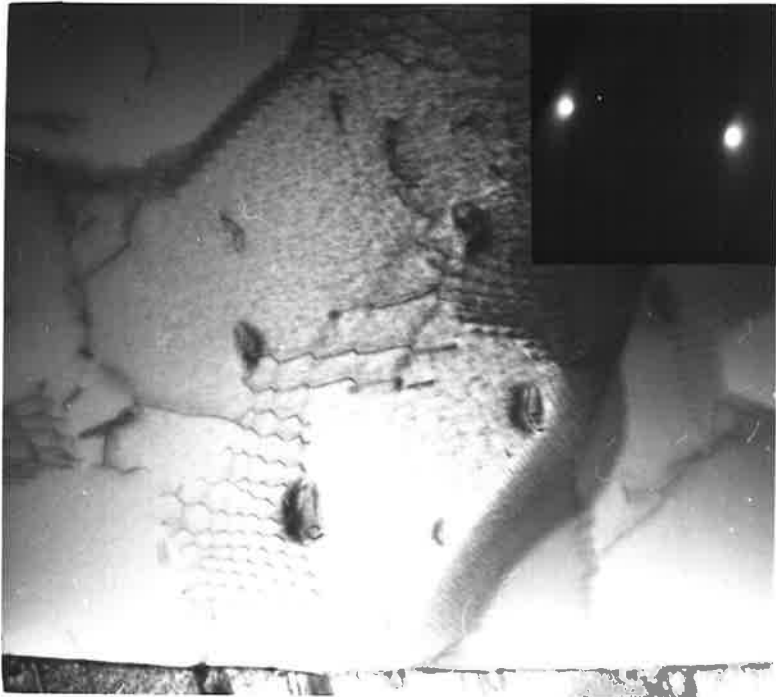
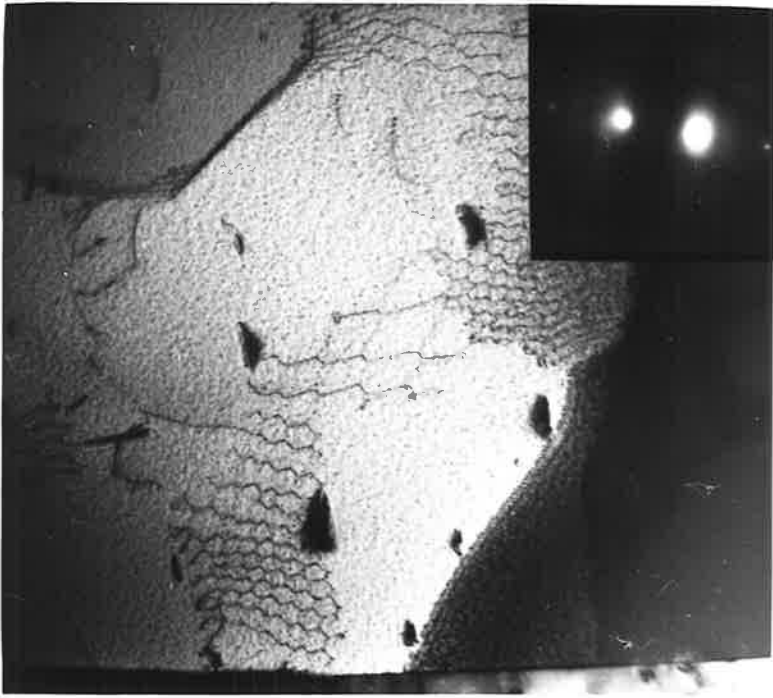
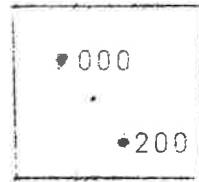


FIG. 4.54 (a) Dislocations Z are out of contrast.
Diffracted beam (200)

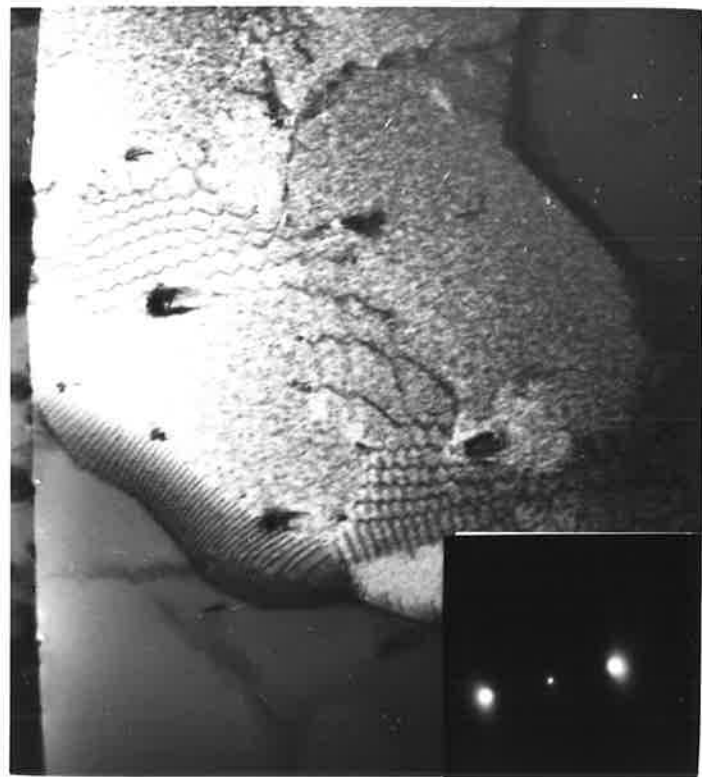
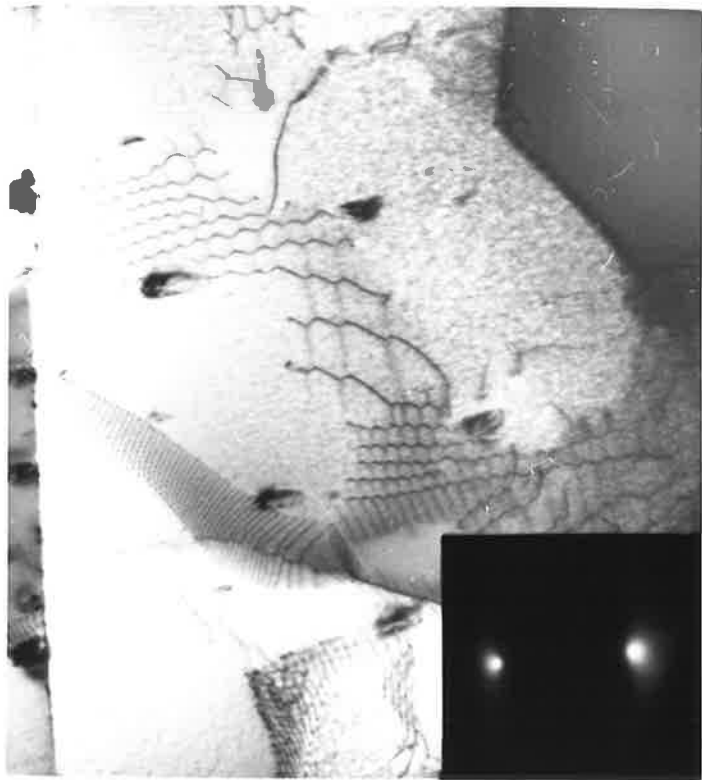
0.5 μ

(b) Dislocations Z are again out of contrast.
Diffracted beam (201)

0.5 μ



for fig. 4.48, to obtain additional information on the spatial behaviour of the dislocations in the network.

Parallax measurements can be made on stereo-pairs so that the position of various points within the thin foil can be estimated (Nankivell (1963), Section 2.3). By using this technique on the stereo-pair, fig. 4.48, the angles that the dislocation lines make with the foil surface (or zone-axis) were calculated. Difficulties were encountered in making accurate measurements of parallax and so large error probabilities had to be allowed for. The results of the measurements made are summarized in table \bar{V} .

From the Burgers vector determination and the parallax measurements the following conclusions were drawn:- Firstly, the dislocations X and Y are mixed dislocations which have a major screw component. Dislocations Z are also mixed dislocations but the major component could be either edge or screw.

Although the parallax measurements gave results which were reasonable, the process was extremely tedious and, as mentioned, suffered from many sources of errors. It has been found that the most convenient way to use the technique of stereo electron microscopy is to visually estimate the angles the relevant dislocations make with the foil and results of an accuracy as good as those produced from parallax measurements are obtained.

TABLE V

ANALYSIS OF DISLOCATIONS IN NETWORK

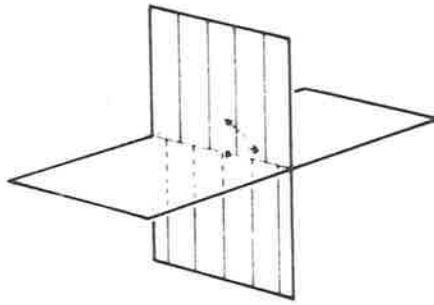
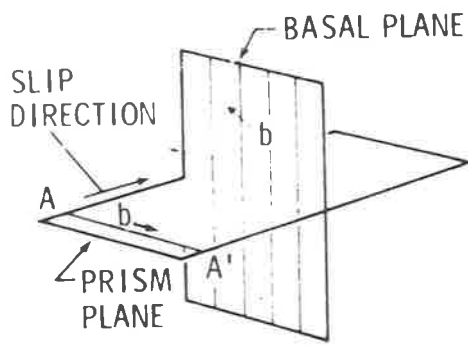
SHOWN IN FIGS. 4.85 - 4.92.

DISLOCATIONS		ANGLE WITH ZONE AXIS	AVERAGE ANGLE	BURGERS VECTOR	ANGLE BETWEEN BURGERS VECTOR AND ZONE AXIS.
X	PM	83	82	[110]	75
	LH	90			(105)
	JF	80			
	EB	76			
Y	ML	81	68	[100]	105
	RN	71			(75)
	HG	71			
	FE	45			
	BA	73			
Z	OP	76	70	[010]	58
	KL	52			(122)
	MN	83			
	HJ	87			
	DE	63			
	BC	62			

4.7 MECHANISMS OF DISLOCATION NETWORK FORMATION.

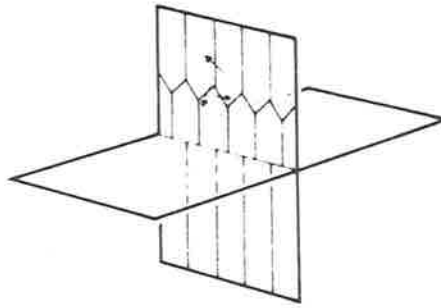
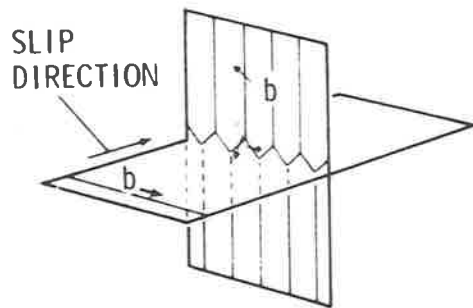
Dislocation networks have been frequently observed in the f.c.c. and b.c.c. metals and the crystallography of some of these networks has been given (e.g. Ohr and Beshers (1963), Miller and Crawford (1968)). Hexagonal dislocation-networks have been observed in many of the h.c.p. metals. Bailey (1963) observed an hexagonal network in α -zirconium which he assumed was a planar network lying in the basal plane. Similar networks have been observed in zinc, by Berghezan et al. (1961) and Price (1963), which also lay on the basal planes. In beryllium, Ranzetta and Scott (1963) and Bonefield (1965) observed hexagonal networks of dislocations on basal planes.

In general, the mechanism used to explain the formation of such hexagonal networks in these metals was based on the mechanism proposed by Whelan (1958) for f.c.c. metals and modified by Meikk-oja (1965). This mechanism was used by Pittinato and Frederick (1969) to explain the formation of networks in a Ti-Al-Sn alloy. The mechanism is represented by fig. 4.55. A screw dislocation in the basal plane intersects an array of dislocations in a prism plane resulting in the formation of three-fold nodes. Since the Burgers vectors of the dislocations all lie in the basal plane, the array of dislocations may cross slip onto this plane and as the mechanism proceeds an hexagonal network is formed on the basal plane.



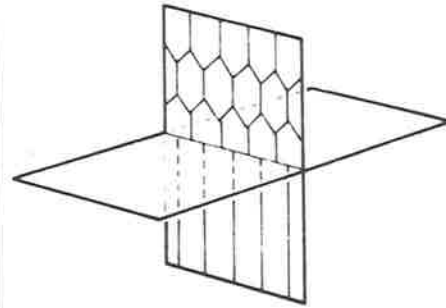
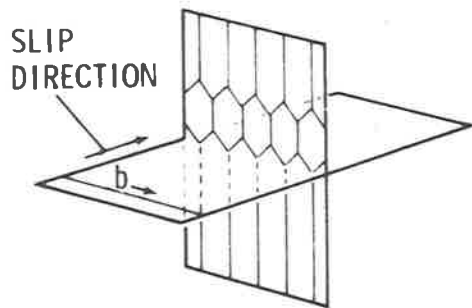
A

B



C

D



E

F

FIG.4.55 HEXAGONAL NETWORK FORMATION.

(AFTER PITTINATO AND FREDERICK, 1969)

Although the results of Pittinato and Frederick show that this method of network formation best explains their results, some of the networks appear to lie on planes other than the basal planes. Also of note is the illustration of piled-up groups of dislocations given by Ranzetta and Scott (1963) which appears, in fact, to be comprised of polygonized dislocation arrays and this could lead to another type of network forming mechanism which will be discussed shortly.

There seems to have been little attempt to completely analyse the Burgers vectors of dislocations in hexagonal networks and to establish the planes on which they lie. The following mechanisms will be shown to be able to account for some of the observations of networks and surrounding dislocations in deformed α -zirconium. The main facts which need be remembered are that the networks are not planar (figs. 4.47 - 4.48) and that the dislocations have Burgers vectors of the type $\langle 100 \rangle$. In addition, in the present work, approximately sixty analyses of dislocations in deformed and heat treated α -zirconium have shown that dislocations have Burgers vectors of the type $\langle 100 \rangle$ and are almost always compatible with slip on $\{100\}$ planes.

4.7.1. The Mechanisms.

(1) Dislocation Arrays on Prism Planes Intersected

by Basal Dislocations

(a) Consider, first, an array of edge dislocations on a prism plane (fig. 4.56 (a)). A screw dislocation moving on a basal plane may intersect the array of edge dislocations giving rise to the interactions shown in fig. 4.56 (b). The reaction is represented by, $[100] + [010] = [110]$, or in the four index notation, $1/3 [2\bar{1}\bar{1}0] + 1/3 [\bar{1}2\bar{1}0] = 1/3 [11\bar{2}0]$. Line tensions will cause the dislocations to relax into the configuration shown in fig. 4.56 (c).

Intersections by other screw dislocations moving in the prism planes will result in the buildup of an hexagonal network of the type represented by fig. 4.56 (d).

(b) If the basal dislocations were other than screw in character an hexagonal network could also be formed (fig. 4.57).

(2) Dislocation Arrays on Prism Planes Intersected by Dislocations on other Prism Planes.

(a) If an array of screw dislocations moving on a prism plane lines up parallel to a basal plane and then is intersected by dislocations moving on another set of prism planes, an hexagonal network could result. Fig. 4.58 (a) represents the planes and

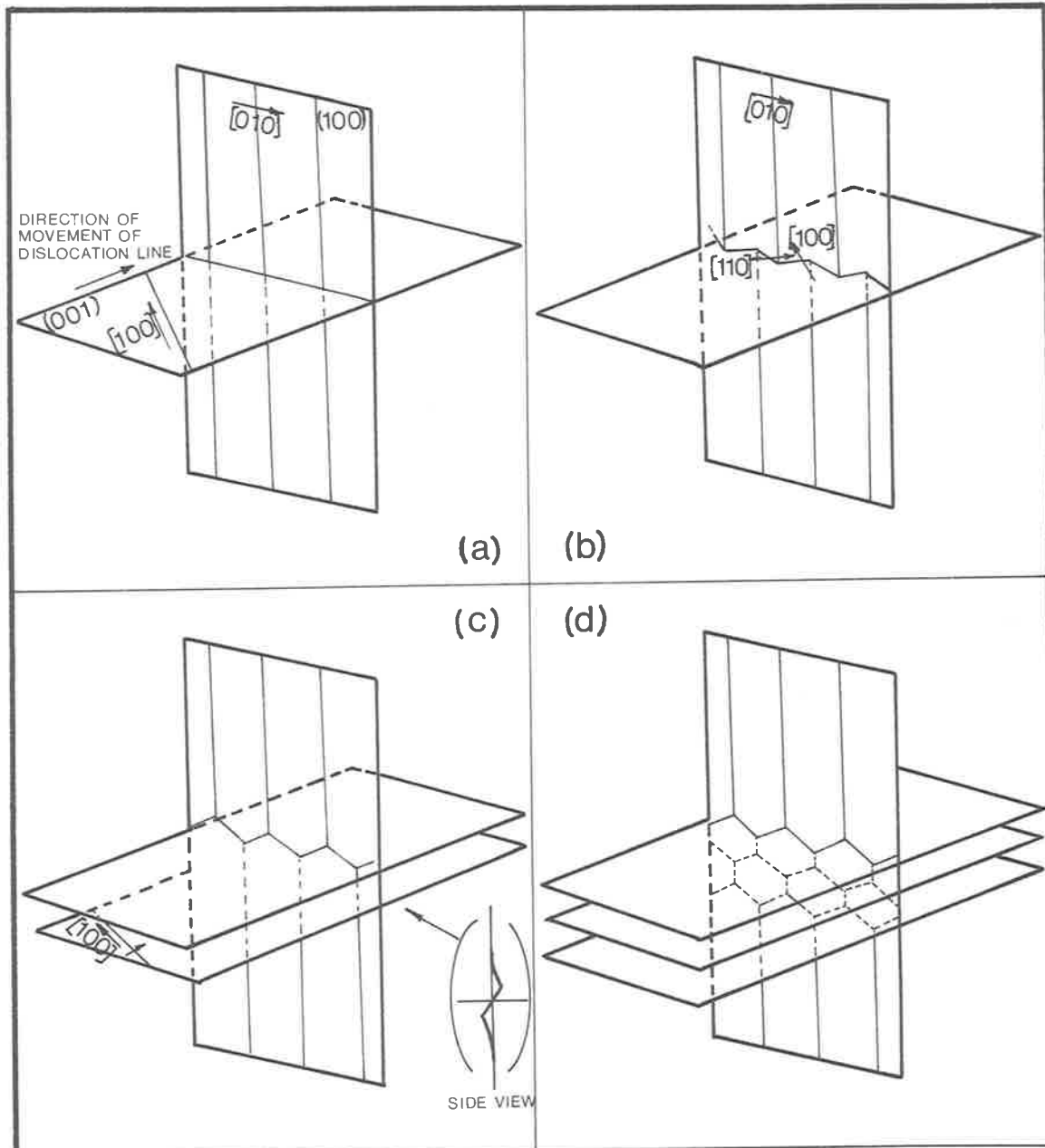
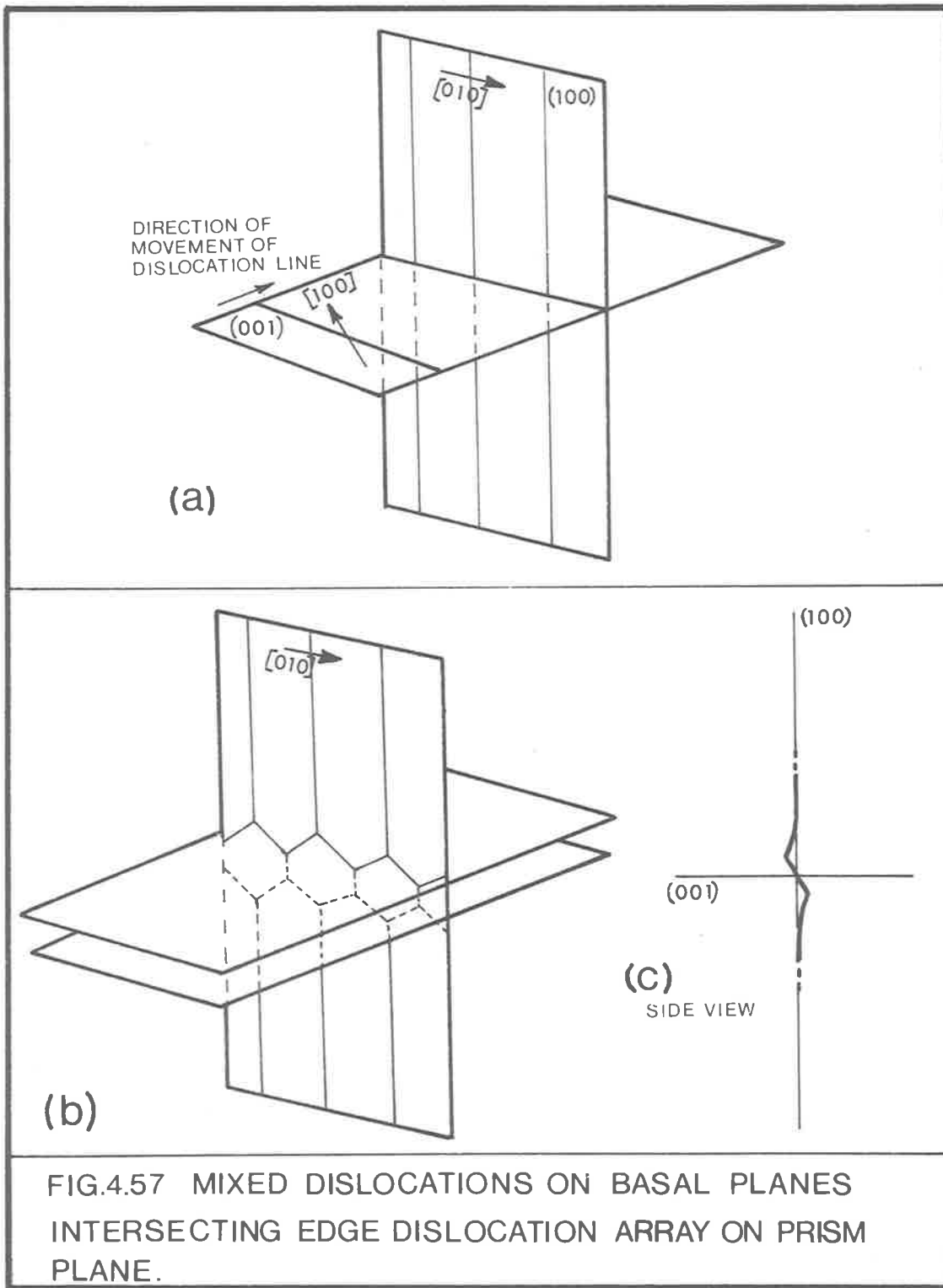


FIG. 4.56 HEXAGONAL DISLOCATION NETWORKS FORMED BY INTERSECTION OF SCREW DISLOCATIONS ON BASAL PLANES WITH EDGE DISLOCATION ARRAYS ON PRISM PLANES.



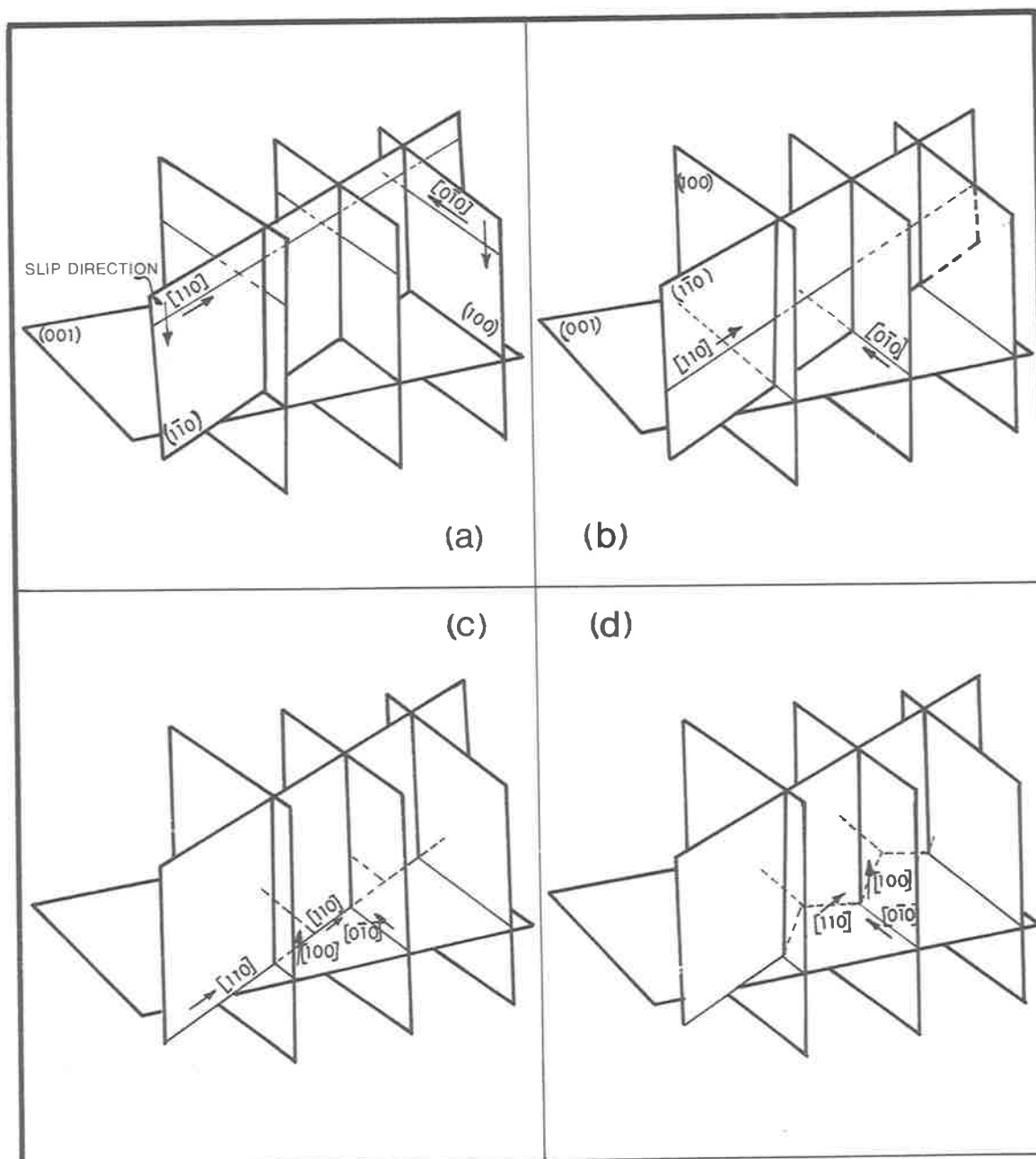
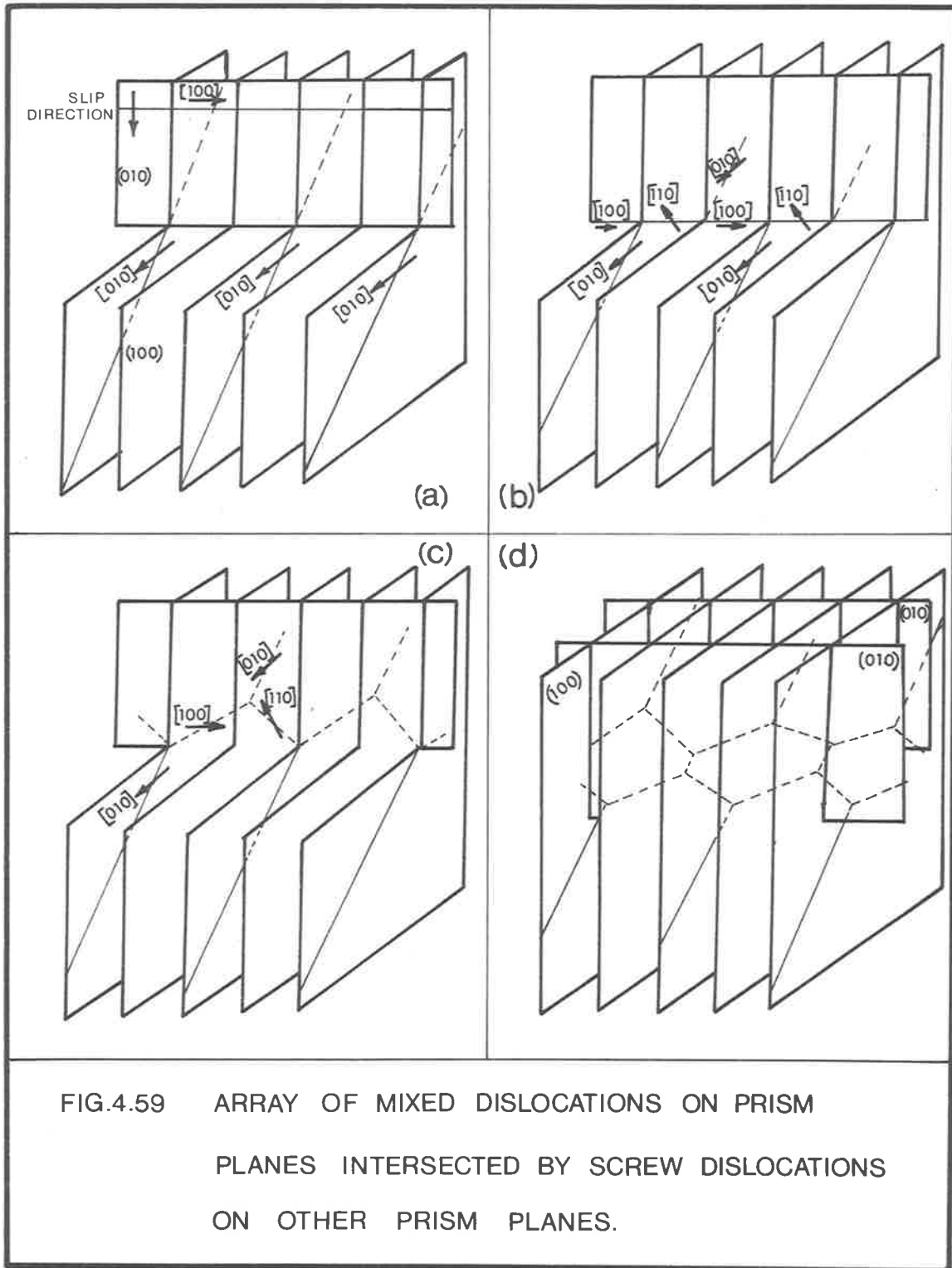


FIG.4.58 ARRAY OF SCREW DISLOCATIONS ON PRISM PLANES INTERSECTED BY SCREW DISLOCATIONS ON OTHER PRISM PLANES.

dislocations and fig. 4.58(b) shows the polygonized array parallel to the basal plane. The dislocation on a $(1\bar{1}0)$ plane with Burgers vector $[110]$ intersects the array of screw dislocations and the reaction $[110] + [0\bar{1}0] = [100]$ takes place as shown in fig. 4.58 (c). The line tensions produce a configuration similar to that shown in fig. 4.58 (d). This network lies in the basal plane which contains all the Burgers vectors and so cross glide can occur. The resultant network could then be produced either by further intersections of $[110]$ dislocations on the other $(1\bar{1}0)$ planes or cross slip could occur so that $[110]$ dislocations on the same $(1\bar{1}0)$ plane could build up a network. This latter case is, in principle, similar to the method given by Pittanato and Frederick and shown in fig. 4.55.

(b) The mechanism is modified if the dislocations in the arrangement formed by glide polygonization on the prism planes are of mixed character. For example, consider the mixed dislocations with Burgers vector $[010]$ on the (100) planes in fig. 4.59 (a). A screw dislocation with Burgers vector $[100]$ moves in the direction shown on the (010) plane. Upon intersection, the reaction $[010] + [100] = [110]$

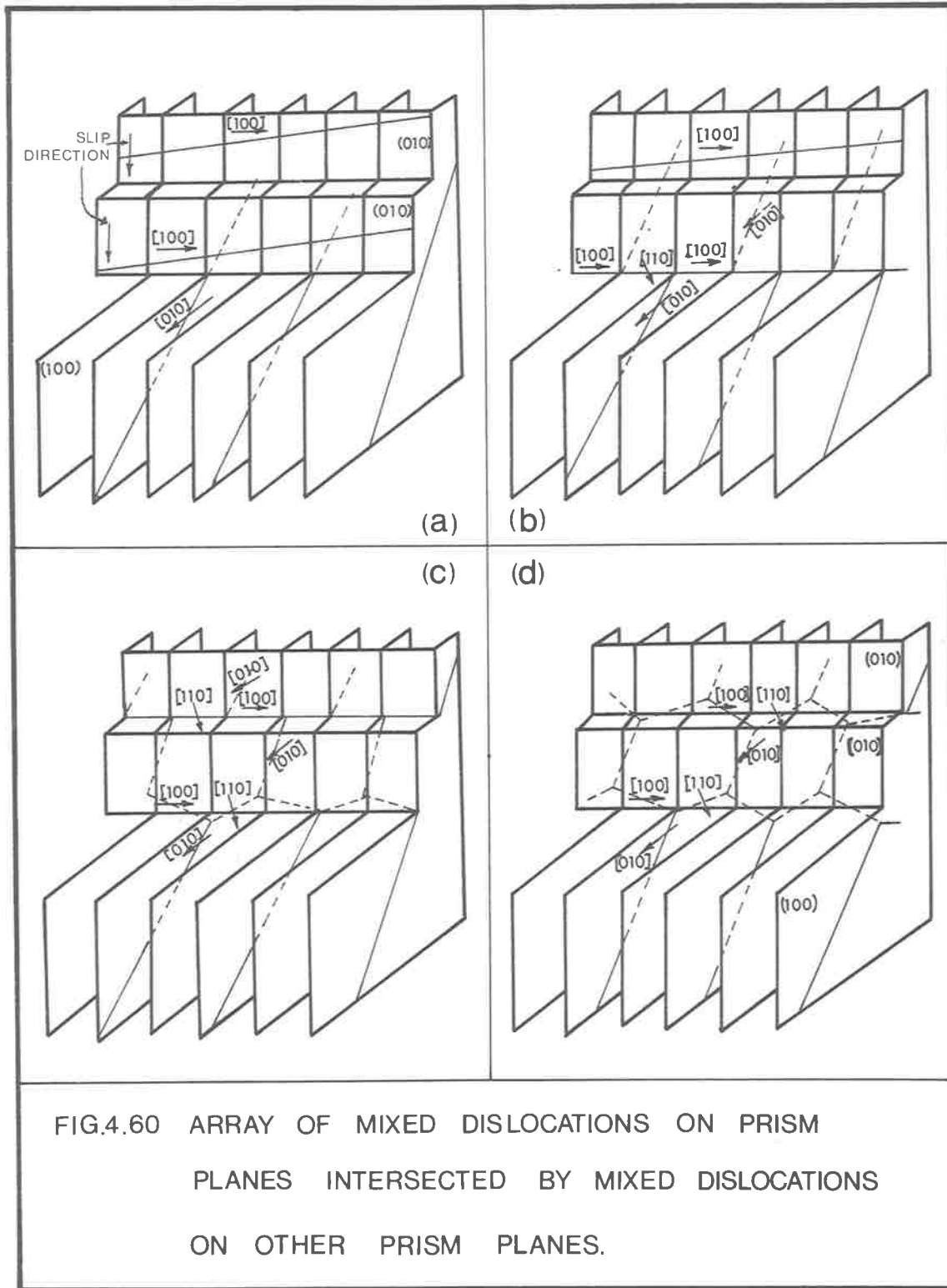


occurs, fig. 4.59 (b). Again, line tension forces will cause the three fold nodes to approach an equilibrium configuration as shown in fig. 4.59 (c). A larger network can then build up from intersections of more $[100]$ dislocations moving on parallel (010) planes resulting in the configuration shown in fig. 4.59 (d).

(c) An array of mixed dislocations lying on prism planes (say (100)) may be intersected by screw or mixed dislocations on another set of prism planes (say (010)) to produce a complicated hexagonal dislocation network. The sequence is illustrated by fig. 4.60.

Only in the special cases where dislocation networks produced from dislocations with Burgers vectors $[100]$, $[010]$ and $[110]$, are formed in the basal plane can the networks glide relatively easily under the influence of a stress. This is because it is only in these cases that all the dislocation lines and the Burgers vectors are contained in the same plane (the basal plane).

In many of the mechanisms proposed, the dislocations in the hexagonal network will have moved out of their slip planes and so the networks are relatively immobile under the influence of an applied stress. However, further modifications



to the networks could result from thermal processes (e.g. climb) and so some mobility could be induced in the networks.

4.7.2. Evidence for the Mechanisms Proposed.

Many of the previously published electron micrographs showing hexagonal dislocation networks in h.c.p. metals (Bailey (1963), Pittinato and Frederick (1968), Ranzetta and Scott (1963)) give some indications that the dislocation networks do not lie in a single plane yet the mechanisms used to explain the production of such networks results only in planar networks. Sterco-electron micrographs of the networks in the α -zirconium of this study show that the networks lie at many different angles in the foils, and indeed, could not lie on any one single set of planes. For this reason the operation of one, or several, different mechanisms of network formation are attractive.

To allow the production of networks by the proposed mechanisms it is usually assumed that an array of dislocations exists which lines up along a single direction. A tilt boundary is a special example of such an array and these are usually assumed to be formed by thermally activated polygonization during recovery or annealing processes.

Another method of obtaining this kind of dislocation array is by glide polygonization which was observed by Price (1963) in zinc. This type of process is possible since the alignment of dislocations in polygonized arrays represents a low

energy configuration.

In recovered zirconium specimens, boundaries containing polygonized arrays of dislocations were commonly encountered (fig. 4.41). It was shown that similar arrays were composed of dislocations whose Burgers vector was $[110]$ and that the probable slip plane was the prism plane $(1\bar{1}0)$, (figs. 4.44 - 4.46).

Further evidence for parallel dislocation arrays forming as a result of glide can be seen in fig. 4.61. The slip traces delineate the slip plane and the thickness of the foil ($\approx 3000\text{\AA}$) confirms that the dislocations have slipped on $(1\bar{1}0)$ planes. The dislocations are tending to arrange themselves in a type of polygonized array.

Therefore, the assumption that parallel arrays of dislocations will be present in zirconium is a reasonable one and thus the proposed mechanisms of network formation are feasible. It would be expected that higher temperatures favour network formation because it is easier for parallel dislocation arrays to be formed. An example of a network which has begun to form as a consequence of the dislocation intersecting an array of dislocations is shown in fig. 4.41.

A complete network analysis is shown in figs. 4.62 - 4.68 and it is again shown that only $[100]$ type Burgers vectors are present. There is also an array of dislocations

FIG. 4.61 Dislocations tending to form tilt boundaries by glide polygonization.

0.5 μ





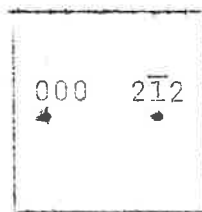
near the dislocation network which suggests that the network could have formed by one of the proposed mechanisms. The network can easily be seen to be non-coplanar in the stereomicrographs, fig. 4.62, and additional information can be gained about the parallel array of dislocations. These have slipped on $(1\bar{1}0)$ planes and have the Burgers vector $[110]$ (fig. 4.65). These dislocations line up near a direction which is parallel to the trace of the (010) plane. If dislocations moving on the (100) or $(1\bar{1}0)$ planes intersect this parallel array the network could form.

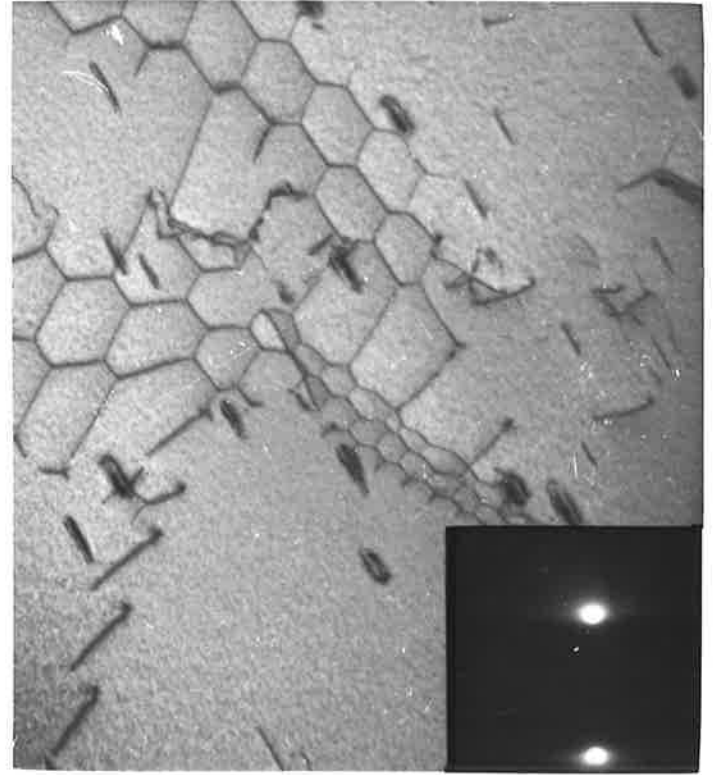
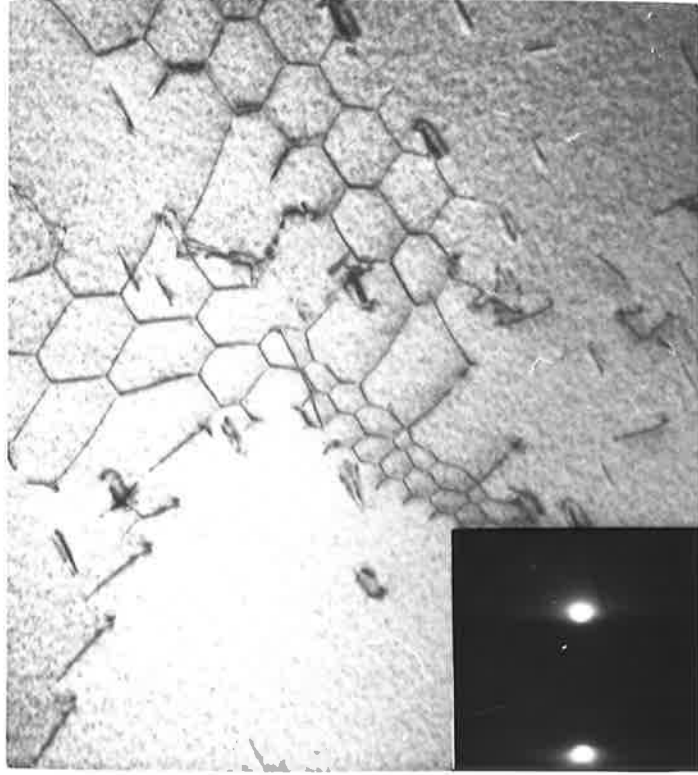
Evidence for the formation of networks due to interactions of prism and basal dislocations was found only in isolated instances. One such instance is shown in fig. 4.69 where again all the dislocations can be shown to have $[100]$ Burgers vectors but the very long dislocations have slipped on either (001) or perhaps $(1\bar{1}1)$ planes.

Therefore, it has been shown that the hexagonal networks of dislocations in α -zirconium are far more complicated in their spatial arrangements than was previously assumed. However, only the simple basal Burgers vectors were observed. The networks may form by a number of mechanisms, most of which involve interactions between dislocations gliding on different prism planes. Only in a few cases can the simplest mechanism involving basal-prism dislocation interactions be used to account for their arrangements into hexagonal networks.

FIG. 4.62 Stereo-electron-micrographs of
(a) and (b) hexagonal network of dislocations.
Tilt axis parallel to $g(2\bar{1}2)$

0.5 μ





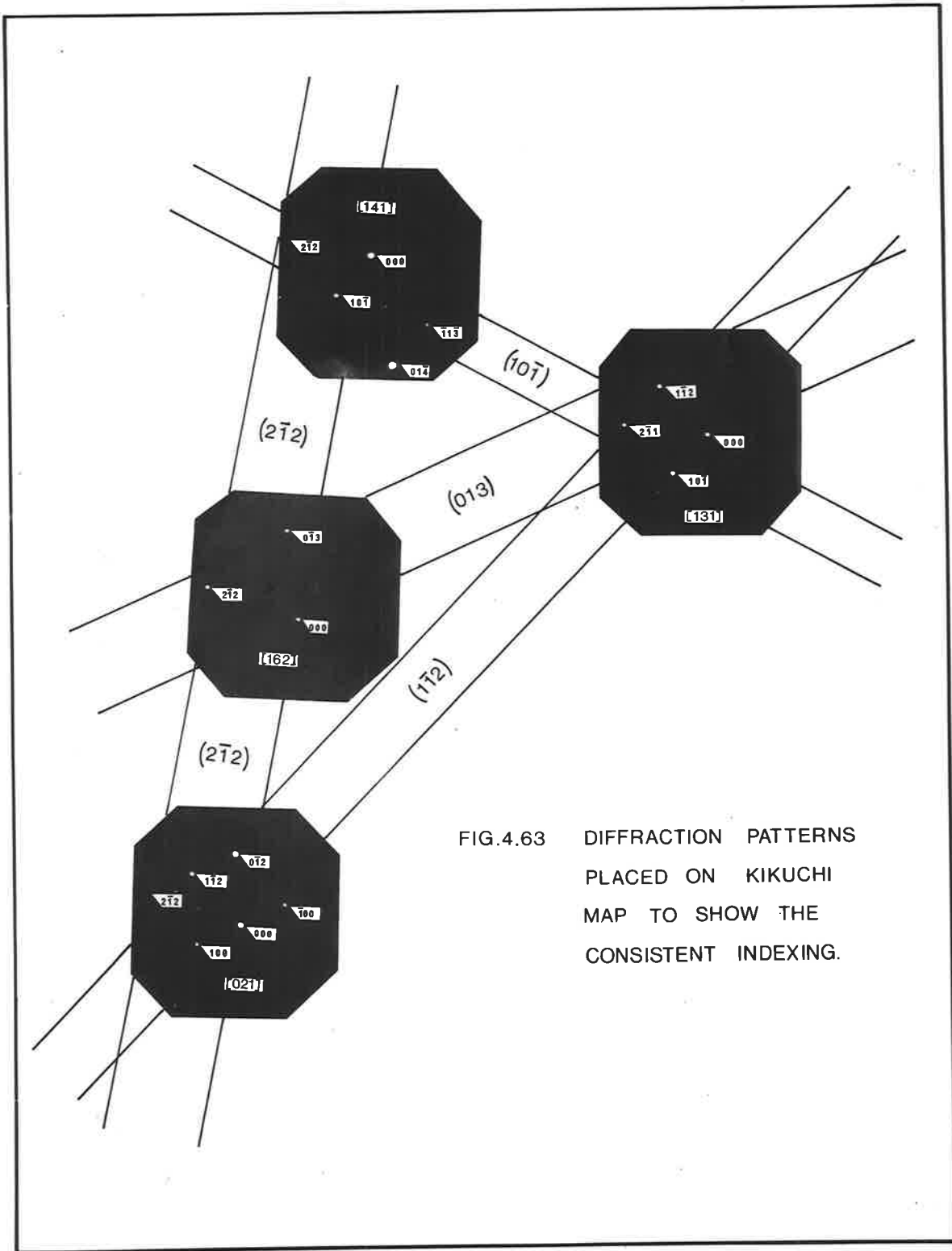


FIG.4.63 DIFFRACTION PATTERNS PLACED ON KIKUCHI MAP TO SHOW THE CONSISTENT INDEXING.

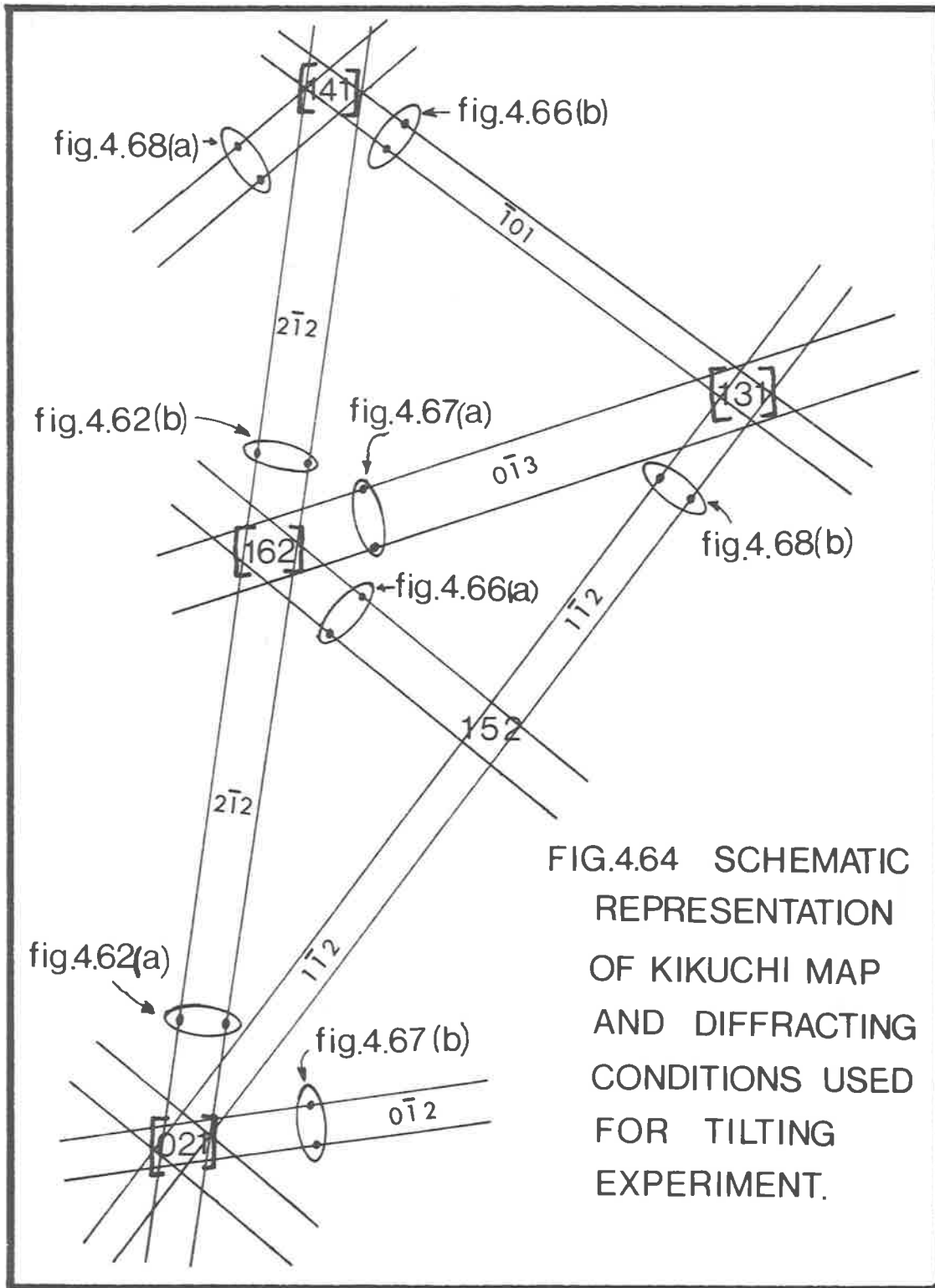


FIG.4.64 SCHEMATIC REPRESENTATION OF KIKUCHI MAP AND DIFFRACTING CONDITIONS USED FOR TILTING EXPERIMENT.

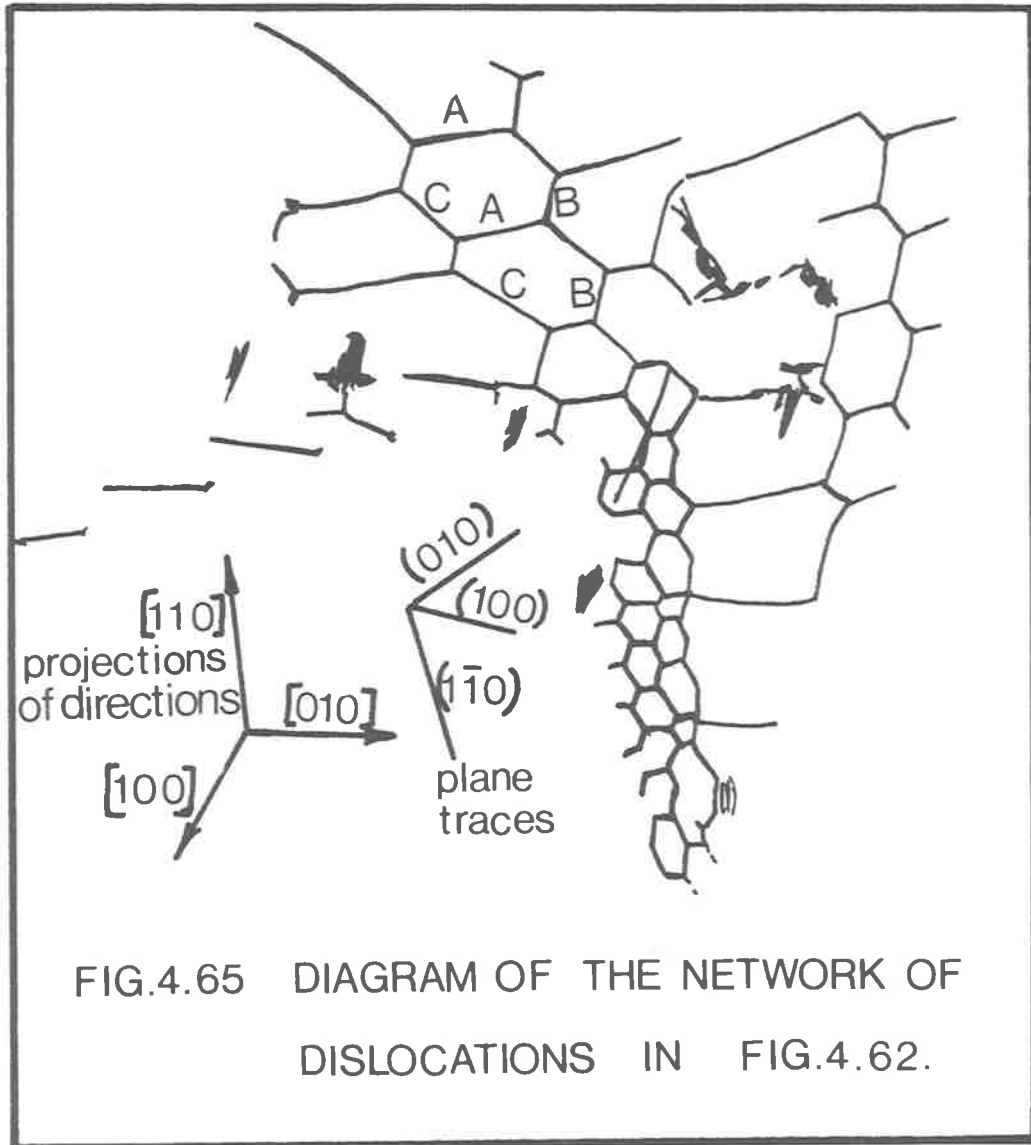
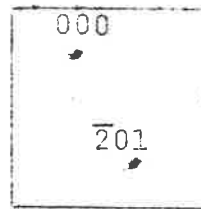


FIG.4.65 DIAGRAM OF THE NETWORK OF DISLOCATIONS IN FIG.4.62.

FIG. 4.66(a) Dislocations A are out of contrast.

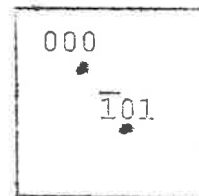
$g(\bar{2}01)$

0.5 μ
└───┘



(b) Dislocations A are again out of contrast. $g(\bar{1}01)$

0.5 μ
└───┘



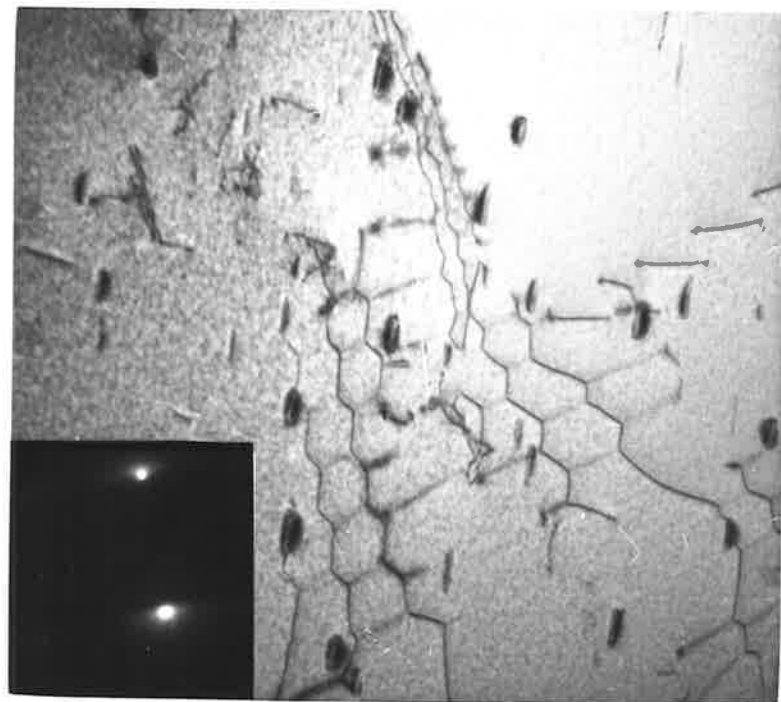
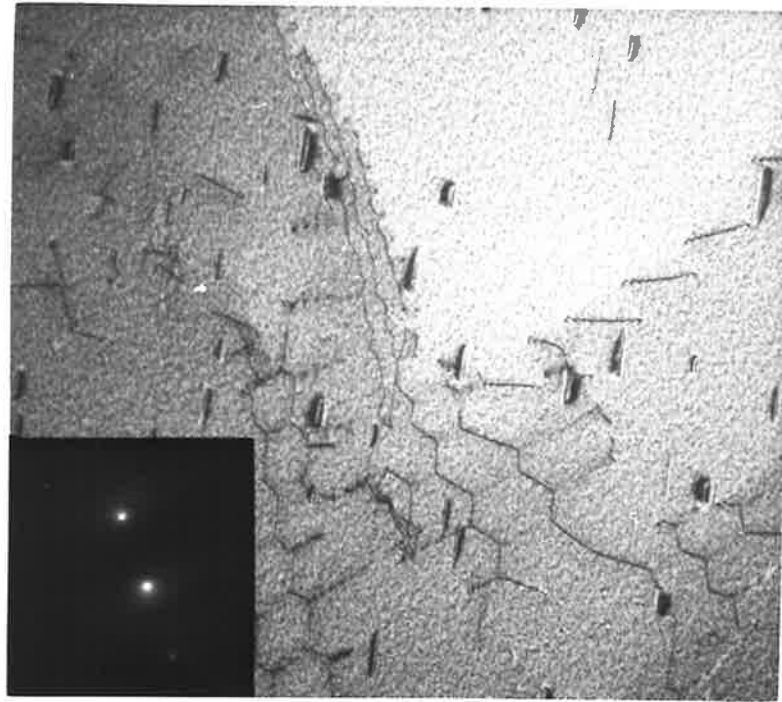
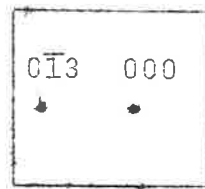


FIG. 4.67 (a) Dislocations \underline{B} are out of contrast.
 $g(0\bar{1}3)$.

0.5 μ
└───┘



(b) Dislocations B are again out of contrast.
 $g(0\bar{1}2)$.

0.5 μ
└───┘



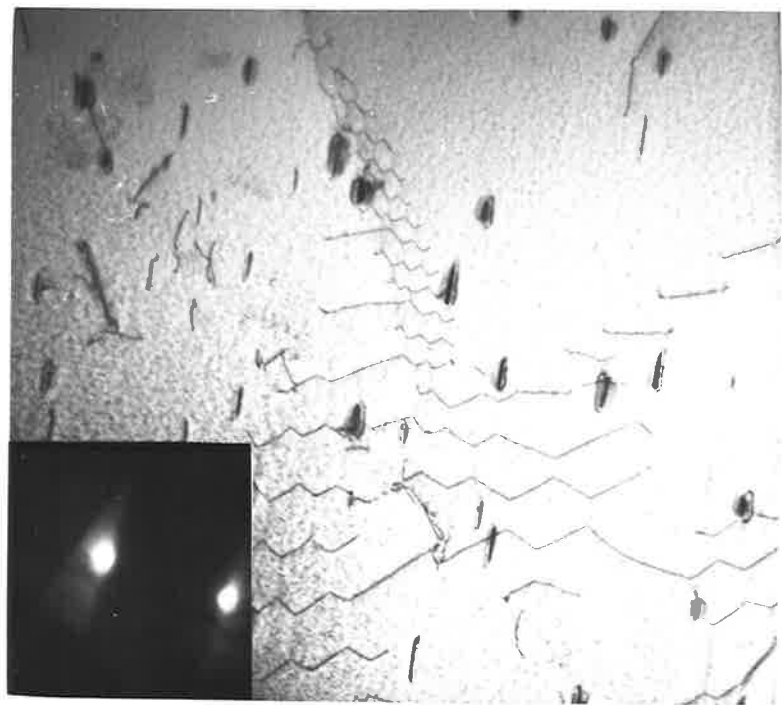
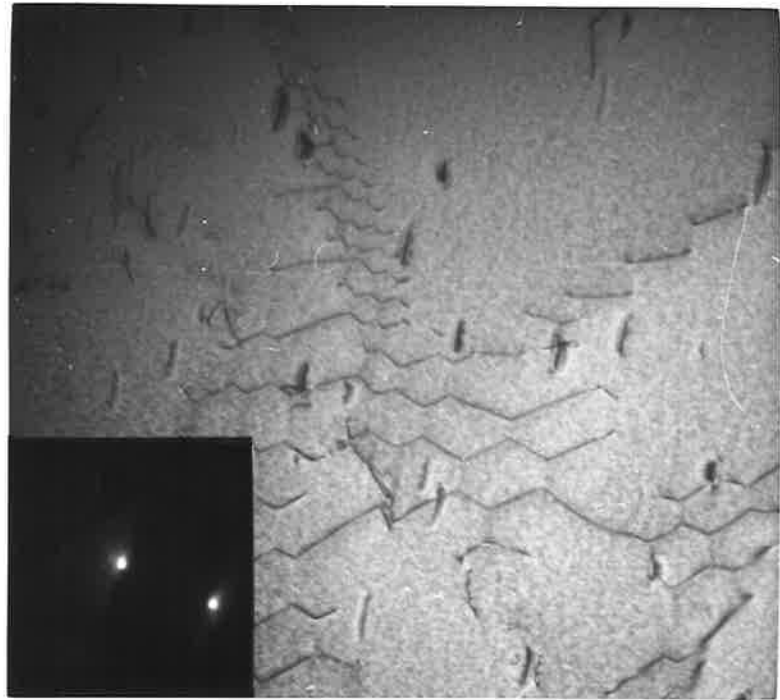
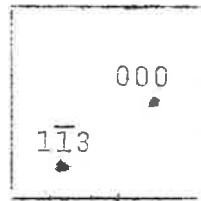


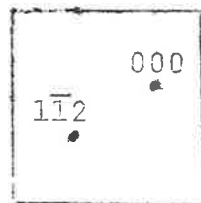
FIG. 4.68 (a) Dislocations C are out of contrast.
 $g(1\bar{1}3)$

0.5 μ
└───┘



(b) Dislocations C are again out of contrast.
 $g(1\bar{1}2)$

0.5 μ
└───┘



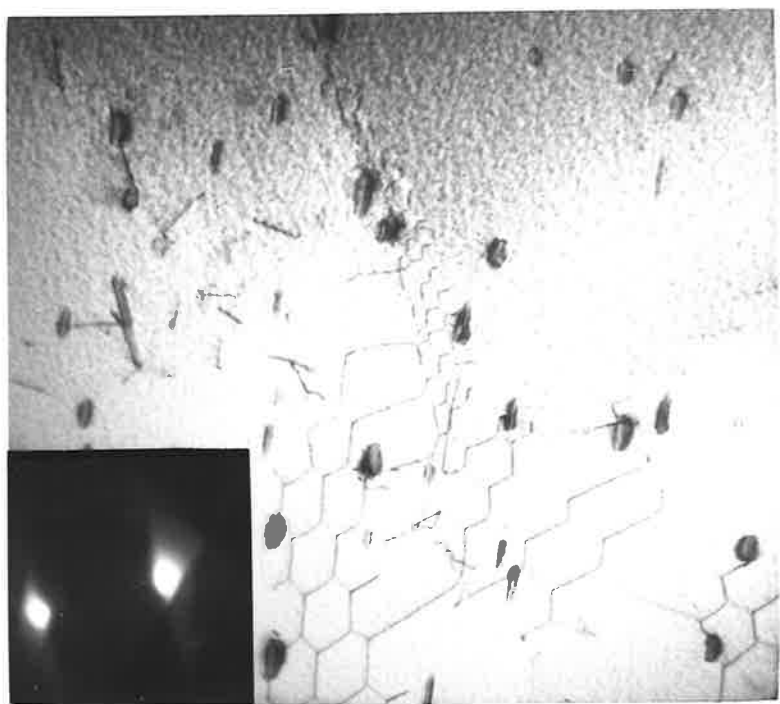
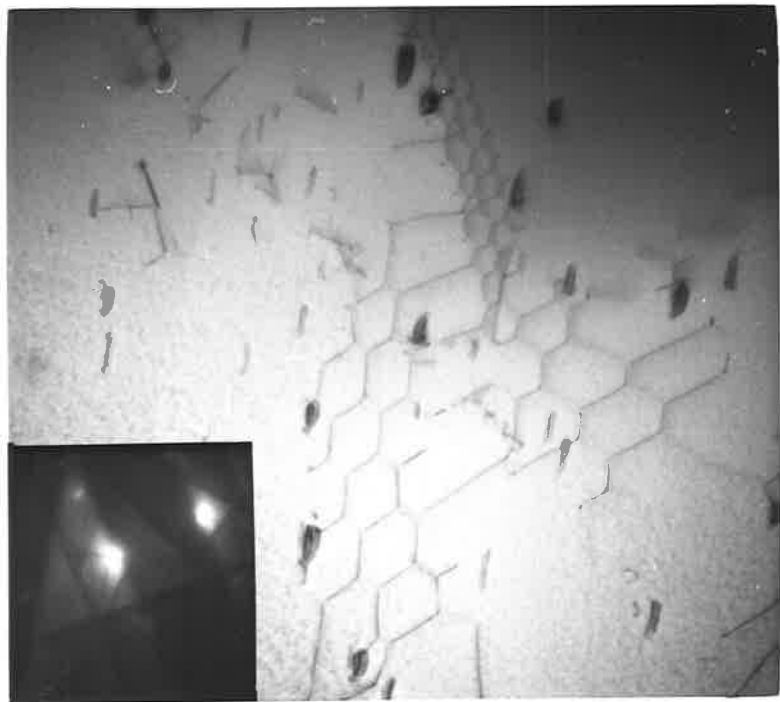
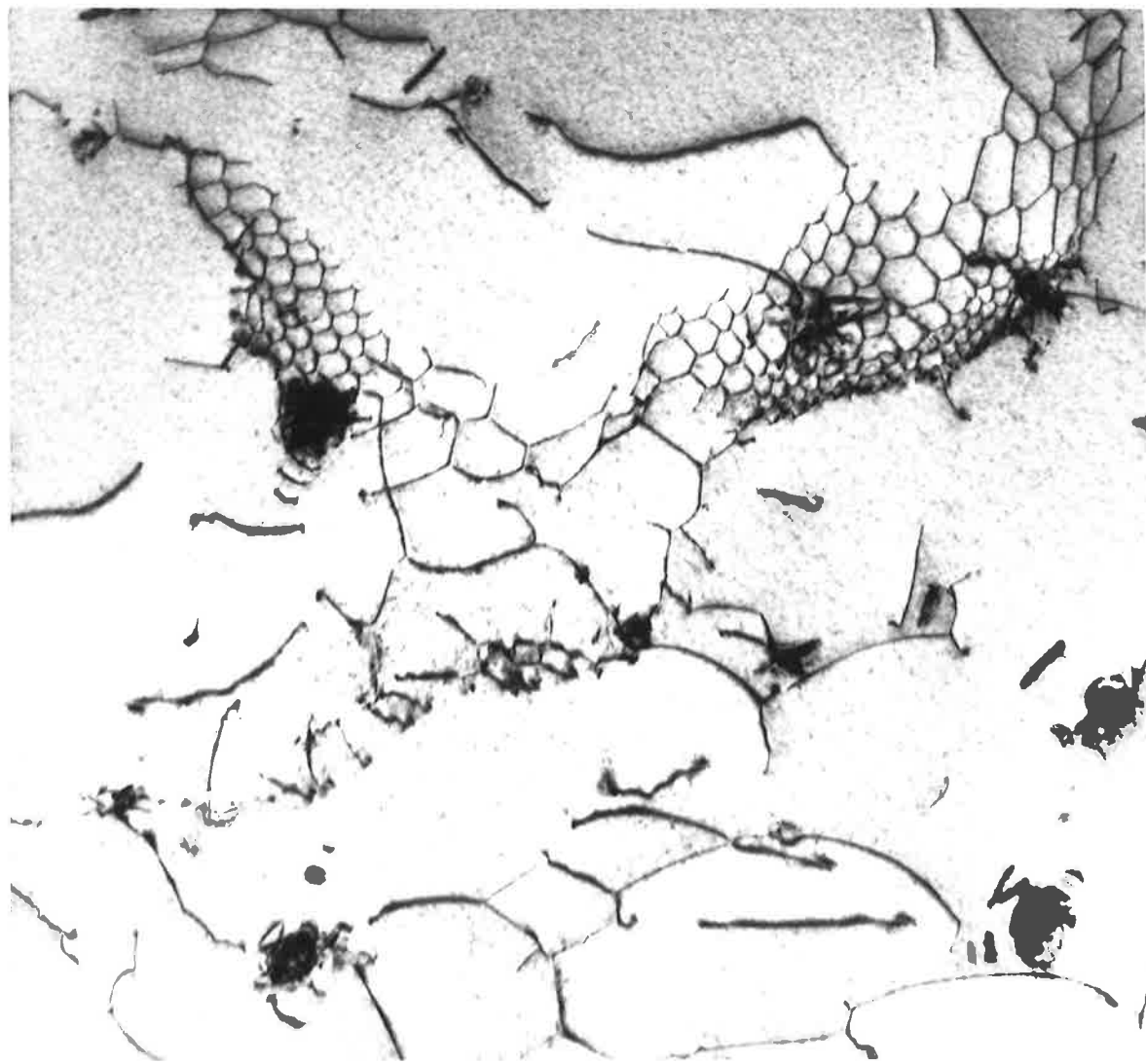


FIG. 4.69 Hexagonal network of dislocations
formed by interaction of prism and
basal dislocations.

0.5 μ



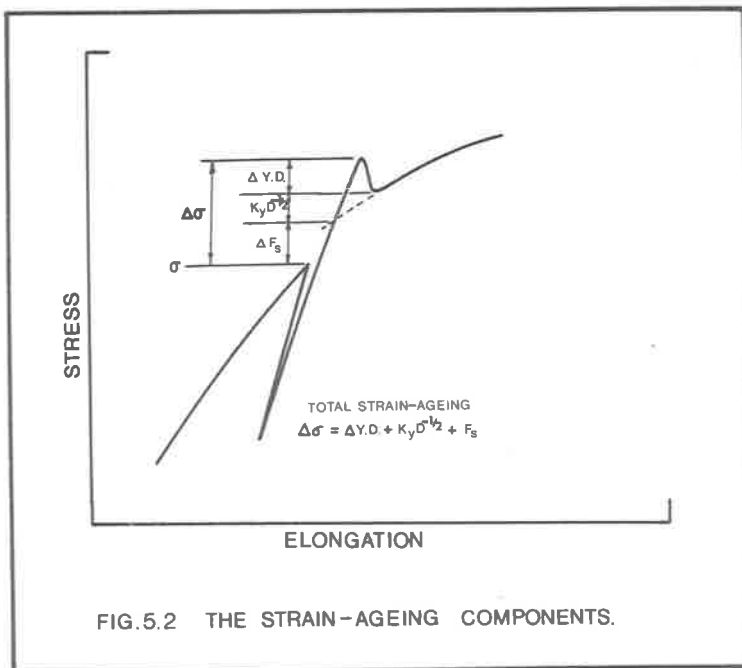
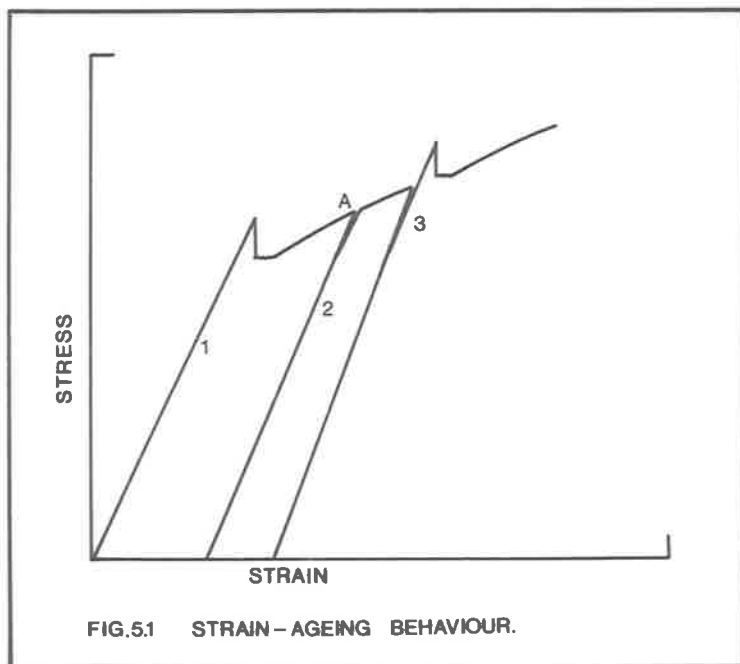


CHAPTER 5. STRAIN-AGEING BEHAVIOUR.

5.1 INTRODUCTION

The early studies of strain-ageing were centred on iron-carbon and iron-nitrogen alloys but it is now widely recognised that strain-ageing may occur in a wide range of alloys. The basic definition of strain-ageing is best presented by reference to fig. 5.1. Curve 1 is the initial tensile stress-strain curve. If the load is removed at point A and then immediately reimposed curve 2 is produced. However, if the load is removed, or reduced to a value below the flow stress, and the alloy is "aged", then on reloading a sharp yield point returns (curve 3). This phenomenon is called strain-ageing, and in the case of iron-carbon-nitrogen alloys it has been shown to be due to diffusion of interstitial carbon or nitrogen atoms to the dislocations to form "Cottrell" atmospheres which lock the dislocations.

In early work on the deformation characteristics of zirconium (Treco (1953), Keeler (1955)) a discontinuous yield point was observed. In fine grain size zirconium, Treco observed a yield point at 300°C but not at room temperature. Keeler also observed a discontinuous yield point in fine grain size zirconium which was most pronounced at temperatures approaching 200°C. In some tests at 300°C an increase in flow



stress was observed after ageing but not a transient yield point. Also a peak occurred in the elongation versus temperature curve at 200°C. Keeler suggested that these effects may have been due to some combination of strain-ageing and recovery phenomena.

Reed-Hill et al. (1969) mentioned that titanium and zirconium were known to exhibit strain-ageing behaviour in several temperature intervals and concluded that the plastic deformation was complex. Two regions in which the deformation was particularly sensitive to strain rate were present in zirconium, one occurring near 30°C and the other near 400°C. This implied that dynamic strain-ageing occurred at temperatures near those two values. No further details of the particular strain-ageing characteristics were given.

In a study of yield point occurrence in polycrystalline α -zirconium, Weinstein (1966) found that ageing did not result in the return of the yield point. This, in conjunction with the temperature dependence of yielding, led Weinstein to conclude that a Cottrell locking-unlocking mechanism did not play a dominant role in the yielding behaviour of zirconium, but instead he was able to explain his results using the Johnston-Hahn theory of yielding based on dislocation dynamics.

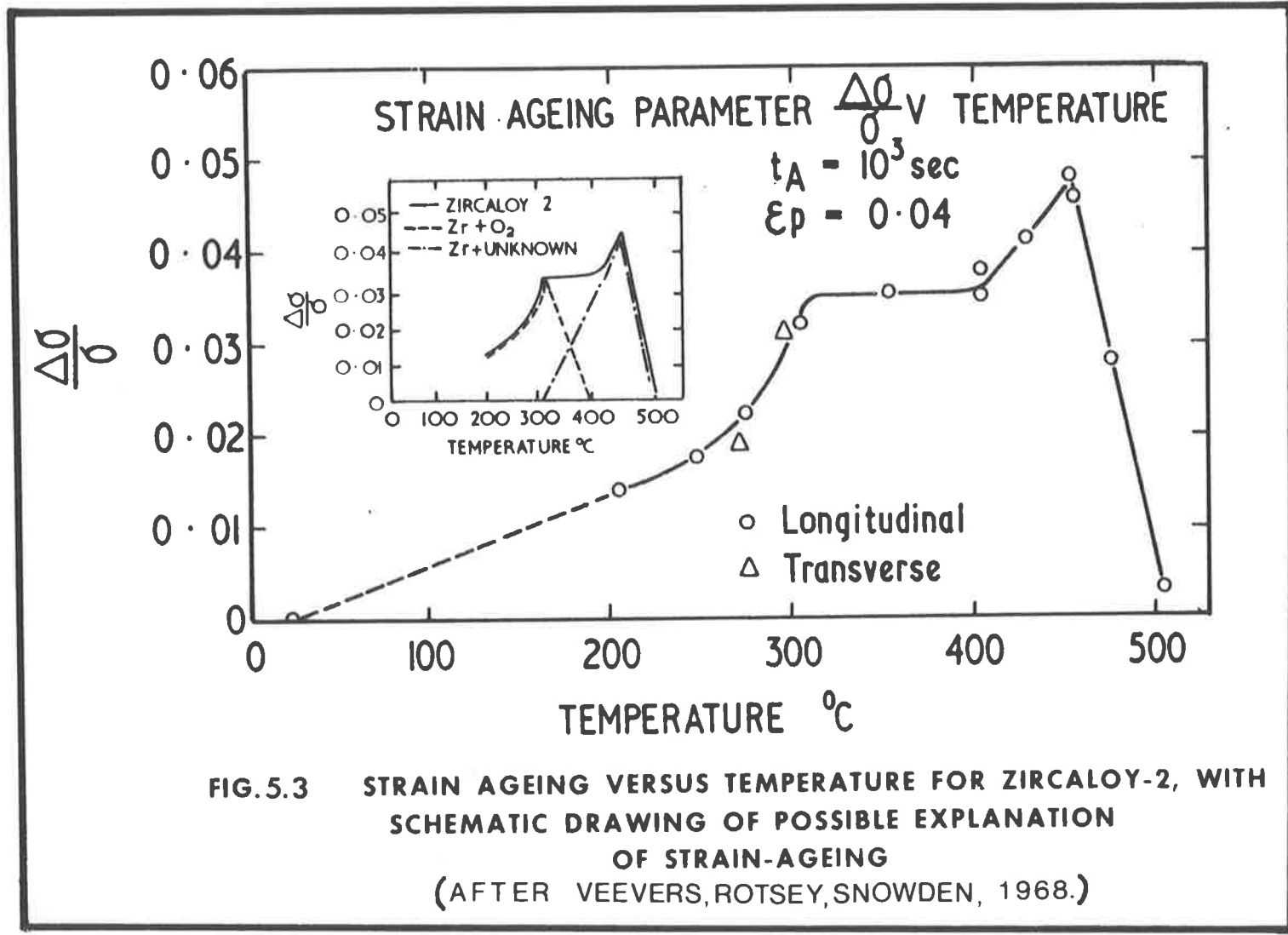
In view of the somewhat conflicting evidence regarding strain-ageing, thorough examination of the deformation

behaviour of zirconium and Zircaloy-2 have been undertaken by the Australian Atomic Energy Commission.

Most of the published work has dealt with Zircaloy-2. Rotsey and his colleagues have studied the strain-ageing behaviour of Zircaloy-2 in the unirradiated and irradiated conditions (Veevers and Rotsey (1968)). They have defined the parameters which contribute to the total strain-ageing effect as shown in fig. 5.2. The total strain-ageing behaviour for unirradiated Zircaloy-2 obtained by Veevers et al. (1968) is as shown in fig. 5.3. The significant strain-ageing behaviour at 300°C shown on that diagram was attributed to the locking of dislocations by oxygen atoms whereas the peak at 450°C was attributed to locking by an unknown element, probably iron (Rotsey et al. (1968-70)).

Irradiation of Zircaloy-2 with fast neutrons was shown to decrease and finally eliminate the strain-ageing behaviour. Locking of oxygen atoms by radiation induced defects was postulated as the possible cause of this suppression of strain-ageing.

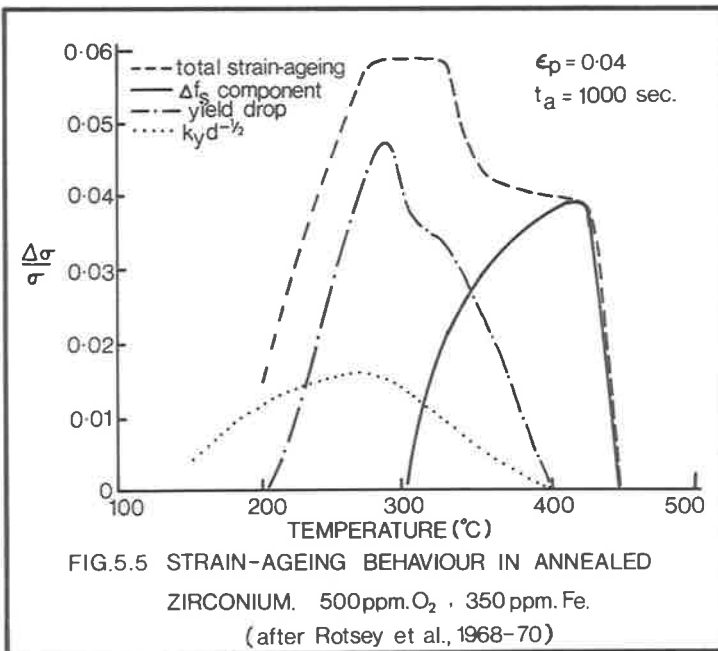
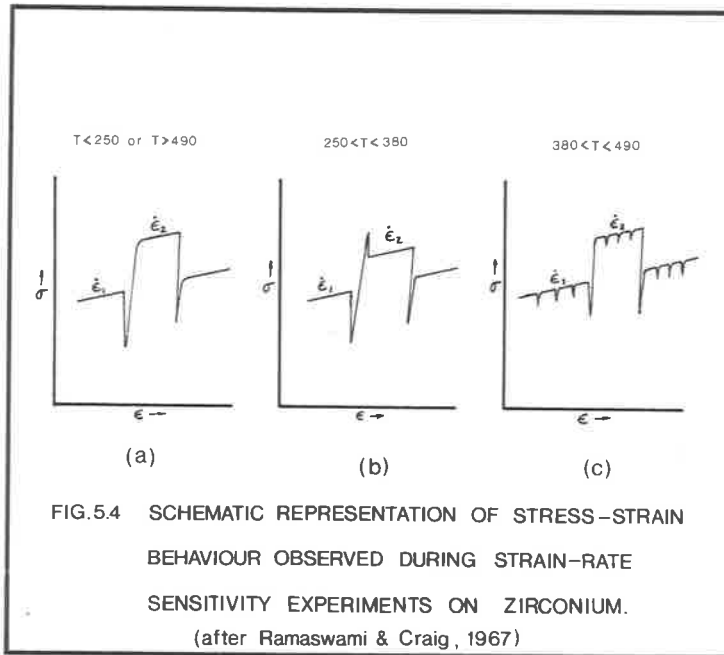
A lesser amount has been published on strain-ageing behaviour in pure zirconium. The best zirconium available commonly contains at least 50 ppm (weight) of oxygen and most experiments on high purity material have utilized zirconium containing much more oxygen than 50 ppm. In his early work,



Keeler (1955), used zirconium containing an estimated 200 ppm oxygen, but based on the hardness values given by Keeler, and using the more recent hardness versus oxygen values of Rosa (1968), the oxygen content of Keeler's material could have been as high as 300 - 1000 ppm.

In studying the thermally activated deformation of α -zirconium, Ramaswami and Craig (1967) observed strain-ageing behaviour over the temperature range 250 - 500°C. The zirconium used contained 130 - 160 ppm oxygen. Their tests involved rapid strain rate increment changes, the results of which were used to calculate activation energies. The shapes of their stress-strain curves are important from the point of view of strain-ageing phenomena in zirconium. Figure 5.4 shows the type of behaviour obtained.

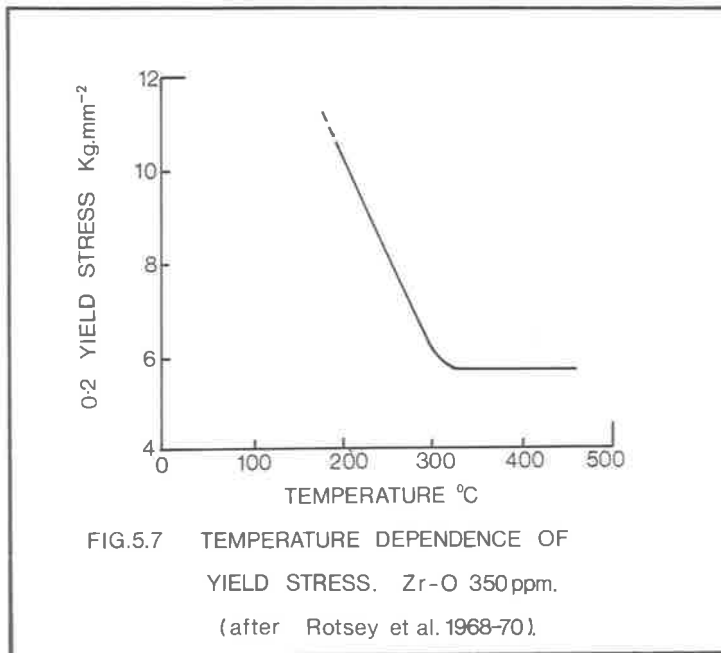
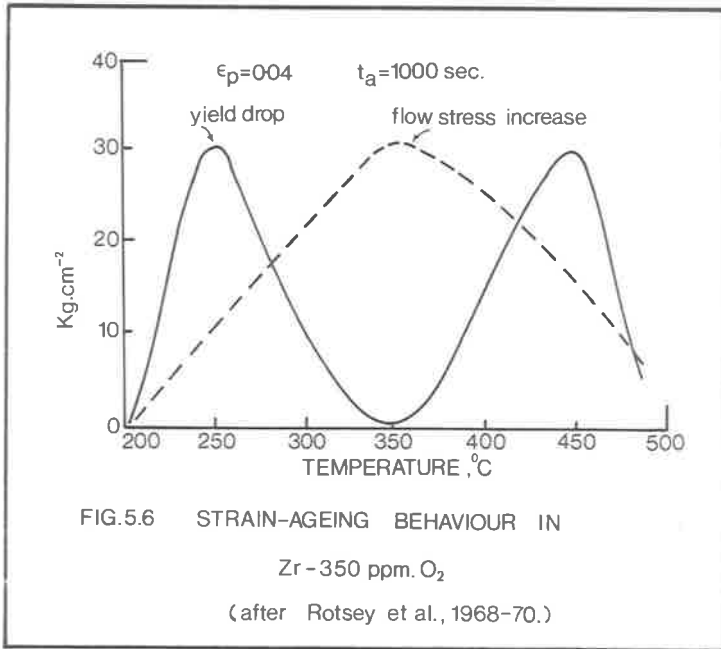
Definite discontinuous yield points were observed in the temperature range 250 - 380°C. There was only a time lapse of 15 - 20 seconds between stopping a test at one strain rate and restarting at a different strain rate. Between 380 and 490°C typical serrated yielding was observed. This has been assumed to be a dynamic effect encompassing strain-ageing, recovery and yielding effects. Ramaswami and Craig were also able to observe a yield point on ageing the specimen under load for 15 - 20 seconds and then resuming the test at the same strain rate.



Rotsey et al. (1968-70) have studied the strain-ageing behaviour of zirconium-oxygen alloys. The purest material used for a complete series of tests contained 350 ppm oxygen (hardness 85 - 90 HV10), and in addition nuclear grade zirconium containing 500 ppm oxygen and 350 ppm iron gave similar results. The overall strain-ageing behaviour for nuclear grade zirconium is shown in fig. 5.5. and it can be seen that a peak occurs at about 250 - 300°C. The results are slightly different for the purer material (350 ppm) in that a definite double peak is obtained in the yield drop component and a single peak for the flow stress component. (fig. 5.6). The addition of these curves gives a broad band of high strain-ageing behaviour from 250 - 450° C.

The yield stress behaviour at the various temperatures at which strain-ageing was studied was also plotted (fig. 5.7) for the zirconium containing 350 ppm oxygen.

From tests on zirconium-oxygen alloys containing up to 6000 ppm oxygen Rotsey et al. (1968-70) produced a plot of temperature of maximum yield drop against nominal oxygen content. This is reproduced in fig. 5.8 and it can be seen, by extrapolating the curve, that for very low oxygen contents a yield drop is still predicted. For this reason material of the highest purity available was prepared under clean conditions to produce specimens whose nominal oxygen content was 50 ppm



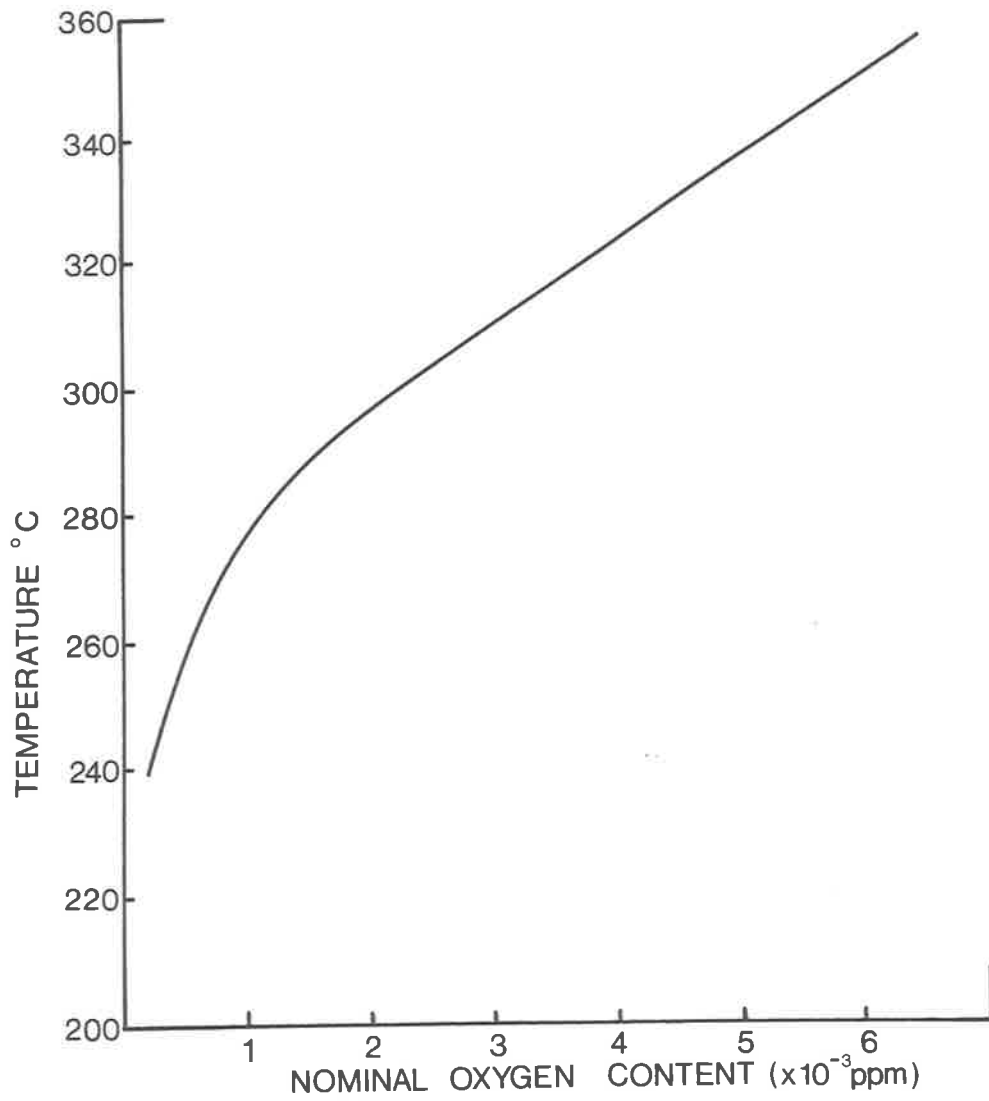


FIG.5.8 TEMPERATURE OF MAXIMUM YIELD DROP
VERSUS OXYGEN CONTENT.

(after Rotsey et al., 1969)

(hardness 65 - 70 HV10). This material had an average grain diameter of 0.3 - 0.5 mm and would not therefore show a yield point on initial straining (Keeler (1955), Weinstein (1966)).

A strain-ageing test at 250°C (Rotsey, 1969) on this high purity material resulted in a sharp yield point (fig. 5.9).

It is important to note here the conditions under which the strain-ageing tests were carried out. The experimental details have been described by Veevers et al. (1968), the relevant values being;

- (1) strain rate; $1 \times 10^{-3} \text{ sec}^{-1}$
- (2) plastic strain at initial test; 4%
- (3) Ageing time; 1000 sec.
- (4) Ageing stress; \approx 50% flow stress.

The increase obtained in the strain-ageing effect when ageing is carried out under stress has been discussed by Almond and Hull (1966) and Almond (1969). Strain-ageing was almost only observed in short time tensile tests when straining, ageing and restraining were carried out at the same temperature. The conventional behaviour for iron carbon alloys in which, for example, strain-ageing is observed in specimens strained at room temperature, aged at elevated temperatures and restrained at room temperature, was not observed in zirconium and zirconium alloys (Rotsey et al. (1968-70)).

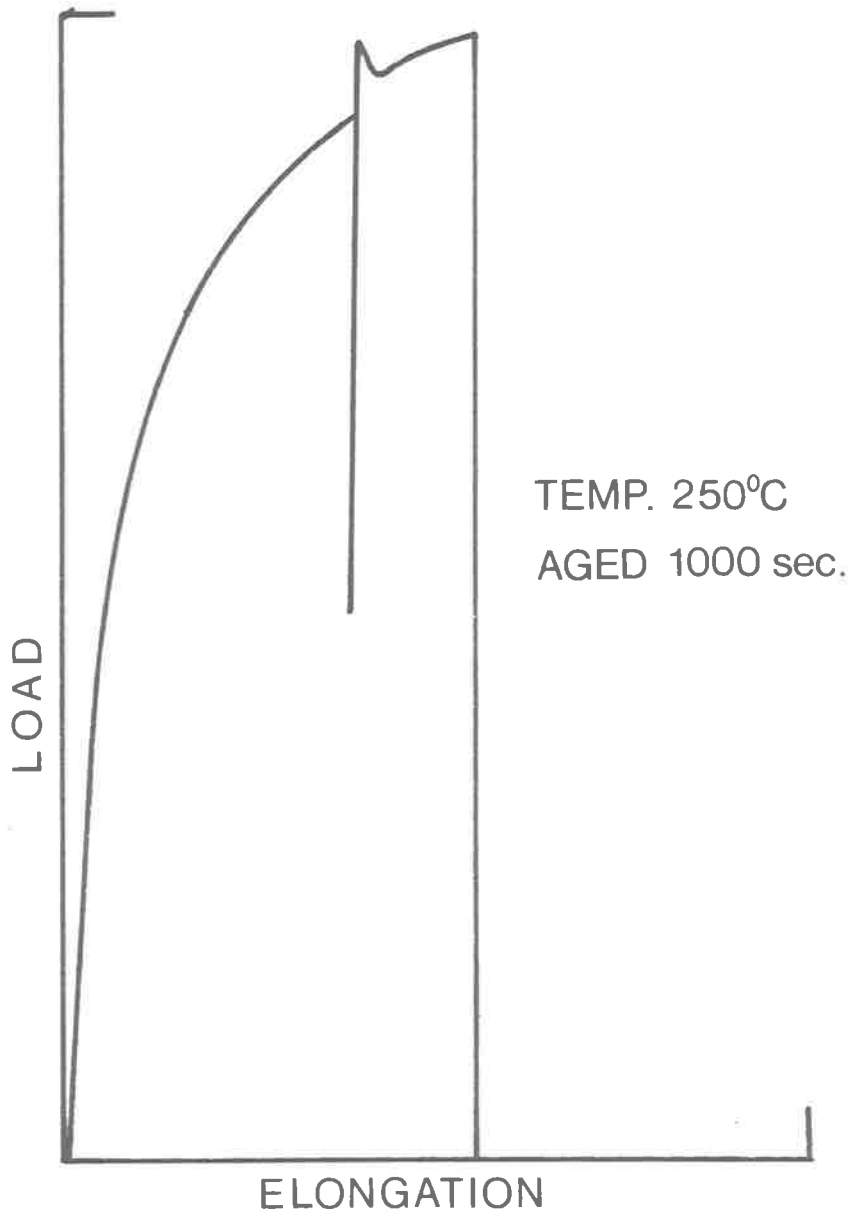


FIG.5.9 RECORDING FROM STRAIN-AGEING EXPERIMENT ON HIGH PURITY ZIRCONIUM.

In addition to the strain-ageing phenomenon observed in short time tensile tests there has been a number of reports dealing with dynamic strain-ageing of zirconium and its alloys which occur during creep experiments.

Holmes (1964) observed an activation energy peak at 350°C in a creep test at 20,000 psi and one at 250°C in a creep test at 30,000 psi. The peak was attributed to a dislocation-interstitial interaction. Fidleris (1968) observed maxima in the activation energy curves for cold worked and annealed Zircaloy-2 and concluded that since strain-ageing occurred in the temperature range in which the peaks occurred, and since continuously decreasing creep curves were evident, there was some doubt over the usefulness of activation energy curves in postulating creep mechanisms for this material.

Snowden (1969) described the creep of Zircaloy-2 at 20,000 psi by the equation $\dot{\epsilon} = \alpha \log_{10} t + \beta$ and plotted the temperature dependence of α , (fig. 5.10). An athermal region was observed between 280 and 340°C, which is the range in which strain-ageing occurs. The temperature dependence of creep rate was examined for Zircaloy-2 specimens by Fidleris (1968). Again a very low creep rate was evident in the temperature range 250 - 320°C which is the range at which the activation energy peak referred to previously occurred. The same athermal creep was obtained in zirconium containing

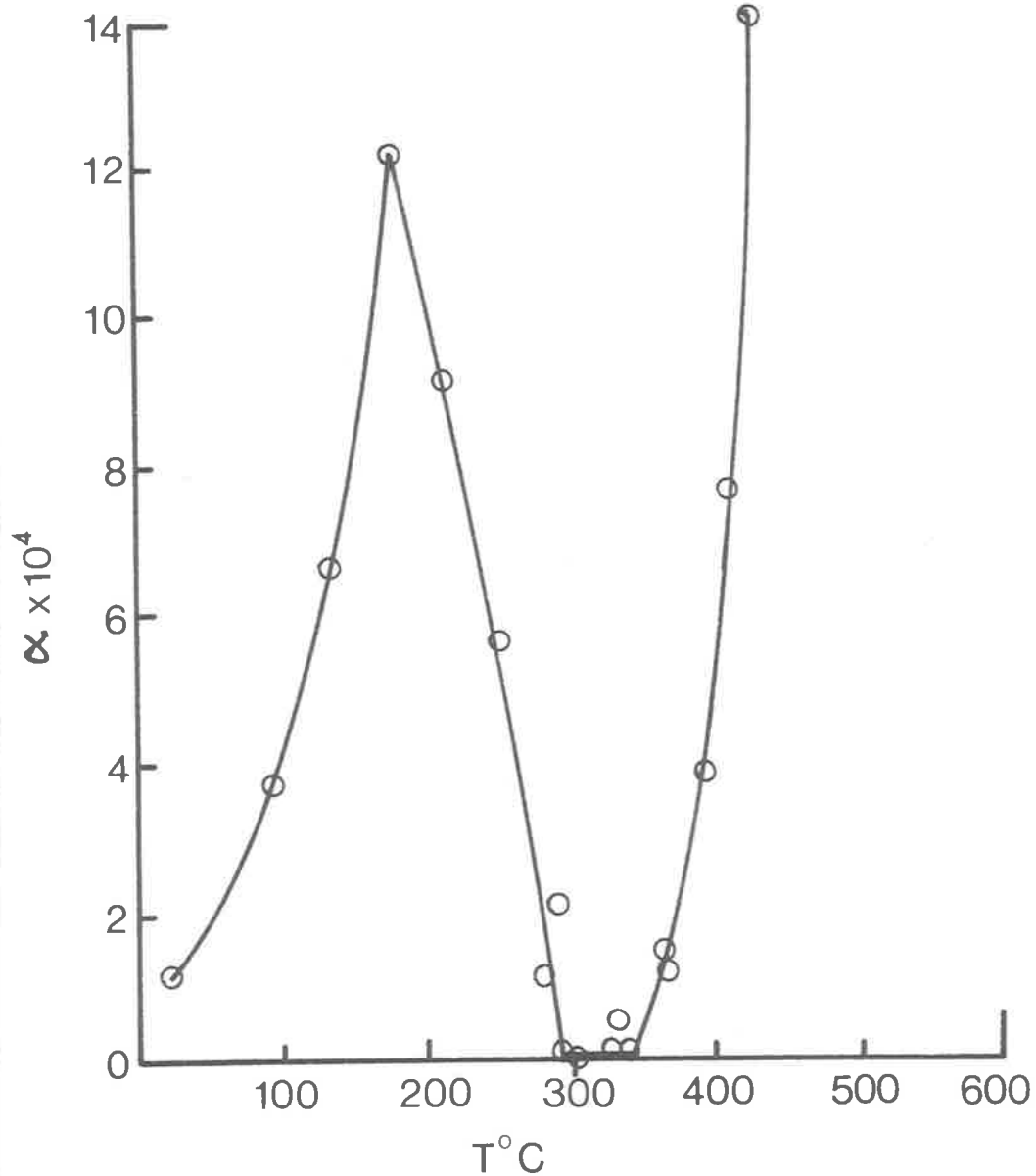


FIG.5.10 TEMPERATURE DEPENDENCE OF ALPHA (proportional to creep rate).

(AFTER SNOWDEN, 1969)

oxygen (200 ppm) and iron (170 ppm) and two activation energy peaks, one near 200°C and the other near 450°C, were observed for high purity crystal bar zirconium.

Strain-ageing can therefore not only occur in Zircaloy-2, which contains numerous alloying elements capable of locking dislocations, but can occur in high purity zirconium whose major interstitial impurity is 30 - 50 ppm oxygen. Oxygen locking of dislocations has been proposed as a mechanism of strain-ageing in zirconium but since strain-ageing only occurs under special conditions, which will be discussed later, some other mechanism, or a combination of several will probably account for the strain-ageing phenomenon.

5.2 INTERNAL FRICTION RESULTS.

Internal friction studies have been made on zirconium-oxygen alloys during a study of the movement of interstitial atoms under the influence of applied stresses, (Fuller, 1968 - 1970). The damping experiments were carried out in a low frequency inverted torsion pendulum apparatus in which the background damping was reduced to a very low level by the use of special techniques (Fuller and Ide, 1970).

The theory of internal friction distinguishes two different groups of energy dissipating mechanisms (Zener, 1948). Firstly, the anelastic mechanisms cause logarithmic

decay of free vibrations, so that a plot of log (strain-amplitude) against time is linear. Secondly, the static hysteresis processes result in non-logarithmic decay of free vibrations. These mechanisms have been reviewed by Nowick (1953) and Entwhistle (1962).

In relation to the strain-ageing phenomenon, the transition from logarithmic to non-logarithmic behaviour is particularly relevant. According to Granato and Lucke (1956) a major cause of non-logarithmic damping is the unpinning of dislocations. The strain at which unpinning begins appears as a departure from linearity on a log (strain-amplitude)/time plot for free oscillations of a torsion pendulum.

The majority of internal friction results which are reported here were obtained using zirconium wires containing 1500 ppm oxygen. The overall strain-ageing phenomenon is similar for zirconium-oxygen alloys containing from 350 - 1500 ppm oxygen (Rotsey et al. (1968-70)) and internal friction experiments carried out on high purity zirconium wires have indicated that little variation occurred over this oxygen concentration when the logarithmic to non-logarithmic transition was studied.

For annealed specimens the torsional vibrations decay logarithmically at all test temperatures between ambient and 450°C. Fig. 5.11 shows the results of tests

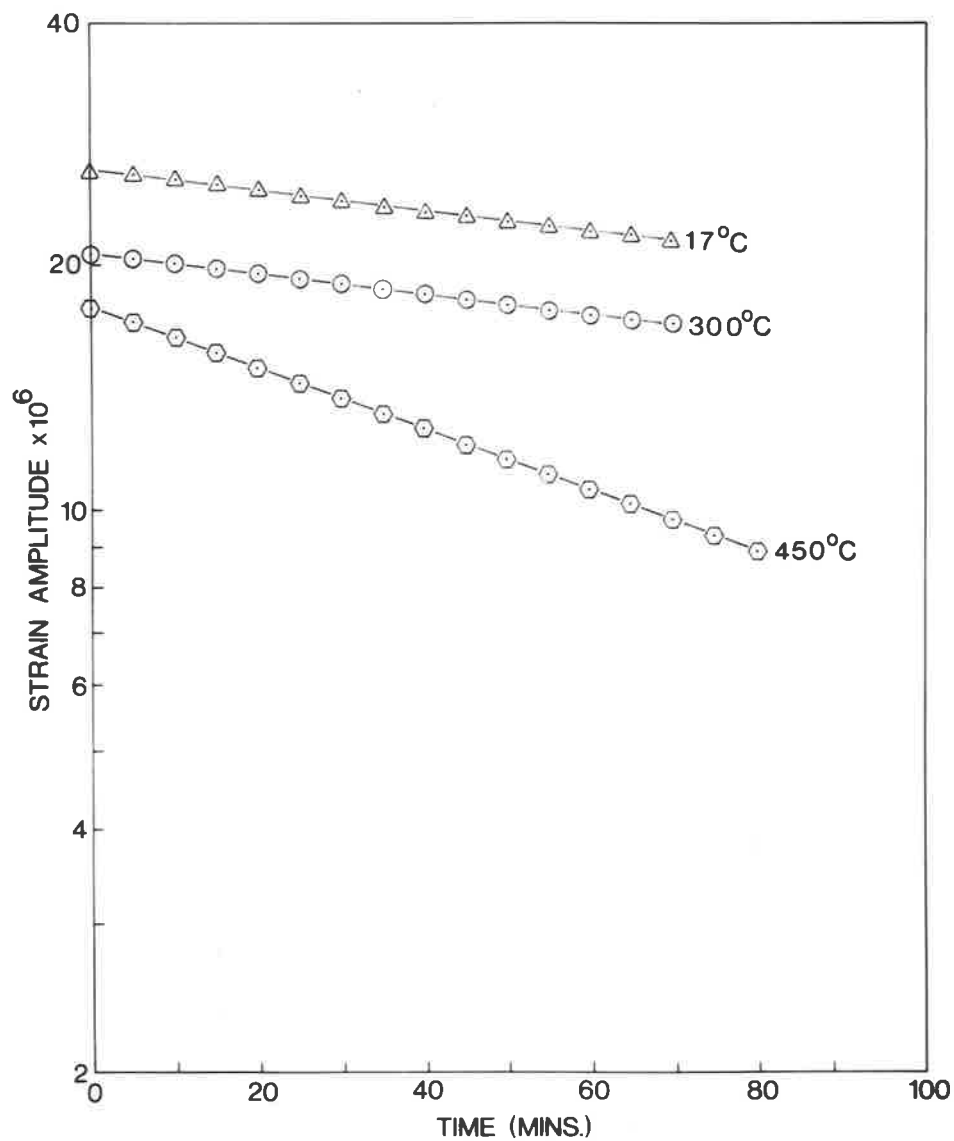
carried out at 17°C, 300°C and 450°C. A transition from logarithmic to non-logarithmic decay may occur if the wire has been deformed prior to testing. The temperature at which the deformation is performed plays a significant role in initiating the transition to non-logarithmic behaviour.

Internal friction results were obtained for wires initially deformed at temperatures of 17°C, 300°C and 450°C to a plastic strain of about 0.03. Figs. 5.12 and 5.13 show that a transition from logarithmic to non-logarithmic behaviour occurs for wires deformed at 17°C or 450°C. However, when the initial deformation was carried out at 300°C no such transition was observed, fig. 5.14.

When specimens originally deformed at 17°C or 450°C were recovered at 600°C for 3 hours, the transition from logarithmic to non-logarithmic decay was eliminated, fig. 5.15.

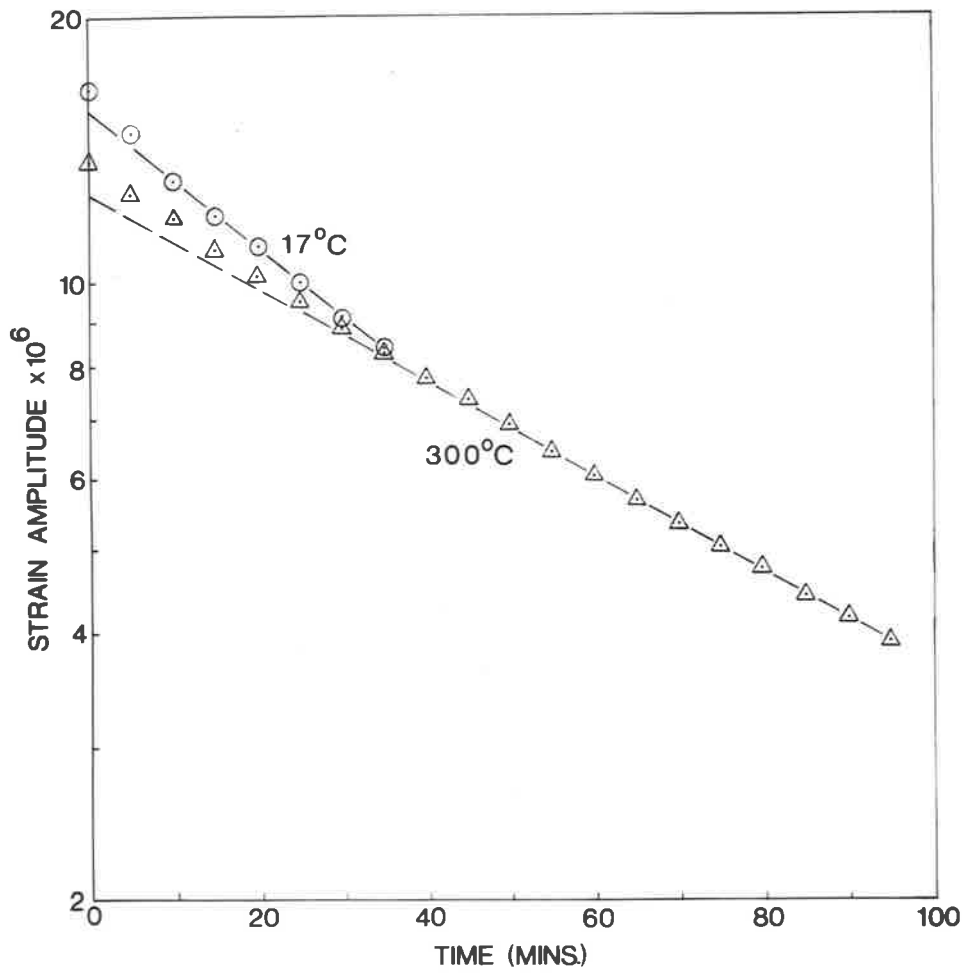
5.3 ELECTRON MICROSCOPY.

The results which have been published dealing with strain-ageing, and which were summarized in section 5.1 dealt largely with the effects of strain-ageing as shown by deformation experiments. The causes of the behaviour have been dealt with briefly by Fidleris (1968), Veevers et al. (1968) and Snowden (1969), but substantiation of the mechanical results from the point of view of dislocation behaviour



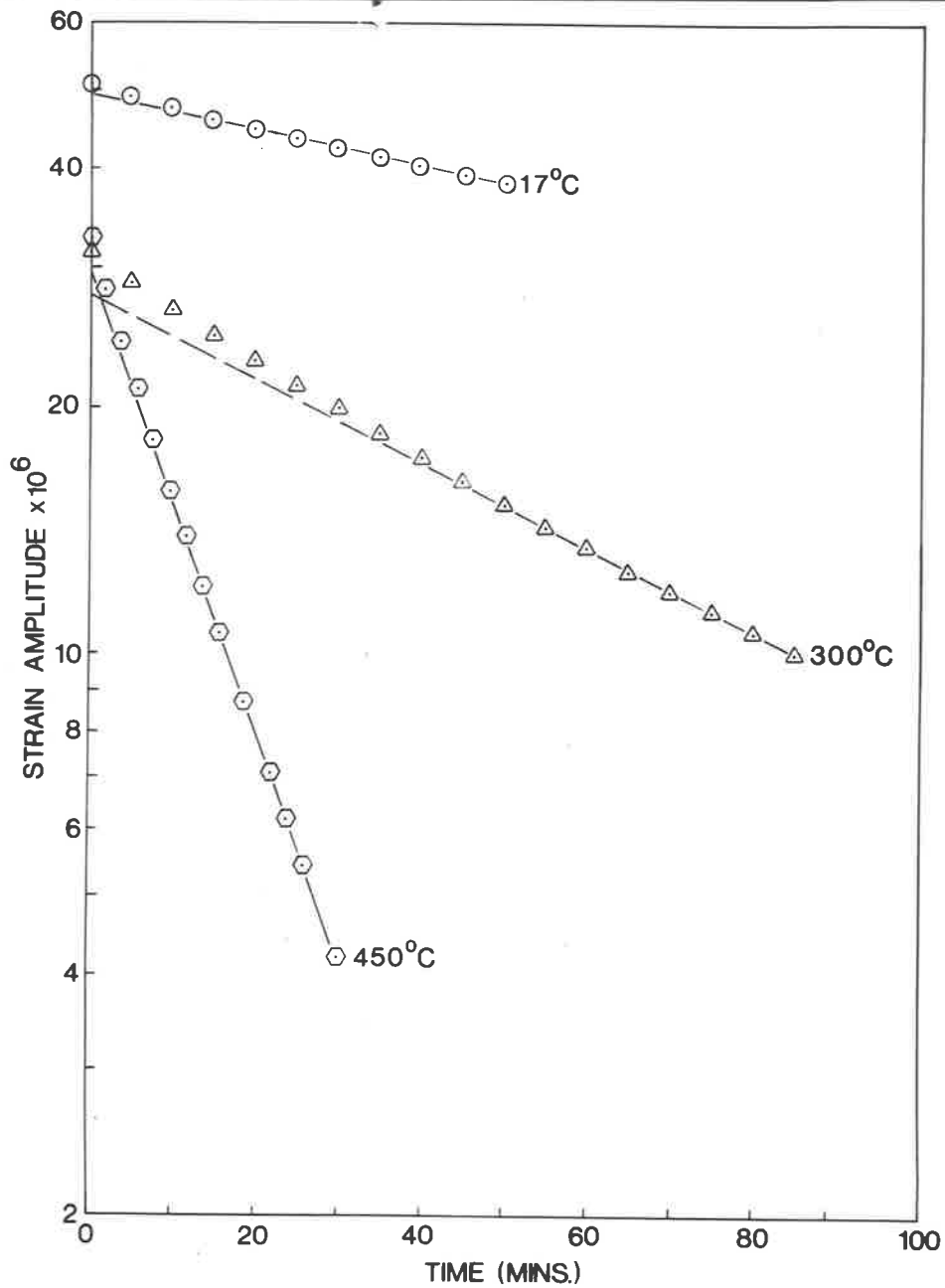
Strain-Amplitude against Time for Zirconium-Oxygen Alloys at Various Temperatures

FIG. 5.11 ANNEALED



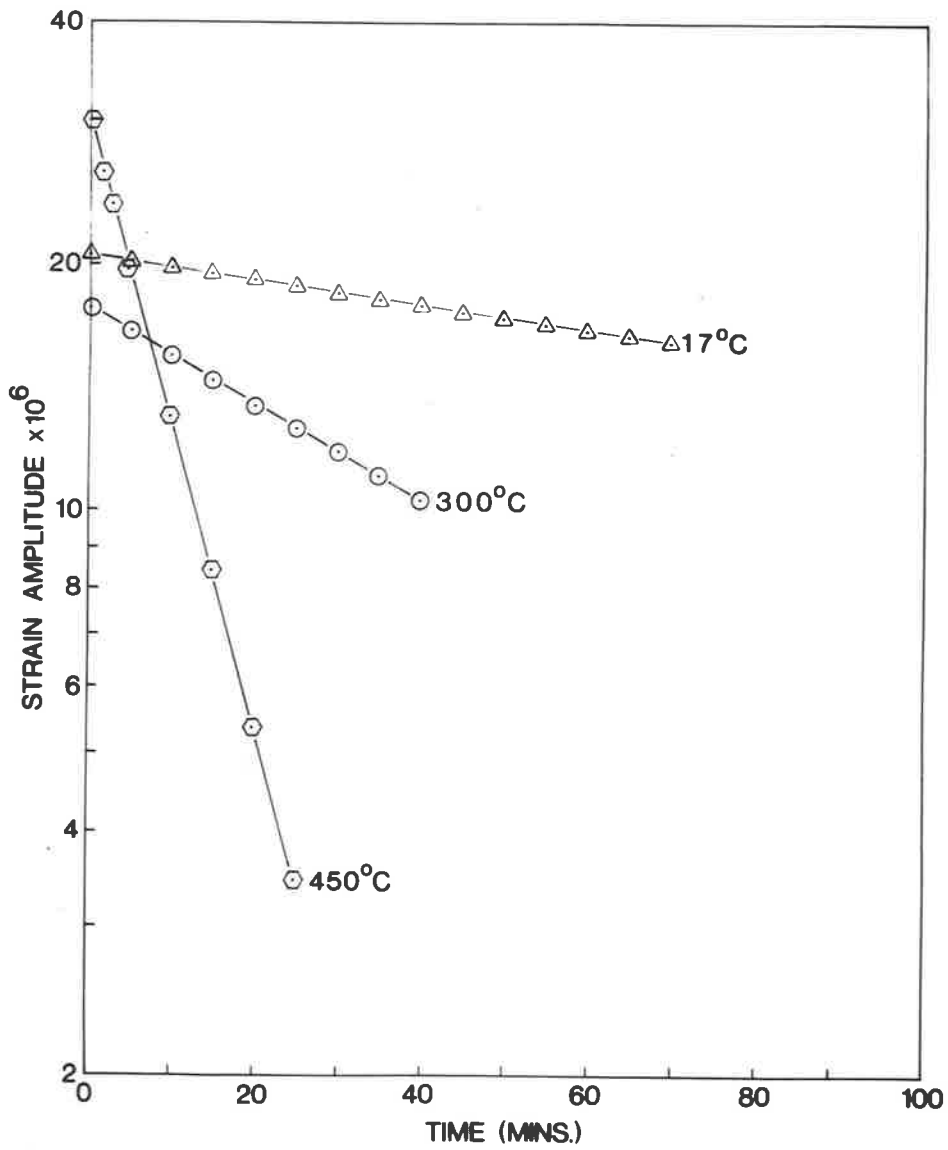
Strain-Amplitude against Time for Zirconium-Oxygen Alloys at Various Temperatures

FIG.5.12 STRAINED 0.03 at 17°C



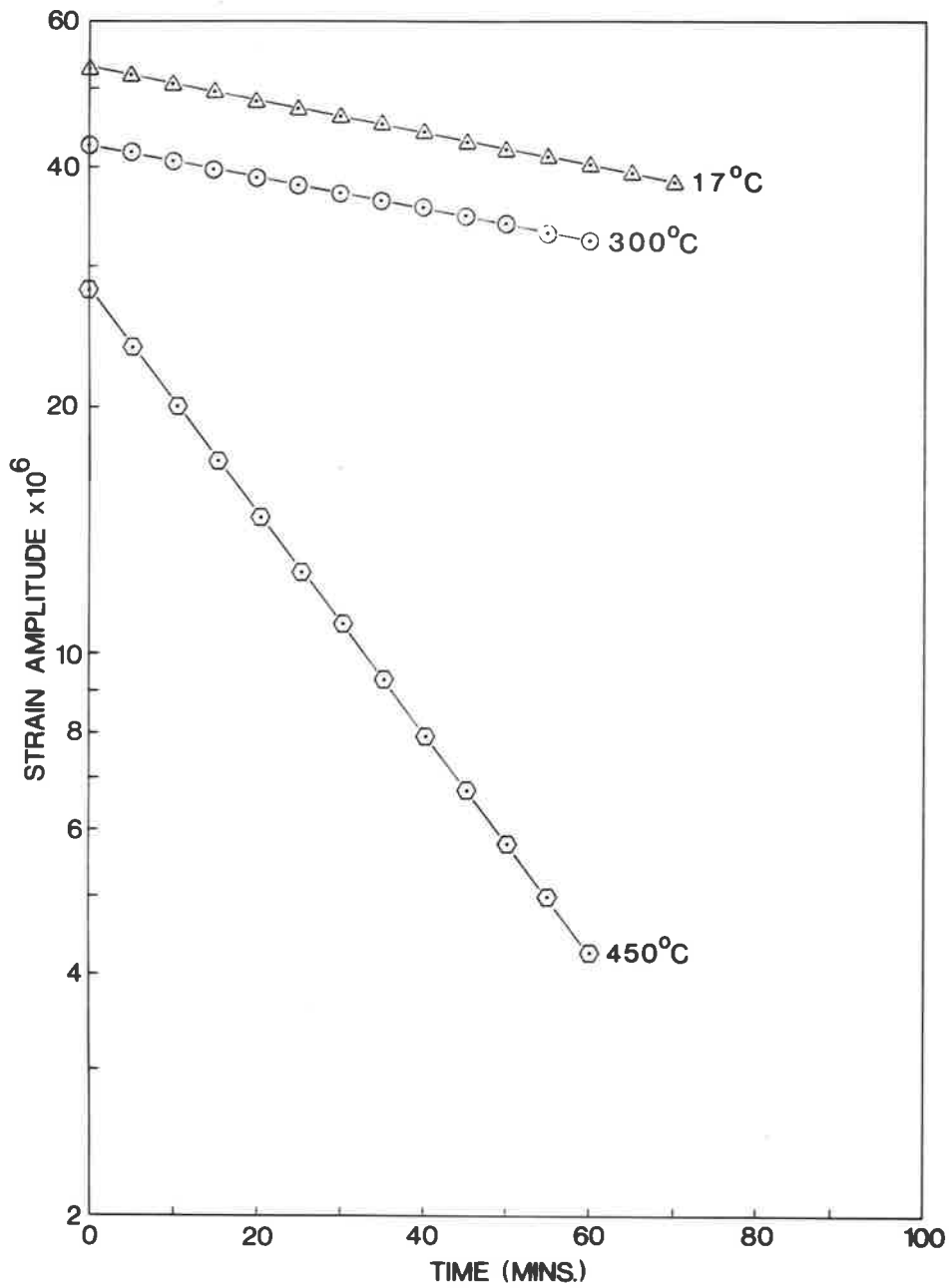
Strain-Amplitude against Time for Zirconium-Oxygen Alloys at Various Tepeatures

FIG.5.13 STRAINED 0.03 at 450°C



Strain-Amplitude against Time for Zirconium-Oxygen Alloys at Various Tepeatures

FIG.5.14 STRAINED 0.03 at 300°C



Strain-Amplitude against Time for Zirconium-Oxygen Alloys at Various Temperatures

FIG.5.15 STRAINED 0.03 at 450°C , RECOVERED at 600°C

seems incomplete. Furthermore, the internal friction work of Fuller (1968-70) required analysis of the dislocation behaviour in similarly treated material to aid in the explanation of those results. Therefore, in conjunction with the slow strain-rate tests referred to in Chapter 4, tests which could be directly correlated with the internal friction work and the strain-ageing work were carried out. From these specimens thin foils were prepared so that the dislocation substructure resulting from the various deformation and heat treatments could be examined. Specimens of coarse grained zirconium sheet (grain diameter 0.5 mm; 0.25 mm thick sheet) were strained to about 3-4% elongation at the temperatures 17°C, 250°C, 300°C, 380°C and 500°C. The strain rate was of the order $1-3 \times 10^{-3} \text{ sec}^{-1}$. In addition to these tests, results at slower strain rates at the above and other temperatures in the range 17 - 600°C were available (Chapter 4). The material used for the experiments reported in Chapter 4 was high purity (50 ppm) iodide refined crystal bar zirconium and the material used for the experiments reported in the following contained about 350 ppm oxygen.

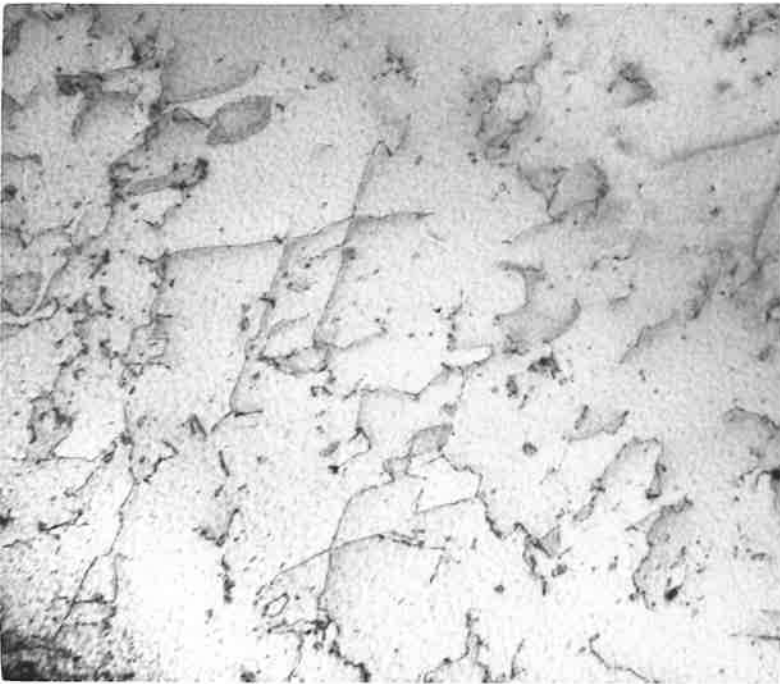
The low dislocation density associated with annealed zirconium is shown in fig. 5.16. Annealed zirconium tends to show more hydride pickup during electropolishing (section 2.2) and this is the reason for the relatively large number of hydride precipitates in this figure.

FIG. 5.16 Very few dislocations are present in
a thin foil of annealed zirconium.
Hydride pickup during electropolishing
is usually marked in such cases.

0.5 μ


FIG. 5.17 Fairly random array of dislocations
after 3% strain at 17°C.

0.5 μ

A zirconium specimen strained about 2.5% at room temperature (17°C) shows a fairly random array of dislocations fig. 5.17. After 3% strain at 250°C , dislocation tangles have begun to form, and although there are relatively large areas containing almost no dislocations, a cell type structure is only barely evident, (fig. 5.18). Fig. 5.19 shows that the dislocation cell structure is well formed in specimens strained $\approx 3\%$ at 300°C . However, in some areas the cell interiors contain a number of free dislocations, fig. 5.20, and in thicker parts of the foil or at higher strains, (fig. 5.21) the two dimensional cell structure is masked because the thicker foil allows the three-dimensional nature of the cells to be seen.

Examination of a specimen which was used in a full strain-ageing experiment at 300°C , (i.e. strained to 3% elongation, unloaded to 50% of the load at 3% elongation, aged 1000 sec, restrained) showed that many more dislocations were present within the cell interiors.

When deformed in tension to 3.5% elongation at 380°C the zirconium showed a fairly uniform array of dislocations and the many nodes which were observed (fig. 5.22) could be interpreted as indicating the early stages of dislocation network formation.

Straining at 500°C produced many more dislocation

FIG. 5.18 Poorly defined cell structure after
a strain of 3% at 250°C.

0.5 μ


FIG. 5.19 Well formed dislocation cell
structure after a strain of 3% at
300°C.

0.5 μ

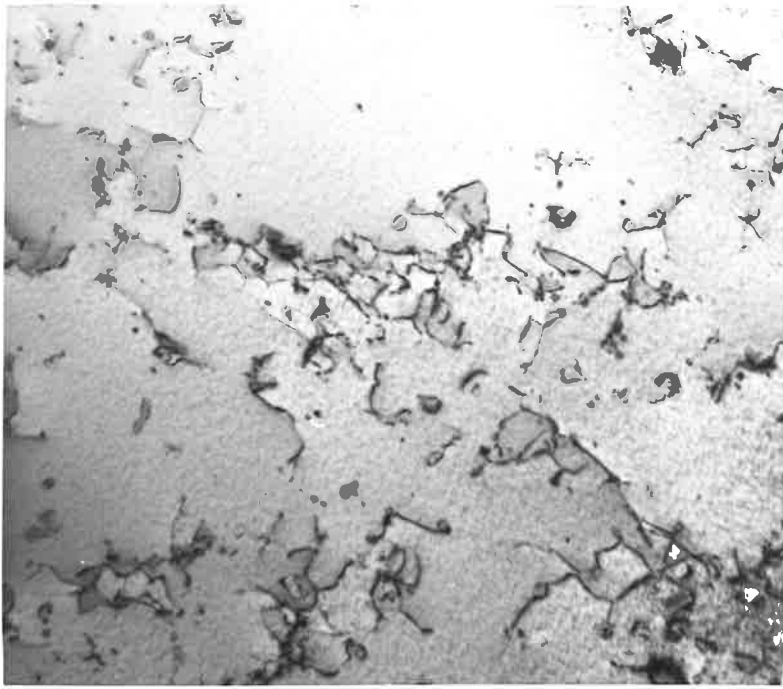



FIG. 5.20 Some areas containing free
dislocations within the cells.
Strain 0.03 Temp. 300°C.

0.5μ


FIG. 5.21 The cell structure is masked to
some extent because of its three
dimensional nature. Strain 0.07
Temp. 300°C.

0.5μ

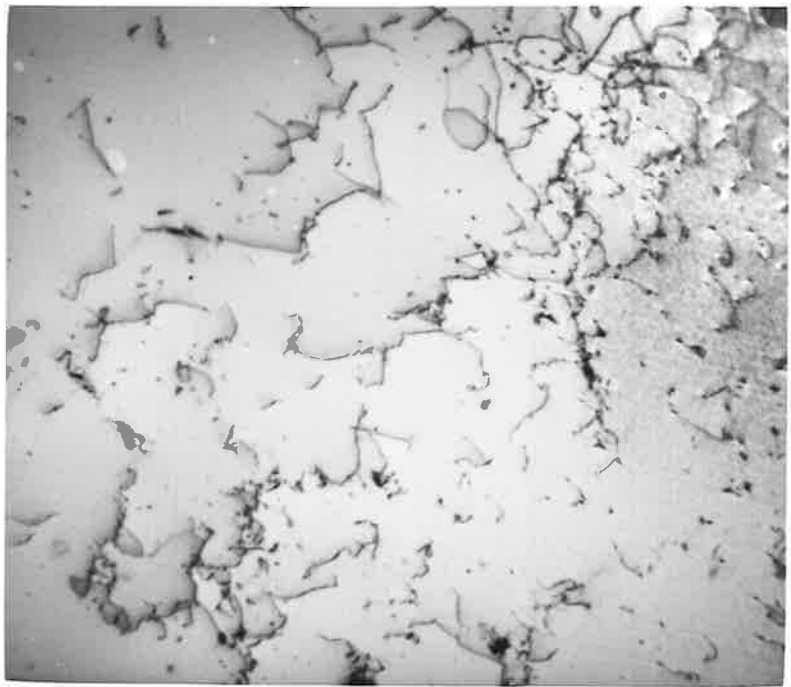
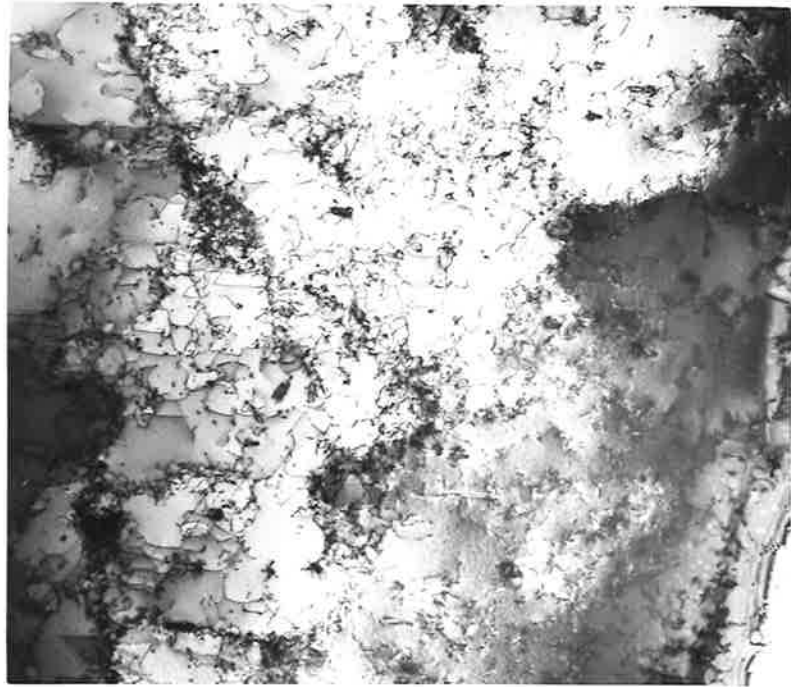
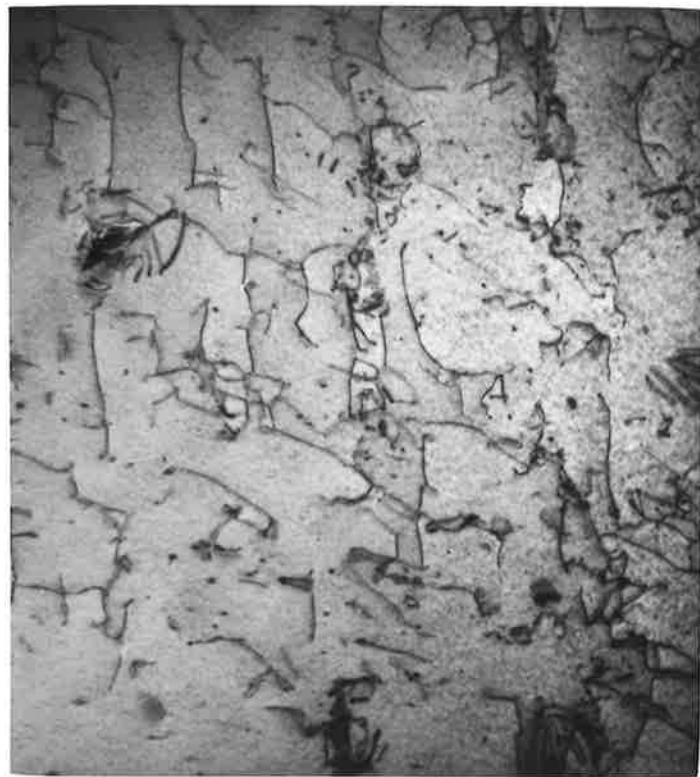
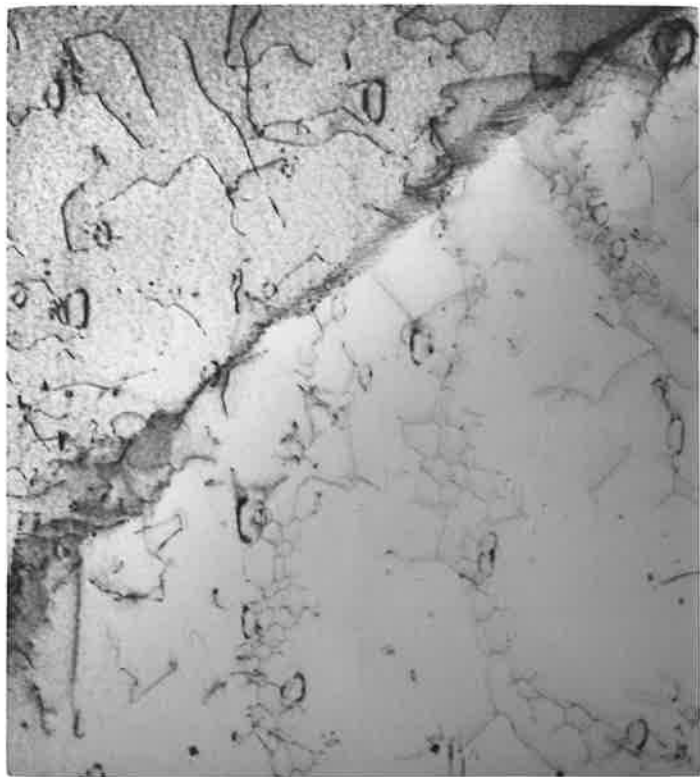



FIG. 5.22 More uniform dislocation array
containing dislocation loops and
nodes. Strain 0.035 Temp. 380°C.

0.5 μ


FIG. 5.23 Greater percentage of dislocation
networks and low angle grain
boundaries formed after 4% strain
at 500°C.

0.5 μ

networks and in general a more ordered array of dislocations, indicative of the high degree of recovery which occurs at this temperature, fig. 5.23.

Slow strain rate tests (strain rates 1×10^{-4} and $1 \times 10^{-5} \text{ sec}^{-1}$) showed a similar trend in the dislocation structures which resulted after about 3 - 4% elongation. Again the four different kinds of substructure were produced by straining in the different temperature intervals.

(1) Fig. 5.24 shows the random array of dislocations which resulted after straining at room temperature, (see also fig. 4.13).

(2) (a) At 200°C a dislocation cell structure formed when the strain rate was 10^{-5} sec^{-1} , (fig. 4.3). When the strain rate was 10^{-4} sec^{-1} the cell structure formed at temperatures nearer 250°C .

(b) At 350°C (fig. 5.25, see also fig. 4.19), a poorly defined cell structure with more ordered dislocation walls was evident. However, within these cells there was a number of free dislocations.

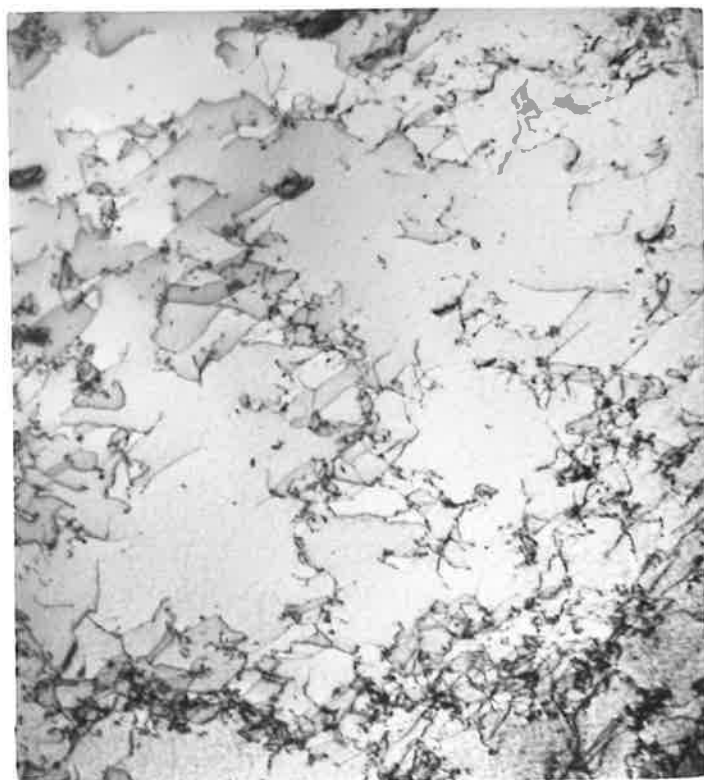
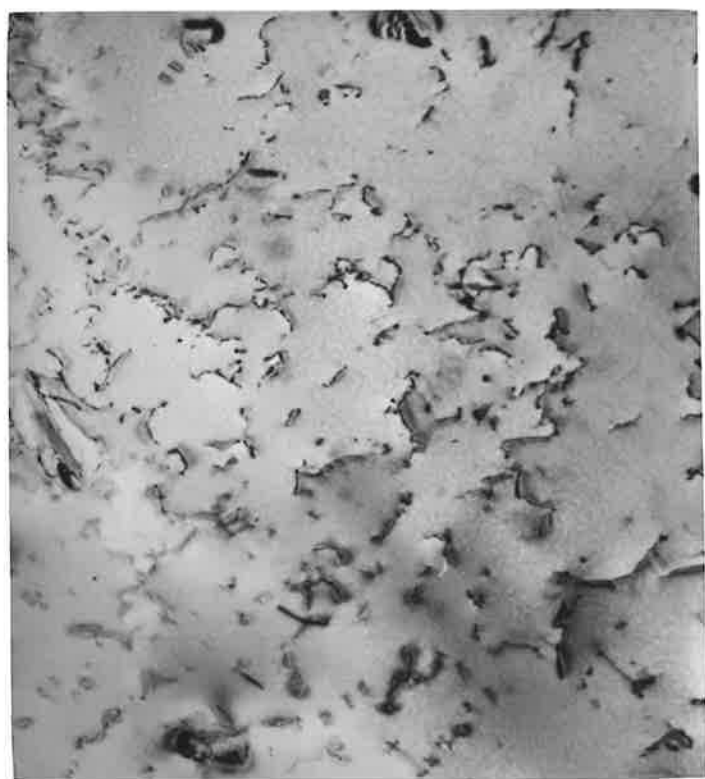
(3) A radical change occurred on straining at 400°C . Uniform dislocation arrays with three-fold nodes, formed as a result of some dislocation

FIG. 5.24 Random dislocation array which results during straining at room temperature.

0.5 μ


FIG. 5.25 Poorly defined cell structure formed during straining at 350°C.

0.5 μ

interactions and recovery, were present. (fig. 5.26, see also fig. 4.6).

(4) Hexagonal dislocation networks and polygonized arrays of dislocations were observed after straining at 500°C, (fig. 5.27, see also figs. 4.7 and 4.8).

The dislocation structure behaved in a similar manner in zirconium specimens which contained 350 ppm oxygen and which were strained at a rate of 10^{-3} sec^{-1} . These specimens were of the same shape as those used by Veevers et al. (1968) and were strained to 2 or 3% elongation*. Grain diameter of these specimens was approximately 0.05 mm. The dislocation cell structure was evident after straining at 200 and 250°C, figs. 5.28 and 5.29 (further evidence for the formation of the cell structure was obtained by straining a very fine grained specimen, 0.02 mm grain diameter, of the shape given in Chapter 2, at a strain rate of 10^{-4} sec^{-1} at 250°C. The resultant well formed dislocation cell structure is shown by fig. 5.30). After straining at 300°C the cell structure was less clearly defined and a more uniform distribution of dislocations containing many three-fold nodes and dislocation loops was present after straining at 350°, 400°, and 500°C, figs. 5.31 and 5.32).

* These tests were carried out at the A.A.E.C. Research Establishment, Lucas Heights.

FIG. 5.26 Uniform dislocation array. Three-fold nodes are present. Dislocation loops and dipoles can be seen. Strain 0.02 Temp. 400°C.

0.5 μ


FIG. 5.27 Hexagonal networks of dislocations and low angle grain boundaries formed during straining at 500°C.

0.5 μ

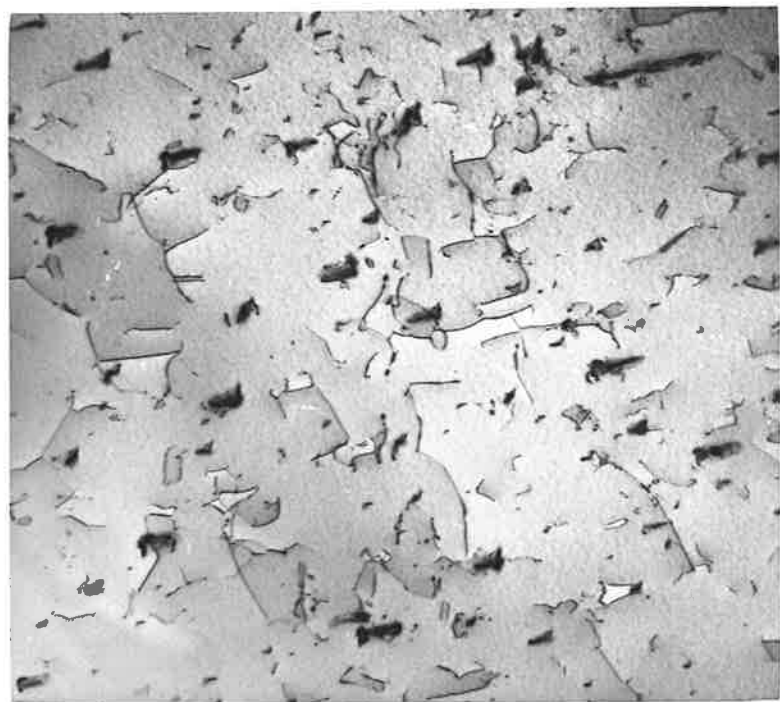
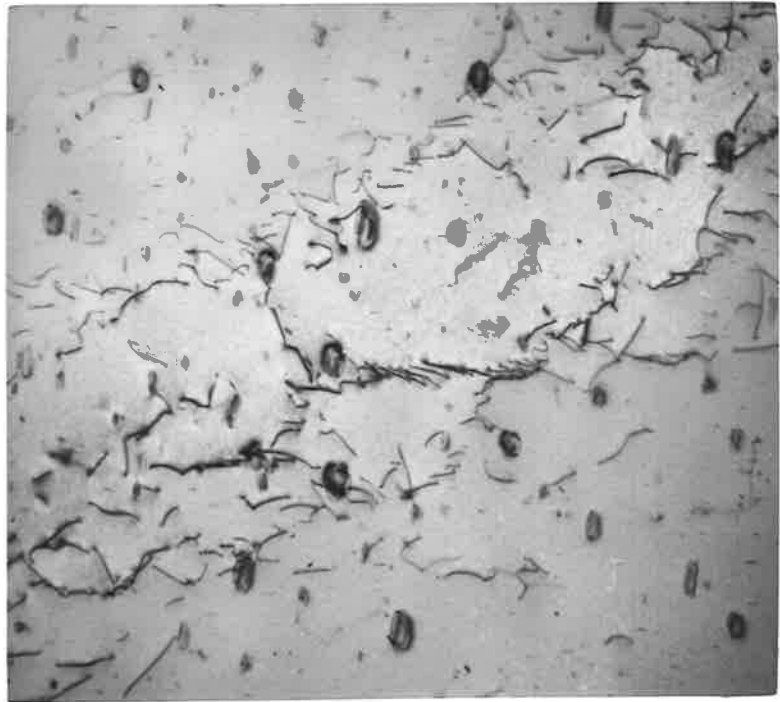



FIG. 5.28 Dislocation cell structure formed during straining of thicker specimens at 200°C. Strain rate 10^{-3} sec^{-1} , strain 0.02.

0.5μ


FIG. 5.29 Dislocation cell structure after strain at 250°C, Conditions as for Fig. 5.28

0.5μ

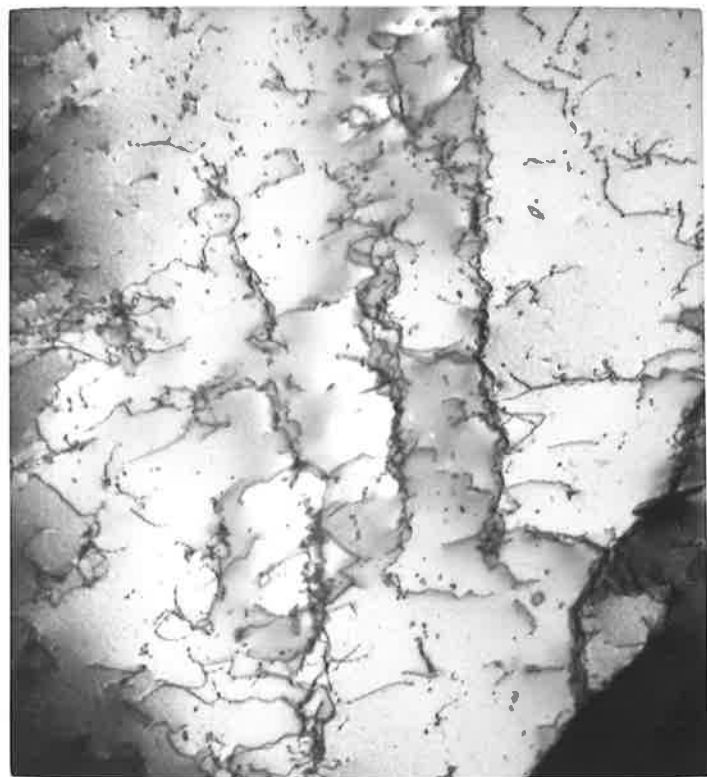



FIG. 5.30 Stereo-electron micrographs showing (a) and (b); dislocation cell structure in specimen deformed at 250°C Tilt axis parallel to $g(0\bar{1}1)$

0.5 μ

A horizontal scale bar with a double-headed arrow at each end, indicating a length of 0.5 micrometers.

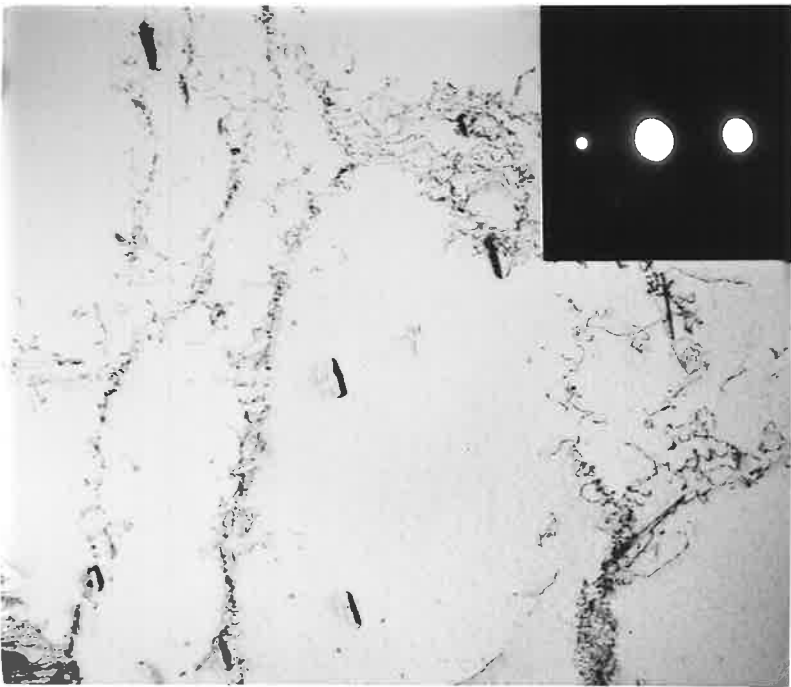
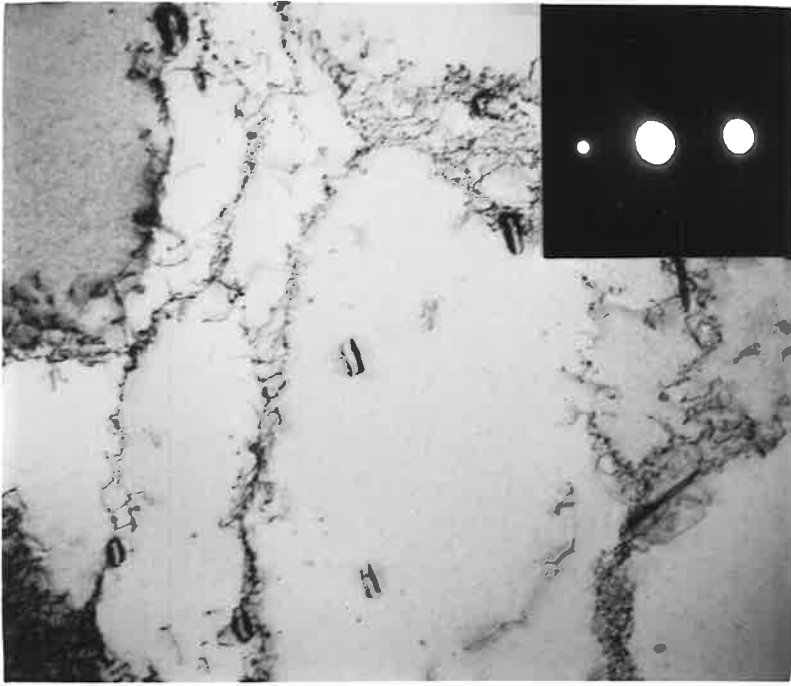
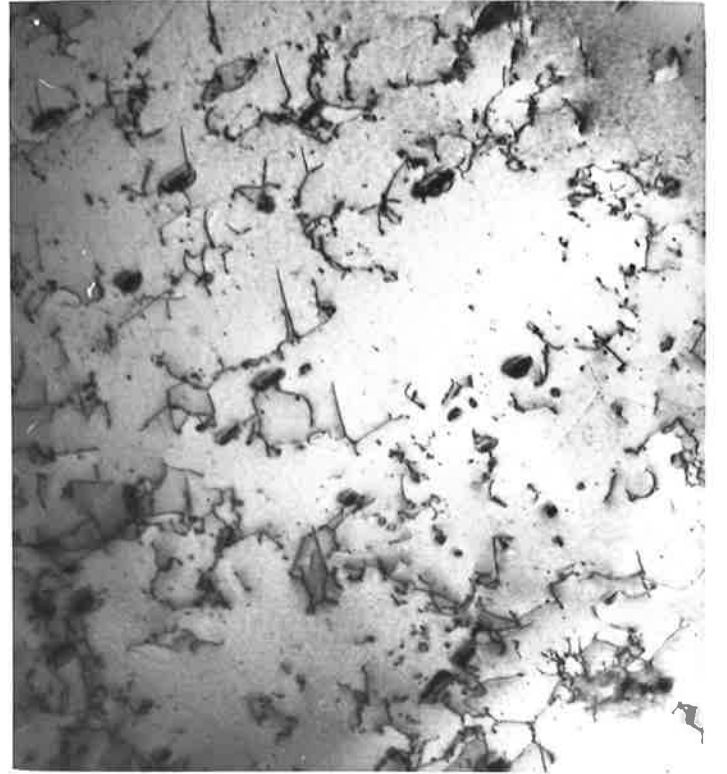
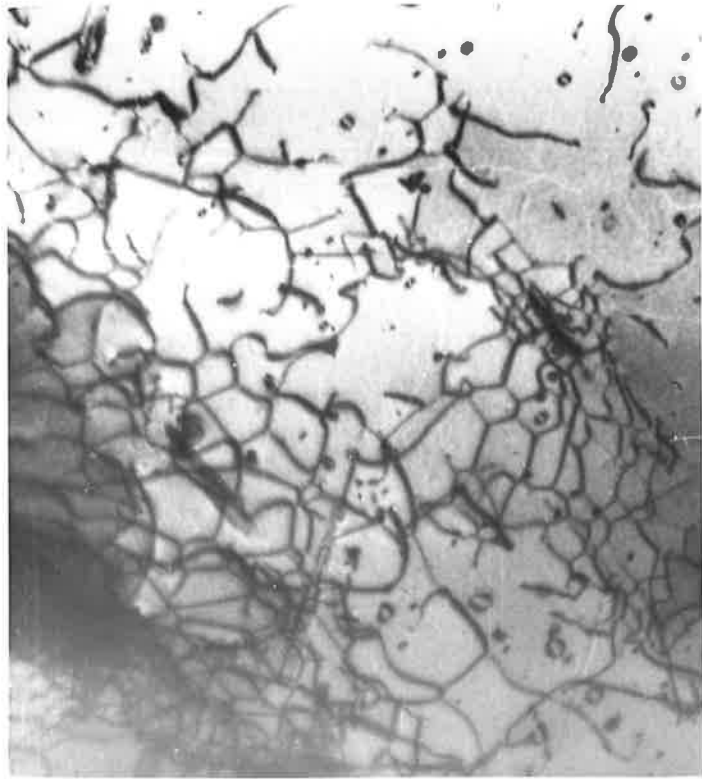


FIG. 5.31 Dislocation Structure formed during straining at 350°C.

0.5μ


FIG. 5.32 Dislocation Structure formed during straining at 450°C.

0.5μ

5.4 DISCUSSION OF STRAIN-AGEING IN ZIRCONIUM.

Two main avenues of approach have been followed to explain discontinuous yielding phenomena. They are the classical dislocation pinning theory of Cottrell and the Gilman-Johnston, and Hahn, theory based on dislocation dynamics.

Cottrell originally proposed that the grown-in dislocations in a b.c.c. metal were locked by an atmosphere formed by impurity atoms and that upon straining, the dislocations remained pinned up to the upper yield point. At this stress the dislocations were able to break free from their atmospheres and the resultant rapid strain caused a drop in the stress.

The dislocation dynamic theory for yielding in b.c.c. metals was explained by Hahn (1962). The abrupt yield point was a consequence of an initial presence of a small number of mobile dislocations, a rapid dislocation multiplication rate, and a stress dependence of dislocation velocity. As the upper yield point was approached the few free dislocations moved rapidly and multiplication occurred at such a rate that the strain rate increased and reduced the stress on the specimens.

Obviously the above are very simplified explanations of the original theories but this was included because the more modern theories of yielding tend to combine these theories

to give a much more attractive account of discontinuous yielding behaviour.

In examining the yield point and work hardening behaviour in b.c.c. metals Conrad (1963) suggested that the yield point was not due to the thermally assisted unpinning of dislocations from their interstitial atmospheres but rather resulted from the sudden multiplication of dislocations by the double cross slip mechanism. This was favoured on the evidence gained from the observations of precipitate pinning of dislocations in annealed metal, as opposed to atmosphere pinning, and the fact that yielding produced a significant increase in dislocation density in iron.

At the same time Cottrell (1963) modified the atmosphere approach to make it much more compatible with results that had been obtained. It was accepted that discontinuous yielding occurred as a result of the release or production of a large number of dislocations at the upper yield point. In the elastic region of the stress-strain curve dislocations were held motionless by some means, this pinning being either weak or strong. For weak pinning, some dislocations were unpinned at the upper yield point and moved at high velocities. These dislocations were able to multiply extremely rapidly either by a Frank-Read mechanism or by the Multiple Cross Glide mechanism. Thus discontinuous

yielding was produced. On the other hand, strongly pinned dislocations remained pinned at the upper yield stress and new dislocations were created at stress concentrations. Again these dislocations rapidly multiplied and caused a yield drop.

Another mechanism due to Crussard (1963) involved the use of parts of both the Cottrell and the dislocation dynamic theories. It was considered that before a yield point occurred a few grain boundaries or inclusions acted as dislocation sources by a thermally activated mechanism. These dislocations tended to build up along grain boundaries and thus produced stress concentrations which could initiate slip in neighbouring grains. Rapid multiplication of dislocations resulted as the stress was increased and a yield drop would occur. This interpretation is supported by observations of dislocation cell and tangle pile-ups or concentrations occurring more often at grain boundaries than in the grain interiors, in the present work on deformed zirconium.

Therefore, it is apparent that to observe a discontinuous yield point, either on initial or subsequent straining, the dislocations present prior to straining must be effectively locked by some mechanism. One of the possible mechanisms is pinning by interstitial or other solute atoms. In addition to this, several other kinds of dislocation locking mechanisms are possible (Hull, 1968). It is also

apparent that the behaviour of dislocations at, and after, the upper yield stress is complicated and may involve a combination of effects (see for example Wilson and Russel (1960 a,b) Gilman and Johnson (1962), Edington et al.(1964), Rosinger et al. (1969-70)).

For strain-ageing to occur in zirconium a unique sequence of deformation procedures is required. An abrupt yield point can only be observed when ;

- (1) A specimen is plastically deformed (up to about 4% strain in the tests referred to in the present work) at a temperature T, in the range 200 - 400°C.
- (2) The specimen is then aged at this same temperature T.
- (3) The specimen is restrained; again at this temperature T.

Only a fairly small variation in the temperature, T, at any one of these steps can be tolerated.

The behaviour cannot, therefore, be explained on the basis of a Cottrell locking mechanism alone. If such a mechanism was responsible then a specimen would show an abrupt yield point after straining at room temperature, ageing at a high temperature (say 250°C) and then restraining at room temperature. This does not occur and so special and unique

conditions must be created by straining at temperatures within the range 200-400°C prior to ageing and restraining. The internal friction results, quoted in section 5.2, can also throw light on this behaviour.

Free dislocation motion may be delineated with the internal friction technique. As discussed previously, if a yield point is to be observed, the dislocations must remain essentially pinned right up to the yield point. Conversely, if significant amounts of free dislocation motion occur at stress levels below the yield stress the sharp yield point would not be observed. The onset of free dislocation motion, which follows unpinning, can be identified by a deviation from logarithmic decay.

Non-logarithmic decay was observed, at the stress levels imposed on the material during damping experiments, in zirconium wires which had been deformed approximately 3% at 17°C and 450°C. The transition from logarithmic to non-logarithmic decay occurred at each of the test temperatures used. (figs. 5.12, 5.13). This means that free dislocation motion occurs at the very low stresses applied during the internal friction measurements and it would therefore be expected that no sharp yield point would result when the material was tested in a tensile test. This was, in fact, the case.

In the specimens which were deformed at 300°C only

logarithmic damping was observed at each of the test temperatures up to a strain amplitude of 3×10^{-5} , (fig. 5.14). This indicates that up to the corresponding stress level the dislocations remain pinned so that it can be suggested that a sharp yield point may occur. As this stress level was well below the yield stress the possibility still exists that unpinning of the dislocations may occur somewhere between this stress and the yield stress. However, the fact that a sharp yield point occurred in experiments conducted by Rotsey et al. (1968-70) on material which had undergone the same deformation and heat treatment, suggests that the pinning is maintained right up to the yield stress.

The question then remaining is, why the dislocations are strongly pinned only when a specimen is initially deformed near 300°C while deformation at either lower or higher temperatures allows dislocation breakaway to take place? It must be again noted that the particular temperatures referred to for the internal friction work correspond to a zirconium-oxygen (1500 ppm weight) alloy, and that the maximum strain-ageing behaviour was obtained near 300°C for this alloy. For purer zirconium the maximum strain-ageing behaviour also occurred at similar temperatures (about 250°C) and internal friction results on this pure material supported the above evidence (Fuller 1968-70).

An explanation of the pinning mechanism can be obtained from the electron microscope observations. The structure which resists unpinning (3-4% strain at 250-300°C) consists of a well defined cellular substructure in which the cell walls are made up of complex tangles of dislocations and the cell interiors are relatively dislocation free. Figs. 5.30 (a) and (b) constitute a stereo-pair of the cellular structure. It can be seen that the three dimensional array is very complex and would indicate quite strong dislocation - dislocation interaction locking. It is therefore suggested that a combination of this locking, and locking by interstitial atom atmospheres (oxygen), results in strong pinning of the dislocations and thus establishes the pre-requisite conditions for the appearance of an abrupt yield point.

On deforming at lower temperatures, pure zirconium and low oxygen alloys contain not a well established cellular array of dislocations which are very strongly locked as a result of interactions with one another, but instead a relatively uniform array in which this strong dislocation interaction type locking is not present. Although these dislocations may be weakly pinned by oxygen atoms, strong pinning of the kind which would lead to the formation of a sharp yield point does not occur. Likewise, the substructure developed on deforming at 450°C again contains a fairly uniform

distribution of dislocations (even though an ill defined cellular structure is occasionally present) and so weak pinning again results. Strong evidence for weak pinning is obtained from the fact that even at the low stresses involved in the internal friction experiments unpinning can be observed.

Support for the view that the transition from logarithmic to non-logarithmic damping is associated with the unpinning of weakly pinned dislocations is obtained from the internal friction results of recovered specimens. Recovery produces well defined polygonized subgrain boundary networks (figs. 4.41, 4.42) and from such specimens no transition in the damping behaviour is observed. Now the dislocations in the subgrain boundaries would be pinned to some extent because the polygonized configuration is a low energy one. However, this pinning would not be expected to be as strong as that due to interaction locking of tangled dislocations but it is, nevertheless, sufficient to withstand the stresses applied in the internal friction experiments. Therefore, it can be concluded that when the transition occurs in the damping measurements the pinning of dislocations is definitely weak and an abrupt yield point could not be observed in a tensile test.

The failure to observe a transition in the internal friction results from the recovered material suggests that a sharp yield point may occur. However, straining of a

recovered specimen does not result in an abrupt yield point and it must be concluded that the dislocations in the recovered subgrains would be unpinned at a stress between the maximum applied in the internal friction apparatus and the yield point. More light can be thrown on this aspect by the work of Abson and Jonas (1970).

Abson and Jonas have applied a Hall-Petch type relation to subgrain structure. The contribution to strength at room temperature which could be attributed to the presence of high temperature sub-boundaries was less than that produced by an equal density of grain boundaries. The sub-boundary strength was found to be dependent on the degree of perfection of the sub-boundaries and the misorientation across them. The narrow, relatively perfect boundaries produced during high temperature creep have relatively low strengths whereas tangled imperfect boundaries produced during hot working have strengths approaching that of grain boundaries.

The above work suggests that the tangled dislocation cell structure will have a strengthening effect greater than the effect from a well formed polygonized structure. Thus the interaction locking of the cell structure is high and so the previous postulate for the abrupt yielding due to strain-ageing is supported. The locking of dislocations in the recovered polygonized sub-boundaries would not be so great, and so abrupt

yielding would not be observed, however, the locking is strong enough to suppress the logarithmic to non-logarithmic transition in the damping measurements.

The effect of the cell structure is also supported by fig. 5.5 which shows that the component $Ky\dot{d}^{-1/2}$ increases to a maximum between 250 and 300°C. This parameter can be interpreted as a measure of the locking effect (or strength) of the subgrain or cellular structure. Hence at 250 - 300°C, the effect of the cell walls is greatest and so the dislocations are most effectively locked. Thus the strain-ageing behaviour is accentuated in this temperature range.

The fact that a well annealed specimen of zirconium showed no logarithmic to non-logarithmic damping and also showed no abrupt yield point on initial straining can be explained. The grain boundaries, or some other nucleation sites, would be expected to be sources of dislocations at stresses below the yield point. Then, since a concentration of mobile dislocations exists, a smooth stress-strain curve will result. As plastic deformation proceeds the sources of dislocations become surrounded by an area of plastic deformation. When the load is released, and the specimen aged, the dislocations surrounding the sources are pinned and on subsequent straining it is much more difficult for these nucleation sites to operate. This type of argument has been used by Cottrell (1963) to

explain the occurrence of larger yield drops in iron single crystals after initial straining and ageing treatments.

This kind of behaviour has also been shown to occur by Bullen et al. (1964) and Besag and Bullen (1965) while examining pressurization effects on yielding in iron.

The anomalies in the creep behaviour, in the temperature range with which this discussion is concerned, has been related to strain-ageing (Fidleris (1968), Holmes (1964)). It has been shown that strain-ageing is most prominent in the temperature range where extremely low creep rates are observed. This can be related to the dislocation cell structure and oxygen locking, as was the strain-ageing phenomenon. Fuller (1968-70) has produced, from internal friction results, a plot of stress induced relaxation time for oxygen jumping against the reciprocal of temperature, (fig. 5.33), and this shows that stress induced diffusion of oxygen in α -zirconium becomes extremely rapid as temperature increases. At 300°C the jump time is about 800 seconds which means that oxygen diffusion occurs relatively slowly at this temperature. However, the oxygen can diffuse to the dislocation cell walls where atmospheres will form and cause an impedance on the dislocations. With the addition of dislocation - dislocation interaction locking in the cell walls the pinning will be strong. At temperatures above 350°C, the oxygen jump time is less than

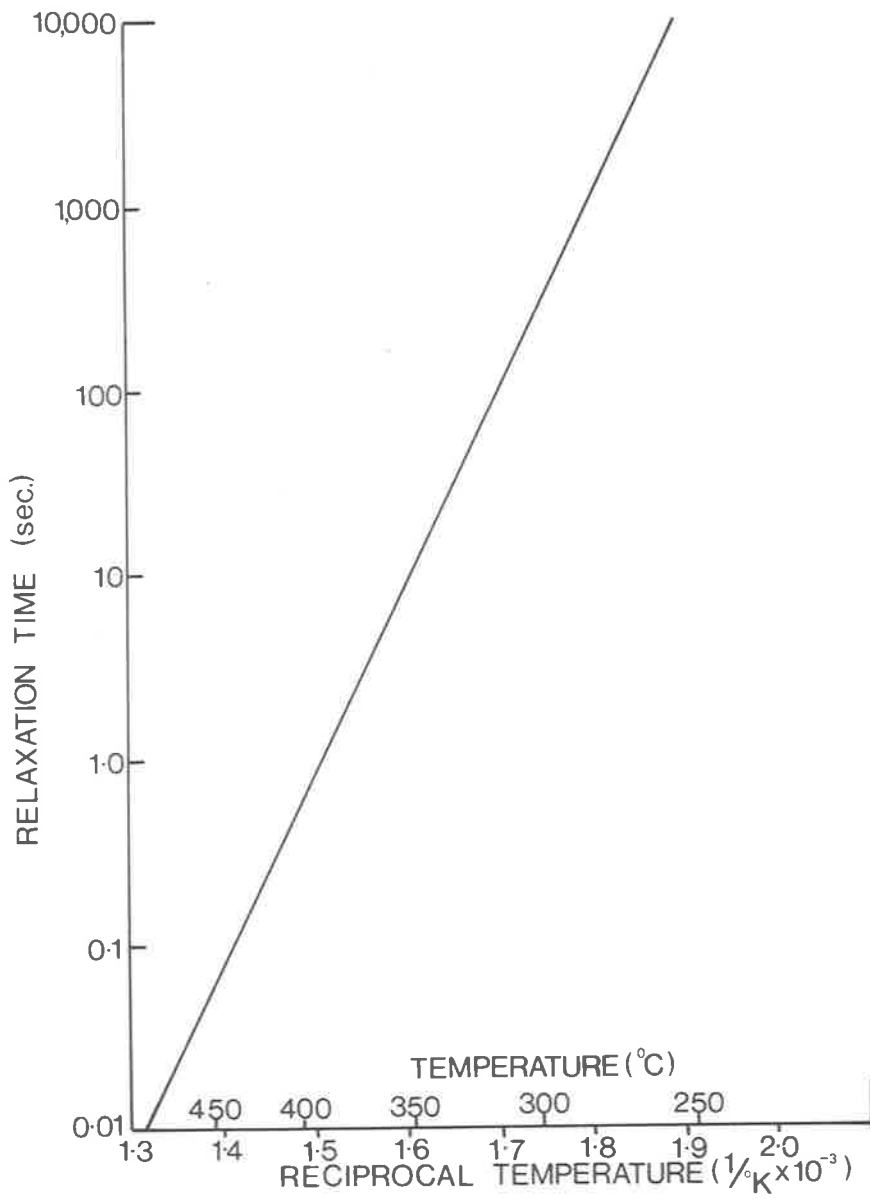


FIG.5.33 RELAXATION TIME – RECIPROCAL TEMPERATURE PLOT FOR OXYGEN IN ZIRCONIUM.

(after Fuller, 1968-70.)

10 seconds and decreases to less than 0.1 seconds at 450°C. These are the temperatures where a dislocation cell structure has given way to more random dislocation arrays and so dislocation interaction locking is much reduced. The diffusion of oxygen to dislocation cores would be very rapid at these temperatures but the interstitial atmospheres so produced can only cause weak pinning of the dislocations. This is because a stress easily moves the oxygen atoms (as indicated by the jump time of fig. 5.33) and so their impedance on dislocation motion is relatively small.

On the other hand, at low temperatures the oxygen jump time is high or the oxygen diffusion rate is extremely slow. Therefore, atmospheres of interstitial atoms would take a long time to form at these temperatures and locking by this means would be small. Also the dislocations are again uniformly distributed and so interaction locking is small.

The temperature of straining has, therefore, an important effect on both the dislocation configuration (and thus the level of interaction locking) and the effect of interstitial oxygen on the dislocations. It is only when both interaction locking and atmosphere locking are operating that strain-ageing behaviour occurs.

Another phenomenon which requires explanation is the fact that when a zirconium-350 ppm oxygen alloy specimen is

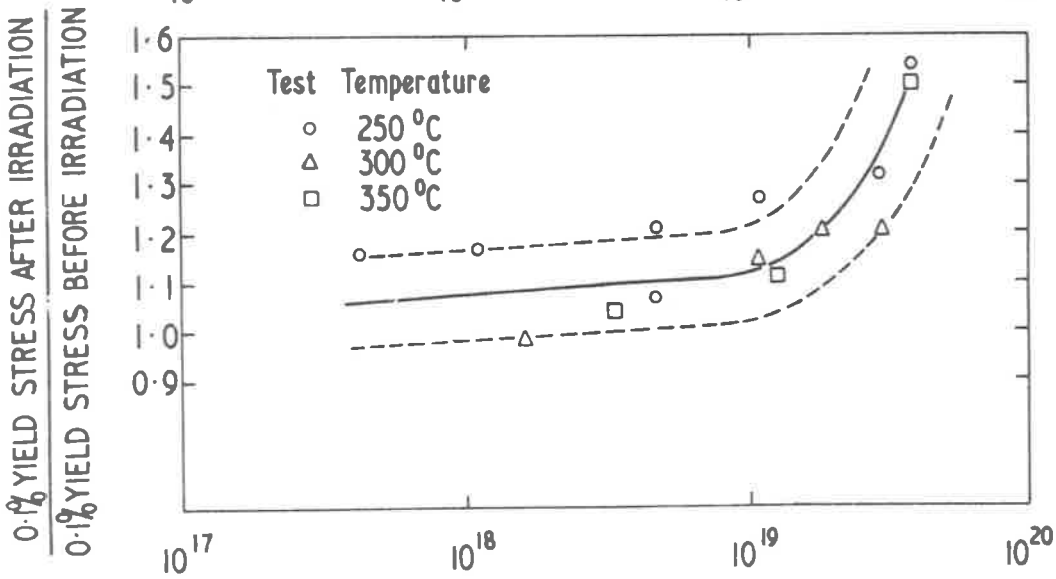
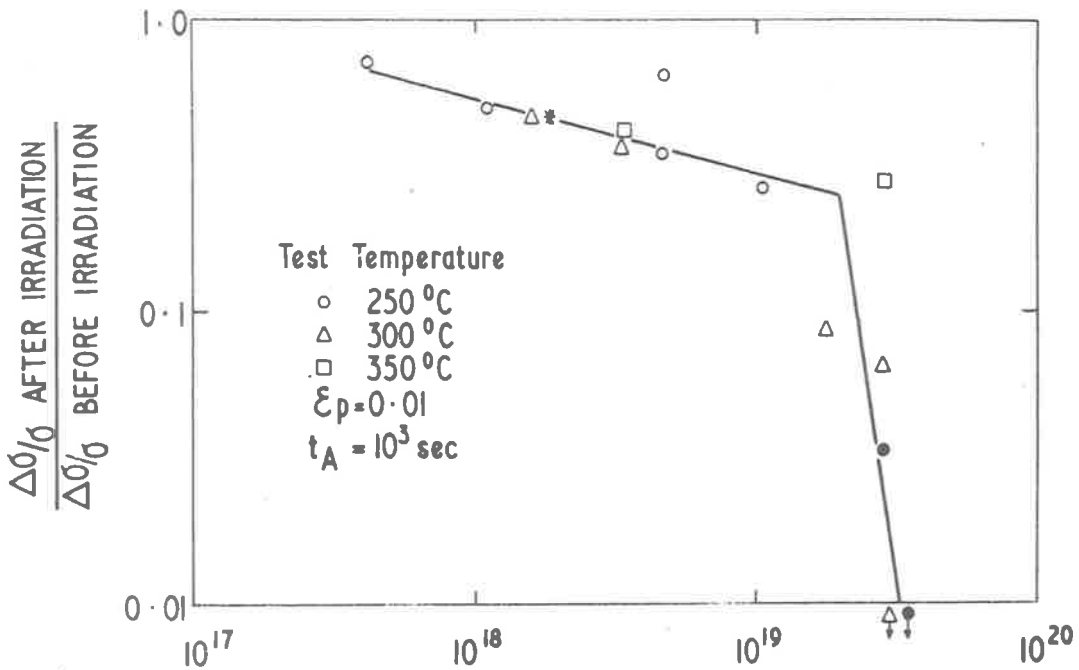
strained approximately 3% at 300°C and then aged at half the flow stress for 1000 seconds at 300°C, but is then restrained at room temperature, no abrupt yield point is observed. Thus, even though the cellular type of dislocation structure, which is the pre-requisite for an abrupt yield point, is introduced, restraining at room temperature instead of 300°C suppresses the yield point. This can be explained on the basis of the yield stress against temperature curve, fig. 5.7. The initial treatment at 300°C involved stressing to about 6 kg/mm² whereas restraining involved stressing to above 10 kg/mm². Between the two stress levels some other sources of dislocations, which would normally be operative if the straining had originally been carried out at room temperature, may create the conditions for masking of the yield point. On the other hand, the dislocations produced and locked during the treatments at 300°C may break away at the higher stresses involved and thus produce the smooth yielding behaviour.

The effects of irradiation on the strain-ageing behaviour of Zircaloy-2 have been discussed by Veevers et al. (1968) and some interesting points arise. It is noted that the strain-ageing behaviour of Zircaloy-2 may be considered to be basically similar to that in Zr-O alloys except that an extra peak is observed in the $\Delta\sigma/\sigma$ vs T curve at 450°C (fig. 5.3). The strain-ageing of the Zircaloy-2 up to about 400°C was

associated with oxygen locking of dislocations but the combined locking as proposed earlier in this section would be more attractive since Veevers et al. also show that a dislocation cell structure results after the initial straining and ageing procedures. Indeed, if oxygen locking alone was the cause of strain-ageing, a test in which the initial strain was carried out at room temperature followed by ageing at 300°C and then restraining at room temperature should show an abrupt yield point. However, this was not the case.

The data of Veevers et al. (1968) showed that strain-ageing was gradually suppressed up to a neutron dose of 2×10^{19} nvt and above this value the decrease in strain-ageing yield behaviour was rapid, (fig. 5.34). This effect was attributed to locking of the interstitial atoms by radiation induced defects so that the effect of oxygen on the dislocations was no longer dominant. On the other hand, it is also possible that radiation induced defects may be able to act as dislocation sources or they may induce cross slip and allow multiplication of existing dislocations. Both of these phenomena would have the effect of suppressing the abrupt yield point due to strain-ageing.

In conjunction with the reduction in the strain-ageing effect, radiation produces a gradual increase in the yield stress up to a dose of 2×10^{19} nvt followed by a rapid



FAST NEUTRON DOSE nvt $E \geq 1 \text{ MeV}$

STRAIN AGEING AND 0.1 PER CENT YIELD STRESS OF ZIRCALOY-2 VERSUS INTEGRATED NEUTRON DOSE

FIG.5.34 (TOP) FIG.5.35 (BOTTOM)

(AFTER VEEVERS, ROTSEY, SNOWDEN, 1968)

increase in the yield stress above this dose (fig. 5.35).

The suggestion that suppression of strain-ageing by irradiation is due to oxygen locking by the defects poses some interesting questions. Firstly, why should the strain-ageing behaviour be suppressed slowly as the neutron dose increases up to 2×10^{19} nvt and then very rapidly above this dose, if the only effect of radiation was to allow more and more oxygen to be absorbed? This could only be resolved by carrying out experiments on specimens containing different amounts of oxygen and which have undergone different amounts of prior strain, to find out whether there is some critical amount of oxygen required to produce the strain-ageing effect as is suggested by the interpretation of Veevers et al.. Secondly, why should the yield stress increase slowly if more and more oxygen atoms are being held by radiation induced defects? Thirdly, why should a rapid increase in yield stress occur after a fast neutron dose of 2×10^{19} nvt if only oxygen atoms have been absorbed? Something significant and more complex than just oxygen absorption by radiation induced defects must occur and it is the increase in yield stress which results that can account for the strain-ageing suppression.

It will be remembered that the suppression of strain-ageing by straining, at room temperature, a specimen which had previously been strained and aged at $250 - 300^{\circ}\text{C}$, was attributed

to the shape of the yield stress against temperature curve (fig. 5.7). Now it is quite possible that a similar type of process occurs due to the irradiation behaviour. Up to an integrated fast neutron dose of 2×10^{19} nvt the strain-ageing decreases slowly in a specimen which was strained and aged at 300°C before irradiation. After doses greater than 2×10^{19} nvt the yield stress curve rises rapidly and so the difference in yield stress before and after irradiation is markedly different and the strain-ageing will be suppressed as before. The way in which the yield stress varied during annealing tests carried out by Veevers et al. on the irradiated material support an explanation of this kind.

CHAPTER 6

SUMMARY, CONCLUSIONS AND SUGGESTIONS
FOR FUTURE WORK.

The affinity of zirconium for oxygen limits the application of zirconium and zirconium alloys in unprotected environments to temperatures below about 500°C but because of the good nuclear properties, favourable mechanical properties and a reasonable ease of fabrication the zirconium and some of its alloys is extensively used within this temperature limit in some types of nuclear reactors. Components such as fuel cans and pressure tubes made from these materials are, however, in quite critical places in the reactors and it is therefore essential to have an understanding of the mechanical properties of the material, and in particular of its creep behaviour, in order to achieve reliable and predictable performance for periods of up to thirty years at operating temperatures.

Studies elsewhere of zirconium and its alloys in the temperature range 0-500°C had revealed that anomalously low creep rates were obtained near temperatures of 300°C (Holmes (1964), Fidleris (1968), Snowden (1969)). This behaviour was associated, in a general way, with strain-ageing, (Rotsey et al. (1968-70), Veevers and Rotsey (1968)), and so too were the variations in yielding behaviour over this same temperature range (Keeler (1955), Weinstein (1966), Ramaswami and Craig(1967)).

These studies of the mechanical properties, while adequately describing the behaviour of zirconium when deformed under various conditions, did not enable the precise cause of the strain-ageing process to be determined. The present program of research was aimed at explaining these mechanical properties of zirconium in a more basic manner by investigating the behaviour of dislocations during slow strain-rate deformation in the temperature range of particular interest.

Because many of the previous studies have been made on zirconium containing high levels of impurities, ambiguities sometimes arose in the interpretation of the deformation behaviour, and so in the present study zirconium of very high purity was used.

One of the major experimental techniques used in this study was electron microscopy and the use of this technique not only involved a rather detailed study of electropolishing procedures, but also entailed a very critical examination of the electron microscopy and crystallography of hexagonal metals from which a number of significantly simplified crystallographic procedures emerged.

From the detailed study of the ways in which dislocations arrange themselves during deformation at various temperatures it has been shown that the strain-ageing, yielding and creep behaviours are dominated by the formation of a

dislocation cell structure.

Straining of a zirconium specimen in the temperature range 250-350°C resulted in the formation of a dislocation cell structure and on subsequent ageing and restraining, these specimens showed a discontinuous yield point. On the other hand, straining at lower or higher temperatures produced only a random dislocation array and ageing and restraining produced no abrupt yield point. With the support of evidence on the behaviour of interstitial oxygen atoms, from the internal friction work of Fuller, it has been possible to propose an explanation of the strain-ageing behaviour based on the combined locking effects of dislocation interactions and pinning by interstitial atoms. The implications that this cell type dislocation structure can cause a high impedance to dislocation motion during creep are then apparent.

The possibility exists that stabilization of this cell structure would lead to very much improved creep behaviour of zirconium and the indications are, from comparable results on Zircaloy-2, that the same sort of effect may occur in the zirconium alloys. It can only be speculated that approaches to this problem may come from interstitial or substitutional alloy studies or that increases in point defect concentration, due perhaps to irradiation, could yield fruitful results.

The transition in dislocation arrangements from random to cellular structures was shown to be the vital step in obtaining the strain-ageing behaviour. Experiments in a hard tensile machine using very small temperature increments in the range 200 - 350°C must be carried out. Very precise values of the yield drop, increase in flow stress, locking parameter and yield point elongation will lead to a clearer understanding of the strain-ageing and yielding behaviour. To augment the study, electron microscopy must be used to determine the cause of the transition from random dislocation arrays to cell-like arrays of dislocations and then the transition back again to a random array at still higher temperatures. It has been shown in the present work that dislocation loops are prevalent when a specimen is strained at 350 - 400°C at which temperatures the dislocation cell structure gives way to a random array and an obvious pointer to the origin of these transformations lies in these dislocation loops. A detailed study of their formation clearly constitutes an important avenue for further work.

The most direct way to establish the effect of oxygen interstitials on strain-ageing would be to use oxygen-free zirconium but even in the present material, which contains approximately 50 ppm oxygen, modern electron microprobe analysers may be sufficiently sensitive to show the distribution

of oxygen in the zirconium specimens. According to the present theory, there should be a concentration of oxygen in the tangled cell walls after ageing and if the resolution of the microprobe is adequate, this should be able to be observed in appropriately prepared specimens. More fundamental research on the precise nature of the interactions between oxygen atoms and dislocations will also aid in the understanding of the strain-ageing behaviour.

Other tests which may show the association of strain-ageing with cell structure can be devised. For example, a cell structure will be produced in zirconium which is deformed at temperatures below that at which strain-ageing was observed in the present experiments provided that the strain rate is sufficiently low. If the specimen was to be aged for a short time, say 1000 sec. at 300°C, to cause oxygen locking of the dislocations in the cell walls, on lowering the temperature again to 150°C and restraining, the present theory would predict an increase in yield and flow stress due to strain-ageing; such an increase would not occur if a normal strain-ageing test was carried out at 150°C.

More experiments should be carried out on the creep behaviour over the temperature range 100 - 450°C, but efforts must be made to resolve or eliminate the effects of yield stress dependence on temperature. Creep tests have been

carried out at constant stress and indeed the anomalous creep behaviour in zirconium was observed in creep tests at 20,000 psi (Fidleris (1968), Snowden (1969), fig. 5.10). Now the yield stress is known to vary in a way similar to that shown in fig. 6.1. If a creep stress (σ_c) is applied and the temperature of testing varied then the ratio $\frac{\sigma_c}{\sigma_1}$ for temperature T_1 is less than $\frac{\sigma_c}{\sigma_2}$ at temperature T_2 . Therefore the creep stress is a varying ratio of the yield stress. To overcome this difficulty, creep tests should be carried out in which the ratio $\frac{\text{creep stress at temperature } T}{0.2\% \text{ yield stress at temp. } T}$ is a constant.

Internal friction has excellent potential for studying the yielding behaviour of metals. The transition from logarithmic to non-logarithmic behaviour was shown to be related to the occurrence of a sharp yield point. However, in view of the uncertainty in the damping behaviour between the maximum stress applied in the internal friction apparatus and the yield stress, internal friction results obtained at much higher strain amplitudes are required. The effects of microyielding before the abrupt yield point will have to be taken into account but the many ways in which thin wires can be treated prior to damping experiments should easily resolve such problems.

Internal friction experiments have also shown

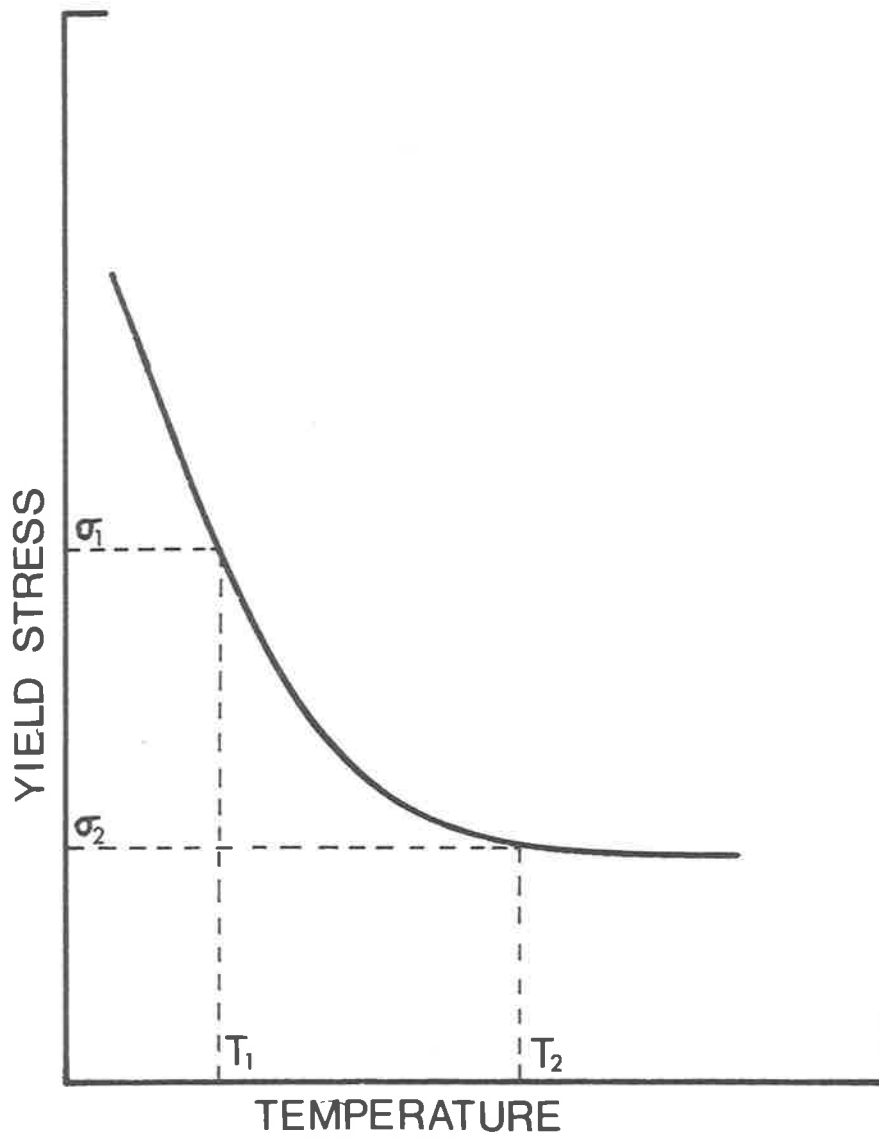


FIG.6.1 SCHEMATIC REPRESENTATION OF TEMP. DEPENDENCE OF YIELD STRESS.

(Fuller 1968-70) that recovered zirconium specimens exhibit damping effects which have been tentatively attributed to subgrain boundary sliding or relaxation and such work on specimens containing a dislocation cell structure will undoubtedly throw further light onto the strain-ageing behaviour.

Allied to the electron microscope research used to explain the mechanical properties were more fundamental studies of the dislocation reactions which occur during high temperature deformation and to the relation between surface slip lines and dislocation substructure.

New mechanisms of formation of hexagonal networks of dislocations have been proposed. These are able to explain the occurrence of networks which do not lie on a single plane, a shortcoming which existed in previously proposed mechanisms of network formation. Careful examination of published results revealed also that the networks observed were probably not all on one plane and, in fact, would be more compatible with the present mechanisms.

The present results have shown that wavy slip lines which appear on polished surfaces of zirconium specimens during deformation were only observed when a dislocation cell structure was known to occur. This supports the contention that wavy slip lines are produced by the motion of sub-grains

or dislocation cells and is not compatible with the other theory that wavy slip is caused by cross slip of the dislocations. Of course motion of tangled walls of dislocations must of necessity involve some cross slip.

It was recognised that texture of zirconium specimens can have important effects on the mechanical properties shown, for instance, by a small difference in yielding behaviour between longitudinal and transverse tensile specimens (Weinstein, 1966) and by the extreme sensitivity of twinning behaviour to texture. Picklesimer (1966) pointed out that the value of many otherwise excellent studies on non-cubic materials was lessened by not having taken texture into account. The texture of the material used in the present study was assumed to be similar to that found from previous texture studies on rolled and annealed sheet and the electron microscope results supported this assumption. Only slow strain rates were used on longitudinal specimens and although twinning was very occasionally observed, it did not have any effect on the dislocation results. However, future detailed work on the mechanical properties and associated dislocation behaviour will have to include a knowledge of the way changes in texture effect these results. This has important practical implications since fabrication methods usually introduce a strong texture and so clearly, the effects of prior cold work on these

considerations must be investigated.

In the present work it was shown that large grain-size zirconium specimens exhibited strain-ageing and the possibility of observing this behaviour in very large grained materials, or single crystals, which can be sectioned on known planes, opens up new avenues for fundamental studies. This approach, which may also resolve the doubt which still remains over the slip systems which operate in zirconium at various temperatures, together with the combination of high strain-amplitude internal friction, precise tensile testing and electron microscopy should enable a firm understanding of the mechanical properties of zirconium to be gained.

APPENDIX 1 HYDRIDES AND ZIRCONIUM THIN FOILS.

Hydrogen has a very low room temperature solid solubility limit in zirconium and nearly always precipitates as Zirconium Hydride. These hydrides precipitate either as needles or plates with a f.c.c. structure and with composition near $ZrH_{1.5}$ (Ells, 1968). Precipitates usually have the effect of either enhancing or impairing the mechanical properties of the unalloyed material. For this reason the shape, disposition and orientation of the precipitates, their effect on texture and their behaviour during forming and mechanical deformation are very important. A number of experiments have been carried out to determine the habit planes of the zirconium hydride, many using optical or X-ray trace analysis techniques and a few using electron microscopy. A review by Ells (1968) has collected much of the information available.

In addition to determinations of habit planes, experiments have been carried out to find the ways in which hydride precipitates alter the mechanical properties of zirconium. Hydride precipitates can initiate cracks which may propagate into the matrix material and cause failure of the component. Hydrogen is easily absorbed into zirconium and so the hydride problem is of major importance when

considerations for structural usage are being made. The effects of hydrides on the mechanical properties of zirconium have been well documented and the main concern of this appendix is the possible habit planes of the hydride.

A. Hydride Precipitate Shape

The nature of the hydride precipitates which form in or on zirconium appears to vary from a needle-like shape to a plate-like shape. Increasing concentration of hydrogen and decreasing cooling rates cause the needle shaped precipitates to become platelets. This was confirmed by Kunz and Bibb (1960) who observed traces due to a single hydride plate on two different surfaces of a crystal.

It has also been found that hydrides often appear as composite platelets made up of several smaller platelets. Replicas from surfaces of Zr-2.5%Nb showed that the smaller platelets were oriented at 45° to the principal direction (Ells, 1968). Babyak (1967) observed hydride plates growing end to end to form composite plates in Zircaloy-4. It would therefore appear that the orientation of the smaller platelets, relative to the principal direction of the composite plate, can vary over a wide angle. Indeed, this has been shown to be true in the present work on pure zirconium and figs. A1 and A2 serve as illustrations of

composite plate behaviour. The hydride precipitate shown by Bailey (1963) (fig. 4 (c)) could have been two or more small platelets, with a high degree of distortion between them, which led to the contrast shown. An example of this type of precipitate, with less distortion between the platelets, is shown in fig. A2 (b).

B. Nucleation Sites for Precipitates.

Grain boundaries appear to be preferred sites for precipitation of hydrides and slow cooling was shown to enhance this effect (Bailey, 1963). However, some of the examples showing precipitates at grain boundaries are high magnification electron micrographs from thin foils and these precipitates may, in fact, be surface hydrides which appear to have different properties to the massive hydride in bulk samples. (See section C).

Twin boundaries have also been shown to be preferred sites for nucleation of hydrides (Ells, 1968). Rapid cooling tended to favour some formation of transgranular hydrides.

Dislocations are also probable nucleation sites and the precipitation of surface hydride at dislocation intersections with the surface of a thin foil is shown in the stereomicrographs of fig. A4.

FIG. A.1 End to end composite hydride needles

(a) and (b). and platelets in pure zirconium.

(a) 0.5μ

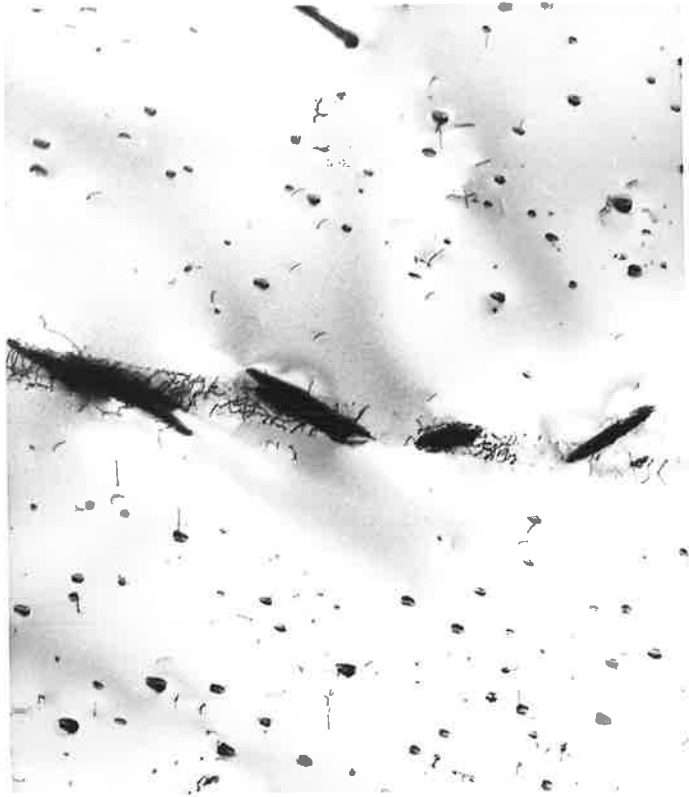

(b) 0.5μ




FIG. A.2 Composite hydride needles and
(a) and (b) platelets in pure zirconium.

0.5 μ





C. Habit planes of Hydrides.

Ells (1968) produced a table which summarized the reported hydride habit planes and showed the materials and methods used for the analyses. From his review, Ells noted that the primary hydride habit plane in pure zirconium was $10\bar{1}0$ and that in Zircaloy-2 and Zircaloy-4 it was $\{10\bar{1}7\}$. However, no distinction was noted between results obtained from X-ray or optical analyses and those obtained from electron microscope analyses. The hydride resolved in the electron microscope was found to be much smaller than that observed on the optical microscope (Arunachalan, 1968) and this has also been shown in the present work. Lengths of hydrides observed on the surface of zirconium specimens, obtained from optical micrographs, range down to 2×10^{-3} mm whereas the maximum length of hydride calculated from electron micrographs was about 1×10^{-3} mm. However, it must be noted that long hydrides could be shortened by the thinning process. When the lengths of composite hydrides, (see figs. A1, A2) was measured the maximum length observed was near 3×10^{-3} mm. Thus the smallest hydride observed in the optical microscope may be associated with the composite hydrides. The larger hydrides observed in the optical microscope may differ markedly from the very small hydrides resolved in the electron microscope.

Therefore, a distinction should be made between large

internal hydride precipitates and the smaller surface hydrides. As discussed in section 2.2, both chemical and electrolytic polishing can result in the precipitation of small hydrides on the surface of thin zirconium foils.

Bailey (1963) observed small precipitate clusters after electropolishing zirconium in a perchloric acid - acetic acid electrolyte which he confirmed to be hydride by heating experiments in the electron microscope. Bailey also observed that some hydride needles were very thin when the plane of the foil was parallel to the basal plane and that larger hydride platelets were present which had dislocations associated with them.

Westlake (1965) claimed that quenching of a 15 ppm hydrogen-zirconium alloy into iced brine still produced needle like precipitates. However, his preparation method for thin foils would almost certainly have resulted in the formation of surface hydrides and these may have been the hydrides which Westlake assumed were formed in the quenching operation.

Arunachalan et al. (1968) said that an advantage of electron microscopy techniques was that the specimen examined was free of surface hydrides. Based on the present observations, this would seem to be incorrect and in fact many of the hydrides shown in their electron micrographs have sizes corresponding to those found to be surface hydrides.

The small hydrides observed in the present work can unambiguously be shown to be surface hydrides by the precipitation at grain boundaries (fig. A3) and by stereo-electron microscopy (fig. A4).

It would therefore appear that two different types of hydrides can be observed. One kind lies within the material and these are probably plate-like while the other type lies on the surface and are often needle-like. The latter are usually precipitated during chemical or electrolytic polishing of zirconium.

The question then raised is; what are the habit planes of the hydrides and are they the same for the two different kinds?

In a study of about 250 electron micrographs of different areas in about 80 different specimens (20 of which were prepared by different thinning procedures) it was found that larger hydrides, which almost always had dislocations associated with them (fig. A5), lay on the primary prism planes $\{100\}$, (i.e. $\{10\bar{1}0\}$). Analyses for possible habit planes of the smaller hydrides, which do not have associated dislocations but whose coherency contrast varies for varying diffracting conditions, resulted in the fact that the long axis of the hydride always lay in an orientation which was very close to the trace of the basal plane in the foil. Of course, a trace of the

FIG. A.3 Zirconium hydride precipitated on
top and bottom of grain boundary in
thin foil.

0.5 μ

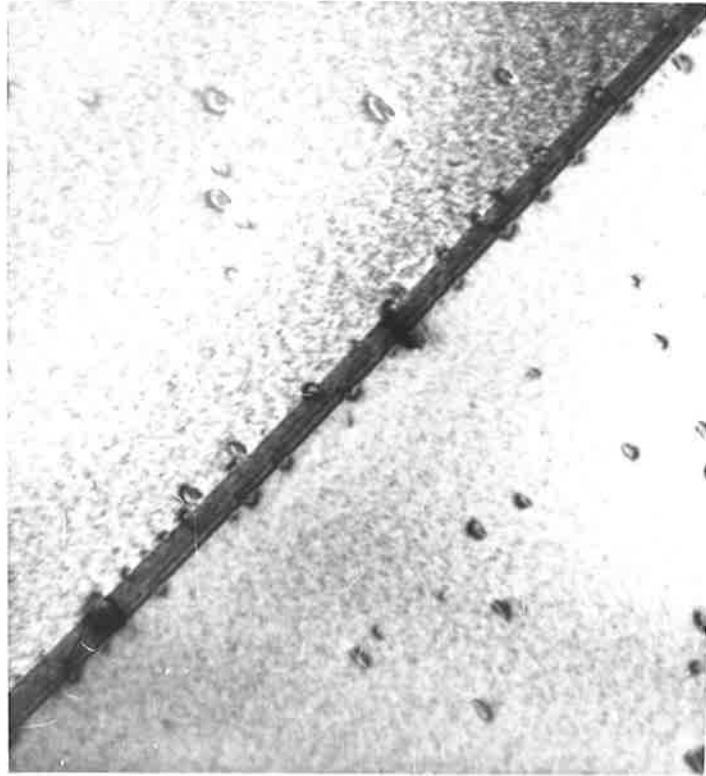
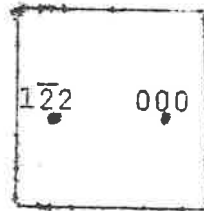
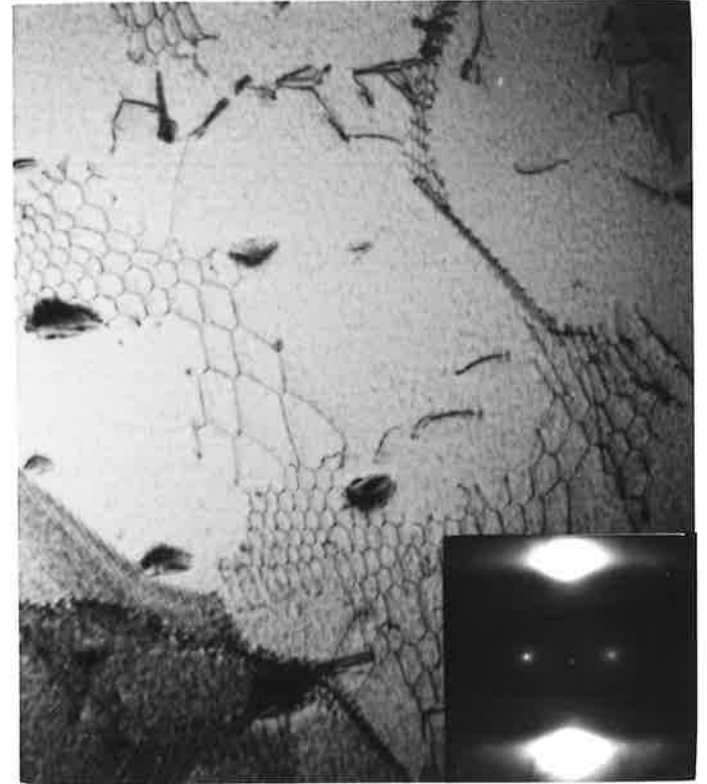
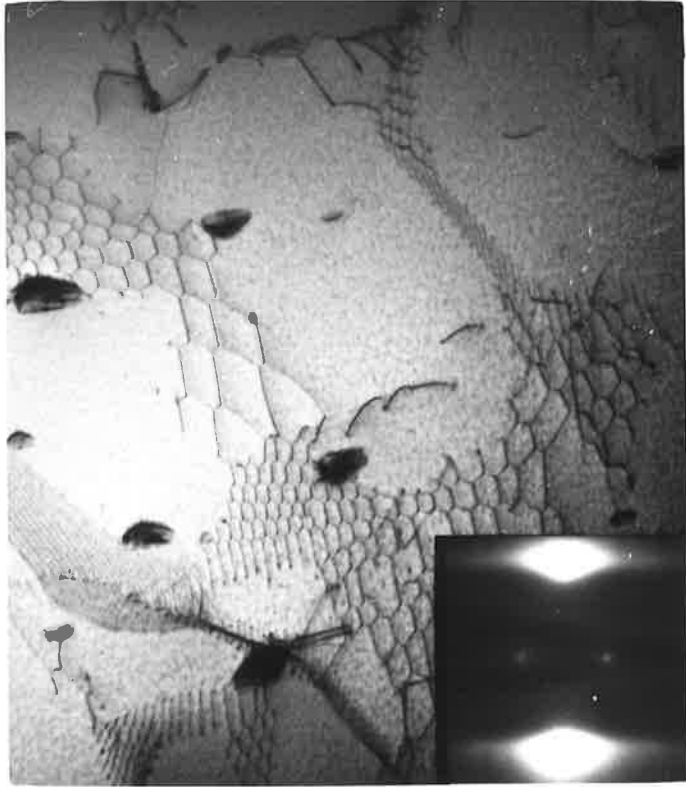



FIG. A.4
(a) and (b).

Stereo-electron micrographs showing zirconium hydride at top and bottom surfaces of thin foil. Note also that dislocation intersections with foil surface act as preferential nucleation sites. Tilt axis parallel $g(1\bar{2}2)$.

0.5 μ
└───┘





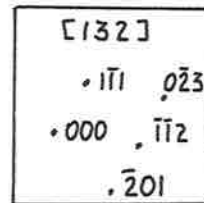


FIG. A.5 Hydrides lying on {100} planes
(i.e. {10 $\bar{1}$ 0}).

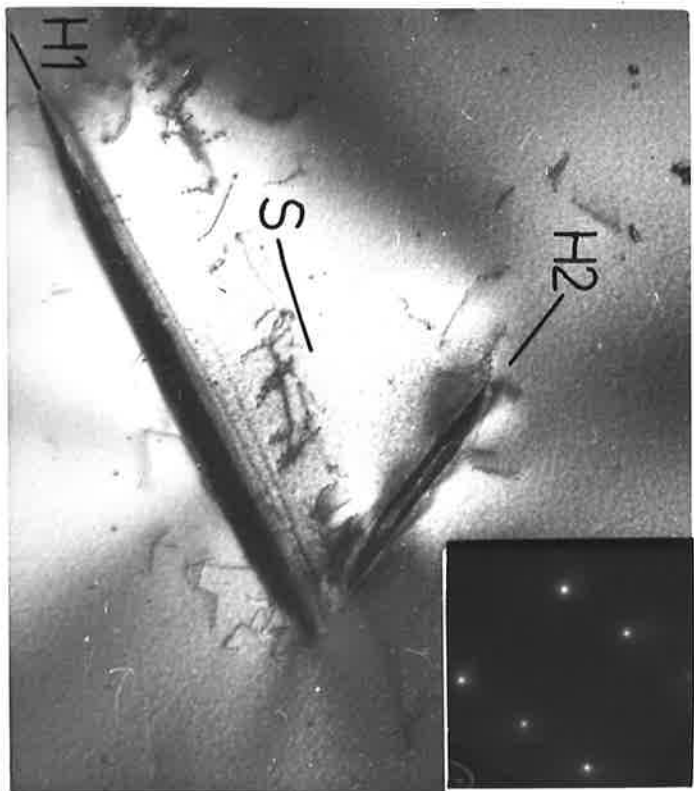
H1 is on ($\bar{1}$ 10) plane

H2 is on (010) plane.

Slip trace, S, corresponds to
slip on (001)

Foil thickness $\approx 3200 \text{ \AA}$ calculated
from hydride platelet H2 and slip
trace width.

0.5 μ
└───┘



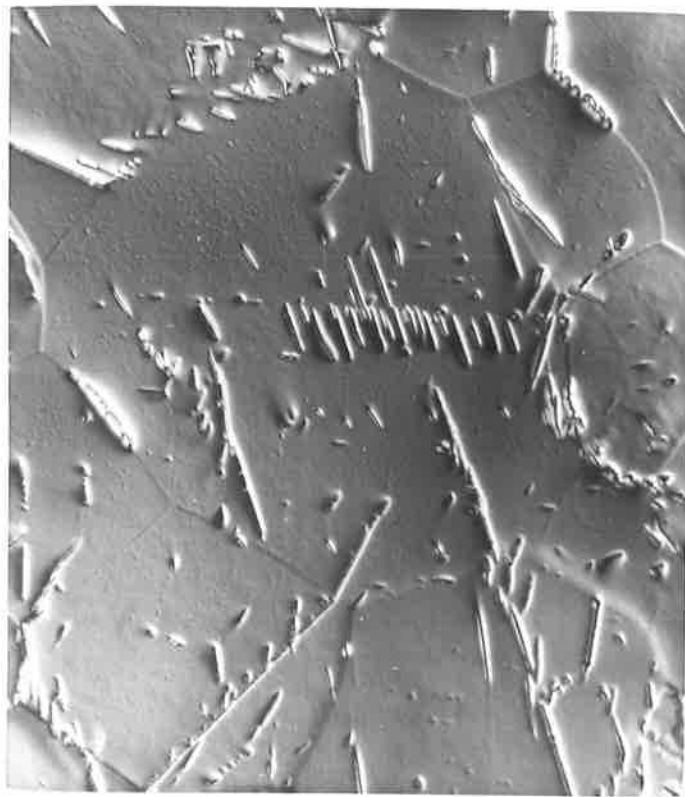
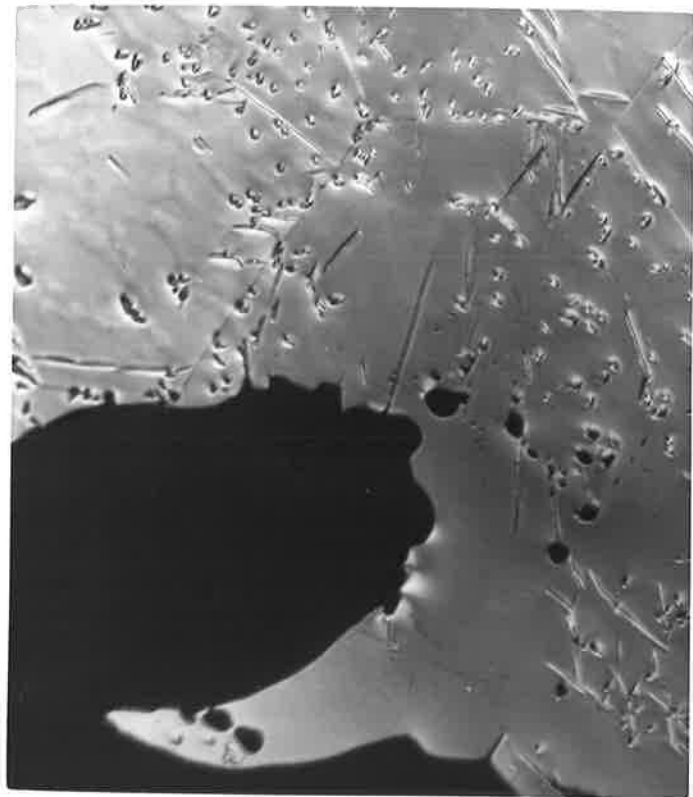
($10\bar{1}7$) plane, which was favoured by Westlake as the habit plane, would be very close to the basal plane trace as would a number of other high order pyramidal planes noted by other authors (Ells, 1968). However, one feature observed in all the electron micrographs examined was that the long axis of the surface hydride appeared in only one direction in any one grain. If the hydride was precipitating on any plane other than the basal plane it would be expected that in some of the micrographs a grain would be observed which contained more than one direction of precipitation. Indeed, the larger hydrides which precipitate on $\{100\}$ planes often occur in more than one direction in a single grain in a thin foil (fig. A5).

A relatively small number of the hydrides which are called internal hydrides and lie on $\{100\}$ planes were observed compared to the large number of the surface variety. This is due to an effect which results during electropolishing. In a hydrided specimen*, fig. A6, polished to produce a thin foil, fig. A7, it can be seen that the thin edge was almost devoid of the larger hydride precipitates and indeed electron microscopy of that foil showed only a few hydrides which could be attributed to precipitation on prism planes. However, a large number of small surface hydrides were evident.

* Hydrogen added at 700°C to pressure of 1 torr

FIG. A.6 Hydrided zirconium specimen.
Optical micrograph - Nomarski
Interference contrast, 250X.

FIG. A.7 Thin edge after final electropolishing
- note depletion of hydride near
edges.
- Nomarski interference contrast,
300X.



Dislocations which were punched out by hydrides were sometimes observed to lie on basal planes by Bailey (1963), and this has been confirmed in the present study (fig. A5). Bailey used this as evidence that high stress fields could cause basal slip in Zirconium.

The fact that there appears to be two different types of precipitate, one which forms in the bulk zirconium matrix due to supersaturation of hydrogen on cooling, and the other which forms on the surface due to the absorption of hydrogen from solutions or atmosphere, can give misleading results when habit planes are being calculated. When such analyses are proposed it would be necessary to take care in differentiating between the two types, since the surface variety would be expected to have little effect on the bulk mechanical properties. Therefore, the knowledge as to what plane or planes the hydrides precipitate on has little importance from this viewpoint, but from the chemical (e.g. corrosion) approach such information would be more useful. However, the hydrides in the bulk material are a different proposition as these would have a marked effect on mechanical properties and thus a knowledge of their habit planes is very relevant.

APPENDIX 2 CRYSTALLOGRAPHIC DATA

This appendix is a shortened collection of crystallographic data used in the present work on hexagonal crystallography. It is assumed that most of this is common knowledge and specific references are not given. For more complete and detailed treatments, the following references may be consulted;

Barrett and Massalski (1966), Hirsch et al. (1965), Frank (1965), Nicholas (1966 and 1970), Okamoto et al. (1967 - 1968), Otte and Crocker (1965), Partridge (1967), Partridge and Gardiner (1967).

1. Reciprocal Lattice

Three-axis, "Miller" System.

Real or direct lattice axes a_1, a_2, c .

Reciprocal lattice axes a_1^*, a_2^*, c^* .

Related on basis of simple reciprocal lattice definition

$$a_1 \cdot a_1^* = a_2 \cdot a_2^* = c \cdot c^* = 1$$

$$a_1^* \cdot a_2 = a_2^* \cdot c = c \cdot a_1^* = \dots = 0$$

2. Indices of Directions.

Directions in an hexagonal lattice may be based on three-axes (a_1, a_2, c) or on four-axes (a_1, a_2, a_3, c),

(fig. A8). In the three-axis system, a direction \underline{d} will be described by the vector

$$\underline{d} = U \underline{\hat{a}}_1 + V \underline{\hat{a}}_2 + W \underline{\hat{c}}$$

where $\underline{\hat{a}}_1$ etc. are unit vectors parallel to the relevant axes. The indices of the direction \underline{d} are then $[UVW]$, and these are usually referred to as "Miller" directional indices.

In the four-axis, four-index system a direction \underline{d} will be described by the vector,

$$\underline{d} = u \underline{\hat{a}}_1 + v \underline{\hat{a}}_2 + t \underline{\hat{a}}_3 + w \underline{\hat{c}}.$$

The condition imposed by the redundant axis, a_3 , is that $u+v+t = 0$. The indices of the direction \underline{d} are then $[uvtw]$, and these are usually called "Miller-Bravais" directional indices.

Since they describe the same direction, the indices UVW and $[uvtw]$ are equivalent and the conversion equations are,

$$U = u - t; V = v - t; W = w$$

or

$$u = 1/3 (2U - V); v = 1/3 (2V - U); t = 1/3 (U + V) = - (u + v); w = W.$$

3. Indices of Planes

To determine the indices of a plane the following steps are followed,

- (1) calculate intercepts of the plane on the

FIG.A8 UNIT CELLS OF H.C.P. LATTICE

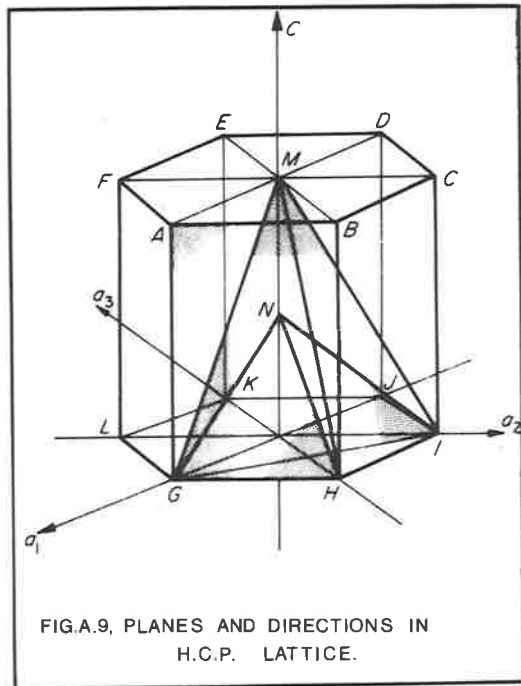
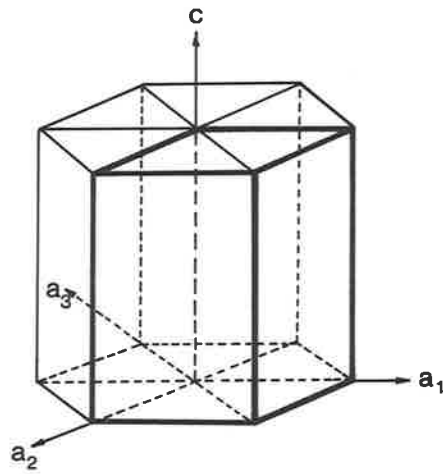


FIG.A.9, PLANES AND DIRECTIONS IN H.C.P. LATTICE.

- axes of the direct lattice as multiples or fractions of the unit lengths of these axes;
- (2) convert these values into reciprocals;
 - (3) reduce the reciprocals to the smallest integers having the same relative ratios. These then are the indices of the plane.

An alternative method is available whereby the indices of a plane are described as components in reciprocal space (Otte and Crocker (1965)). This of course follows from the definition of a reciprocal lattice since the definition is based on interplanar spacings and angles in the direct lattice. However, the method proposed by Otte and Crocker is useful when dealing with diffraction patterns (Partridge (1967)).

The definition of a plane based on three-axes results in the familiar "Miller" indices (HKL). The same plane has indices (hkil) based on the four-axes and these are called "Miller-Bravais" indices. The interconversion is simple;

$$(HKL) = (hkil)$$

where $h = H$; $k = K$; $i = -(H + K) = -(h+k)$; $l = L$.

If one or both of the above methods of indexing directions and planes are used exclusively, errors can normally be eliminated with the proper care. However, an additional complication may arise if another variation based on the four-axis, system is used. The four-axis, three-index system is

sometimes used and has resulted in confusion especially when directions are being indexed. For planes, $(hkil)$ becomes $(hk.l)$ which poses no problem in converting to the Miller system since the plane is merely (hkl) . However, for directions, the indices $[uv\bar{t}w]$ become $[uv.w]$. In some instances the dot has been left out and unless this is clearly stated a gross error can be made since the indices $[uvw]$ are not Miller indices.

It is therefore an advantage to standardize on either the Miller or Miller-Bravais system.

4. Common planes and Directions in the H.C.P. Lattice.

The following refer to fig. A9

A. Planes.

- (1) Basal Plane, (001) ; $(00\bar{0}1)$ ABCDEF
- (2) Prism Planes,
 - (a) 1st Order $\{100\}$; $\{10\bar{1}0\}$ ABHG
 - (b) 2nd Order $\{110\}$; $\{11\bar{2}0\}$ ACIG
- (3) Prymamidal Planes
 - (a) 1st Order - Type I ; $\{101\}$; $\{10\bar{1}1\}$... GHM
- Type II; $\{111\}$; $\{11\bar{2}1\}$... GIM
 - (b) 2nd Order - Type I ; $\{102\}$; $\{10\bar{1}2\}$... GHN
- Type II; $\{112\}$; $\{11\bar{2}2\}$... GIN

B. Directions.

$$(1) \langle 100 \rangle = [100], [010], [110] \dots \text{GJ, LI, etc.} \\ = \langle 11\bar{2}0 \rangle$$

$$(2) \langle 111 \rangle = [111], [0\bar{1}1], [101] \dots \text{AH, GB, etc.} \\ = \langle 11\bar{2}3 \rangle$$

$$(3) [001] ; [0001] \dots \text{NMC}$$

APPENDIX 3 PUBLISHED PAPERS.

A. CRYSTALLOGRAPHIC PROCEDURES FOR THE ELECTRON MICROSCOPY
OF HEXAGONAL METALS

A.J. Bedford* and D.R. Miller*

Journal of the Australian Institute of Metals

15, (1970) 179 - 184

SYNOPSIS. Procedures for solving crystallographic problems arising during the electron microscopy of zirconium are discussed. The use of Miller indices for planes and directions in both real and reciprocal space is advocated.

A Kikuchi map covering a large range of orientations has been constructed for a hexagonal lattice with $c/a = 1.59$. The use of this map, in conjunction with a series of standard diffraction patterns, for the rapid determination of Burgers vectors of dislocations is described.

1. INTRODUCTION.

The crystallography of hexagonal metals is more complex than that of cubic lattices and for the electron microscopist, who must make rapid and precise changes in

* Department of Chemical Engineering (Materials Science Group)
The University of Adelaide, South Australia. Manuscript
received 13th July, 1970.

the orientation of thin foils in the microscope, quick analysis of crystallographic problems is most desirable.

The techniques discussed in this paper have been developed during a research program on zirconium ($c/a = 1.593$). They are mainly geometrical techniques so that there is little necessity to use extensive calculations. Since stereographic projections and photographed diffraction patterns are used, the accuracy is not great but it is adequate for the solution of crystallographic problems of the kind usually encountered in metallurgical applications of the electron microscope.

2. STEREOGRAPHIC PROJECTIONS, INDEXING PROCEDURES.

There have been many papers on the indexing of hexagonal lattices using both "Miller" indices and "Miller-Bravais" indices and the review by Partridge (1) contains an extensive bibliography of many of these. The stereographic projection is one of the most important tools for use in solving crystallographic problems but the difficulty which arises with the hexagonal crystals is that the indices of a direction are usually not the same as the indices of the plane to which that direction is normal. A simple stereographic projection of the kind used for cubic crystals cannot then be used.

In an attempt to overcome this problem Rarey et al. (2) plotted a "double-stereogram" which contained both plane normal and directional indices in the Miller-Bravais notation. This stereogram is limited by the fact that only the simple low index planes and directions can be fitted onto a reasonably sized projection and the difference between directional and plane normal indices must be shown either by including brackets or by marking planes and directions with different type points. Subsequently, Packer and Miller (3) developed two stereographic projections, one for plane normals and one for directions.

These projections were produced using the three-axis, three-index Miller system for both plane normals and directions. The use of two such stereographic projections allows a large number of plane normals and directions to be indexed and by superimposing them the direction which is parallel to a particular plane normal can be readily determined.

(a) The Three-index and Four-index Notations.

The relative merits of the 3 - and 4 - index notations have been debated before (1,4,5,7) but one advantage of the Miller system, often overlooked, is that it is frequently easier to visualize a direction in an hexagonal unit cell when the three-index system is used. For example, the $[111]$ direction is easily visualized and only one unit cell is needed for its construction. However, this same direction has

the indices $[11\bar{2}3]$ in the Miller-Bravais notation and its construction requires the use of several unit cells (fig. 1).

On the other hand, a notable disadvantage of the Miller system is that the indices of equivalent planes and directions are often not recognized until conversion to the Miller-Bravais system is made. During the present study it has been found that for the solution of the kind of crystallographic problem which arises during electron microscope studies of thin foils, the use of the three-index Miller notation for both planes and directions offers significant advantages over the Miller-Bravais notation. To recognize equivalent planes and directions, interconversion to Miller-Bravais indices is often required but for plane normal indices this conversion is trivial (3,4) and for directions, frequent use of the relatively simple conversion formulae makes them easily remembered. It is sometimes convenient however, to use conversion tables which can easily be prepared with the help of a simple computer program.

(b) The Reciprocal Lattice.

A reciprocal lattice may be generated from the real lattice by using the conventional definition of the reciprocal lattice (6). To do this the three-axis, three-index Miller system is most convenient but the reciprocal lattice axes bear a more complex relation to the real axes

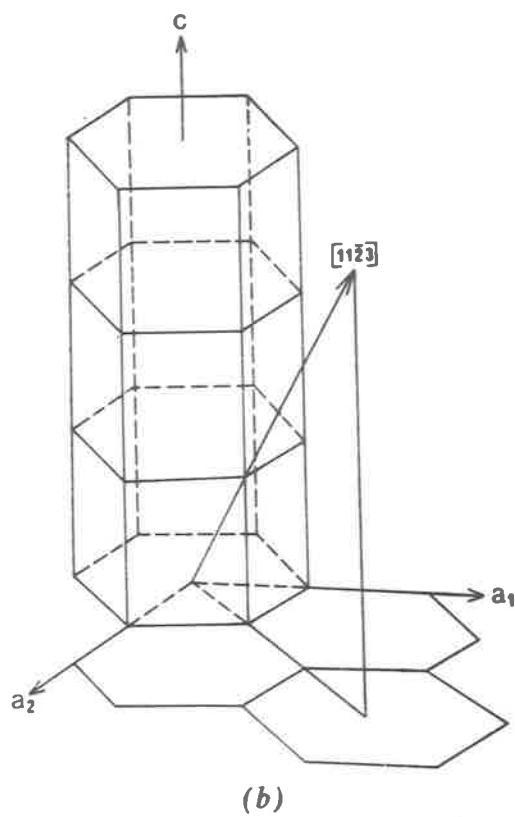
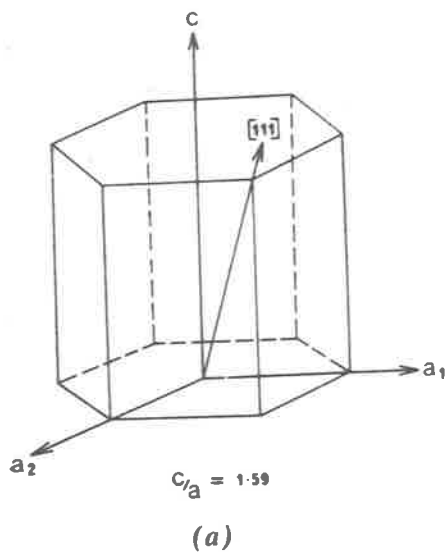


Fig. 1. Unit cells and construction needed to specify and index a simple direction: (a) Miller indices; (b) Miller-Bravais notation.

than is the case for cubic lattices (1,7). Okamoto and Thomas (8) and Partridge and Gardiner(4) have considered the problems associated with the notations in reciprocal hexagonal space and Okamoto and Thomas have discussed a reciprocal lattice based on the four-index system. This reciprocal lattice is defined by basis vectors which are parallel to the basis vectors of the real lattice.

This, in effect is a new definition of a reciprocal lattice since a reciprocal lattice cannot be constructed using the normal definition when the four-axis notation is used (7). It was shown (9) that this method satisfied all the necessary criteria in relation to reciprocal and real space, but the concept introduces more points to the reciprocal lattice than are real, and the unreal ones can be recognized and eliminated because they have fractional indices. Recently, Nicholas (7) has fully defined the reciprocal lattice in the general hexagonal case and recommended the use of the Miller-Bravais notation for most problems.

When the three-index Miller notation is used and the conventional definition of the reciprocal lattice is applied, a rather complex relationship between directions in real and reciprocal space is introduced. However, this need not involve any significant difficulty provided that each direction in reciprocal space is considered in terms of the corresponding

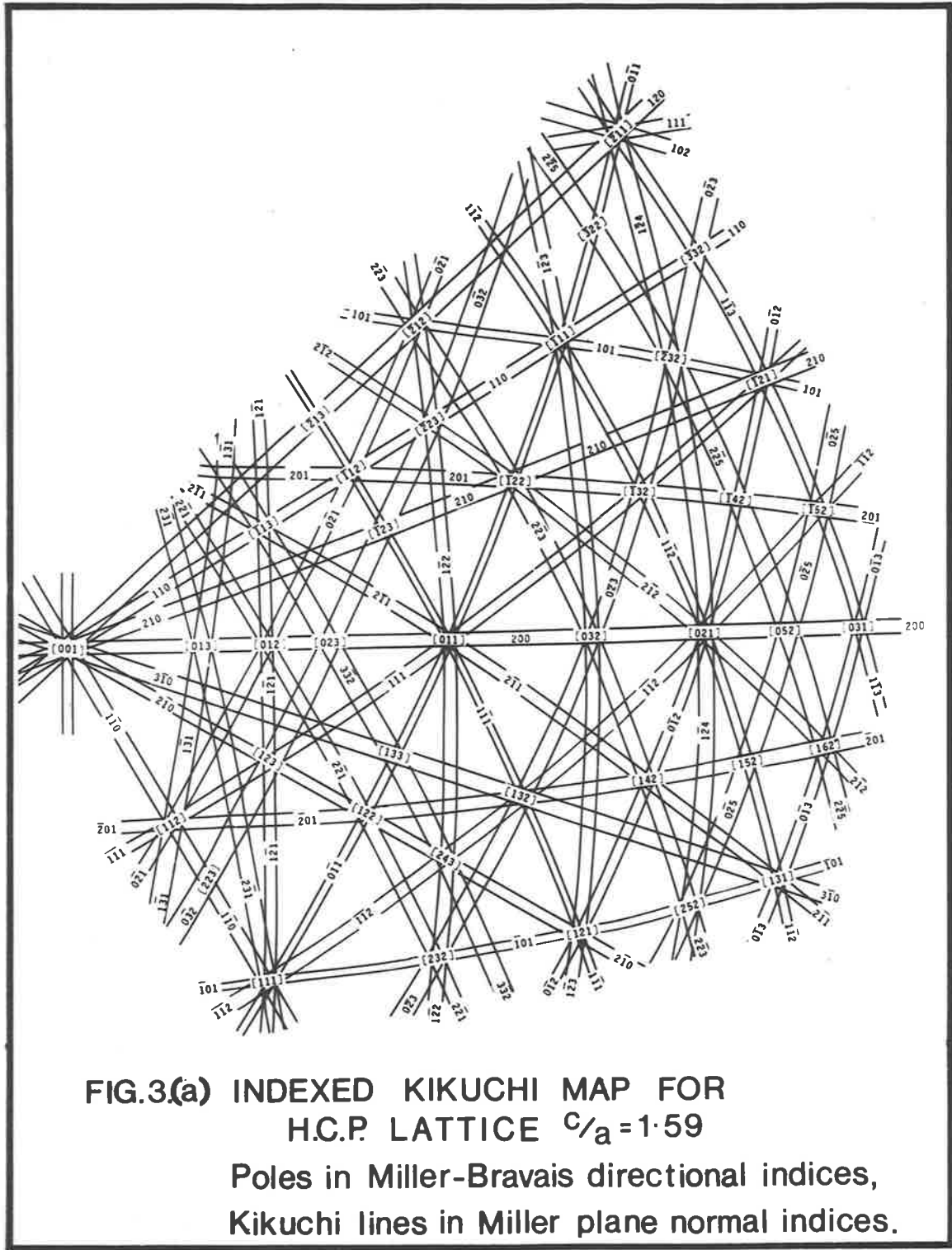
reciprocal lattice vector (which is the vector parallel to the normal to the planes represented by the reciprocal lattice point). The following example illustrates the procedure. If a diffraction point has been indexed as $(\bar{1}\bar{1}1)$, (fig. 2), the vector passing from (000) to $(\bar{1}\bar{1}1)$ is normal to the $(\bar{1}\bar{1}1)$ plane, and is denoted by the reciprocal lattice vector $g(\bar{1}\bar{1}1)$. (This is not the $[\bar{1}\bar{1}1]$ direction, as it would be in a cubic lattice, but instead, represents the direction which is parallel to the $[\bar{5}\bar{5}1]$ direction in real space). The reciprocal lattice vectors are then located on the stereographic projection of plane normals and when corresponding directions in real space are required, the lattice direction stereographic projection can be superimposed in the usual way (3). This procedure eliminates the necessity for specifying directions in reciprocal space using directional indices and thereby removes the complications which that process involves.

3. KIKUCHI MAPS AND DIFFRACTION PATTERNS.

The value of a Kikuchi pattern for carrying out tilting experiments was established by Thomas and his colleagues (10,11,12,13). Their maps were, however, found to be inadequate for the present study on zirconium because the preferred orientation, which is developed in cold rolled and annealed zirconium, such that the zone-axes of the grains

examined in the electron microscope often fall outside the range of orientations covered by the maps.

It was therefore necessary to prepare a Kikuchi map (fig. 3a) which covered a very much larger range of orientations. Adequate allowance for the curvature of the Kikuchi lines introduced by the stereographic projection must then be made and the map shown in fig. 3a was constructed to be free of the distortion which would have resulted from the use of straight lines as in previous maps (12,13). Each pair of Kikuchi lines in fig. 3a has been given the indices of the planes from which that pair is produced - i.e. they have plane normal indices. The poles of the Kikuchi map have been given the indices of the zone axis of the planes which produce the Kikuchi lines converging to that pole, and hence the poles of the map have directional indices. For cross-reference purposes the Kikuchi map has also been indexed using Miller-Bravais indices and this map is shown in fig. 3b. Because of the closeness of some of the interplanar spacings in hexagonal lattices and the fact that Kikuchi lines are often diffuse, it is sometimes difficult to identify a pair of Kikuchi lines, or even a Kikuchi pole which does not have an array of sharp diffraction spots associated with it (10,12,14,15). This difficulty can be overcome by recording a spot diffraction pattern at one or more nearby poles and relating the orient-



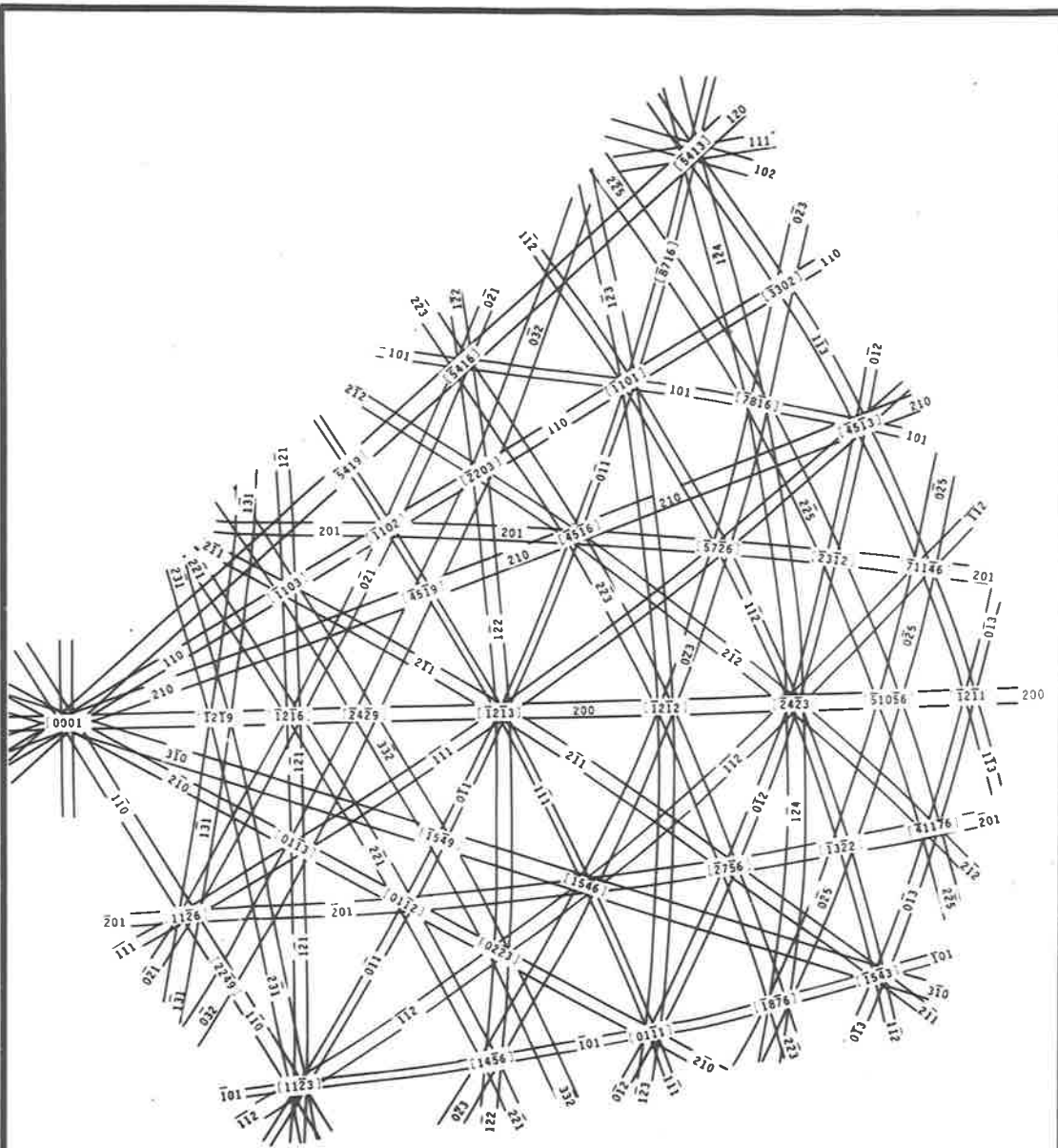


FIG.3(b) INDEXED KIKUCHI MAP FOR
H.C.P. LATTICE $c/a = 1.59$
Poles in Miller-Bravais directional indices;
Kikuchi lines in Miller plane normal indices.

ation of the crystal to these easily identified orientations with the help of the Kikuchi map.

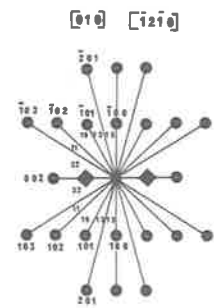
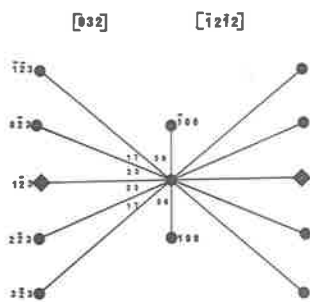
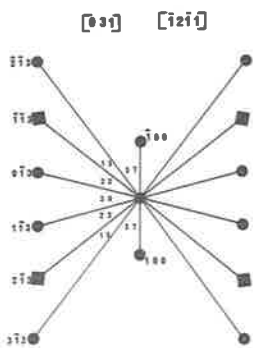
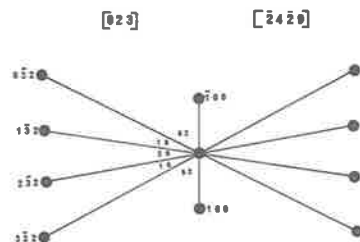
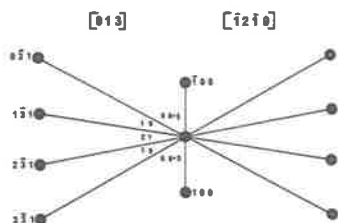
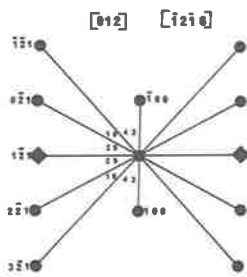
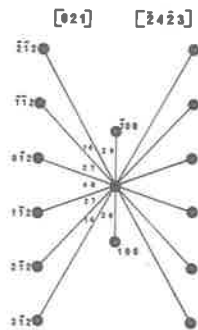
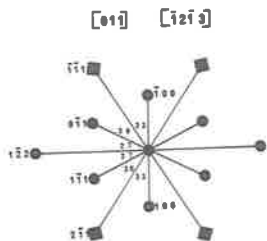
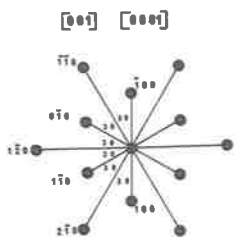
In many kinds of metallurgical investigation it is useful to be able to recognize a diffraction pattern while observing the specimen in the electron microscope. To facilitate this, scale drawings of the diffraction patterns, with zone axes corresponding to the indexed poles of the Kikuchi map, have been prepared, (fig. 4). The angles between the reciprocal lattice vectors (g) are shown to the nearest $1/2^\circ$ for $c/a = 1.59$. These diffraction patterns (or reciprocal lattice planes) have been indexed in a consistent manner using the stereographic projections referred to earlier (3). The importance of using a consistent indexing procedure for diffraction patterns has been discussed elsewhere(16).

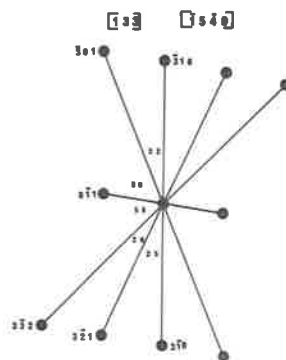
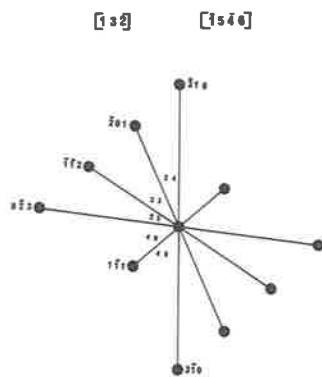
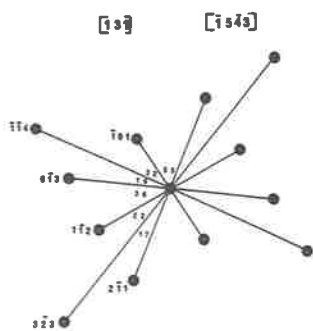
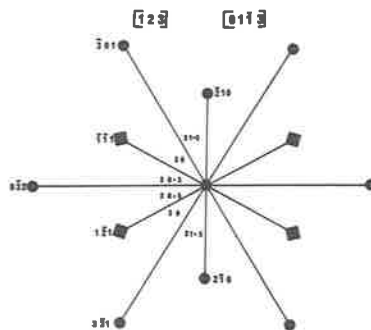
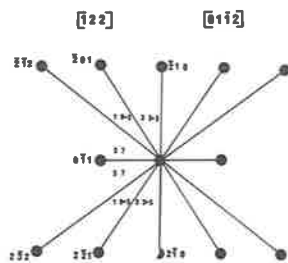
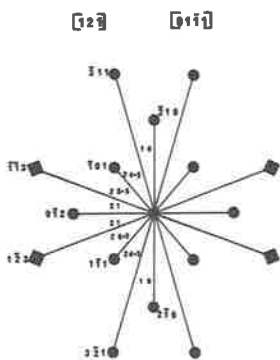
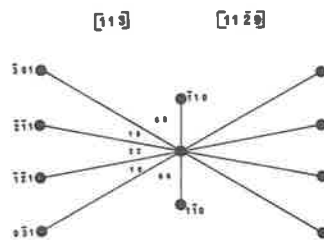
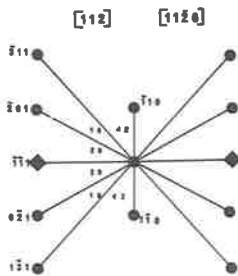
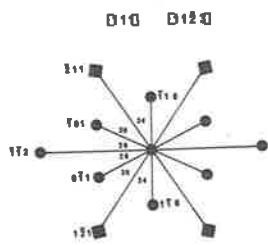
4, BURGERS VECTOR DETERMINATION.

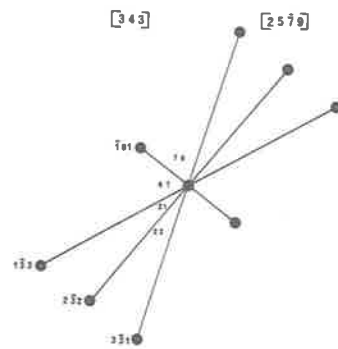
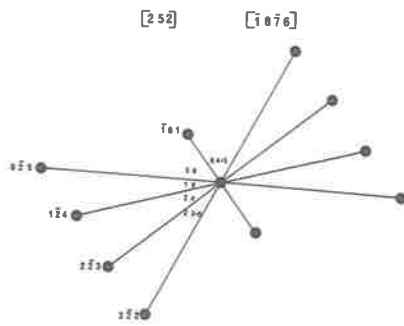
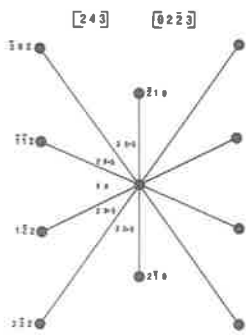
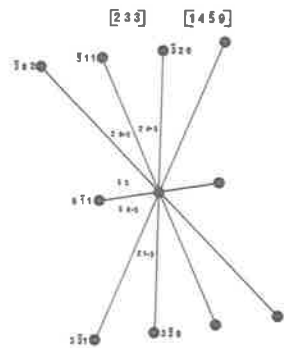
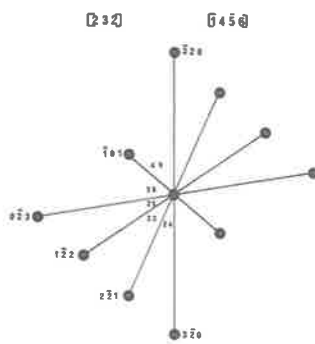
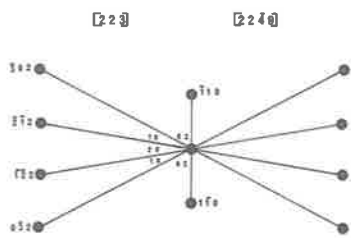
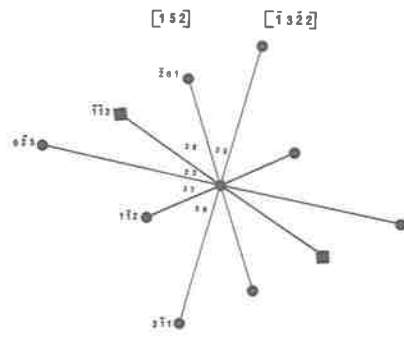
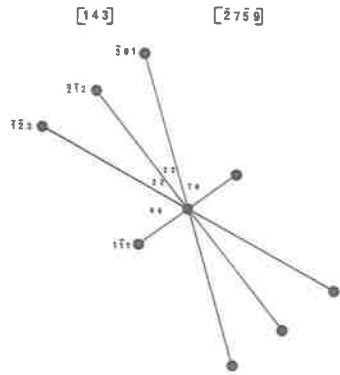
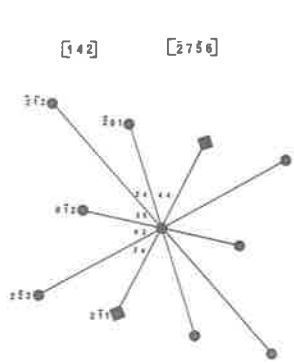
The unique determination of Burgers vectors in the electron microscope always requires careful manipulation and, for zirconium or other materials with c/a near 1.59, the above Kikuchi map, diffraction patterns and stereographic projections are invaluable.

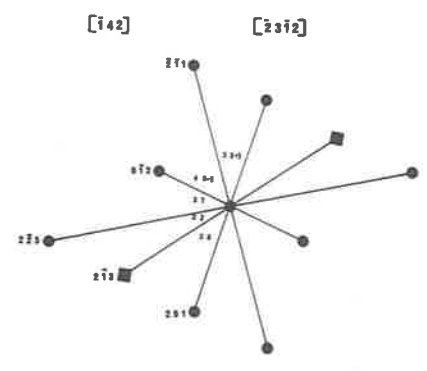
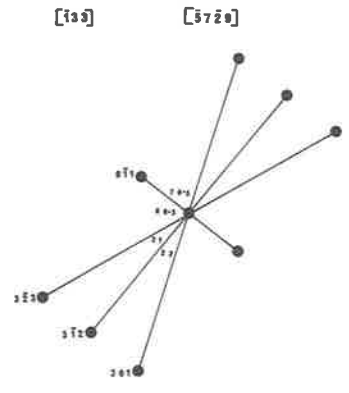
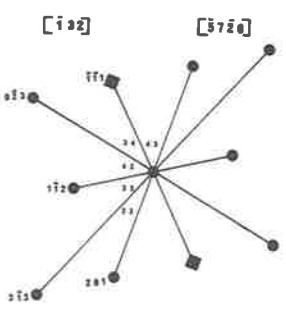
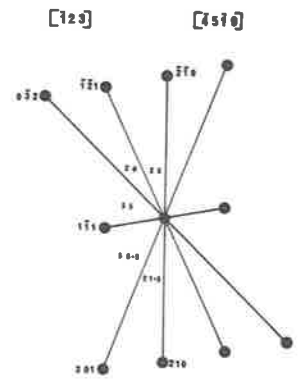
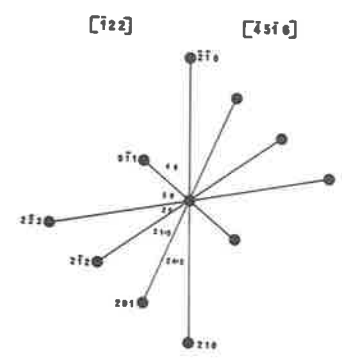
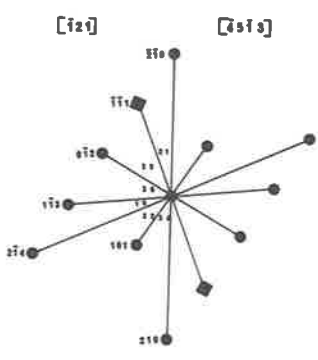
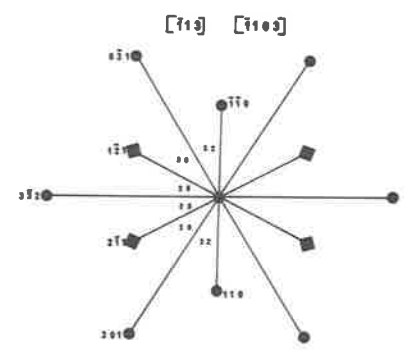
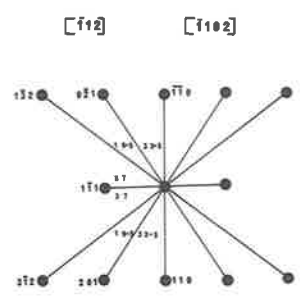
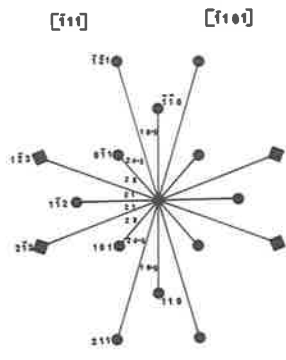
When the orientation of the specimen can be recognized in the microscope (and it is here that the plotted diffraction patterns, fig. 4, are useful), this orientation can be

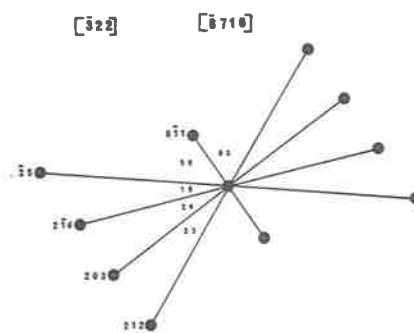
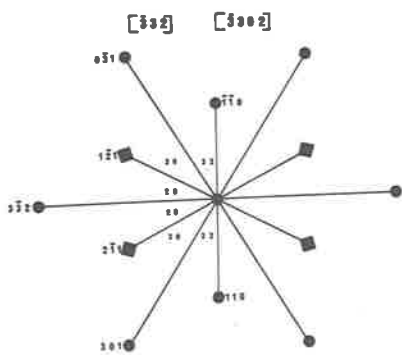
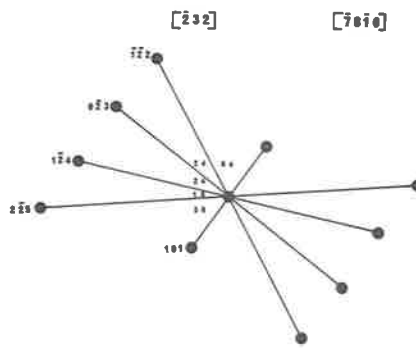
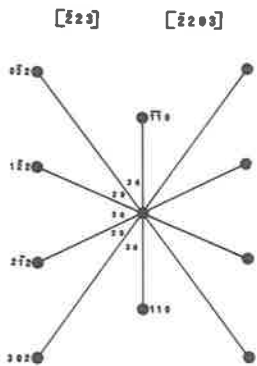
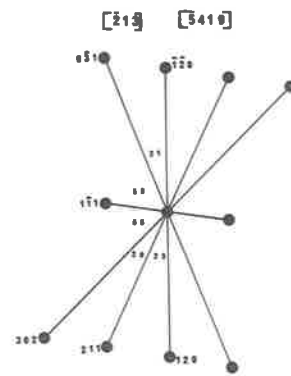
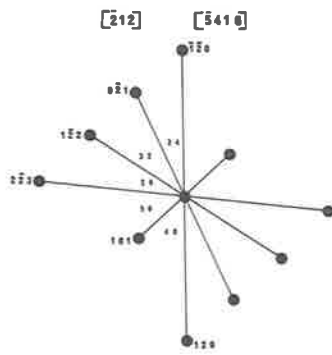
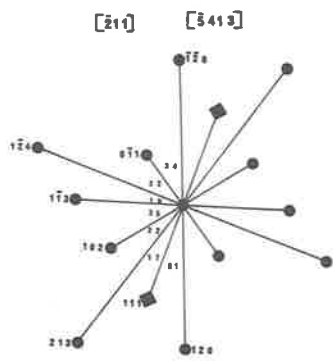
FIG. 4. Indexed diffraction patterns corresponding to poles of the Kikuchi map. Zone axes are given in both Miller and Miller-Bravais directional indices. Forbidden spots which arise due to double diffraction are indicated by diamond shaped spots.











located on the Kikuchi map and the tilting experiments necessary to uniquely determine the Burgers vector of the dislocations under examination are then fairly obvious. The principle to be remembered is that the Kikuchi lines which establish the two beam conditions for the dislocations to go out of contrast converge to the pole of the Burgers vector of those dislocations (12). It is desirable that the specimen be tilted into two or three different orientations for which the dislocations are out of contrast, and the sequence of manipulations required to produce this can be conveniently recorded on the Kikuchi map. This procedure helps in avoiding unnecessary steps which may prolong the examination of the area of interest until specimen contamination becomes a problem.

An alternative procedure for determining the Burgers vectors does not require the orientation of the specimen to be determined while it is actually in the microscope. The technique is to find, by rapidly tilting the specimen, a two-beam diffracting condition for which the dislocations are out of contrast. The image of the dislocations, the diffraction pattern which defines the two-beam conditions, and a nearby Kikuchi pole are photographed. It is then fairly simple to find another set of two-beam conditions for which the same dislocations are again out of contrast. This is done by moving along a Kikuchi line which makes a high angle with the one used

for the first extinction, to find another Kikuchi line, often nearly parallel to the first, which will again give extinction of dislocation contrast. Again, the image, the diffraction pattern and the diffraction pattern at a nearby Kikuchi pole are photographed. This process is repeated as many times as necessary. The value of the Kikuchi map then becomes apparent. After analysing the diffraction patterns, the path taken during the tilting experiments can be followed on the Kikuchi map, so that consistent indices can be given to the set of orientations for which the dislocations go out of contrast. As before, the Kikuchi lines corresponding to these two-beam conditions converge to the pole of the Burgers vector of the dislocations so that the Burgers vector can be readily determined (i.e. in each case $g \cdot b = 0$).

The above procedures are particularly valuable when it is necessary to distinguish between three Burgers vectors of the same type; e.g. $[100]$, $[110]$ and $[010]$, which are of the family $1/3 \langle 11\bar{2}0 \rangle$. Just such a problem occurs in the analysis of hexagonal dislocation networks which are produced during the high-temperature deformation of zirconium (17).

ACKNOWLEDGEMENTS.

The support of the Australian Research Grants Committee (F65/15853) and the Australian Atomic Energy

Commission (contract 69/C/13) is gratefully acknowledged. One of us (A.J.B.) is grateful for a Post-graduate Studentship provided by the Commonwealth of Australia (Department of Supply).

BIBLIOGRAPHY

1. P.G. Partridge, *Met. Rev.* (1967), 169 - 194.
2. C.R. Rarey, J., Stringer, J.W., Edington, *TMS - A.I.M.E.*, 236, (1966), 811.
3. M.E. Packer and D.R. Miller, *J. Aust. Inst. Met.*, 12, (1967), 299 - 301.
4. P.G. Partridge and R.W. Gardiner, *Acta. Met.*, 15, (1967), 387.
5. H.M. Otte and A.G. Crocker, *Phys. Stat. sol.* 9, (1965), 441.
6. C.S. Barrett and T.B. Massalski, - *Structure of Metals*. McGraw Hill, 1966, p. 84.
7. J.F. Nicholas, *Phys. Stat. Sol.*, (a), 1, (1970),
8. P.R. Okamoto and G. Thomas, *Scripta Met.*, 1 (1967), 25 - 28.
9. P.R. Okamoto and G. Thomas, *Phys. Stat. Sol.*, 25, (1968) 81 - 91.
10. M. von Heimendahl, W. Bell and G. Thomas, *J. App. Phys.*, 35, (1964), 3614 - 3616.
11. G. Thomas, *TMS - AIME*, 233, (1965), 1608 - 1619.
12. P.R. Okamoto, E. Levine and G. Thomas, *J. App. Phys.* 38, (1967), 289 - 296.
13. P.R. Okamoto and G. Thomas, *Acta. Met.* 15, (1967), 1325 - 1335.
14. E. Levine, *J. Less Common Metals*, 16, (1968), 157 - 161.
15. P.B. Hirsch, A. Howie, R.B. Nicholson, D.W. Pashley, M.J. Whelan. "Electron Microscopy of Thin Crystals", (Butterworths, London), 1965, p. 498.
16. A.J. Bedford, *J. Less Common Metals*, 22, (1970), 141 - 148.
17. A.J. Bedford and D.R. Miller (to be published).

APPENDIX 3

PUBLISHED PAPERS

B. ON INDEXING ELECTRON DIFFRACTION PATTERNS FOR HEXAGONAL ZIRCONIUM ALLOYS

J. Less-Common Metals, 22 (1970), 141 - 148.

A recent paper by Chaturvedi and Singh (1) on standard single crystal electron diffraction patterns contains a number of errors and inconsistencies which may cause difficulties if the patterns are used for the solution of crystallographic problems.

Tables I and II of that paper contain several numerical errors which are important if the implied accuracy of the tables is to be achieved. Further, the type of bracketing used in the heading of Table II is incorrect, while the indices 200, wherever they appear in Tables I and II, should be replaced by 201. Tables I, II and III in the present paper have been produced using the values of a and c given by Chaturvedi and Singh (α' phase, $a = 3.225\text{\AA}$, $c = 5.132\text{\AA}$; ω phase $a = 5.019\text{\AA}$, $c = 3.089\text{\AA}$) and a computer program developed by Packer and Miller (2) and modified by Borland (3). Interplanar spacings (Table I) are accurate to 0.0001\AA , and angles (Tables II and III) are accurate to 0.01 degrees. The scope of these tables has been increased by the inclusion of many more of the planes which give rise to Bragg reflections. Some indices of equivalent planes have been included for reference purposes, and their interplanar spacings and the

angles which they make with (001), (100) and (101) planes calculated. However, it must be noted that for general usage, Tables II and III will still be found inadequate.

There are also some errors in the indexing of the diffraction patterns of Chaturvedi and Singh. For example, the $\bar{2} 1 \bar{3}$ spot of the (031) pattern in fig. 1b is a double diffraction spot and the $\bar{1} 2 \bar{2}$ index on the (011) diagram of fig. 2a is on the wrong spot. Again, in all figures, round brackets should be replaced by square brackets since the indices represent the direction which is parallel to the normal to the plane of the foil and not the indices of the plane of the foil. The importance of adhering to this convention in hexagonal lattices, where the indices of a direction are not, in general, the same as those of the plane to which it is normal, cannot be emphasized too strongly. This point has been made previously by, for example, Partridge (4) who corrected several confusing errors in earlier literature concerned with plane normals and directional indices in hexagonal lattices.

An inconsistency occurs in the indexing of the twelve diffraction patterns for each hexagonal lattice. In each of the groups, three of the patterns (011), (001) and (211), have been indexed in the opposite sense to the others so that all the diffraction patterns cannot be referred to a single

stereographic projection. As a result, a great deal of confusion would arise if the diffraction patterns of Chaturvedi and Singh were to be used to do more than merely recognize the general type of orientation to which the patterns belong.

The diffraction patterns for the hexagonal lattice given by Hirsch et al. (5) are also defective in the ways referred to above, and indeed this is widely known. However, since that book is almost universally used as a text and reference book the point is again made here.

Difficulties of this kind can be avoided by referring to stereographic projections of the kind published by Packer and Miller (2) who, using a computer program, prepared stereographic projections of both plane normals and directions in the three-index notation for hexagonal crystals whose c/a ratio was near 1.59.

Another important point is that if detailed crystallographic data are to be obtained from a group of diffraction patterns they should all relate to one symmetry area of the stereographic projection. The patterns illustrated by Chaturvedi and Singh with zone-axes other than $[211]$, $[311]$, 411 and 100 are in the segment $[001] - [010] - [110]$. Furthermore, $[211]$ belongs to the same family of directions as $[121]$ and is therefore redundant. To place the other patterns in the same area, $[231]$ should be used instead of

[311], [341] should replace [411], and [110] should replace [100]. It is especially important to use consistently-indexed diffraction patterns belonging to one symmetry area of the stereographic projection if different Burgers vectors of the same type are to be distinguished.

It is hoped that the following twenty-four consistently-indexed diffraction patterns, figs. 1 and 2, which correspond approximately to those of Chaturvedi and Singh (1), will serve to eliminate difficulties of the kind referred to above. The [121] pattern has been included twice in each figure to show that what was indexed as (211), is in fact the same as the [121] pattern.

The ratios of reciprocal lattice vectors have been given to three decimal places in all cases (± 0.001) and the angles to two decimal places (± 0.01). In many instances the chosen angles and ratios differ from those given by Chaturvedi and Singh, thus giving a more uniform and useful coverage of the diagrams. The accuracy given in these diagrams is only warranted if results are to be computerized and if the electron microscope used is calibrated extremely accurately.

The patterns of figs. 1 and 2 have been plotted to a scale based on reciprocal lattice dimensions and if they are to be used only for comparison purposes, they may be enlarged from the figures to a size appropriate to the particular camera

length used. However these will only be approximate and for greater accuracy it would be necessary for each user to redraw the diagrams to scale using the computed angles and ratios.

ACKNOWLEDGEMENTS

The work on hexagonal crystallography is involved in projects supported by grants to Professor D.R. Miller by the Australian Research Grants Committee (F65/15853) and the Australian Atomic Energy Commission (69/C/13). Acknowledgement is also gratefully given to Dr. J.F. Nicholas for his helpful comments and criticisms during the preparation of the manuscript. The author also acknowledges the tenure of a Commonwealth Post Graduate Studentship.

A.J. BEDFORD.

Material Science Group,
Chemical Engineering Department,
The University of Adelaide,
North Terrace,
ADELAIDE, 5000,
South Australia.

REFERENCES

1. M. CHATURVEDI and R.N. SINGH, J. Less Common Metals, 18
(1969), 71
2. M.E. PACKER and D.R. MILLER, J. Aust. Inst. Metals, 12, 4,
(1967) 299
3. D.W. BORLAND, - Private Communication
4. P.G. PARTRIDGE, Met. Rev., (1967), 169 - 194.
5. P.B. HIRSCH, A. HOWIE, R.B. NICHOLSON, D.W. PASHLEY,
M.J. WHELAN (eds.) Electron Microscopy of Thin Crystals,
Butterworths, London, 1965, p. 503.

TABLE I

Interplanar Spacings of various planes in α' and ω phases.

No.	(hkl)	d-Spacings (Å) *	
1	100	2.7929	4.3466
2	002	2.5660	1.5445
3	101	2.4532	2.5179
4	102	1.8896	1.4554
5	110, $2\bar{1}0$, $1\bar{2}0$	1.6125	2.5095
6	111, $2\bar{1}1$	1.5383	1.9478
7	103	1.4588	1.0019
8	200	1.3964	2.1733
9	112, $2\bar{1}2$	1.3653	1.3153
10	201	1.3476	1.7775
11	202	1.2266	1.2590
12	113, $2\bar{1}3$	1.1734	0.9526
13	104	1.1659	0.7603
14	203	1.0818	0.9305
15	210, $3\bar{1}0$	1.0556	1.6429
16	211, $3\bar{1}1$	1.0340	1.4505
17	114	1.0040	0.7380
18	212, $3\bar{1}2$	0.9762	1.1253
19	105	0.9634	0.6116
20	204	0.9448	0.7277
21	213, $3\bar{1}3$	0.8984	0.8725

* Accuracy of interplanar spacings $\pm 0.0001\text{\AA}$.

TABLE II

Angles between planes (hkl) and (pqr) of the α' phase.

No.	(pqr)	(hkl) Angles (deg.)		
		001	100	101
1	100	90.00	0.00	28.56
2	001	0.00	90.00	61.44
3	101	61.44	28.56	0.00
4	102	42.58	47.42	18.87
5	110, $2\bar{1}0$	90.00	30.00	40.48
*	$1\bar{2}0$	90.00	90.00	90.00
6	111, $2\bar{1}1$	72.56	34.29	29.66
7	103	31.49	58.51	29.96
8	200	90.00	0.00	28.56
9	112, $2\bar{1}2$	57.85	42.84	26.05
10	201	74.78	15.22	13.33
11	202	61.44	28.56	0.00
12	113, $2\bar{1}3$	46.69	50.94	28.19
13	104	24.67	65.33	36.77
14	203	50.77	39.23	10.67
15	210, $3\bar{1}0$	90.00	19.11	33.90
16	211, $3\bar{1}1$	78.38	22.25	24.60
17	114	38.51	57.37	32.04
18	212, $3\bar{1}2$	67.64	29.09	18.30
19	105	20.18	69.82	41.27
20	204	42.58	47.42	18.87
21	213, $3\bar{1}3$	58.32	36.47	16.80

* As an example, the $(1\bar{2}0)$ plane is included to show that not all the (110) planes make the same angle with (hkl). Thus the table is limited to only the specific planes given.

TABLE III

Angles between planes (hkl) and (pqr) of the ω phase.

No.	(pqr)	(hkl) Angles (deg)		
		001	100	101
1	100	90.00	0.00	54.60
2	001	0.00	90.00	35.40
3	101	35.40	54.60	0.00
4	102	19.56	70.44	15.84
5	110, $2\bar{1}0$	90.00	30.00	59.89
*	$1\bar{2}0$	90.00	90.00	90.00
6	111, $2\bar{1}1$	50.91	47.77	25.40
7	103	13.33	76.67	22.07
8	200	90.00	0.00	54.60
9	112, $2\bar{1}2$	31.61	63.00	16.84
10	201	54.87	35.13	19.47
11	202	35.40	54.60	0.00
12	113, $2\bar{1}3$	22.31	70.81	19.17
13.	104	10.08	79.92	25.33
14	203	25.35	64.65	10.05
15	210, $3\bar{1}0$	90.00	19.11	56.81
16	211, $3\bar{1}1$	61.99	33.46	30.00
17	114	17.10	75.25	22.08
18	212, $3\bar{1}2$	43.23	49.67	14.35
19	105	8.08	81.92	27.32
20	204	19.56	70.44	15.84
21	213, $3\bar{1}3$	32.08	59.88	11.08

* As for Table II

Fig. 1.

Twelve common electron diffraction patterns for an h.c.p. alloy with $c/a = 1.591$. Spots which appear due to double diffraction are marked with an "X".

12i⊙	200⊙	32i⊙B	21a⊙B	11a⊙C	01a⊙D	20f⊙B	210⊙C	22i⊙D
02i⊙	100⊙A	22i⊙C						
i2i⊙	000⊙O	12i⊙D	100⊙A	000⊙O	100⊙	01i⊙A	000⊙O	01i⊙
22i⊙	100⊙	02i⊙						
32i⊙	200⊙	i2i⊙	01a⊙	11a⊙	21a⊙	22i⊙	210⊙	20a⊙

[012]

[031]

[122]

AOB=42.23	$\frac{OA}{OB}=0.370$	AOB=50.93	$\frac{OA}{OB}=0.420$	AOB=56.68	$\frac{OA}{OB}=0.549$
AOC=61.15	$\frac{OA}{OC}=0.482$	AOC=74.86	$\frac{OA}{OC}=0.522$	AOC=90.00	$\frac{OA}{OC}=0.657$
AOD=90.00	$\frac{OA}{OD}=0.551$	AOD=105.14	$\frac{OA}{OD}=0.522$	AOD=123.32	$\frac{OA}{OD}=0.549$

01a⊙B	10a⊙C	21i⊙D
11i⊙A	000⊙O	11i⊙
21i⊙	10a⊙	01a⊙

[231]

01a⊙B	10a⊙C	21i⊙D
11i⊙A	000⊙O	11i⊙

[341]

01a⊙B		
11i⊙C	10i⊙A	
210⊙D	000⊙O	210⊙
10f⊙	11f⊙	
01a⊙		

[121]

AOB=50.43	$\frac{OA}{OB}=0.595$	AOB=51.85	$\frac{OA}{OB}=0.475$	AOB=49.52	$\frac{OA}{OB}=0.770$
AOC=86.85	$\frac{OA}{OC}=0.770$	AOC=79.73	$\frac{OA}{OC}=0.595$	AOC=99.05	$\frac{OA}{OC}=1.000$
AOD=125.62	$\frac{OA}{OD}=0.627$	AOD=112.94	$\frac{OA}{OD}=0.557$	AOD=139.52	$\frac{OA}{OD}=0.657$

Fig. 2.

Twelve common electron diffraction patterns for an h.c.p. alloy with $c/a = 0.615$. Spots which appear due to double diffraction are marked with an "X".

112⊙ 002⊙A 112⊙B 222⊙

111⊙ 001⊙ 111⊙C 221⊙

110⊙ 000⊙O 110⊙D 220⊙

111⊙ 001⊙ 111⊙ 221⊙

[110]

AOB=19.56 $\frac{OA}{OB}=0.942$
 AOC=35.40 $\frac{OA}{OC}=1.630$
 AOD=90.00 $\frac{OA}{OD}=2.815$

212⊙ 002⊙A 212⊙B

210⊙ 000⊙O 210⊙C

212⊙ 002⊙ 212⊙D

[120]

AOB=31.61 $\frac{OA}{OB}=0.852$
 AOC=90.00 $\frac{OA}{OC}=1.625$
 AOD=148.39 $\frac{OA}{OD}=0.852$

⊙ 122⊙D ⊙

211⊙ 111⊙ 011⊙C 111⊙B

200⊙ 100⊙ 000⊙O 100⊙A 200⊙

111⊙ 011⊙ 111⊙ 211⊙

⊙ 122⊙ ⊙

[011]

AOB=47.77 $\frac{OA}{OB}=0.448$
 AOC=73.16 $\frac{OA}{OC}=0.579$
 AOD=90.00 $\frac{OA}{OD}=0.303$

120⊙D

210⊙ 110⊙ 010⊙C 110⊙B

100⊙ 000⊙O 100⊙A

110⊙ 010⊙ 110⊙ 210⊙

120⊙

[001]

AOB=30.00 $\frac{OA}{OB}=0.577$
 AOC=60.00 $\frac{OA}{OC}=1.000$
 AOD=90.00 $\frac{OA}{OD}=0.577$

212⊙ 112⊙D 012⊙C 112⊙B

200⊙ 100⊙ 000⊙O 100⊙A 200⊙ 300⊙

112⊙ 012⊙ 112⊙ 212⊙ 312⊙

[021]

AOB=63.00 $\frac{OA}{OB}=0.303$
 AOC=80.36 $\frac{OA}{OC}=0.335$
 AOD=99.64 $\frac{OA}{OD}=0.335$

210⊙D 110⊙C 010⊙B

101⊙ 000⊙O 101⊙A

012⊙ 111⊙ 210⊙

[121]

AOB=30.11 $\frac{OA}{OB}=0.578$
 AOC=60.22 $\frac{OA}{OC}=1.000$
 AOD=120.11 $\frac{OA}{OD}=0.997$

212 ⊙ B 113 ⊙ C 113 ⊙ D 113 ⊙

121 ⊙ 200 ⊙ 321 ⊙ B
 021 ⊙ 100 ⊙ A 221 ⊙ C
 121 ⊙ 000 ⊙ O 121 ⊙ D
 221 ⊙ 100 ⊙ 021 ⊙
 321 ⊙ 200 ⊙ 121 ⊙

[012]

201 ⊙ B 210 ⊙ C 221 ⊙ D
 011 ⊙ A 000 ⊙ O 011 ⊙
 221 ⊙ 210 ⊙ 211 ⊙

[122]

113 ⊙ 013 ⊙ 113 ⊙ 213 ⊙

[031]

AOB=48.13	$\frac{OA}{OB}=0.334$	AOB=70.81	$\frac{OA}{OB}=0.219$	AOB=45.10	$\frac{OA}{OB}=0.706$
AOC=65.86	$\frac{OA}{OC}=0.409$	AOC=83.38	$\frac{OA}{OC}=0.231$	AOC=90.00	$\frac{OA}{OC}=0.997$
AOD=90.00	$\frac{OA}{OD}=0.448$	AOD=96.62	$\frac{OA}{OD}=0.231$	AOD=134.90	$\frac{OA}{OD}=0.706$

102 ⊙ B 211 ⊙ C 320 ⊙ D 102 ⊙ B 112 ⊙ C 121 ⊙ D 130 ⊙
 111 ⊙ A 000 ⊙ O 111 ⊙ 222 ⊙ 111 ⊙ A 000 ⊙ O 111 ⊙ 122 ⊙
 210 ⊙ 211 ⊙ 102 ⊙

[231]

AOB=47.84	$\frac{OA}{OB}=0.578$	AOB=43.41	$\frac{OA}{OB}=0.398$	AOB=30.11	$\frac{OA}{OB}=0.578$
AOC=82.84	$\frac{OA}{OC}=0.774$	AOC=64.45	$\frac{OA}{OC}=0.522$	AOC=60.22	$\frac{OA}{OC}=1.000$
AOD=123.19	$\frac{OA}{OD}=0.652$	AOD=95.77	$\frac{OA}{OD}=0.576$	AOD=120.11	$\frac{OA}{OD}=0.997$

[341]

[121]

012 ⊙ B
 211 ⊙ 111 ⊙ C 100 ⊙ A 210 ⊙
 210 ⊙ D 000 ⊙ O 100 ⊙ 120 ⊙
 101 ⊙ 111 ⊙ 120 ⊙
 010 ⊙

BIBLIOGRAPHY

- ABSON, D.J., and JONAS, J.J., (1970), *Met. Sci. Jnr.*, 4, 24.
- ALMOND, E.A., and HULL, D., (1966), *Phil. Mag.*, 14, 515.
- ALMOND, E.A., (1969), *TMS-AIME*, 245, 2519.
- AMBLER, J.F.R., (1968), *J. Nucl. Mat.*, 28, 237.
- ARUNACHALAM, V.S., LEHTINEN, B., OSTBERG, G., (1967),
J. Nucl. Mat., 21, 241.
- ARUNACHALAM, V.S., OSTBERG, G., LEHTINEN, B., (1968),
J. Nucl. Mat., 28, 336.
- ASHBEE, K.H.G., and HEAVENS, J.W., (1967), *TMS-AIME* 239, 1859.
- BABYAK, W.J., (1967), *TMS-AIME*, 239, 252.
- BAILEY, J.E., (1962), *J. Nucl. Mat.*, 7, 300.
- BAILEY, J.E., (1963), *Acta Met.*, 11, 267.
- BAILEY, J.E. and HIRSCH, P.B., (1960), *Phil. Mag.*, 5, 485.
- BALDWIN, D.H., and REED-HILL, R.E., (1965), *TMS-AIME*, 233, 248.
- BALDWIN, D.H., and REED-HILL, R.E., (1968), *TMS-AIME*, 242, 661.
- BARRETT, C.J., and MASSALSKI, T.B., (1966), "Structure of
Metals", McGRAW-HILL (N.Y. and London).
- BASINSKI, Z.S., (1962), *Fifth International Congress for
Electron Microscopy (Academic Press - N.Y.)*, p. B-13.
- BEDFORD, A.J., (1970), *J. Less-Common Metals*, 22, 141.
- BEDFORD, A.J. and MILLER, D.R., (1970), *J. Aust. Inst. Met.*,
15, 179.
- BERGHEZAN, A., FOURDEUX, A., AMELINCKX, S., (1961), *Acta Met.*,
9, 464.
- BESAG, F.M., and BULLEN, F.P., (1965), *Phil. Mag.*, 12, 41.

- BLACKBURN, M.J., and WILLIAMS, J.C., (1967), TMS-AIME 239, 287.
- BOKROS, J.C., (1960), TMS-AIME, 218, 351.
- BONEFIELD, W., (1965), TMS-AIME, 233, 1719.
- BOYD, J.D., HAHN, G.T., ROSENFELD, A.R., VOTAVA, E., (1969),
Trans-ASM, 62, 206.
- BRAMMER, I.S. (1965), Techniques for Electron Microscopy,
2nd Edition, Editor D.H. Kay, (Oxford-Blackwell
Scientific Publications).
- BULLEN, F.P., HENDERSON, F., HUTCHINSON, M.M., WAIN, H.L.,
(1964), Phil. Mag., 8, 285.
- CAPLAN, I.L., (1967), Rev. Sci. Instrum., 38, 1489.
- CHATURVEDI, M., and SINGH, R.N., (1969), J. Less-Common
Metals, 18, 71.
- COLEMAN, C.E., and HARDIE, D., (1966), J. Inst. Metals, 94, 387.
- CONRAD, H., (1963), N.P.L. Symposium No. 15, 479.
- COTTRELL, A.H., (1963), N.P.L. Symposium No. 15, 456.
- CRUSSARD, C., (1963), N.P.L. Symposium No. 15, 548.
- DAMIANO, V.V., (1963), TMS-AIME 227, 788.
- DESALVO, A., and ZIGNANI, F., (1966), J. Nucl. Mats., 20, 108.
- DIETER, G.E., (1961), "Mechanical Metallurgy", McGraw-Hill,
p. 125.
- DOUGLASS, D.L. (1963), Atomic Energy Review, 1, 71.
- EDINGTON, J.W., LINDLEY, T.C., SMALLMAN, R.E., (1964), Acta.
Met., 12, 1025.
- EDMONDS, D.V., and BEEVERS, C.J., (1968), Met. Sci. Jnr., 2, 228.
- ELLS, C.E., (1968), J. Nucl. Mat., 28, 129.
- ENTWHISTLE, K.M., (1962), Met. Rev., 7, 175.
- FIDLERIS, V., (1968a), J. Nucl. Mat., 26, 51.

- FIDLERIS, V., (1968b), ASTM Symposium, "Application Related Phenomena in Zirconium and Hafnium Alloys", Philadelphia.
- FISHER, E.S., and ALFRED, L.C.R., (1968), TMS-AIME, 242, 1575.
- FRANK, F.C., (1965), Acta Cryst., 18, 862.
- FULLER, P.G., (1968-70), PhD Research - Private Communications.
- FULLER, P.G. and IDE, B.H., (1970), J. Phys. E. (Scientific Instruments), 3.
- GIDLEY, J.A.F., and DAVIES, R.A., (1967), J. Sci. Instrum., 44, 297.
- GILMAN, J.J., and JOHNSTON, W.G., (1962), Solid State Physics, 13.
- GRANATO, A., and LUCKE, K., (1956), J. App. Phys., 27, 583.
- GUARD, R.W., and KEELER, J.H., (1957), Trans-ASM 49, 449.
- HAHN, G.T., (1962), Acta Met., 10, 727.
- HIRSCH, P.B., HOWIE, A., NICHOLSON, R.B., PASHLEY, D.W., WHELAN, M.J., (1965), "Electron Microscopy of Thin Crystals". (Butterworths - London).
- HIRSCH, P.B., HOWIE, A., WHELAN, M.J., (1960), Proc. Roy. Soc. Lond., A252, 61.
- HOLMES, J.J., (1964), J. Nucl. Mat., 13, 137.
- HONEYCOMBE, R.W.K., - Deformation of Metal Crystals.
- HOWE, L.M., WHITTON, J.L., McGURN, J.F., (1962), Acta. Met., 10, 773.
- HULL, D., (1968), Introduction to Dislocations, (Pergamon Press) p. 247.
- JACQUET, P.A., (1950), Metallurgia, 270.
- KEELER, J.H., (1955), Trans-ASM 47, 157.
- KEELER, J.H., HIBBARD, W.R. Jr., DECKER, B.F., (1953), Trans-AIME (J. of Metals) p. 932.

- KEH, A.S., and WEISSMANN, S., (1963), "Electron Microscopy and Strength of Crystals", Eds. G. Thomas and J. Washburn, (Interscience, N.Y.) P. 231.
- KUHLMAN-WILSDORF, D., MADDIN, R., WILSDORF, H.G.F., (1962), ASM Symposium on Strengthening Mechanisms in Solids p. 137.
- KUHLMAN-WILSDORF, D., and WILSDORF, H.G.F., (1963), "Electron Microscopy and Strength of Crystals", Eds. G. Thomas and J. Washburn (Interscience, N.Y.) p. 575.
- KUNZ, F.W., and BIBB, A.E., (1960), TMS-AIME, 218, 133.
- LEVINE, E., (1968), J. Less-Common Metals 16, 157.
- LEVINE, E., BELL, W.L., THOMAS, G., (1966), J. App. Phys., 37, 2141.
- LORKING, K.F., (1959), J. Aust. Inst. Metals, 9, 22.
- LOUTHAN, M.R., and ANGERMAN, C.L., (1966) TMS-AIME, 236, 221.
- MANJOINE, M.J., and MUDGE, W.L., (Jr.), (1954), Proc. ASTM, 54, 1050.
- MARTIN, J.L., and REED-HILL, R.E., (1964), TMS-AIME, 230, 780.
- MIEKK-OJA, H.M., (1966), Phil. Mag., 13, 367.
- MILLER, D.R., and CRAWFORD, R.C., (1968), Phil. Mag., 17, 333.
- McGEARY, R.K., and LUSTMAN, B., (1953), Trans-AIME, (Journal of Metals), p. 284.
- McLEAN, D., (1962), Mechanical Properties of Metals, John Wiley, N.Y. - London, p. 144.
- NANKIVELL, J.F., (1963), Optik, 20, 171.
- NICHOLAS, J.F., (1966), Acta Cryst., 21, 880.
- NICHOLAS, J.F., (1970), Phys. Stat. Sol., (a) 1.
- NOWICK, A.S., (1953), Prog. Met. Phys., 4, 1.
- OHR, S.M., and BESHES, D.N., (1963), Phil. Mag., 8, 1343.
- OKAMOTO, P.R., LEVINE, E., THOMAS, G., (1967), J. App. Phys., 38, 289.

- OKAMOTO, P.R., and THOMAS, G., (1967a) Scripta Met., 1, 25.
- OKAMOTO, P.R., and THOMAS, G., (1967b) Acta Met., 15, 1325.
- OKAMOTO, P.R., and THOMAS, G., (1968), Phys. Stat. Sol., 25, 81.
- OTTE, H.M., and CROCKER, A.G., (1965), Phys. Stat. Sol., 9, 441.
- PACKER, M.E., and MILLER, D.R., (1967), J. Aust. Inst. Met., 12, 299.
- PARTRIDGE, P.G., (1967), Met. Rev., 12, 169.
- PARTRIDGE, P.G., and GARDINER, R.W., (1967), Acta Met., 15, 387
- PICKLESIMER, M.L., (1966), "Zirconium and Its Alloys".
(Eds. J.P. Pensler, E.C.W. Perryman, W.W. Smeltzer)
Electrochemical Society Inc. - N.Y., p. 289.
- PITTINATO, G.F., and FREDERICK, S.F., (1969), TMS-AIME, 245
2299.
- PRICE, P.B., (1963), "Electron Microscopy and Strength of
Crystals", Eds. G. Thomas and J. Washburn,
(Interscience, N.Y.), p. 41.
- RAMASWAMI, B., and CRAIG, G.B., (1967), TMS-AIME, 239, 1226.
- RANZETTA, G.V.T., and SCOTT, V.D., (1963), J. Nucl. Mats., 10,
113.
- RAPPERPORT, E.J., (1959), Acta Met., 7, 254.
- RAPPERPORT, E.J., and HARTLEY, C.S., (1960), TMS-AIME 218, 869.
- RAREY, C.R., STRINGER, J., EDINGTON, J.W., (1966), TMS-AIME,
236, 811.
- RATY, R., LINDROOS, V., SAARINEN, A., FORSTEN, J., MEIKK-OJA,
H.M., (1966), J. Sci. Instrum., 43, 367.
- REED-HILL, R.E., BUCHANAN, E.R., CALDWELL, F.W. (Jr.), (1965),
TMS-AIME, 233, 1716.
- * REED-HILL, R.E. RAMACHANDRAN, V., SANTHANAM, A.J., (1969), An
Investigation of the components of the flow stress in
titanium and zirconium, Progress Report to U.S.A.E.C.,
ORO-AT-(40 - 1)-3262-10.

- REGNIER, P., and DUPOUY, J.M., (1970), Phys. Stat. Sol., 39, 79.
- ROSA, C.J., (1968), J. Less-Common Metals, 16, 173.
- ROSINGER, H.E., CRAIG, G.B., BRATINA, W.J., (1969/70), Mater. Sci. Eng., 5, 163.
- ROTSEY, W.B., VEEVERS, K., SNOWDEN, K.U., (1968-70), Private Communications.
- ROTSEY, W.B., (1969) - Tests Carried out at A.A.E.C.
- ROY, R.B., (1967), Phil. Mag., 15, 477.
- ROY, C., and JACQUES, J.G., (1969), J. Nucl. Mat., 31, 233.
- SEEGER, A., (1956), Dislocations and Mechanical Properties of Crystals, John Wiley, N.Y., p. 243.
- ** SNOWDEN, K.U., (1969), The Effect of Temperature on the Logarithmic Creep of Zircaloy-2 (To be published - Private Communication).
- SWANN, P.R., (1963), "Electron Microscopy and Strength of Crystals", Eds., G. THOMAS and J. WASHBURN (Interscience N.Y.), p. 131.
- TEGART, W.J. McG., (1959), The Electrolytic and Chemical Polishing of Metals in Research and Industry, 2nd Ed. (London - Pergamon).
- THOMAS, G., (1965), TMS-AIME, 233, 1608.
- TRECO, R.M., (1953), TRANS-ASM, 45, 872.
- TRECO, R.M., (1956), TMS-AIME, 206, 1304.
- TYSON, W.R., (1967), Acta Met., 15, 574.
- TYSON, W.R., (1969), Acta Met., 17, 863.
- VAHLDIEK, F.W., (1969), J. Less-Common Metals, 19, 83.
- VEEVERS, K., and ROTSEY, W.B., J. Nucl. Mat., 27, 108.
- VEEVERS, K., ROTSEY, W.B., SNOWDEN, K.U., (1968), Australian Atomic Energy Commission AAEC/TM491.

- VON-HEIMENDAHL, M., BELL, W., THOMAS, G., (1964), J. App. Phys., 35, 3614.
- WAHI, R.P., BHATTACHARYA, D.L., ANANTHARAMAN, T.R., (1968), J. Sci. Instrum, Ser.2, 1, 1231.
- WARRINGTON, D.H., (1970), J. Sheffield Univ. Met. Soc., 9, 23.
- WEINSTEIN, D., (1966), Electrochem. Tech., 4, 307.
- WESTLAKE, D.G., (1965), J. Nucl. Mat., 16, 215.
- WESTLAKE, D.G., (1965), TMS-AIME, 233, 368.
- WESTLAKE, D.G., (1968), J. Nucl. Mat., 26, 208.
- WHELAN, M.J. (1958), Proc. Roy. Soc. Lond., A249, 114.
- WHELAN, M.J. (1958-9), J. Inst. Metals, 87, 392.
- WILLIAMS, J.C., and BLACKBURN, M.J., (1968), Phys. Stat. Sol., 25, K1.
- WILSON, D.V., and RUSSELL, B., (1960a), Acta Met., 8, 36.
- WILSON, D.V., and RUSSELL, B., (1960b), Acta Met., 8, 468.
- YOO, M.H., and WEI, C.T., (1967), J. App. Phys., 38, 4317.
- ZENER, C., (1948), "Elasticity and Anelasticity of Metals", University of Chicago Press.

* see Metallurgical Transactions, (1970), 1, 2105.

** see J. Nucl. Mat. (1970), 36, 347.